



HAL
open science

Refined predictions for cosmic rays and indirect dark matter searches

Yoann Genolini

► **To cite this version:**

Yoann Genolini. Refined predictions for cosmic rays and indirect dark matter searches. Astrophysics [astro-ph]. Université Grenoble Alpes, 2017. English. NNT : 2017GREAY049 . tel-01736216

HAL Id: tel-01736216

<https://theses.hal.science/tel-01736216>

Submitted on 16 Mar 2018

HAL is a multi-disciplinary open access archive for the deposit and dissemination of scientific research documents, whether they are published or not. The documents may come from teaching and research institutions in France or abroad, or from public or private research centers.

L'archive ouverte pluridisciplinaire **HAL**, est destinée au dépôt et à la diffusion de documents scientifiques de niveau recherche, publiés ou non, émanant des établissements d'enseignement et de recherche français ou étrangers, des laboratoires publics ou privés.

THÈSE

Pour obtenir le grade de

DOCTEUR DE LA COMMUNAUTÉ UNIVERSITÉ GRENOBLE ALPES

Spécialité : **Physique théorique**

Arrêté ministériel du 25 mai 2016

Préparée au sein de **Laboratoire d'Annecy-le-Vieux de Physique Théorique**
et de l'école doctorale **École doctorale de physique de Grenoble**

Refined predictions for cosmic rays and indirect dark matter searches

Présentée par

Yoann Génolini

Thèse dirigée par **Pasquale Serpico et Pierre Salati**

Thèse soutenue publiquement le **10 Juillet 2017**,
devant le jury composé de :

M, Laurent Derome	DR	LPSC	Président
M, Fiorenza Donato	Prof.	Torino	Rapporteur
M, Philipp Mertsch	Prof.	TTK Aachen	Rapporteur
M, David Maurin	CR	LPSC	Examineur

Acknowledgments

Tout d'abord mes deux guides, mes étoiles bienveillantes ! Vous m'avez octroyé la liberté immense dont j'avais besoin, et toujours rappelé la bonne direction dans les moments de doute. Ma grande chance est d'avoir pu bénéficier de votre redoutable complémentarité. Pasquale mon précepteur impressionniste (et impressionnant) de la physique au quotidien et Pierre qui avec son esprit géométrique éclairé, m'expliquant et vérifiant mes résultats par sa savante calligraphie. On pourrait ainsi croire que la pierre angulaire de l'édifice ne jouait peut être que le rôle de parure, néanmoins elle permettait de se sortir des cheminements de pensée à la mode du type "win the yes need the no to win against the no". Merci pour votre humour à tous les deux, essentiel pour la motivation et la santé mentale. Pierre : responsable du rire, avec lequel, à chacune de tes venues, tu inondes au moins le premier étage ; et Pasquale : responsable culture et animation des pauses cafés. Durant ces trois années vous m'avez aussi permis de découvrir le monde : Allemagne, Hollande, Brésil, Italie, Russie, Irlande, Norvège, Corée, Vietnam...ouille surtout ne pas compter pour éviter les vertiges devant ma dette carbone..

Merci à l'administration du LAPTh, nos trois fées comme on les appelle ici qui avec précision et efficacité assure le bon fonctionnement de la machine et exhaussent nos vœux de téléportation aux quatre coins du monde. Aux Directeurs du laboratoire, (Et la on a deux concurrent niveau rire, mais peut être il leur manque un peu de coffre) qui ont su conserver une ambiance chaleureuse et familiale.

Parmi toute la colonie je tenais à remercier en VRAC: Mathieu Gauthier Lafaye pour les formules magiques à employer pour communiquer avec la matrice, Geneviève pour les sorties ski à 6h00 du mat par moins 15, Eric pour les excursions au lac à midi, Laurent et Eric pour les cols de la Forclaz à midi et les conseils vélo, Jean Philippe pour les conseils escalade, Cédric de toujours prendre le temps de répondre à mes questions naïves de physique des particules. Enfin un grand merci à tous les doctorants et post doctorants, évidemment Mathieu, Sami et Vivian avec qui ça a toujours été un plaisir de travailler, une mention particulière pour Pierre Aubert sans qui je serais encore en train de taper mon clavier en me rongant les ongles devant mes bugs de compilation, et tous les autres : Meryl, Vincent, Jordan, Thibaud, Anne, (pour les mises à jour quotidiennes sur les derniers scandales politiques !) Daniel, Romain, Thomas, Jill, Dimitri, Céline, Antje, Vincent Biz., Leo, Luis, Laura, Nina, Olympia, Angela, Kirill,..Une dédicace spéciale à notre groupe de musique, grâce à qui j'ai réalisé que si je rate ma carrière en physique je n'aurais pas non plus le charisme d'une rock-star.

Merci à mes amis de Lyon et d'ailleurs qui sont venus me rendre visite sur Annecy pour profiter de la nature de l'escalade ou du lac ! Chloé, Jeff, Arthur, Nicolas, Arnaud, Mathilde, Francois, Maelle, Elo, Jean Loup et tous les autres que je n'oublie pas ! Merci aussi à mes amis sportifs de l'aviron et du ski Bastien et Valentin, pour les weekend compèt qui nous vident bien la tête ! Et les jambes ! Je n'oublie pas mes colloc' qui m'ont supporté au quotidien et avec qui j'ai partagé

tellement de fous rires ! Cosmic CéCé spéciale dédi ! Enfin ma famille et mes parents qui chérissent sans cesse leurs trois petites poussières d'étoile, mais aussi bien sûr ces autres planètes et nos pôles attracteurs. Vous m'avez tous fait l'immense plaisir de venir ici. Et enfin Typhanie, merci pour ton soutien et l'énergie que tu m'insuffles chaque jour !

Voilà donc c'est fait !

Chers collègues, famille, amis l'heure n'est plus au discours mais à la gargantuesquerie.

Refined predictions for cosmic ray astrophysics

Abstract:

One hundred years ago, pioneering observations of air ionization revealed that the Earth is showered with particles coming from the Galaxy and beyond. Because of their high energies, these particles, or cosmic rays, are still a crucial tool in the field of particle physics, complementary to man-made accelerators. From an astrophysical point of view, the origin of cosmic rays and the mechanisms which accelerate them remain poorly understood. The current paradigm involves the sporadic production of the particles, associated with expanding shock waves from dying stars, or supernova remnants (SNRs).

Recent experiments (notably PAMELA and, more recently, AMS-02) are ushering us into a new era of measurements of cosmic ray fluxes with greatly reduced statistical uncertainties. In this dissertation, we propose and investigate new theoretical refinements of our predictions to fully benefit from these advances.

After a general introduction on cosmic ray physics, we first focus on the so-called primary species, which are directly produced by SNRs. In the context of precision measurements, the discrete nature of the SNRs in space and time, together with our substantial ignorance of their precise age and location (with the possible exception of the nearest and most recent ones) results in significant uncertainties in the predictions of fluxes on Earth. Until now, the conventional approach has relied on average trends. Here, we elaborate a statistical theory in order to compute the probability of measuring the actual flux, with respect to the ensemble average. Using the generalized version of the central limit theorem, we demonstrate that the probability distribution function of the flux is intimately related to the source distribution and follows a stable law with a heavier tail than the Gaussian distribution. Not only can our theoretical framework be extended to other cosmic ray observables, such as the lepton flux, it also can be enhanced to include a more comprehensive description of the correlations between the sources. Moreover, the method which we have developed may be applied to a variety of problems in physics/astrophysics involving heavy tail distributions.

Then, we concentrate on secondary CRs, for example the boron nuclei, which are thought to be produced only by the collisions of cosmic rays on the interstellar medium. More precisely, the boron to carbon flux ratio is a traditional tool used to understand and gauge the propagation of cosmic rays in the Galaxy. Hence a precise measurement of this ratio leads to stringent constraints on the propagation scenario. However we show that this theoretical calculation strongly depends on where these secondary species are produced, as well as on the chosen set of nuclear cross-sections. Hence, we have shown that there is at least 20% uncertainty on propagation parameters. Following novel data from AMS-02 that has just been published, we present early results of a comprehensive analysis for which we use

the semi-analytical code USINE.

Finally, these high precision measurements offer new opportunities when applied to a number of astroparticle problems. The third and final part of the thesis targets one such problem, indirect dark matter searches. Antimatter cosmic rays are thought to be secondary species and their relatively low flux make them the perfect target to look for rare processes, such as dark matter annihilation. Nonetheless, predictions of the expected background rely on the precise modelling of cosmic ray propagation and interactions in the Galaxy. We assess them under simplified assumptions and discuss two studies where we re-evaluate respectively the antiproton and the positron fluxes in light of the new AMS-02 data. Finally, we discuss some implications of our results on dark matter and astrophysics.

Keywords:

Cosmic rays phenomenology, local sources, stable laws, boron over carbon ratio, indirect dark matter searches.

Contents

1	Introduction: an overview of cosmic ray physics	1
1.1	A picture of Galactic cosmic ray physics	2
1.1.1	A brief story of cosmic rays	2
1.1.2	Salient features of cosmic rays	3
1.1.3	Sources and acceleration of cosmic rays	9
1.1.4	The magnetic environment of the Galaxy	14
1.2	Diffusion and transport of cosmic rays in the Galaxy	15
1.2.1	Transport equation of cosmic rays from microphysics	15
1.2.2	Considerations on the spatial diffusion	23
1.2.3	Reacceleration from plasma waves	23
1.2.4	Convection of cosmic rays	24
1.2.5	Isotropization of CRs in the diffusive regime	25
1.3	Interactions with the interstellar medium	28
1.3.1	The composition of the interstellar medium	28
1.3.2	Continuous energy losses	30
1.3.3	Nuclear reactions	32
1.3.4	Solar modulation	37
1.4	Summary: propagation equation and timescale comparison	39
	Bibliography	43
2	Refinements on primary species	51
2.1	On cosmic ray source discreteness in spacetime	52
2.2	Description of the problem	55
2.3	Technical aspects	59
2.3.1	Generalized central limit theorem: mathematical statement	59
2.3.2	Application of the theorem to the probability of measuring a Galactic CR flux	60
2.3.3	The case with an upper cut on the flux	64
2.3.4	Causality effect	65
2.3.5	Absence of very close and/or young sources	68
2.4	Comparison with numerical simulations	70
2.4.1	Simulation settings	72
2.4.2	Simulation results	73
2.5	Applications	76
2.6	Conclusions of the section	81
	Bibliography	84

3	Refinements on secondary species	87
3.1	Boron to carbon ratio and CR propagation	88
3.1.1	Parametric dependence	88
3.1.2	Dependence on theoretical hypotheses	94
3.2	Propagation parameters extraction and AMS-02 new release	113
3.2.1	A review of previous analyses	113
3.2.2	AMS-02: preliminary analysis	120
	Bibliography	127
4	Dark Matter searches in cosmic ray antiparticles	133
4.1	A short story of dark matter evidences	134
4.1.1	Observing the present sky	134
4.1.2	Observing the primordial sky	140
4.2	The quest of dark matter particles	144
4.2.1	Necessary dark matter properties	144
4.2.2	Indirect detection of dark matter and constraints	150
4.3	Exotic production of positron cosmic rays	153
4.3.1	Revisiting the DM hypothesis with the pinching method	154
4.3.2	Pulsars as astrophysical sources of positrons	178
4.4	Refined constraints on dark matter using the antiproton flux	185
4.4.1	Re-evaluation of the astrophysical antiproton background	186
4.4.2	Updated constraints on Dark Matter	192
4.4.3	Final remarks	195
	Bibliography	197
5	Conclusion and prospects	217
A	Solutions of the transport equation	221
A.1	Analytical solutions	221
A.1.1	Simplification and solution at high energies	221
A.1.2	Table of the high energy solutions for the 1D geometry	223
A.2	Semi-numerical solutions	226
A.2.1	Numerical method and convergence	226
A.2.2	The example of the MIN, MED, and MAX models	230
	Bibliography	232
B	On the mean galactic flux	233
C	Primary fits for antiproton computation	239
	Bibliography	239
D	French summary	245

Introduction: an overview of cosmic ray physics

Contents

1.1	A picture of Galactic cosmic ray physics	2
1.1.1	A brief story of cosmic rays	2
1.1.2	Salient features of cosmic rays	3
1.1.2.1	Composition	4
1.1.2.2	Spectrum	6
1.1.3	Sources and acceleration of cosmic rays	9
1.1.3.1	The origin of the shock	9
1.1.3.2	Fermi acceleration of particles	11
1.1.3.3	Spatial distribution of the sources	13
1.1.4	The magnetic environment of the Galaxy	14
1.2	Diffusion and transport of cosmic rays in the Galaxy	15
1.2.1	Transport equation of cosmic rays from microphysics	15
1.2.2	Considerations on the spatial diffusion	23
1.2.3	Reacceleration from plasma waves	23
1.2.4	Convection of cosmic rays	24
1.2.5	Isotropization of CRs in the diffusive regime	25
1.3	Interactions with the interstellar medium	28
1.3.1	The composition of the interstellar medium	28
1.3.2	Continuous energy losses	30
1.3.3	Nuclear reactions	32
1.3.4	Solar modulation	37
1.4	Summary: propagation equation and timescale comparison	39
	Bibliography	43

1.1 A picture of Galactic cosmic ray physics

1.1.1 A brief story of cosmic rays

The discovery of cosmic rays (CRs) occurred in the last century, although some observable consequences were noticed much earlier, in the first electrostatic experiments during the XVII century. In these experiments people made the curious observations that isolated charged objects were spontaneously discharging with time. Interestingly Charles Augustin de Coulomb (1736-1806) concluded in one of the three reports addressed to French Royal Academy of Sciences that his electroscope, made with a torsion balance, was spontaneously discharging due to the action of the air. An answer to this puzzle came almost one century later with the discovery of radioactivity by Henri Becquerel, and dedicated experiments to study its impact on air ionization were performed by Marie Skłodowska Curie with the help of the sensitive electrometer invented by her husband. At that time it was believed that the discharge was caused by the radioactive materials in Earth crust, though this was difficult to prove. A milestone was reached by Julius Elster and Hans Geitel in 1899 who shielded a gold leaf electroscope with a thick metal box. Observing that it was still spontaneously discharging, they concluded that it was probably due to highly penetrating ionizing agents outside of the container and may be outside the atmosphere like X rays or cathodic rays discovered in 1895 and 1897, respectively.

Latter in 1909 Theodor Wulf, a Jesuit priest, designed and built a more sensitive and more transportable electrometer than the gold leaf electroscopes. To test the hypothesis that the radioactivity of the Earth is the principal source of air ionization, he performed measurements with his apparatus at the top of the Eiffel tower and showed that the intensity of radiation *decreases at nearly 300 m of [altitude, to] not even to half of its ground value* corresponding to a too small decrease to confirm the hypothesis. Latter it appears that his measurements were actually biased by the radioactive iron of the Eiffel tower, although the quest for ionization continued. Pioneer balloon flights of the early 20th century were used by researchers like Albert Gockel who measured the level of ionizing radiation up to a height of 3000 meters. He coined the term *kosmische Strahlung*, cosmic radiation. He observed that ionization was not decreasing with altitude and so could not solely come from Earth radioactivity. Few months later in 1911, the Italian physicist Domenico Pacini made use of Wolf device to study ionization under water and, noted a decrease of 20% of the radiations at only 3 meters below the water. Meanwhile the Austrian physicist Victor Hess made a series of flights in a balloon to take measurements of radiation in the atmosphere, concluding that *The results of the present observations seem to be most readily explained by the assumption that a radiation of very high penetrating power enters our atmosphere from above*. Interestingly he added that *Since I found a reduction...neither by night nor at a solar eclipse, one can hardly consider the Sun as the origin*. Thus, we see that many researchers have paved the way for Hess discovery, for which he shared the 1936 Nobel prize.

Since then, cosmic rays became a tool for particle physicists with the discovery

of positrons (Anderson 1932), muons (Anderson & Seth H. Neddermeyer 1936), charged pions (Cecil Powell, César Lattes, Giuseppe Occhialini, et al 1947), strange particles (G. D. Rochester & C. C. Butler 1947), and triggered the excitement for the construction of particle colliders. While the high luminosity reached by colliders opened up the study of low probability interactions, the quest for cosmic rays has never stopped, also thanks to more and more refined measurements, because they still hide many mysteries. In the following parts we briefly review some of the main features of CR observables.

1.1.2 Salient features of cosmic rays

In this section we recall the salient features of cosmic rays based on the observables accessible from the experiments. We will give an overview of the observations which support the current paradigm in which Galactic cosmic rays are produced by dying stars, named supernova remnants (SNRs) and then propagate through the Galaxy by diffusing on its tangled magnetic field. I will highlight the successes of such a picture and the problems which are still under discussion and challenge it.

Before beginning let us introduce some useful notations. We denote by $f_a(\mathbf{r}, \mathbf{p})$ the phase space density of a CR species a . It is defined as follows:

$$f_a(\mathbf{r}, \mathbf{p}) = \frac{d^6 N_a}{d^3 x d^3 p} = \frac{d^3 n_a}{d^3 p}, \quad (1.1)$$

with n_a the density of cosmic rays per unit of volume. Assuming the momenta are isotropically distributed, f_a no longer depends on \mathbf{p} but on its module p , and $\phi_a(\mathbf{r}, p)$ is defined as the integration of f_a over the zenith and azimuthal angles:

$$\phi_a(\mathbf{r}, p) = \frac{dn_a}{dp} = 4\pi p^2 f_a(\mathbf{r}, p). \quad (1.2)$$

It is also possible for convenience to express a density in unit of energy, and in this case we define $\psi_a(\mathbf{r}, E)$, which is simply:

$$\psi_a(\mathbf{r}, E) = \frac{dn_a}{dE} = \frac{E}{p} \phi_a = 4\pi p E f_a(\mathbf{r}, p). \quad (1.3)$$

The flux of cosmic rays \mathcal{J} expressed in number of particles per unit of energy, surface, time and solid angle, is thus defined as:

$$\mathcal{J}_a(\mathbf{r}, E) = \frac{v}{4\pi} \psi_a(\mathbf{r}, p) = \frac{1}{4\pi} \phi_a = p^2 f_a(\mathbf{r}, p). \quad (1.4)$$

Note that sometimes we will express the energies in unit of kinetic energy per nucleon, and we will use the symbol E_{kn} instead of E . If the total kinetic energy is denoted E_k and with A the number of nucleons in the nucleus, we have the equality: $E_k = A E_{kn}$.

1.1.2.1 Composition

The composition of cosmic rays was the first debated topic right after their discovery in a very publicized quarrel opposing Robert Millikan and Arthur Compton (1932). The first one was arguing that CRs were composed of high energy photons, whereas the latter thought there were charged particles. Three independent observations (Alvarez & Compton, Johnson, Rossi) of an East-West asymmetry in the intensity of CRs proved Compton's ideas right: most primary cosmic rays are positively charged particles. In the following of the dissertation, the term cosmic rays refers to charged particles. Although it is somewhat "fashionable" in the so-called multi-messenger astrophysics to refer collectively to charged particles, gamma rays and neutrinos as cosmic rays. In fact, neutral high energy particles provide a wealth of complementary information since their production mechanisms rely on CR interactions. More precisely, we focus here on the composition of *Galactic* cosmic rays, that are thought to dominate above 50-100 MeV. Below this energy, several components of solar origin dominate the CR flux: the Anomalous CRs component (from MeV to some dozens of MeV), the solar flare particles (from 0.1 MeV to 100 MeV) and, the solar wind particles (which peak around the keV energy).

The composition of cosmic rays is usually meant as integral over their energy. As the quantity of CRs decreases very fast with energy, the composition is thus determined by the low energies CRs¹. Galactic CRs are mainly made of protons and helium nuclei contributing to 85% and 12.5% of the total, plus 1.5% of electrons. The remaining 1% presents an extremely rich composition with heavier nuclei and antiparticles. The wide diversity of production processes and interactions (notably between different isotopes), makes this tiny fraction a very powerful tool to unveil details of CR physics. The study of the chemical composition of cosmic rays shows a strong similarity with the one of the Solar system. This suggests that most cosmic rays are particles of the diffuse interstellar medium that have been accelerated up to very high energies thanks to some process that we discuss in section 1.1.3. However, one can notice in figure 1.1 that some elements contradict this interpretation, notably a bunch of light nuclei below carbon, and some heavier nuclei below iron. These elements are very rare in the Galactic medium because they are easily consumed by fusion reactions in the hearts of stars. In cosmic rays, we believe they are produced by so-called spallation processes, which correspond to the fragmentation of heavier nuclei colliding the interstellar medium. Hence, we distinguish amongst two different populations. The first one is made of Galactic matter accelerated by some astrophysical phenomena, and injected at high energy in the interstellar medium: this component is called *primary* component. The second is coming from the interaction of the first with the interstellar medium, and is called *secondary* component². This sharp distinction is actually very simplified as all the species do

¹Dominated by the 'GeV bump' if the integral spans this region of the spectrum. Solar modulation cuts particles off at lower energies.

²Note that this is only true when dealing with interstellar or *top of the atmosphere* fluxes. In the context of air shower experiments people call *secondary* species the high energy particles

contain some fraction of primary and secondary. Furthermore, *secondaries* may also collide the interstellar medium (ISM) and in turn produce smaller fragments which are also called secondaries. This process links the production of a light nucleus to a heavier element through a myriad of intermediate species. The understanding of all the nuclear reactions, or spallation network, is essential to predict the abundances of each element.

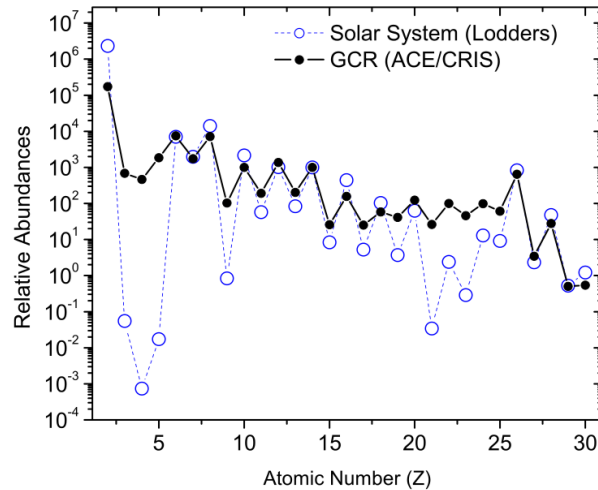


Figure 1.1: Chemical composition of CRs (integration from 50 MeV to 500 MeV) as measured at 1AU from the Sun by ACE compared to the abundances in the Solar System for elements with $Z=2-30$. Relative abundances are normalized to the Silicon abundance. Adapted from [Israel 2005]

Not shown in figure 1.1, the antiparticles are contributing a tiny amount to the total CRs content. Until now, experiments have measured only positrons and antiprotons, although ongoing searches try to observe other antinuclei, to begin with antideutons with the GAPS experiment recently funded. Detecting these antiparticles is a real challenge since for example we count only one positron for 10^3 protons and one antiproton each 10^4 protons. Hence experiments need an excellent rejection of the proton background. Up to now, theoretical predictions have shown that most (if not all) of the antiparticle cosmic rays can be accounted for by secondaries production. Radioisotopes, also measured in very tiny quantities, are a unique tool to explore CR physics. The so-called "clock" nuclei are β radioactive nuclei with life times comparable or longer than the typical acceleration and propagation timescales. Species like ^{10}Be , ^{14}C , ^{26}Al , ^{36}Cl , and ^{54}Mn are commonly invoked to constrain the propagation timescale, which is found to be 10-20 Myr for $E \simeq 1$ GeV. This is much longer than the ballistic crossing time—thus independently confirming the confinement of cosmic rays inside the galactic magnetic field—and quite short compared to the solar system age ($\approx 5 \times 10^3$ Myr). On the other hand, K-capture nuclei, notably produced in air shower and *primary* the ultra-high energy particle seed.

isotopes of Ni, Co and Fe, are used to gauge the acceleration timescale which is of the order of 10-100 kyr. The identification of these radioisotopes is very challenging because it needs instruments with a good mass and charge resolution. To maximize the effect on the observables and cancel some systematics, experiments often present ratios of parent over daughter species, or unstable to stable species (like $^{10}\text{Be}/^9\text{Be}$).

1.1.2.2 Spectrum

A striking property of the CR spectra is their power-law behaviors over many decades in energy. The highest energy CRs reach 10^{20}eV corresponding to roughly ten million times the energy achieved by man-made accelerators³. The decreasing power law spectrum makes the highest energy particles very scarce (less than 1 particle per km^2 per century), that is why many questions on their spectrum and composition are still waiting an answer. The wide range of variation of the flux makes possible the direct measurement of low energy CRs while the highest energy ones are only detected thanks to the byproducts from their interactions with the atmosphere.

A schematic view of the current measurements is given in figure 1.2. As noted in the previous section, the lowest energy part of the spectrum is dominated by solar CRs. Then, for energies between $\sim 1\text{GeV}$ and $\sim 1\text{PeV}$, CRs are expected to be of Galactic origin, and exhibit a quasi featureless power law, roughly scaling as $\propto E^{-2.75}$. The transition to extragalactic cosmic rays is believed to happen at some energy above the *knee* ($\sim \text{few PeV}$) which defines a softening of the spectrum varying now as $\propto E^{-3.2}$. However it is still not known exactly for which energy the extragalactic component becomes dominant. Around the energy of $3 \times 10^{18}\text{eV}$ the spectrum hardens again as $\propto E^{-2.7}$, before a sharp cut-off at $E \approx 5 \times 10^{19}\text{eV}$, possibly due to the photo-pion production on the CMB photons, and so-called GZK cut-off [Zatsepin 1966, Greisen 1966]. All these spectral features appear more clearly when the flux is multiplied by its mean energy dependence (see figure 1.3). The interpretation of these changes of slope is quite challenging, and in general spectral hardenings are attributed to a transition between two different populations of sources whereas softenings would come from astrophysical processes of production or propagation of cosmic rays.

In figure 1.3, the change of the energy scale reveals that above 100 TeV it becomes very difficult to identify experimentally the composition of the CR flux. Below this energy, current technologies are able to measure the charge of the particles and so the elemental flux. In the GeV energy range, spectrometers such as PAMELA⁴ and AMS-02⁵, have the required resolution to separate the different isotopes.

³However, note that the energy available in the center of mass at the LHC is only ten times lower than the energy available in a collision of the highest energy CRs with a steady particle in the lab frame.

⁴The Payload for Antimatter Matter Exploration and Light-nuclei Astrophysics (PAMELA) is a satellite-borne experiment which was launched in June 2006. Its orbit altitude is varying between 350 km and 600 km.

⁵The Alpha Magnetic Spectrometer (AMS-02) is a CR detector onboard the International Space

Let us focus on two features recently confirmed by the novel data from AMS-02. As shown in figure 1.4, it becomes now evident that there is a slight difference in the power-law index of proton and helium spectra. Several theoretical explanations have been proposed in the literature using spallations, different acceleration efficiencies, spatial segregation between the species and others. A second noticeable feature is a small kink at around 200 GV which seems to be shown by all the fluxes (right panel of figure 1.4). Many explanations have been proposed challenging either the propagation or the production of CRs, and some of them involving the prominent contribution of a local source. A review of these features and a discussion about attempts of explanations can be found in [Serpico 2015].

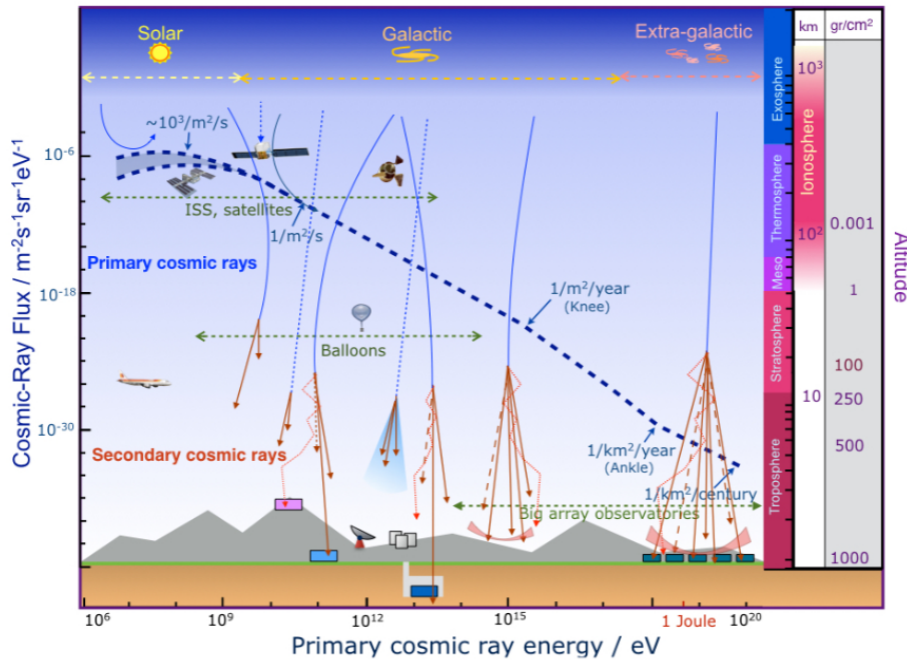


Figure 1.2: Primary cosmic ray spectrum as a function of energy. The blue dashed line represents the CR flux using the scale units shown on the left vertical axis. Below energies of $\sim 10^{14}$ eV, primary cosmic rays are measured directly with detectors placed in satellites and balloons. At higher energies indirect measurements done by ground-based arrays of detectors are used. The right vertical axis shows the atmosphere layers, their heights and the corresponding air pressure. This figure is taken from [Garzón 2017]

Station (ISS) since 2011. Its orbit altitude is varying between 330 km and 420 km.

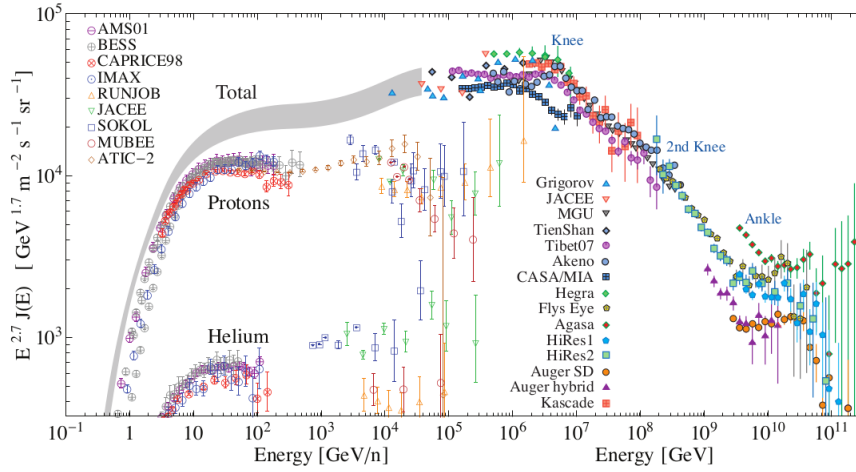


Figure 1.3: cosmic ray spectrum rescaled by multiplying by E^3 as a function of energy. This figure is taken from [Mertsch 2010].

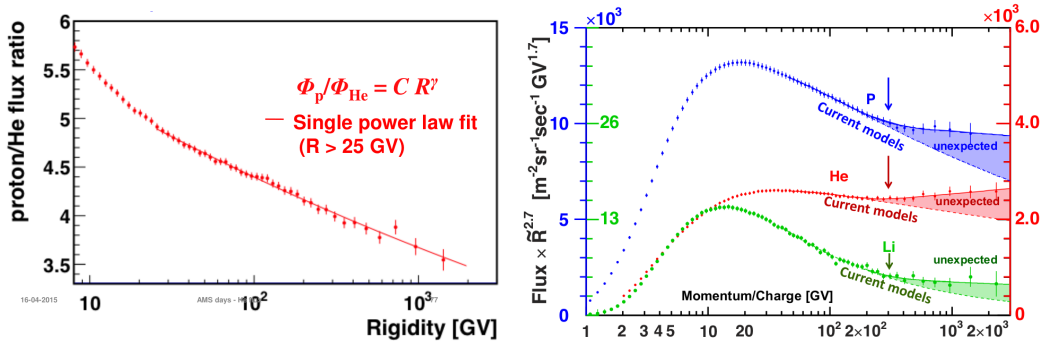


Figure 1.4: *Left*: Ratio of proton and helium fluxes measured by the AMS-02 experiment. *Right*: Cosmic ray spectra of proton, helium and lithium (preliminary) measured by the AMS-02 experiment.

1.1.3 Sources and acceleration of cosmic rays

Cosmic rays account for a significant portion of the total Galactic energy density, which is contributed to by: starlight (0.5 eV cm^{-3}), cosmic rays ($U_{CR}=1.5 \text{ eV cm}^{-3}$), thermal pressure of gas in clouds (0.3 eV cm^{-3}), gas kinetic motions (1 eV cm^{-3}) and, magnetic field (0.6 eV cm^{-3}). The first argument relating the explosion of stars, namely supernovae (SN), with CRs production was given in [Baade 1934] using the following simple energetic argument: to maintain the level of CRs energy density to the one observed despite their leakage out of the Galaxy, the injection power of CRs sources should be:

$$\mathcal{P}_{CR} \approx \frac{U_{CR}V_{CR}}{\tau_{res}} \approx 10^{40} \text{ erg s}^{-1}, \quad (1.5)$$

where V_{CR} is the volume occupied by the CRs (Galactic halo described next section) and τ_{res} the typical leakage time. This is about $10^{6.5}$ times the *bolometric* solar luminosity, a non-trivial amount to supply with known Galactic astrophysical sources. In [Shklovskii 1953] it was noticed that the kinetic energy released in the expanding shell of a supernovae is of the order of $\mathcal{E}_{SNR} = 10^{51} \text{ erg}$. With the rate ν_{SNR} of supernovae explosion in the Galaxy which is around 3 SNRs per century, it leads to a released power,

$$\mathcal{P}_{SNR} = \nu_{SNR} \mathcal{E}_{SNR} \approx 10^{42} \text{ erg s}^{-1}. \quad (1.6)$$

meaning that it is enough that $\mathcal{O}(10\%)$ of this energy is transferred to the acceleration of particles to explain their local density. The mechanism able to transfer such an energy was discovered in the 70's, the so-called diffusive shock acceleration (DSA) corresponding to the stochastic acceleration of particles at the SNR shock. This scenario was then supported by numerous observations in radio, X-rays and gamma rays.

1.1.3.1 The origin of the shock

Let us first review some important features of supernovae. Astronomers have observed two different kind of SN, thermonuclear and core collapse. In the first case a white dwarf is accreting mass from a companion star until it reaches the Chandrasekhar mass for which the degeneracy pressure of electrons cannot balance any longer the gravitational force. The contraction of the star triggers the ignition of carbon. This reaction releases such an energy that the star is blown out. These kinds of events are named SNIa⁶ and are characterized by the absence of hydrogen line in their spectral emission. At variance with thermonuclear SN, core collapse SN originate from much heavier stars. In that case the thermonuclear reactions in the core continue, possibly till the production of iron. When the radiative pressure

⁶The peak-width characteristics of their light curves are “universal”, ultimately due to the Chandrasekhar mass threshold effect. Therefore these objects are used as standard candles to measure the Hubble constant.

cannot balance the gravitational force, the star starts to collapse. Then as for SNIa the core of the star is sustained by the degeneracy pressure of electrons till it reaches the Chandrasekhar mass. Eventually the pressure in the core attains such high values that protons mostly convert into neutrons, forming a sort of giant nucleus. Since nuclear matter is almost incompressible, this process brutally stops the collapse and generates an outgoing shock wave which sweeps out the outer layers of the star. Usually at the center remains a neutron star, or even a black hole if further material accretes on the remnant and even quantum pressure is unable to stop the collapse. Depending on their spectroscopic signatures, these events are named SN Ib, Ic or II.

In both of the cases which we have just described, the kinetic energy released in the ejecta is similar, with initial speed around thousands of kilometers per second, thus much higher than the sound speed in the ISM. The evolution of these ejecta called supernova remnants (SNRs) is well-described by a four-stage model which was introduced in [Woltjer 1972]. It begins with a short (some dozens of years) free expansion phase where the ejecta of the supernova sweeps up matter as it expands freely. A shock wave is created since the expansion is highly supersonic with velocities close to 10^4 km s^{-1} . Then it passes to an adiabatic phase only driven by the high temperature of the gas inside the sphere (heated by a reverse shock), and for which radiative energy losses are negligible. This phase is well described by the Sedov-Taylor [Sedov 1946, Taylor 1955] self-similar solution. The third stage occurs when the mass of the swept-up material has dramatically increased, and forces the velocity of the shock front to decrease down to $\sim 200 \text{ km/s}$. The temperature behind the shock front drops and the energy losses due to recombination become significant. This is the first time the SNR is radiating in the optical band. The final stage of evolution occurs when the velocity of the shock reaches the sound speed of the ambient ISM and the SNR dissipates.

During the SNRs lifetime, a strong shock pervades the interstellar medium with a Mach number $\mathcal{M} \gg 1$, where $M = u_1/C_{s,1}$, the ratio of the velocity of the upstream material over its characteristic sound speed. The left panel of figure 1.5 shows the characteristic discontinuities of a shock wave observed in the reference frame of the shock. The matter is flowing from right to left, moving with supersonic speed $u_1 > C_{s,1}$ in the upstream region and with subsonic speed $u_2 < C_{s,2}$ in the downstream region. The conservation of mass, momentum and energy across a planar, adiabatic shock front lets define the relations between the upstream and downstream thermodynamical parameters. These relations, also named Rankine-Hugoniot, give for the compression ratio $r = n_1/n_2$:

$$\frac{u_2}{u_1} = \frac{1}{r} = \frac{\gamma - 1}{\gamma + 1} + \frac{2}{\gamma + 1} \frac{1}{\mathcal{M}^2}, \quad (1.7)$$

where n_1 and n_2 are the densities upstream and downstream, and γ is the heat capacity ratio of the gas. In the case of a strong non-relativistic shock in a monoatomic gas $\gamma = 5/3$ and so $r = 4$, while in relativistic shock conditions $\gamma = 4/3$ and so $r = 7$.

1.1.3.2 Fermi acceleration of particles

The seminal idea of stochastic acceleration of particles was introduced by Fermi in [Fermi 1949, Fermi 1954]. He proposed that CRs undergo a stochastic scattering on the Galactic magnetic field, modeled as magnetized clouds moving inside the Galaxy with random velocities. However it is easy to show that for each scattering the energy gain is close to $\beta^2 \approx 10^{-8}$ for typical velocities in the ISM. The quadratic dependence on β is the reason why this mechanism is called second order Fermi mechanism, making it not efficient enough to explain the spectrum and the total energy density of CRs.

However in the seventies the idea of Fermi was applied to particles moving back and forth across a shock wave (see for example [Skilling 1975a, Skilling 1975b, Bell 1978]). In this configuration the results change dramatically, and lead to the diffusive shock acceleration also called first order Fermi process. Let us precise a bit the physics following a micro-physics approach (for example see [Bell 1978]) which shows how the first order Fermi mechanism leads to the production of a particle spectrum with a universal power law.

Let us assume that a fast particle of velocity $\sim c$ comes from upstream, scatters downstream and comes back upstream. This particle has gained an energy amount:

$$\delta E = -2 (\mathbf{u}_2 - \mathbf{u}_1) \cdot \mathbf{p} , \quad (1.8)$$

Assuming the distribution of particles in phase space is quasi isotropic, which holds as long as the scattering process is the fastest diffusion process, the average energy gained over a single cycle is:

$$\frac{\delta E}{E} = \frac{4}{3} \frac{(u_2 - u_1)}{c} . \quad (1.9)$$

Compared to the first idea of Fermi, the shock acceleration is more efficient and results in an energy gain proportional to the relative velocity between upstream and downstream plasmas. Furthermore we can define the probability p_{esc} for a particle to escape from the shock vicinity. p_{esc} can be defined as the ratio of the particle flux carried by the downstream flow at a velocity u_2 over the particles flux that cross the front shock with speed v . The calculation shows that this probability is:

$$p_{esc} \approx \frac{4u_2}{c} . \quad (1.10)$$

Let us denote with $\xi = \delta E/E$ the energy gained in each cycle. Starting from an initial energy E_0 , after k cycles the particle will have the energy $E_k = E_0(1 + \xi)^k$. Furthermore, after each cycle the particle has a probability $1 - p_{esc}$ to undergo another cycle of acceleration. So after k cycles, the number of particle with an energy $E > E_k$ is:

$$N(E > E_k) \propto \sum_{i=k}^{\infty} (1 - p_{esc})^i = \frac{(1 - p_{esc})^k}{p_{esc}} = \frac{1}{p_{esc}} \left(\frac{E}{E_0} \right)^{-\delta} ; \quad (1.11)$$

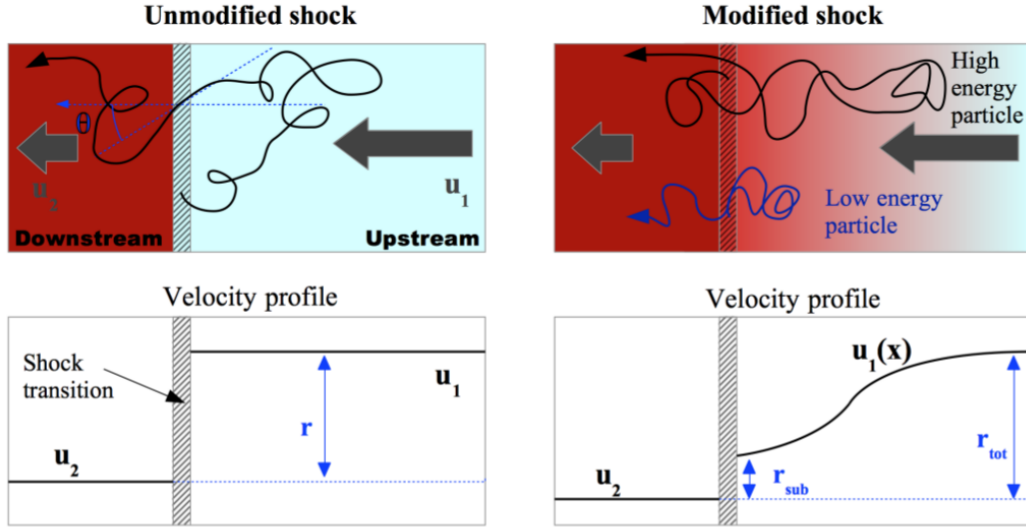


Figure 1.5: *Left:* Structure of an unmodified plane shock wave. Particle diffusing from upstream to downstream feel the compression factor r in the velocity of the plasma, which is the same at all energies. *Right:* Shock structure modified by the presence of accelerated particles. The pressure exerted by accelerated particles diffusing upstream slows down the plasma creating a *precursor*. High energy particles, which propagate farther away from the shock, feel now a larger compression factor with respect to low energy particles which diffuse closer to the shock. Figure and legend taken from [Morlino 2016]

where $\gamma = -\ln(1 - p_{esc})/\ln(1 + \xi) \approx p_{esc}/\xi$, since ξ and p_{esc} are small quantities with respect to unity. Hence the differential energy spectrum dN/dE will have the energy dependence $E^{-\alpha}$, with:

$$\alpha = 1 + \delta = 1 + p_{esc}/\xi = 1 + \frac{3u_2}{u_1 - u_2} = \frac{r + 2}{r - 1} \quad (1.12)$$

Hence taking $r = 4$ we obtain a universal spectrum in energy with $\alpha = -2$. This result relies on multiple ingredients, among them the independence of the escape probability on the particle energy, and that the energy gained is proportional to the particle energy. One should also note that there are some approximations in this derivation, for example the shock is assumed to be invariant during the whole process. This approximation is known to be false due to effect of an increasing CRs pressure which modifies the velocity profile as shown in the right panel of figure 1.5. Hence the universal power law dependence may depend on the microphysics of the shock, and strictly speaking refers to the accelerated particles, not the ones escaping into the ISM (*escape problem*). The traditional argument that this prediction is reflected in the data collected at the Earth is anyway currently

challenged by a precise measurement of the fluxes (for example proton and helium), although it is not clear to what extent other effects (propagation, local sources . . .) contribute to these observations.

In any case, the derivation performed in the stationary state would formally imply that an infinite energy can be reached for an infinite time. In general, for an accelerator such as SNRs, there are two main limitations for the maximal energy: either the age of the accelerator compared with the acceleration time, or the size of the system compared with the diffusion length. In the case of SNRs the latter limits the maximal energy not to exceed E_{max} with in the Sedov-Taylor phase can be expressed as:

$$E_{max} \approx 23 Z \left(\frac{B}{1\mu\text{G}} \right)^{1/2} \left(\frac{E_{SNR}}{10^{51}\text{erg}} \right)^{1/2} \left(\frac{n_{ISM}}{\text{cm}^{-3}} \right)^{-1/3} \left(\frac{M_{ej}}{M_{\odot}} \right)^{-1/6} \text{TeV} \quad (1.13)$$

Hence we see that to reach the energy of the knee $E_{knee} \approx 3 \times 10^3$ TeV within the SNR paradigm, requires the magnetic field which prevails at the shock to be amplified with respect to the one in the ISM. This amplification is currently thought to be provided by CRs streaming ahead of the shock [Bell 2004].

1.1.3.3 Spatial distribution of the sources

The sources of Galactic CRs (until now SNRs) are thought to be confined, as well as the gas, inside the disk of matter of the Galaxy whose radius is about 20 kpc and height 200 pc. As it is impossible to observe all of them (one of the main motivations of Chapter 2), one has to rely on a modelling of their location in the Galaxy. Since $\sim 2/3$ of the SNRs are of core collapse origin, the distribution of the resulting pulsars is often used to infer the distribution of SNRs which are harder to detect. In the literature, such a distribution is always factorized in its vertical and radial part. Vertically, all the authors agree with an exponential decrease of the density with the distance from the Galactic plane. Radially, different parameterizations have been proposed, one of the most recent one can be found in [Yusifov 2004]:

$$\rho(r) \propto \left(\frac{r + 0.55}{8.5 + 0.55\text{kpc}} \right)^{1.64} \exp \left(-6.8 \frac{r - 8.5}{8.5 + 0.55\text{kpc}} \right). \quad (1.14)$$

The normalization of the distribution is then fixed by a fit to data, and depends on the frequency of the impulsive source events as well as the total power released per source. A precise description of the source distribution is essential in the study e.g. of anisotropies, or local source effects, notably in the case where the overall normalization can be fixed via independent observations or theoretical considerations. In this thesis, we will consider primary sources spread homogeneously inside the Galactic disk, or following the more complexe distribution just mentioned. Loosely motivated by the favoured shock acceleration mechanism, we will take the energy dependence of the fluxes to be a power law in rigidity, with a spectral index close to -2 , possibly with mild variations among different species.

Also, although till now we have only considered SNRs as main accelerators of Galactic cosmic rays, other objects are also likely contributing: the most notable example are spinning neutron stars, or pulsars, which may have a sizable if not dominant contribution to the CR *lepton* flux. We will discuss their contribution in some details in the last chapter, since they can be responsible for the so-called *positron excess*.

1.1.4 The magnetic environment of the Galaxy

Since CRs are charged particles, another essential ingredient of their dynamics is the magnetic environment of the Galaxy. Indeed, the interstellar medium is magnetized, and we can distinguish among two components of the magnetic field: The regular component, which follows the spiral arms of the Galaxy, and a stochastic one on small scales. Stellar activity is pushing the plasma and the magnetic lines out of the Galactic plane at a speed V_c (later referred to as the convective wind). Thanks to the synchrotron non-thermal emission from CRs electrons trapped in the magnetic field, a large magnetic structure has been unveiled in several galaxies. A pioneering observation is presented in figure 1.6. The optical signal in the background allows one to gauge the extension of the magnetic field, which extends much beyond the disk of matter. This structure is named magnetic halo and its size depends on the galaxy, but is typically of several kpc. In CRs phenomenology, the magnetic halo corresponds to the confinement zone of CRs where the turbulent magnetic field is efficiently scattering charged particles.

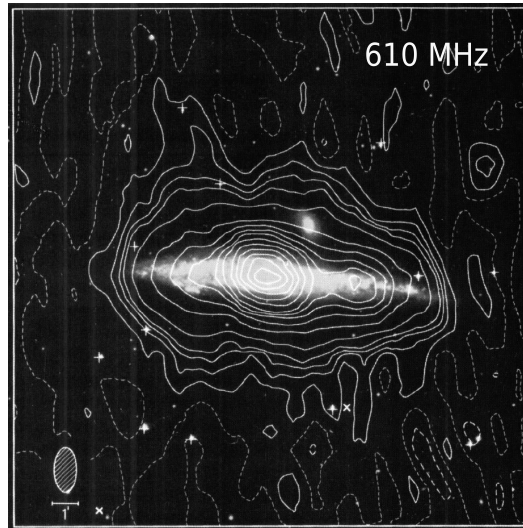


Figure 1.6: Isocontours of the radio emission at 610MHz from NGC 4631. The optical signal lies in the background. Figure extracted from [Ekers 1977].

In this thesis we often refer to two different modelling of the halo geometry. These models are presented in figure 1.7. On the right panel of this figure is sketched the *Slab model*: the Galaxy is assumed to be contained in an infinite plan sandwiched

inside a diffusive volume vertically limited. As this model only depends on one coordinate it is often referred as the *1D* model. On the right panel of the same figure, the 2D model or cylindrical model gets closer to the reality by adding a radial bound to the halo extension. In this model the Earth is located at a distance of 8.5 kpc from the Galactic center.

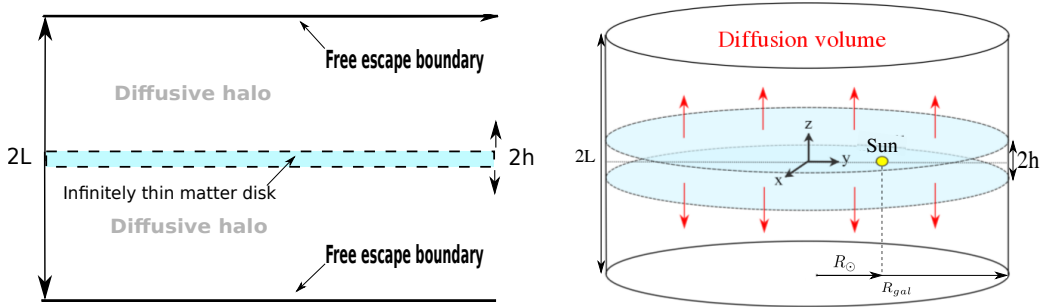


Figure 1.7: *Left*: Sketch of the 1D slab model of the Galaxy, with matter homogeneously distributed inside an infinite plane of thickness $2h$ sandwiched between two thick diffusive layers of thickness $2L$. *Right*: Cylindrical or 2D model. The radius of the Galaxy is taken as $R_{\text{gal}} = 20$ kpc. For both models the thickness of the Galactic disk is $2h$ with $h = 100$ pc.

1.2 Diffusion and transport of cosmic rays in the Galaxy

This section justifies the phenomenological transport equation of Galactic CRs. We sketch its rationale, both from first principles of plasma physics and observational facts.

1.2.1 Transport equation of cosmic rays from microphysics

Cosmology teaches us that since the recombination ($z \sim 10$) most of the visible matter of the universe is made of ionized gas. The behavior of these charged particles, including CRs themselves, is governed by the laws of plasma physics. This domain is of the utmost importance in astrophysics, since electromagnetic processes may dominate at every scale ranging from large structures to stellar physics.

One important feature of plasmas, that will be used later, is that the charged particles must be close enough together so that one particle influences not only its closest neighbour, but many nearby charged particles. The plasma approximation is valid when the number of charge carriers within the sphere of influence (called the Debye sphere, of radius λ_D , also named the Debye screening length) of a particular particle is higher than unity. This configuration provides collective behaviour of the charged particles. Galactic cosmic rays are one of the best cases for applying this

approximation, with:

$$\lambda_D = \sqrt{\frac{k_B T}{4\pi q^2 n}} = 2 \times 10^{11} \text{ cm} , \quad (1.15)$$

and, a plasma parameter (number of particles within Debye distance) of:

$$\Lambda \simeq \lambda_D^3 n \sim 10^{26} . \quad (1.16)$$

The most straightforward approach to plasma physics is to consider a group of charged particles defined by their position \mathbf{x}_i and their speed \mathbf{v}_i both depending on the time t . One can define the so-called Klimontovich density as:

$$W_\alpha(\mathbf{x}, \mathbf{v}, t) = \sum_{i=1}^N \delta^3(\mathbf{x} - \mathbf{x}_i(t)) \delta^3(\mathbf{v} - \mathbf{v}_i(t)) , \quad (1.17)$$

where the index α allows to consider different kinds of particles, each with charge q_α . As a consequence of the equations of motion of the particles, W_α satisfies an equation known as Klimontovich equation, which one can specify to the case where particles are subject to electromagnetic fields. In turn, the fields are generated by the particles themselves, i.e. the microscopic Maxwell equations must supplement the Klimontovich equation. This leads to the following system of equations:

$$\frac{\partial W_\alpha}{\partial t} + \mathbf{v} \cdot \frac{\partial W_\alpha}{\partial \mathbf{x}} + \frac{q_\alpha}{m_\alpha} \left(\mathbf{e} + \frac{\mathbf{v} \times \mathbf{b}}{c} \right)' \cdot \frac{\partial W_\alpha}{\partial \mathbf{v}} = 0 \quad (1.18)$$

$$\nabla \times \mathbf{b} = \frac{1}{c} \frac{\partial \mathbf{e}}{\partial t} + \frac{4\pi}{c} \sum_{\beta} q_{\beta} \int d\mathbf{v} \mathbf{v} W_{\beta} \quad (1.19)$$

$$\nabla \cdot \mathbf{b} = 0 \quad (1.20)$$

$$\nabla \times \mathbf{e} = -\frac{1}{c} \frac{\partial \mathbf{b}}{\partial t} \quad (1.21)$$

$$\nabla \cdot \mathbf{e} = 4\pi \sum_{\beta} q_{\beta} \int d\mathbf{v} W_{\beta} , \quad (1.22)$$

where \mathbf{e} and \mathbf{b} are the microscopic electromagnetic fields. The prime indicates that in the computation of \mathbf{e} and \mathbf{b} , the field produced by the particle itself has to be omitted. These microscopic equations are not practical for a macroscopic study of the plasma, unless we average them and move toward a statistical description. The usual procedure for averaging a microscopic equation is to take its ensemble average. However, hereafter we use a spatial average which is more physical since one has only access to the number of particles, and electromagnetic fields in small but finite volume $\Delta\mathcal{V}_v \Delta\mathcal{V}_x$ of the phase space. Hence, we define the average density $f_\alpha(\mathbf{x}, \mathbf{v}, t)$ such that:

$$f_\alpha(\mathbf{x}, \mathbf{v}, t) = \frac{1}{\Delta\mathcal{V}_x \Delta\mathcal{V}_v} \int_{\Delta\mathcal{V}_x} d\mathbf{x} \int_{\Delta\mathcal{V}_v} d\mathbf{v} W_\alpha(\mathbf{x}, \mathbf{v}, t) = \frac{N}{\Delta\mathcal{V}_x \Delta\mathcal{V}_v} = \langle W_\alpha(\mathbf{x}, \mathbf{v}, t) \rangle , \quad (1.23)$$

and in the same way the density of correlated pairs:

$$g_\alpha(\mathbf{x}_1, \mathbf{v}_1, \mathbf{x}_2, \mathbf{v}_2, t) = \langle W_\alpha(\mathbf{x}_1, \mathbf{v}_1, t) W_\alpha(\mathbf{x}_2, \mathbf{v}_2, t) \rangle - \delta(\mathbf{x}_1 - \mathbf{x}_2) \delta(\mathbf{v}_1 - \mathbf{v}_2) \langle W_\alpha(\mathbf{x}_1, \mathbf{v}_1, t) \rangle \quad (1.24)$$

The size of the integration box needs to be large compared to the mean spacing of particles in the plasma, i.e $\Delta \mathcal{V}_x^{1/3} \gg n^{-1/3}$ and $\Delta \mathcal{V}_v^{1/3} \gg v_T / (n \lambda_D^3)^{1/3}$, where v_T is the local thermal speed and λ_D the Debye length of the plasma. Thus the number of particles is sufficiently large so that statistical fluctuations ($\delta N / N \sim 1 / \sqrt{N}$) are expected to be small. However, this integration volume should not be so large that macroscopic properties of the plasma vary significantly within the box, thus making the kinetic description useless. Performing this average one can rewrite the microscopic quantities as a sum of a smoothed and a discrete component:

$$W_\alpha = f_\alpha + \delta f_\alpha \quad (1.25)$$

$$\mathbf{e} = \mathbf{E} + \delta \mathbf{E} \quad (1.26)$$

$$\mathbf{b} = \mathbf{B} + \delta \mathbf{B} , \quad (1.27)$$

$$(1.28)$$

where by definition $\langle \delta \mathbf{E} \rangle = \langle \delta \mathbf{B} \rangle = \langle \delta f_\alpha \rangle = 0$. By introducing these quantities in the Klimontovitch-Maxwell system of equations and by taking the dedicated phase space average, the system turns into:

$$\frac{\partial f_\alpha}{\partial t} + \mathbf{v} \cdot \frac{\partial f_\alpha}{\partial \mathbf{x}} + \frac{q_\alpha}{m_\alpha} \left(\mathbf{E} + \frac{\mathbf{v} \times \mathbf{B}}{c} \right) \cdot \frac{\partial f_\alpha}{\partial \mathbf{v}} = - \left\langle \frac{q_\alpha}{m_\alpha} \left(\delta \mathbf{E} + \frac{\mathbf{v} \times \delta \mathbf{B}}{c} \right)' \cdot \frac{\partial \delta f_\alpha}{\partial \mathbf{v}} \right\rangle \quad (1.29)$$

$$\nabla \times \mathbf{B} = \frac{1}{c} \frac{\partial \mathbf{E}}{\partial t} + \frac{4\pi}{c} \sum_\beta q_\beta \int d\mathbf{v} f_\beta \quad (1.30)$$

$$\nabla \cdot \mathbf{B} = 0 \quad (1.31)$$

$$\nabla \times \mathbf{E} = - \frac{1}{c} \frac{\partial \mathbf{B}}{\partial t} \quad (1.32)$$

$$\nabla \cdot \mathbf{E} = 4\pi \sum_\beta q_\beta \int d\mathbf{v} \mathbf{v} f_\beta . \quad (1.33)$$

When neglecting the right hand side term of the first equation, the system becomes the so-called Vlasov-Maxwell system, where the electromagnetic field is computed self-consistently with the particle distribution f_α , in absence of fluctuations. This first equation is formally identical to the first equation of the BBGKY hierarchy, arising in kinetic theory, although the latter requires short-range mutual interactions: for a system of particles described by a Hamiltonian \mathcal{H} defined as a sum over the particles of the kinetic energy terms $T_k(\mathbf{x}_k)$, the potential energy terms $U_k(\mathbf{x}_k)$ and pair interaction terms $V_{kl}(|\mathbf{x}_k - \mathbf{x}_l|)$:

$$\mathcal{H} = \sum_k (T_k + U_k) + \sum_{kl} V_{kl}. \quad (1.34)$$

The first equation of the BBGKY hierarchy (Liouville equation integrated by part) which relates f_α to g_α writes:

$$\frac{\partial f_\alpha}{\partial t} + \dot{\mathbf{x}}_1 \cdot \frac{\partial f_\alpha}{\partial \mathbf{x}_1} - \frac{\partial U_1}{\partial \mathbf{x}_1} \frac{\partial f_\alpha}{\partial \mathbf{p}_1} = \int d\mathbf{x}_2 d\mathbf{p}_2 \frac{\partial V_{12}}{\partial \mathbf{x}_1} \frac{\partial g_\alpha}{\partial \mathbf{p}_1}. \quad (1.35)$$

In the usual statistical mechanics applications, if the range λ of the force $\mathbf{f}_{12} = -\partial V_{12}/\partial \mathbf{x}_1$ is short, the right hand side is suppressed by a factor $\lambda^3/\Delta \mathcal{V}_\mathbf{x}$ with respect to the LHS term. In a plasma, the situation is somehow opposite, in the sense that the two-body interactions are very long range (infinite); nonetheless, single charge-carrier effects are shielded beyond the Debye length, so that inter-particle collisional effects are suppressed at larger distances, and a natural description emerges in terms of collective (or emergent) degrees of freedom in the plasma fluid subject to self-consistently computed electromagnetic fields. The difficulty is to solve this entangled system of equations, which can exhibit a very nonlinear behavior, admitting several equilibrium solutions, as well as metastable states with very long relaxation time (e.g. dynamo effect). A first understanding of the system can be achieved in two limits: in *the test wave approach*, the particle distribution function is fixed in order to study for instance the electromagnetic modes supported by the system. In the opposite limit, *the test particle approach* is the most relevant case for CR study, where electromagnetic fields are fixed to study the evolution of the particle distribution function(s). Let us consider a plasma dominated by “thermal” particles, which are in turn responsible for the generation of the “background electro-magnetic fields”. We want to study the evolution of the sole distribution function of the CR particles in this framework. To leading order, the evolution of the phase space density is described by the relativistic Vlasov equation:

$$\frac{\partial f_\alpha}{\partial t} + \mathbf{v} \cdot \frac{\partial f_\alpha}{\partial \mathbf{x}} + q_\alpha \left(\mathbf{E} + \frac{\mathbf{v} \times \mathbf{B}}{c} \right) \cdot \frac{\partial f_\alpha}{\partial \mathbf{p}} = 0, \quad (1.36)$$

where \mathbf{E} and \mathbf{B} are the electric and magnetic fields generated by the dominant interstellar “thermal” plasma, which we take as externally given ⁷. Due to the high conductivity of the plasma, the large scale electric field can be neglected. Since we are ignoring for the moment the turbulent component, one has:

$$\mathbf{B} = \mathbf{B}_0 \quad (1.37)$$

$$\mathbf{E} = 0 \quad (1.38)$$

where we further simplify the problem to the case of a uniform background magnetic field which, without loss of generality, we can assume as $\mathbf{B}_0 = B_0 \mathbf{e}_z$. For convenience

⁷Of course, this means that they evolve over timescales much longer than the dynamical timescales of interest for CR propagation. For instance, the magnetic field of the Galaxy is presumably due to dynamo effects whose evolutionary scales are at least of the order of hundreds of millions of years.

we decompose the momentum of the particle in spherical coordinates, introducing the *pinching angle* $\mu = \cos \theta$, a conserved quantity:

$$p_x = p \cos \phi \sqrt{1 - \mu^2} \quad (1.39)$$

$$p_y = p \sin \phi \sqrt{1 - \mu^2} \quad (1.40)$$

$$p_z = p \mu \quad (1.41)$$

$$(1.42)$$

The motion of a charged particle in a constant magnetic field is helicoidal, with a gyration frequency Ω and a gyration radius (Larmor radius) R_L around \mathbf{B}_0 defined as:

$$\Omega = \frac{q_\alpha B_0}{m \gamma c} \approx 10^{-3} \frac{q_p}{e} \frac{\text{GeV}/c}{m_p \gamma} \frac{B_0}{\mu\text{G}} \text{ rad.s}^{-1}, \quad (1.43)$$

$$R_L = \frac{p \sqrt{1 - \mu^2}}{\gamma m \Omega} = \frac{pc \sqrt{1 - \mu^2}}{q_\alpha B_0} \approx 10^{11} \frac{e}{q_p} \frac{p_\perp c}{\text{GeV}} \frac{\mu\text{G}}{B_0} \text{ m}. \quad (1.44)$$

Since the timescales of interest in the Galactic propagation are of the order of 1 million year ($\sim 3 \times 10^{13}$ s) and the spatial scales certainly not below the parsec ($\sim 3 \times 10^{16}$ m), there is a large hierarchy between the fast gyrating motion—the ϕ coordinate—and the slow evolution of the guiding center of the particle, defined by

$$\mathbf{R} = (X, Y, Z) = \mathbf{x}(t) + \frac{\mathbf{v}(t) \times \mathbf{e}_z}{\varepsilon \Omega}, \quad (1.45)$$

where ε is the sign of the particle charge. Making the change of coordinates $(x, y, z, p_x, p_y, p_z) \rightarrow \mathbf{x}_\sigma = (X, Y, Z, p, \mu, \phi)$, the Vlasov equation (equation 1.36) transforms into:

$$\frac{\partial f_\alpha}{\partial t} + v \mu \frac{\partial f_\alpha}{\partial Z} - \varepsilon \Omega \frac{\partial f_\alpha}{\partial \phi} = 0, \quad (1.46)$$

which simply means that the density stays constant along the trajectories of the particles.

Till now, we have neglected any perturbation in the fields. Let us now develop a heuristic understanding of the modification of the above picture in such a case (See [Schlickeiser 2013] for a more rigorous but lengthy justification). Let us consider a fluctuating magnetic field around its regular component $\mathbf{B}_0 = B_0 \mathbf{u}_z$. In a plasma, fluctuations of \mathbf{B} are typically associated with Alfvén waves, which are perpendicular, low frequency waves, with dispersion relation $\omega = k \nu_A$, where $k = 2\pi/\lambda$ and $\nu_A = B_0/\sqrt{4\pi n_i m_i}$, m_i and n_i being the mass and the number density of the background ions. The equation of motion writes:

$$\frac{d\mathbf{p}}{dt} = q \frac{\mathbf{v} \times (\mathbf{B}_0 + \delta\mathbf{B})}{c}, \quad (1.47)$$

where we assume:

$$|\delta\mathbf{B}| \ll \mathbf{B}_0 \quad \text{and} \quad \delta\mathbf{B} \perp \mathbf{B}_0. \quad (1.48)$$

Contrarily to the above case, the pitch angle μ is now evolving. From equation 1.47, in presence of a *single wave*:

$$\dot{\mu} = \frac{d\mu}{dt} = \frac{q v_{\perp}^0}{c p} [\cos(\Omega t) \delta B_y - \sin(\Omega t) \delta B_x] \quad (1.49)$$

$$= \frac{q \sqrt{1 - \mu^2} |\delta \mathbf{B}|}{c m \gamma} [\cos(\Omega t) \cos(kz + \psi) - \sin(\Omega t) \sin(kz + \psi)] \quad (1.50)$$

$$= \frac{q \sqrt{1 - \mu^2} |\delta \mathbf{B}|}{c m \gamma} \cos[(\Omega - kv\mu)t + \psi], \quad (1.51)$$

where in the last two steps we have assumed that the particle is ultra relativistic and that the magnetic perturbation is a circular polarized wave which evolves much slower than the propagation of the particle. The angle ψ denotes here the phase of the wave. One can easily see that, averaging over an ensemble of waves with random ψ (but also over a sufficiently long time $\gg \Omega^{-1}$), $\langle d\mu/dt \rangle = 0$. However, if we introduce the second moment $D_{\mu\mu}$

$$D_{\mu\mu} = \int_0^{\Delta t} dt \langle \dot{\mu}(t) \dot{\mu}(0) \rangle, \quad (1.52)$$

it is straightforward to check that:

$$D_{\mu\mu} = \left(\frac{q \sqrt{1 - \mu^2} |\delta \mathbf{B}|}{c m \gamma} \right)^2 \int_0^{\Delta t} dt' \cos[(\Omega - kv\mu) t'] \quad (1.53)$$

$$\rightarrow \left(\frac{q \sqrt{1 - \mu^2} |\delta \mathbf{B}|}{c m \gamma} \right)^2 \delta(k - k_{res}) \quad \text{with } k_{res} \equiv \frac{\Omega}{v\mu}. \quad (1.54)$$

where the limits holds under the condition $\Delta t \gg \Omega^{-1}$. The function is then not vanishing when the resonant condition $k = k_{res}$ is fulfilled. In general, the magnetic perturbations are composed of several waves, and from equation 1.49 it is possible to calculate the two point correlation function of the magnetic turbulence. Assuming the turbulence is magnetostatic and homogeneous, the expression can be generalized 1.54 as follow:

$$D_{\mu\mu} = \frac{\pi}{4} (1 - \mu^2) \Omega k_{res} \int dk \frac{\mathcal{E}(k)}{B_0^2/8\pi} \delta(k - k_{res}) \quad (1.55)$$

$$= \frac{\pi}{4} (1 - \mu^2) \Omega \frac{k_{res} \mathcal{E}(k_{res})}{B_0^2/8\pi} \equiv (1 - \mu^2) \nu. \quad (1.56)$$

with \mathcal{E}_k the wave total energy density [Blandford 1987]. The emerging heuristic picture is thus the following: In absence of perturbations, the phase-space density is just conserved along the trajectory, which for the simple case considered is a gyration along the guiding center, itself drifting with constant velocity (in a more general case, slowly evolving according to the large-scale features of the background field). If perturbations are present, in the magnetostatic limit μ is not a constant

anymore, but evolves with time. For timescales longer with respect to the gyroperiod, the evolution of μ follows a *diffusive* law with diffusion coefficient $D_{\mu\mu}$. In turn, this can be interpreted as a resonant scattering of the CR particle on background waves. The resonance condition depends on the rigidity of the particle and on the wavenumber, see eq. 1.43. The pitch angle diffusion clearly tends to isotropize the particles distribution. Analytically, what we have achieved is an estimate of the RHS of equation 1.29 for our simplified problem, under two further approximations: we average over timescales long compared to the gyroperiod (equivalently, we integrate the distribution over ϕ), and we ensemble-average over realizations of magnetic fluctuations (remember the wave phase ψ). The corresponding distribution $\langle f_\alpha \rangle$ should thus obey:

$$\frac{\partial \langle f_\alpha \rangle}{\partial t} + v\mu \frac{\partial \langle f_\alpha \rangle}{\partial Z} = \frac{\partial}{\partial \mu} \left(D_{\mu\mu} \frac{\partial \langle f_\alpha \rangle}{\partial \mu} \right). \quad (1.57)$$

We further split $\langle f_\alpha \rangle$ into its average pitch angle and an anisotropic part:

$$\langle f_\alpha \rangle(\mathbf{x}, p, \mu, t) = f_0(\mathbf{x}, p, t) + f_1(\mathbf{x}, p, \mu, t) \quad (1.58)$$

$$\text{with: } f_0(\mathbf{x}, p, t) = \frac{1}{2} \int_{-1}^1 d\mu \langle f_\alpha \rangle(\mathbf{x}, p, \mu, t) \quad (1.59)$$

$$\text{and: } \frac{1}{2} \int_{-1}^1 d\mu f_1(\mathbf{x}, p, \mu, t) = 0. \quad (1.60)$$

Hence

$$\frac{\partial f_0}{\partial t} + \frac{\partial f_1}{\partial t} + v\mu \frac{\partial f_0}{\partial Z} + v\mu \frac{\partial f_1}{\partial Z} = \frac{\partial}{\partial \mu} \left(D_{\mu\mu} \frac{\partial f_1}{\partial \mu} \right). \quad (1.61)$$

Let us integrate over μ between -1 and μ

$$(\mu + 1) \frac{\partial f_0}{\partial t} + \frac{\partial}{\partial t} \int_{-1}^{\mu} d\mu' f_1 + v \frac{\mu^2 - 1}{2} \frac{\partial f_0}{\partial z} + v \int_{-1}^{\mu} d\mu' \mu' \frac{\partial f_1}{\partial z} = D_{\mu\mu} \frac{\partial f_1}{\partial \mu}, \quad (1.62)$$

where physically there cannot be flux across the boundaries at $\mu = \pm 1$, hence $D_{\mu\mu}$ should vanish at $\mu = \pm 1$. We see that at $\mu = +1$ some terms automatically vanish, but for others we must require explicitly so. If we range the terms according to this criterion, we get:

1) a *continuity equation*

$$2 \frac{\partial f_0}{\partial t} + v \int_{-1}^{+1} d\mu' \mu' \partial_z f_1 = 0 \iff \partial_t f_0 + \partial_z j = 0 \quad (1.63)$$

where

$$j \equiv \frac{v}{2} \int_{-1}^{+1} d\mu' \mu' f_1. \quad (1.64)$$

2) The additional equation is

$$v \frac{\mu^2 - 1}{2} \frac{\partial f_0}{\partial z} = D_{\mu\mu} \frac{\partial f_1}{\partial \mu} - \frac{\partial}{\partial t} \int_{-1}^{\mu} d\mu' f_1. \quad (1.65)$$

At the RHS of this equation, the first term is much larger than the second, since it is proportional to the frequency ν of “wave scattering”, a much faster process than the time variation of f_1 . Physically, this is equivalent to say that CRs change directions on a much smaller timescale than their propagations times, equivalent to a condition for diffusion. This leads to:

$$D_{\mu\mu} \frac{\partial f_1}{\partial \mu} \simeq v \frac{\mu^2 - 1}{2} \frac{\partial f_0}{\partial z} \implies f_1 = C - \frac{v}{2} \frac{\partial f_0}{\partial z} \int_{-1}^{\mu} dw \frac{1 - w^2}{D_{ww}} \quad (1.66)$$

where C is a constant, fixed by the conservation equation 1.63. From equation 1.64, we deduce

$$j = 0 - \frac{v^2}{4} \frac{\partial f_0}{\partial z} \int_{-1}^{+1} d\mu \mu \int_{-1}^{\mu} dw \frac{1 - w^2}{D_{ww}}. \quad (1.67)$$

Integrating by parts (one function being μ with primitive $\mu^2/2$, the other being the integral up to μ whose derivative is the integrand) we obtain

$$j = -\frac{v^2}{8} \frac{\partial f_0}{\partial z} \left\{ \mu^2 \int_{-1}^{\mu} dw \frac{1 - w^2}{D_{ww}} \Big|_{\mu=-1}^{\mu=+1} - \int_{-1}^{+1} dw w^2 \frac{1 - w^2}{D_{ww}} \right\}. \quad (1.68)$$

The above expression is nothing but Fick’s law, where the spatial diffusion coefficient K is now expressed in terms of the pitch angle diffusion coefficient as

$$j = -K \frac{\partial n}{\partial z} \implies \frac{\partial f_0}{\partial t} = \frac{\partial}{\partial Z} \left(K \frac{\partial f_0}{\partial Z} \right), \quad \text{with } K = \frac{\beta^2}{8} \int_{-1}^{+1} dw \frac{(1 - w^2)^2}{D_{ww}}. \quad (1.69)$$

These equations also justify the typical formula for the leading dipolar anisotropy for CRs in the diffusive regime (one can show for instance that $f_1/f_0 \sim K/(Hc)$). Actually, the above equation, or its generalization to 3D, assumes that the scattering centers are static. In fact, in many situations, including in the Galactic case of interest, the plasma is moving with respect to “the Lab frame”, with a coherent, large scale convective velocity \mathbf{V}_c (this is the case of the first-order Fermi mechanism previously discussed). Additionally, perturbations are usually moving in the plasma “stochastically” with a motion characterized by the Alfvén velocity \mathbf{V}_a (this is the case of the second-order Fermi mechanism introduced above). Note that this generalization allows now for *momentum-changing* operators, since in the Lab frame we have now moving B -fields, hence associated with electric fields. To account for these effects one typically rewrites the equation in mixed coordinates, where spatial coordinates \mathbf{x} are measured in the laboratory system, while p and μ are still measured in the plasma frame. Without entering into such details, let us just report the form that the equation takes accounting for these effects, plus a “source – loss” term S at the RHS:

$$\frac{\partial f_0}{\partial t} - \nabla_{\mathbf{x}} \cdot (K \nabla_{\mathbf{x}} f_0) - \frac{1}{p^2} \frac{\partial}{\partial p} \left(p^2 K_{pp} \frac{\partial f_0}{\partial p} \right) + \mathbf{V}_c \cdot \nabla_{\mathbf{x}} f_0 - \frac{(\nabla_{\mathbf{x}} \cdot \mathbf{V}_c)}{3} p \frac{\partial f_0}{\partial p} = S \quad (1.70)$$

We now describe the link of the parameters/functions in the above equation with the microscopic understanding of CR physics.

1.2.2 Considerations on the spatial diffusion

In CR phenomenology it is often assumed that diffusion is homogeneous and isotropic within the galactic halo volume. This diffusion is encoded by a rigidity dependent diffusion coefficient of the form:

$$K(R) = K_0 \beta R^\delta, \quad (1.71)$$

where K_0 and δ are let free to vary to adjust the chosen dataset. Microscopically we saw that small fluctuations of the magnetic field lead to a diffusion in the direction of the regular component,

$$K = \frac{v^2}{8} \int_{-1}^1 d\mu \frac{(1 - \mu^2)^2}{D_{\mu\mu}(\mu)}. \quad (1.72)$$

At the same time, using equation (1.56), a scale-free power spectrum of the wave $\mathcal{E}_k \propto k^{-\nu}$ implies:

$$K \propto R^{2-\nu}, \quad (1.73)$$

which for the case of the Kolmogorov [Kolmogorov 1941] turbulence with $\nu = 5/3$ gives $\delta = 1/3$. This very common turbulence where the energy cascades down from the large to the small scales assumes that the small scale turbulent motions are statistically isotropic. Primarily established for viscous fluids, this power-law dependence was shown to be also valid for strong magnetic turbulence in a plasma [Verma 1999], where the fluctuations dominate the mean magnetic field. In the presence of a strong magnetic field, the turbulence is anisotropic. In this case, it was shown by [Iroshnikov 1964] and [Kraichnan 1965] that $\mathcal{E}_k \propto k^{-\nu}$ with $\nu = -3/2$. To know whether one or the other is actually dominating the interstellar medium is still a debated question, although the Kolmogorov-like turbulence seems to be preferred for the case of the solar plasma [Roberts 1991]. Furthermore, numerical studies (e.g [Shalchi 2005]) which challenge some approximation (in particular the quasi-linear approximation), exhibit significant deviations from the idealized single power-law dependence quoted above. Hence in the following, δ is a phenomenological parameter let free to vary to best adjust the data. The β dependence of the diffusion coefficient in equation 1.71 is obtained for a specific 1D geometry of the turbulence. However, this might not be the one realized in the ISM and it should also be considered as a free parameter.

1.2.3 Reacceleration from plasma waves

In the same vein as the diffusion coefficient, the reacceleration is phenomenologically parameterized by K_{pp} which, in the literature, is often written in one of these two forms:

$$K_{pp}(R) = \begin{cases} \frac{1}{9} \frac{p^2 V_a^2}{K(R)} \\ \frac{4}{3\delta(4-\delta^2)(4-\delta)} \frac{p^2 V_a^2}{K(R)} \end{cases} \quad \text{or,} \quad (1.74)$$

with V_a the Alfvénic speed often introduced as a free parameter. Note that these two coefficients do have the same energy dependence, and once δ is fixed, a simple renormalization allows to switch from one to the other. In the following we highlight the physical origin of this reacceleration term as well as its energy dependence.

By definition of a diffusion process, the coefficient \mathbf{K}_{pp} can be written as (see for example [Blandford 1987] p18):

$$\mathbf{K}_{pp} = \frac{1}{2} \left\langle \frac{\Delta \mathbf{p} \Delta \mathbf{p}}{\Delta t} \right\rangle. \quad (1.75)$$

Now, assuming isotropic scattering by an isotropic distribution of Alfvén waves moving with $V_a \ll c$, the change in the momentum of the particle transforming into the frame of the scatterer and transforming back again to the original frame, is $\Delta \mathbf{p} = -(\mathbf{p} \cdot \mathbf{V}_a)/v$. Furthermore, such a change happens every $\Delta t = l/v$, where l is the mean free path of the particle. Under these assumptions, \mathbf{K}_{pp} becomes isotropic and we obtain:

$$\mathbf{K}_{pp} = K_{pp} = \frac{1}{2} \times 2 \times \frac{\langle (\mathbf{p} \cdot \mathbf{V}_a)^2 \rangle v}{v^2 l} = \frac{1}{3} \frac{p^2 V_a^2}{v l} \quad (1.76)$$

It is now possible to introduce the diffusion coefficient in space which can be written as $K(R) = vl/3$, and this leads to the first expression 1.74. The second expression of K_{pp} requires a more specific form for the diffusion coefficient, using a normalized turbulence density, for details see [Seo 1994]. Once more, constraints on reacceleration strength are set by fitting CR fluxes, notably secondary to primary ratios, and the order of magnitude for the Alfvénic' speed turns out to be $V_a \approx 20 \text{ km s}^{-1}$. An upper limit of the reacceleration strength was set by [Thornbury 2014].

In this thesis we always assume that the typical size of the main region of reacceleration, above and below the Galactic plane, is much smaller than the size of the diffusive halo. In the following we always consider this effect to be pinched inside the Galactic disk. Given these approximations, our V_a cannot be expected to be more than an effective parameter.

1.2.4 Convection of cosmic rays

Theoretically, it is expected that the halo plasma is not static, and that two main types of wind are expected, according if the origin of the wind is the thermal plasma or the non-thermal CR population itself [Maurin 2001]:

Temperature driven galactic wind: This class of models is based on the simple idea that a sufficiently hot gas will create a pressure gradient, eventually dominating gravity [Johnson 1971]. On a smaller scale, this mechanism is at the origin of the solar wind. However to be efficient, it was shown that this wind would require temperatures above 10^6 K [Habe 1980], whereas the plasma inside the disk is one order of magnitude cooler. Nonetheless, this kind of wind might partially contribute to the total one.

Cosmic ray driven wind: We saw that the local energy density of cosmic rays is quite high and actually comparable to the one of the thermal plasma. Moreover, CRs are coupled to the thermal plasma via frozen-in magnetic field lines. In this picture, the CR confinement creates a gradient pressure. As this gradient induces a current of cosmic rays at subalfenic speed outward the Galaxy, it triggers the so-called streaming instability which leads to a resonant generation of waves in order to remove the cause of the instability. The overall effect is a net momentum transfer from CRs to the gas via waves as a mediator, pushing away the gas from the disk into the halo [Breitschwerdt 2000]. The fluctuation amplitudes remain finite through nonlinear wave dissipation. Taking into account details of this physics, self consistent propagation models can be derived, where the static halo is replaced by a boundary whose position depends on particle momentum (see for example [Völk 2014] for a review, [Zirakashvili 1996] for an example, and [Recchia 2017] for recent phenomenology).

Obviously, our model cannot account for a coupled CR-wind system. However, since the structure and the value of wind speed is very uncertain for our Galaxy, it makes sense to replace this function via a constant parameter, which is let free to vary in the following. Typical values constrained by secondary over primary CR flux ratios are order 10 km s^{-1} .

1.2.5 Isotropization of CRs in the diffusive regime

One of the most intriguing facts about cosmic rays is the quasi perfect isotropy of their arrival directions. Actually this apparent isotropy is a direct consequence of CR deflections on the turbulent Galactic magnetic field. Only relatively weak anisotropies are expected from the current understanding of the sources and the propagation of cosmic rays. For example, the motion of the Earth with respect to the isotropic diffusion frame, or an inhomogeneous distribution of sources around the solar system, would induce a small dipole in the arrival directions of CRs. Numerous experiments – ground-based air shower arrays and underground muon detectors – do show the existence of small anisotropies with relative amplitudes of order 10^{-4} - 10^{-3} at energies from 100 GeV to hundreds of TeV. Before giving any clue for interpreting these values, let us specify first how we define CR anisotropies and some theoretical expectations in the diffusive regime. As mentioned in introduction, we denote the phase space density $f(\mathbf{r}, \mathbf{p})$ for a given species. One can rewrite this function with its decomposition on a sphere in momentum space. At a given $p = \|\mathbf{p}\|$ the angular dependence of $f(\mathbf{r}, \mathbf{p})$ can be projected on the basis of the spherical harmonics $Y_\ell^m(\theta, \varphi)$. Omitting the position \mathbf{r} in the argument, it leads to:

$$f(\mathbf{p}) = \sum_{\ell=0}^{\infty} \sum_{-l}^{\ell} f_\ell^m Y_\ell^m(\theta, \varphi). \quad (1.77)$$

f_ℓ^m corresponds to the weight of the spherical harmonic Y_ℓ^m in the decomposition

and is defined as:

$$f_\ell^m = \int_{\Omega} f(\mathbf{p}) Y_\ell^{m*}(\theta, \varphi) d\Omega \quad (1.78)$$

Motivated by the approximation equation 1.58, we stop the expansion at $\ell = 1$, equation 1.77 results in:

$$f(\mathbf{p}) = f_0^0 Y_0^0 + f_1^{-1} Y_1^{-1} + f_1^0 Y_1^0 + f_1^1 Y_1^1 + \mathcal{O}(Y_{\ell>1}) \quad (1.79)$$

Each of the terms in the sum are given by:

$$f_0^0 Y_0^0 = \frac{1}{4\pi} \int_{\Omega} f(\mathbf{p}) d\Omega \quad (1.80)$$

$$f_1^{-1} Y_1^{-1} = \frac{3}{4\pi} \sin \theta \cos \phi \underbrace{\int_{\Omega} \sin \theta' \cos \phi' f(\mathbf{p}) d\Omega}_X \quad (1.81)$$

$$f_1^0 Y_1^0 = \frac{3}{4\pi} \sin \theta \sin \phi \underbrace{\int_{\Omega} \sin \theta' \sin \phi' f(\mathbf{p}) d\Omega}_Y \quad (1.82)$$

$$f_1^1 Y_1^1 = \frac{3}{4\pi} \cos \theta \underbrace{\int_{\Omega} \cos \theta' f(\mathbf{p}) d\Omega}_Z \quad (1.83)$$

The first term of this expansion is the isotropic term, denoted hereafter $f_0(p)$. Here we introduce the unit vector \mathbf{n} in the direction of \mathbf{p} so that $\mathbf{p} = np$. Furthermore we define the dipole vector $\boldsymbol{\delta}$ by:

$$\boldsymbol{\delta} = \frac{3}{4\pi} \frac{\mathbf{X}}{f_0(p)} \quad \text{with: } \mathbf{X} = (X, Y, Z). \quad (1.84)$$

This definition let us rewrite equation 1.83 as:

$$f(\mathbf{p}) = f_0(p)[1 + \mathbf{n} \cdot \boldsymbol{\delta}] + \mathcal{O}(Y_{\ell>1}). \quad (1.85)$$

Thus we obtain the dipolar expansion of $f(\mathbf{p})$. For a sufficiently large energy, above which one can neglect all lower energy processes except diffusion, it is possible to relate the anisotropy vector $\boldsymbol{\delta}(\mathbf{r}, \mathbf{p})$ with the spatial gradient of $f_0(\mathbf{r}, p)$. We define the local current of cosmic rays as:

$$\mathbf{j}(\mathbf{r}, \mathbf{p}) = \mathbf{v} f(\mathbf{r}, \mathbf{p}) \quad (1.86)$$

$$= c\beta \mathbf{n} f(\mathbf{r}, \mathbf{p}) \quad (1.87)$$

$$\approx c\beta \mathbf{n} f_0(\mathbf{r}, p) [1 + \mathbf{n} \cdot \boldsymbol{\delta}] \quad (1.88)$$

Taking the isotropic part in momentum space of $\mathbf{j}(\mathbf{r}, \mathbf{p})$, the previous equation results in:

$$\mathbf{j}_0(\mathbf{r}, p) = \frac{1}{4\pi} \int_{\Omega} \mathbf{j}(\mathbf{r}, \mathbf{p}) d\Omega \simeq \frac{c\beta}{3} f_0(\mathbf{r}, p) \boldsymbol{\delta} \quad (1.89)$$

In the isotropic diffusion approximation the Fick law writes:

$$\mathbf{j}_0^D(\mathbf{r}, p) = -K \nabla_x f_0(\mathbf{r}, p). \quad (1.90)$$

Assuming the only physical current comes from diffusion, one obtains:

$$\delta(\mathbf{r}, p) \simeq \frac{3}{c\beta} \frac{\mathbf{j}_0^D(\mathbf{r}, p)}{f_0(\mathbf{r}, p)} = -\frac{3K}{c\beta} \frac{\nabla_x f_0(\mathbf{r}, p)}{f_0(\mathbf{r}, p)}. \quad (1.91)$$

One can note that the dipolar anisotropy is in the opposite direction of the CR gradient $\nabla_x f_0$. This formula can be generalized to the case of anisotropic diffusion. If the tensor K_{ij} depends only on p , one can directly replace $K\nabla_x f_0$ by $K_{ij}\partial_j f_0$, and for example in the presence of a coherent magnetic field \mathbf{B}_0 , $K_{ij} = \text{diag}(K_{\parallel}, K_{\perp}, K_{\perp})$, and we obtain:

$$\delta(\mathbf{r}, p) \simeq -\frac{3K}{c\beta f_0} [K_{\parallel} \nabla_{\parallel} f_0 + K_{\perp} \nabla_{\perp} f_0], \quad (1.92)$$

where ∇_{\parallel} and ∇_{\perp} correspond to the gradients parallel and orthogonal to the direction of \mathbf{B}_0 . In the quasilinear theory $K_{\perp} \ll K_{\parallel}$, so if $\nabla_x f_0$ is orthogonal to \mathbf{B}_0 the anisotropy becomes much smaller than expectations based on the isotropic model.

Not only spatial diffusion can be the origin of a dipole anisotropy, but also the simple relative motion of the reference frame with respect to the plasma frame in which CRs are isotropized yields a similar anisotropy named Compton-Getting effect (CG). The particularity of this effect is to be energy independent, and so acts as a global shift on the measured anisotropy as a function of energy.

Experimentally, the data can be studied in equatorial coordinates, a natural choice to highlight the effects of our environment in the Galaxy. To avoid the CG effect due to the relative motion of the Earth in the solar system, it is also possible to move in the solar frame. Measured anisotropy by IceCube and Tibet are shown in figure 1.8, as well as the evolution of the dipole anisotropy with the energy. The very low level of anisotropy $\delta \sim 1.5 \times 10^{-4}$ around 100 GeV, if attributed to the sole CG effect, would imply a drift velocity $v_D \approx c\delta \approx 50 \text{ km.s}^{-1}$ [Amato 2011]. As this speed is comparable with the Alfvénic velocity in the ionized ISM, it suggested (as already noticed in the seventies) that isotropization could be provided by wave-particle interaction. This also requires the time needed for isotropization to be much shorter than the confinement time in the Galaxy, another hint in favour of the simple diffusion models usually adopted.

The present situation is not yet clear. On the one hand, the observed level of anisotropy is consistent with the CG effect of a plasma co-rotating with the average motion of the stars around the Galactic center. Anisotropy of the order of 10^{-4} is expected from the proper motion of the Sun with respect to this average trend. On the other hand, simple models of isotropic CR diffusion predict dipole anisotropies of TeV-PeV CRs that are much larger than the observed values. This problem was dubbed *anisotropy problem* [Hillas 2005] and is illustrated in figure 1.8. It is

shown that the anisotropy amplitude does not evolve with energy as the diffusion coefficient, and that the phase does not point (at least below 100 TeV) toward the Galactic center. Moreover, using the secondary to primary ratio to calibrate the normalization and energy dependence of the diffusion coefficient yields a dipole anisotropy two orders of magnitude higher than the observed one. Possible solutions to this problem are discussed for example in [Ahlers 2016]. One of the most viable invokes a projection effect of the CR gradient on the local magnetic field (first term of equation 1.92).

Despite longstanding issues, these large scale anisotropies were expected by diffusion models. However, when recent experimental results unveiled small-scale anisotropy down to 10° , it came as a surprise. These small scale anisotropies are obtained by removing the fit of the large scale ones (dipole, quadrupole, octupole.) Several explanations have been proposed, considering effects of the heliosphere, non-diffusive propagation, modifications of pitch-angle diffusion, stochasticity effects, specific realization of the local turbulent magnetic field and some others. A review of this problem can be found in [Ahlers 2016].

On top of that, anisotropies may arise from the discrete distribution of the sources, often considered to as a continuum in space and time. A similar probabilistic framework as the one developed in chapter 2, should allow us to compute the probability to obtain a given anisotropy with respect to the ensemble average one.

1.3 Interactions with the interstellar medium

In our simplified view of the Galaxy for CR phenomenology, we consider all gas and stars to be pinched inside an infinitely thin disk. Despite this approximation, self-consistency requires at least to include all the relevant interaction processes that cosmic rays undergo when crossing the disk. These depend on the matter composition of the Galactic interstellar medium (ISM) which we describe now.

1.3.1 The composition of the interstellar medium

The interstellar medium is made of gas and dust. The gas is the most abundant component and so the main ingredient for computing interaction of CRs. Due to heating and cooling processes in the ISM, the gas can be found in a few different states that we describe in the following:

Cold gas, at a temperature around 80 K. This component is made of neutral and molecular hydrogen (HI and H₂ respectively) as well as helium (He) often distributed inside clouds of density above 10 cm^{-3} . The (HI,He) and H₂ are both closely confined to the plane (although they do not have the same radial distribution), vertically distributed up to 120 pc and 6 pc, respectively.

Warm gas, at a temperature around 8000 K. This diffuse component is mainly made of HI and ionized hydrogen (HII) with densities below 10 cm^{-3} . The latter component is the main responsible for the free electron density. Its vertical spread is wider and goes up to 500 pc or 1 kpc above the disk. HII is also found in much

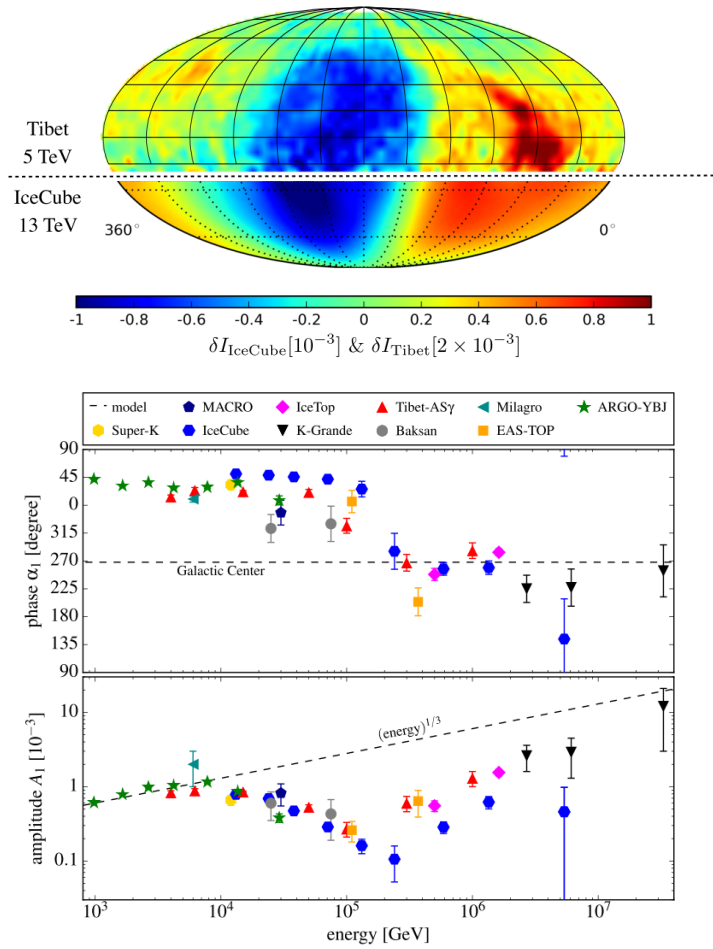


Figure 1.8: Top: Combined CR anisotropy of Tibet-AS γ and IceCube in the equatorial coordinate system. Bottom: phase and amplitude of the (equatorial) dipole anisotropy extracted from recent measurements Figures taken from [Ahlers 2016]

Element	H ₂	HI (cold)	HI (warm)	HII (warm)	HII (hot)
Total mass [M _⊙]	2.5×10^9	3×10^9		$\sim 10^{8-9}$	
Local surface density [M _⊙ .pc ⁻²]	3.3	3.2	0.7	1.54	0.2
Local midplane density [cm ⁻³]	0.6	0.3	0.1	0.040	0.002
Temperature [K]	10	80	8000	8000	10 ⁶

Table 1.1: Components of the Galactic hydrogen. Table adapted from [Cox 2015]

denser regions but does not weight much in the total HII density. A recent analysis of these regions is presented in [Gaensler 2008].

Hot gas, at a temperature around 10⁶ K. This diffuse component is mainly made of HII. Its spatial extension is of the order of the magnetic halo size, i.e. over kpc distance. Recent surveys ([Salem 2015] and [Nugaev 2015]) indicate that this gas, albeit with a much smaller density than in the disk, could contribute to a significant fraction of the mass of the galaxies. Some simulations even try to predict its distribution [Peters 2015].

The spatial distributions of these components might be biased by our local observations and extrapolations hampered by dust absorption. In table. 1.1 we summarize the different characteristics of these components. There, the helium mass is always included and thought to be a bit larger abundant than the primordial one, with $n(\text{He})/n(\text{H}) \approx 0.11$ [Cox 2015]. Notice that values as low as 0.08 seem also to be consistent with data (see discussion in [Strong 1998]). Typical values taken in the semi-analytical code USINE⁸ are $n(\text{He}) = 0.1 \text{ cm}^{-3}$ and $n(\text{H}) = 0.9 \text{ cm}^{-3}$ according to [Ferrière 2001].

In our approach, the impossibility to factorize the solution in space and energy by using a gaseous distribution of sparse material justifies the use of a thin disk where all the matter is concentrated. However, if matter actually extends over a large distance, over the entire Galactic magnetic halo for instance, it could impact the propagation of cosmic rays through the spallation reactions it would generate there. Hereafter we detail the different processes of energy loss a CR undergoes when it interacts with the gas.

1.3.2 Continuous energy losses

The presence of gas located in the Galactic disk, considered to be infinitely thin in our simplified model, is responsible for continuous energy losses.

Coulomb energy losses:

The rate of energy loss of a charged particle of mass M and charge Z moving in a fully ionized plasma is dominated by the collisions with the thermal electrons

⁸This code was devised by David Maurin and is able to compute the fluxes of CR nuclei in the energy range [$\mathcal{O}10\text{MeV}, \mathcal{O}(10\text{TeV})$]. More information on its functioning can be found in [Putze 2010]

[Mannheim 1994]. Above a very low energy threshold related to the plasma temperature, this term writes as follow:

$$b_{coul}(E) \simeq -4\pi r_e^2 c m_e c^2 Z^2 n_e \ln \Lambda_c \frac{\beta^2}{x_m^3 + \beta^3}, \quad (1.93)$$

where $x_m = (3\sqrt{\pi}/4)^{1/3} \sqrt{2k_B T_e / m_e c^2}$ with n_e and T_e corresponding to the electron density and temperature in the plasma, and r_e the classical radius of the electron. The Coulomb logarithm $\ln \Lambda_c$ writes:

$$\ln \Lambda_c \simeq \frac{1}{2} \ln \left(\frac{m_e^2 c^4}{\pi r_e \hbar^2 c^2 n_e} \frac{M \gamma^2 \beta^4}{M + 2\gamma m_e} \right) \quad (1.94)$$

Using a value of the density $n_e \approx 0.033 \text{ cm}^{-3}$ [Nordgren 1992] and $T_e = 10^4 \text{ K}$ used in the USINE code, the Coulomb energy loss for a carbon nuclei at 1 GeV/nuc is evaluated as:

$$|b_{coul}(E = 1 \text{ GeV/nuc})| \approx 3 \times 10^{-2} \text{ GeV Myr}^{-1}. \quad (1.95)$$

Ionization energy losses:

Energetic charged particles can transfer part of their energy to bound electrons of the interstellar matter. When their velocity is above the characteristic velocity of the bound electron, the energy loss rate writes:

$$b_{ioni}(E) \simeq -\frac{2\pi r_e^2 c m_e c^2 Z^2}{\beta} \sum_{H, He} n_s B_s, \quad (1.96)$$

$$B_s = \ln \left(\frac{2m_e c^2 \beta^2 \gamma^2 Q_{max}}{\tilde{I}_s} \right) - 2\beta^2, \quad (1.97)$$

where \tilde{I}_s is the geometrical mean of the ionization potentials of the atom excited states ($\tilde{I}_H = 19 \text{ eV}$ and $\tilde{I}_{He} = 44 \text{ eV}$). The maximal energy transferred by the particle to the electron is:

$$Q_{max} = \frac{2m_e c^2 \beta^2 \gamma^2}{1 + [2\gamma m_e / M]}. \quad (1.98)$$

Using reference USINE values for the densities of HI and He, one finds for a carbon nucleus at 1 GeV/nuc:

$$|b_{ioni}(E = 1 \text{ GeV/nuc})| \approx 0.22 \text{ GeV Myr}^{-1}. \quad (1.99)$$

In the case of leptons, for which Thomson cross-section is $\sim 10^7$ larger than the nuclear one, additional energy losses must be taken into account: the inverse Compton scattering on the interstellar radiation field, the synchrotron emission within the galactic magnetic field, and the Bremsstrahlung braking radiation. We will not enter in the details of these effects since we are mainly dealing with nuclei in this thesis.

In contrast with continuous energy losses which do not affect the relative composition of the species, catastrophic losses can occur with the fragmentation of heavy nuclei into smaller ones. In the following section we describe such processes and the cross-sections of the interactions that rule their frequencies.

1.3.3 Nuclear reactions

Nuclear reactions are omnipresent in nature from nucleosynthesis in the cores of stars to fission of radioactive nuclei in the Earth crust. Understanding these processes requires a precise knowledge of the nuclei and their interactions. In the case of CR physics, we are mainly interested in characterizing the nuclear interactions of CR species with the ISM. Such a goal is also of relevant interest in many areas of research, including medical applications and detector simulation for high energy physics. The energy range we are focusing on is the one of galactic CR measurements and extends from $O(100)$ MeV to TeV. Because of the significant dependence of the nuclear interaction strength on energy, a study over this broad spectrum is needed.

The most relevant interactions involve a CR nucleus colliding a proton or a helium target nucleus, since these are the two main components of the ISM. We recall some details of such a collision [Longair 2011]. In the target frame, a high energetic proton is incoming with a small effective size corresponding to the De Broglie wavelength which is $\sim 0.02 \times 10^{-15}$ m at an energy of 10 GeV. Thus, for sufficiently high energies the proton will interact with individual nucleons, leaving the others unaltered, and this justifies the so-called *straight-ahead approximation*, where the kinetic energy per nucleon is conserved during the collision⁹. Eventually the proton can undergo multiple scatterings in the nucleus, with a number of interactions roughly proportional to the number of nucleons along the line of sight, $\approx A^{1/3}$. The interacting nucleons are generally removed from the nucleus, leaving it in a very excited state. Hadronic activity (with the production of pions, for instance) is possible along the collision axis, while the residual nucleus is often unstable. For light nuclei, in particular, the resulting imbalance between neutrons and protons might prove fatal. Hence the nucleus may fragment by emitting quasi isotropically daughter fragments, which in turn may be unstable to further decay or fragmentation.

In this typical process, several parameters are relevant for CR predictions. First, the probability that the nucleus loses energy or converts into one or several different nuclei is ruled by the total inelastic cross-section $\sigma^{\text{inelastic}}$ often written as σ^{tot} , with a slight abuse of notation. Generically the total interaction cross-section is written as the sum of the elastic cross-section and the inelastic one:

$$\sigma^{\text{interaction}} = \sigma^{\text{elastic}} + \sigma^{\text{inelastic}}. \quad (1.100)$$

For all the nuclei (except in the case of antiprotons) we neglect the non destructive part of the total inelastic cross-section. Then, σ_{tot} is simply the destruction

⁹This is actually the main reason why fluxes are often presented by experiments as a function of kinetic energy per nucleon. Such a conversion does not go without problems since one has to assume or measure the isotopic composition of the species.

cross-section. Other important ingredients for CR studies are the isotopic production cross-sections, which secondary species abundances crucially depend upon. Formally, the link between both cross-sections is the following:

$$\sigma_i^{\text{tot}} = \sum_{P_k} \sigma_{i \rightarrow p_1 + p_2 \dots + p_n} , \quad (1.101)$$

where $P_k = \{p_1 + p_2 \dots + p_n\}$ is a list of products whose sum of masses is below the mass of the species i .

Several strategies have been used to determine the destruction and the production cross-sections. While the first are mainly based on fitting existing data, less efforts have been put in the measurements of production cross-sections certainly because there are much more numerous with less side applications. Hence Monte Carlo models and semi-empirical formulae are often used for their determination. Typical uncertainties of 10 to 20% on these cross-sections are commonly observed between different studies. As the measurement of CR fluxes is reaching an unprecedented accuracy it is timely to reconsider launching measurement campaigns, and this was the main motivation of a recent conference at CERN [XSC]. In the following we give some details on both destruction and production cross-sections, reporting the benchmark parameterizations that we use in this thesis.

Destruction cross-section

A naive approach for the parameterization of the destruction cross-section is to assume that it is proportional to the geometrical area of the colliding nuclei, hence proportional to R^2 , with R the sum of radii of the nuclei. Since for a nucleus $R \propto A^{1/3}$, the total cross-section can be written as: $\sigma^{\text{tot}} = \pi r_0^2 (A_{\text{proj}}^{1/3} + A_{\text{target}}^{1/3} - b_0)^2$. This approach was chosen in [Bradt 1950] where the authors introduced an energy dependence of r_0 and b_0 , the effective radius and the transparency of the nucleons.

Later, in the eighties, strenuous efforts were made to measure these cross-sections and figure 1.9 features the example of the total inelastic cross-section for carbon-proton reaction. Notice that the cross-section varies with energy: a low energy hump is followed by a dip before reaching a plateau often extrapolated as a constant value at high energies. Such large variations coming from nuclear resonances are not necessarily present with the same amplitude in other nuclei, and for example light nuclei are often peculiar because of their smaller number of nucleons.

Among papers fitting empirical formulae to the data, [Letaw 1983] claims a precision $< 2\%$ for kinetic energies above 2 GeV/nuc where data precise at the percent level are available. Below this energy the fit degrades, yielding 10% uncertainty for energies around 100 MeV. Their best fit parameterization is shown in Figure 1.9 for the total inelastic cross-section for carbon-proton reaction.

After the release of a new collection of data [Bauhoff 1986] it was possible to reconsider a parameterization, and in [Wellisch 1996] the authors claim a 2% precision with respect to the high energy data (> 2 GeV). In the interval [6.8 MeV/nuc, 20 GeV/nuc] the authors claim an overall spread of 4%. Note that this paper is only dealing with elements with $Z > 4$.

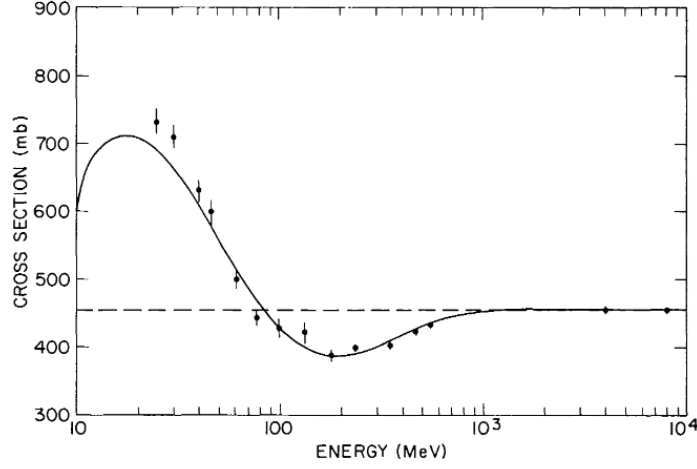


Figure 1.9: Carbon-proton total inelastic cross-section data with the energy-dependent fit of [Letaw 1983]

Finally, at the end of the twentieth century, researchers from NASA built up a universal parameterization for nucleus-nucleus total inelastic cross-sections [Tripathi 1999] taking into account Pauli blocking and Coulomb potential. Since then, their result is often used in propagation codes. It takes the form:

$$\sigma_{tot} = \pi r_0^2 \left(A_{proj}^{1/3} + A_{target}^{1/3} + \delta_E \right)^2 \left(1 - R_c \frac{B}{E_{cm}} \right) X_m, \quad (1.102)$$

where the last term accounts for Coulomb interaction, whose importance decreases with energy. Hence the authors name B the energy-dependent Coulomb interaction barrier, with

$$B = \frac{1.44 Z_p Z_t}{R}. \quad (1.103)$$

Here, R is the distance for evaluating the height of the Coulomb barrier:

$$R = r_p + r_t + \frac{1.2 \left(A_p^{1/3} + A_t^{1/3} \right)}{E_{cm}^{1/3}}, \quad (1.104)$$

where $r_i = 1.29 r_{rms,i}$ is the radius of the nuclear sphere, while in the formula $r_0 = 1$ fm. Transparency and Pauli blocking are taken into account through:

$$\delta_E = 1.85 S + \frac{0.16 S}{E_{cm}^{1/3}} - C_E + \frac{0.91 (A_t - 2Z_t) Z_p}{A_t A_p}, \quad (1.105)$$

$$\text{with: } S = \frac{A_p^{1/3} A_t^{1/3}}{A_p^{1/3} + A_t^{1/3}}, \quad (1.106)$$

$$\text{and: } C_E = D \left[1 - \exp \left(-\frac{E}{T_1} \right) \right] - 0.292 \exp -\frac{E}{792} \cos (0.229 E^{0.453}). \quad (1.107)$$

Finally the factors $X_m \sim \mathcal{O}(1)$ and R_c are used to adjust the cross-section for lighter nuclei.

Production cross-section

Concerning production cross-sections, the situation is much more ambiguous, mainly due to the lack of data, their low quality, and the absence of a reference database. This situation possibly reflects the fact that no other application except for CR astrophysics motivates these measurements. Three complementary approaches can be distinguished. When the data from collision experiment (typically proton beam crossing a fixed target) are available, the best estimation is a simple fit using empirical or semi-empirical formulae which can reproduce the low energy dependence of the cross-sections. When no data is available (majority of the cases) both empirical and semi-empirical formulae calibrated on other channels are extrapolated. Finally another option is to use Monte-Carlo simulations which track the interactions of a proton crossing a nucleus, calculate the transferred energy and compute the probability of fragmentation. Yet, even this option requires a calibration with data. Hereafter we discuss some references for each approach.

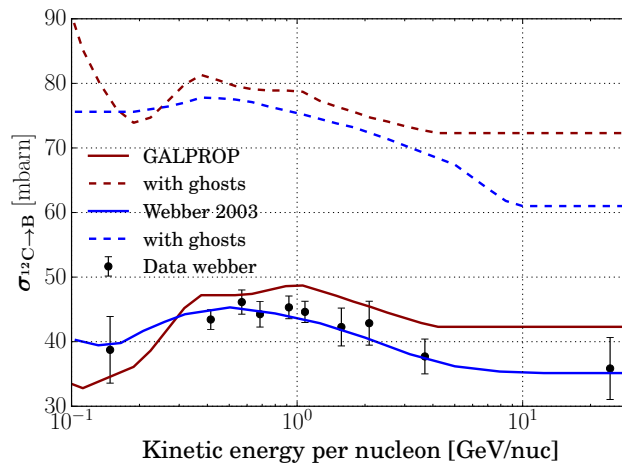


Figure 1.10: The black dots correspond to the production cross-section of boron from ^{12}C measured by Webber in [...]. The solid curves are two models from Webber and GALPROP. The dashed lines show the effective cross-section for cosmic rays when including the contributions from *ghost nuclei*.

For a semi-empirical approach, one can cite the benchmark work of Silberberg and Tsao [Silberberg 1973a, Silberberg 1973b], initially motivated by the lack of measurements and the slowness of Monte Carlo estimation. A refreshed version of their semi-empirical formulae using Webber data [Webber 1998a] can be found in [Silberberg 1998].

Strenuous efforts were made in the nineties by the Webber's group [Webber 1990,

Webber 1998a, Webber 1998b, Webber 1998c] to precisely measure and parameterize isotopic production cross-sections with empirical formulae. An example of the production cross-section of boron from ^{12}C is shown in figure 1.10. In the USINE code as well as in this thesis, the nuclear flux calculations benefit from a revision of Webber cross-sections of 2003 [Webber 2003] which is preferentially used. As the empirical formula from Webber is not extended to all nuclei, the spallation cross-sections on helium are calculated using the prescription of [Ferrando 1988]. Interestingly, the numerical code GALPROP presents its own library of cross-sections. Several options can be chosen, but it often uses a mixture of several codes and tables found to better fit the data collected by the authors. As an example, the adopted parameterization for the production of boron from ^{12}C is shown in figure 1.10 compared with Webber data, although other data are also used to justify their choice.

Finally, a fully numerical determination of these cross-sections is adopted in Monte Carlo codes like Fluka [FLU] and GEANT4 [GEA]. In these cases, the codes track the interactions of protons crossing the nuclei, calculating the transferred energy as well as the probability of fragmentation.

Remarks:

i) Some refinements should be mentioned when dealing with production cross-sections. Indeed as a product of the fragmentation process, many daughter nuclei are actually unstable and decay *rapidly* into more stable ones. Provided that their lifetime are much shorter than the Galactic propagation time, it is more meaningful to include these nuclei via *effective* production cross-sections. A comprehensive overview of these so-called *ghost nuclei* is given in [Maurin 2001], where the author defines the lifetime range: $\text{ms} \leq \tau^{\text{ghost}} \leq \text{kyr}$. As an example, let us focus on the production of ^{11}B . It may be the decay product of four *ghost* nuclei: ^{11}Li , ^{11}Be , ^{12}Be , ^{11}C . The *effective* production cross-section of ^{11}B from a nucleus i writes:

$$\sigma_{i \rightarrow ^{11}\text{B}}^{\text{effective}} = \sigma_{i \rightarrow ^{11}\text{B}} + \sum_{\text{ghost } X} Br(X \rightarrow ^{11}\text{B}) \sigma_{i \rightarrow X} \quad (1.108)$$

$$= \sigma_{i \rightarrow ^{11}\text{B}} + 78.4\% \sigma_{i \rightarrow ^{11}\text{Li}} + 97.1\% \sigma_{i \rightarrow ^{11}\text{Be}} + 0.52\% \sigma_{i \rightarrow ^{12}\text{Be}} + 100\% \sigma_{i \rightarrow ^{11}\text{C}}, \quad (1.109)$$

where the percentages correspond to the different branching ratios $Br(X \rightarrow ^{11}\text{B})$ of each ghost into ^{11}B . As shown in figure 1.10, the inclusion of ghost nuclei in the effective production cross-sections is crucial, and should motivate a precise experimental estimation of their production. Remark that, when the lifetime of secondary radioactive species is close to the propagation time, these latter can serve as *cosmic ray clocks* and we will see that their fluxes can be used to break degeneracies between propagation parameters.

ii) We previously assumed that during a fragmentation process the kinetic energy per nucleon is conserved. Although this approximation is not perfectly true in general, it can safely be used at high energies, above few GeV per nucleon. Below,

challenging this hypothesis was shown to decrease the pic of the B/C ratio by 5% at 1 GeV/nuc [Tsao 1995]. Reinvestigating such effect seems to be important in the context of AMS-02 data precision, which reaches 2%. Nonetheless, as the uncertainties on the production cross-sections are typically larger than 10%, we will not discuss this effect further in this thesis.

iii) Production of anti-nuclei such as antiprotons will be detailed in chapter 4 devoted to the analysis of AMS-02 data.

1.3.4 Solar modulation

The Sun—just like other stars—accelerates ionized particles by releasing part of its magnetic energy (through magnetic reconnection for example) during sporadic events called *flares*. Although this phenomenon only accounts for CR particles at Earth below 1 MeV/nuc, intriguingly even detected Galactic CR particles with energies in the GeV/nuc range are very sensitive to the solar activity. Indeed, Galactic cosmic rays encounter the solar wind, made of a fully ionized plasma embedded in the heliospheric magnetic field. This wind propagates radially from the Sun at a typical supersonic speed of 400 km s⁻¹. This velocity, above the average thermal velocity of particles in the corona, reveals that some processes of acceleration are at stake. The transition from a supersonic wind to a subsonic one is realized at the termination shock, which was crossed successively by the space probes Voyager 1 and 2 in December 2004 and August 2007, respectively. Within the sphere delimited by this shock, the heliospheric magnetic field was predicted to have a spiral geometry [Parker 1965]. Such a structure comes mainly from two ingredients: the rotation of the Sun and the inversion of polarity of the magnetic field every 11 years.

The interaction of cosmic rays with the solar wind leads to significant global and temporal variations in their intensities and in their energies as a function of position inside the heliosphere. Due to its periodicity, this process is identified as the solar modulation of cosmic rays. Qualitatively, the same phenomena affecting CR propagation in the Galaxy also affect their propagation in the heliosphere, although with a different geometry and relative importance of different terms, notably the convective wind. The equation which rules the density of cosmic rays is then a Fokker plank equation [Parker 1965] which can be solved numerically (First works by Fisk in the seventies) using Monte Carlo codes like HELIOPROP [Gaggero 2014] or SOLARPROP [Kappl 2016]. However, under the following assumptions:

- the solar wind V is radial and constant,
- diffusion is isotropic and homogeneous (with κ the diffusion coefficient),
- the density of cosmic rays in momentum space is spherically symmetric,
- the convective current cancels the diffusive one (which is a good approximation above 400 MeV/nuc),

[Gleeson 1967, Gleeson 1968] have shown that a stationary solution of the problem satisfies the following equation,

$$\frac{\partial f}{\partial r} + \frac{VR}{3\kappa} \frac{\partial f}{\partial R} = 0, \quad (1.110)$$

with r the distance to the Sun and R the rigidity. As the dimension of the second term is the one of an electric field, this approximation was coined *Force field approximation*. Actually this equation is similar to the equation satisfied by charged particles in a radial electric field. This equation can be readily solved with the method of the characteristics. Assuming $\kappa = \kappa_0 \beta R$, one has to solve:

$$\frac{dR}{dr} = \frac{V}{3\kappa_0\beta} \Leftrightarrow \frac{dE}{|Z|e} = \frac{V}{3\kappa_0} dr, \quad (1.111)$$

by introducing the total energy E and the charge Z of the cosmic particle. Then integrating from r_{TOA} (standing for *top of the atmosphere*) which corresponds to the position of Earth with respect to the Sun, to r_{IS} (*interstellar*) outside the heliosphere, we obtain:

$$E_{IS} - E_{TOA} = |Z|e \frac{V}{3\kappa_0} (r_{IS} - r_{TOA}) \equiv |Z|e \Phi_{fisk} \equiv A |Z|e \phi_{fisk}. \quad (1.112)$$

In the last equation we defined the Fisk potential per unit of charge Φ_{fisk} , or per unit of charge and nucleon ϕ_{fisk} , henceforth a phenomenological parameter. As f is constant along the characteristic, we get

$$f(r_{TOA}, E_{TOA}) = f(r_{IS}, E_{IS}), \quad (1.113)$$

the fluxes are related by

$$\begin{aligned} \mathcal{J}_{TOA}(E_{TOA}) &= \frac{p_{TOA}^2}{p_{IS}^2} \mathcal{J}_{IS}(E_{IS}) \\ &= \frac{E_{TOA}^2 - m^2}{(E_{TOA} + A |Z|e \phi_{fisk})^2 - m^2} \mathcal{J}_{IS}(E_{TOA} + A |Z|e \phi_{fisk}). \end{aligned} \quad (1.114)$$

$$(1.115)$$

Thanks to this simple relation, it becomes easy to calibrate the Fisk potential directly with temporal variations of the flux, or indirectly with neutron monitors. The latter experiments are designed to measure the flux of fast neutrons produced by CRs interacting with the atmosphere. An important turning point was achieved by the Voyager mission which, by crossing the termination shock, was able to measure the interstellar CR spectrum. So far the force field has shown a good flexibility in fitting the spectra, and that is why this very simple model is still widely used. Although it is known to be inadequate for instance to capture charge dependent solar modulation. Presently, the main shortcoming to go beyond this approximation is the knowledge of the spatial, rigidity and especially the temporal dependence of the diffusion coefficients within the heliosphere, covering the underlying features of solar wind and magnetic field turbulence [Potgieter 2013].

1.4 Summary: propagation equation and timescale comparison

Starting from equation 1.70, we develop the source term S for a species α decomposing it as follows:

$$S(\mathbf{x}, p, t) = q_\alpha + \sum_{Z_\beta \geq Z_\alpha}^{Z_{max}} \sigma_{\beta \rightarrow \alpha} v_\beta n f_\beta + \frac{f_\beta}{\tau_\beta}, \quad (1.116)$$

where the first term corresponds to the primary injection from SNRs, the second is the fragmentation from heavier species, and the third the decay of parent radioactive species β into α . In the right hand side of equation 1.70, one can add energy losses, and sink terms from fragmentation and possible decay of α if it is unstable. Introducing these processes, the time dependent propagation equation takes the form:

$$\begin{aligned} \frac{\partial f_\alpha}{\partial t} + \mathbf{V}_c \cdot \nabla_{\mathbf{x}} f_\alpha - \frac{1}{3} (\nabla_{\mathbf{x}} \cdot \mathbf{V}_c) p \frac{\partial f_\alpha}{\partial p} - \nabla_{\mathbf{x}} \cdot K \nabla_{\mathbf{x}} f_\alpha - \frac{1}{p^2} \frac{\partial}{\partial p} p^2 K_{pp} \frac{\partial f_\alpha}{\partial p} \\ + \frac{1}{p^2} \frac{\partial}{\partial p} (p^2 b_{loss}(p) f_\alpha) + \sigma_\alpha v_\alpha n f_\alpha + \frac{f_\alpha}{\tau_\alpha} = q_\alpha + \sum_{Z_\beta \geq Z_\alpha}^{Z_{max}} \sigma_{\beta \rightarrow \alpha} v_\beta n f_\beta + \frac{f_\beta}{\tau_\beta}. \end{aligned} \quad (1.117)$$

In this section we still focus on nuclei CRs for which energy losses and spallations are exclusively located inside the Galactic disk, following the gas distribution. Concerning reacceleration, as previously assumed, the typical size of the main region of reacceleration is much smaller than the size of the diffusive halo. Taking into account these assumptions we can redefine pinched quantities, introducing the Galactic disk height h :

$$n \rightarrow 2h\delta(z) n \quad \nabla_{\mathbf{x}} \cdot \mathbf{V}_c \rightarrow 2h\delta(z) \nabla_{\mathbf{x}} \cdot \mathbf{V}_c \quad (1.118)$$

$$K_{pp} \rightarrow 2h\delta(z) K_{pp} \quad b_{loss} \rightarrow 2h\delta(z) b_{loss} \quad (1.119)$$

$$(1.120)$$

For convenience, this equation may also be rewritten in terms of the energy density $\psi = 4\pi p E f_\alpha$, more closely related to the flux. The equation becomes:

$$\begin{aligned} \frac{\partial \psi_\alpha}{\partial t} + \nabla_{\mathbf{x}} (\mathbf{V}_c \psi_\alpha - K \nabla_{\mathbf{x}} \psi_\alpha) - \frac{\partial}{\partial E} K_{EE} \frac{\partial \psi_\alpha}{\partial E} \\ + \frac{\partial}{\partial E} (b_{tot}(E) \psi_\alpha) + \sigma_\alpha v_\alpha n \psi_\alpha + \frac{\psi_\alpha}{\tau_\alpha} = q_\alpha + \sum_{Z_\beta \geq Z_\alpha}^{Z_{max}} \sigma_{\beta \rightarrow \alpha} v_\beta n \psi_\beta + \frac{\psi_\beta}{\tau_\beta}, \end{aligned} \quad (1.121)$$

where we introduce the reacceleration diffusion coefficient energy defined as $K_{EE} = \beta^2 K_{pp}$, the source term is redefined as $q_\alpha = E p q_\alpha$, and the total energy losses term

$b_{tot}(E) = \beta b_{loss}(p) + b_{drift}(E) + b_{adia}(E)$ with:

$$b_{drift}(E) = \frac{1 + \beta^2}{E} K_{pp}, \quad \text{and} \quad b_{adia}(E) = -\frac{1}{3} (\nabla_{\mathbf{x}} \cdot \mathbf{V}_c) \frac{p^2}{E}. \quad (1.122)$$

In the next section we give the solutions of this equation for the fluxes expressed per unit of kinetic energy per nucleon (E_{kn}). The equation becomes:

$$\begin{aligned} \frac{\partial \psi_{\alpha}}{\partial t} + \nabla_{\mathbf{x}} (\mathbf{V}_c \psi_{\alpha} - K \nabla_{\mathbf{x}} \psi_{\alpha}) - \frac{\partial}{\partial E_{kn}} \frac{K_{EE}}{A^2} \frac{\partial \psi_{\alpha}}{\partial E_{kn}} \\ + \frac{\partial}{\partial E_{kn}} \left(\frac{b_{tot}(E)}{A} \psi_{\alpha} \right) + \sigma_{\alpha} v_{\alpha} n \psi_{\alpha} + \frac{\psi_{\alpha}}{\tau_{\alpha}} = q_{\alpha} + \sum_{Z_{\beta} \geq Z_{\alpha}}^{Z_{max}} \sigma_{\beta \rightarrow \alpha} v_{\beta} n \psi_{\beta} + \frac{\psi_{\alpha}}{\tau_{\beta}}, \end{aligned} \quad (1.123)$$

with A the number of nucleons of the species α , and ψ_{α} now expressed in term of kinetic energy per nucleon.

In simplified cases it is possible to integrate this equation across the galactic plane, and to define a typical time scale for each process at a given energy. Since the strength of some effects depends drastically on the energy, a comparison of these timescales is useful to know which mechanism is actually dominating and which one can be safely neglected. In the following we define the different timescales at stake and then we compare them.

We first define effective times of disappearance of nuclei from the magnetic halo volume, which correspond to the typical times of leakage in the former leaky box model. First, we define the time spent by a nucleus inside the Galactic thin disk before escaping the diffusive halo in which convection and diffusion are taking place:

$$\tau_{\text{disk}} = \frac{h}{V_c} \left(1 - \exp \left(-\frac{V_c L}{K} \right) \right). \quad (1.124)$$

We also define timescales of remanence in the disk, for convection and diffusion, separately:

$$\tau_{\text{conv}} = \frac{h}{V_c} \quad \text{and} \quad \tau_{\text{diff}} = \frac{h L}{K}. \quad (1.125)$$

The other time at stake is the destruction timescale from fragmentation on the ISM:

$$\tau_{\text{frag}} = \frac{1}{\sigma_{\alpha} v_{\alpha} n} \quad (1.126)$$

More precisely, as fragmentation happens through collisions on both helium and hydrogen of the ISM, $\sigma_{\alpha} n = \sigma(\alpha \rightarrow \text{H}) n_{\text{H}} + \sigma(\alpha \rightarrow \text{He}) n_{\text{He}}$. From these two timescales one can define an effective leakage timescale:

$$\frac{1}{\tau_{\text{leak}}} = \frac{1}{\tau_{\text{disk}}} + \frac{1}{\tau_{\text{frag}}} \quad (1.127)$$

Concerning the ionization, Coulomb and adiabatic energy losses, we estimate their typical timescales as

$$\tau_{\text{loss}} = \frac{T}{|b(E)|}, \quad (1.128)$$

where T stands for the total kinetic energy of the nucleus. The ionization and Coulomb expression for $b(E)$ are directly extracted from formulae 1.93 and 1.96, whereas for the adiabatic energy losses, a good estimate can be deduce by averaging the corresponding term across the thin disk, leading to $b_{adia}(E) = -V_c p^2/3hE$. We also define a timescale corresponding to the sum of all theses the energy loss processes:

$$\frac{1}{\tau_{losses}} = \frac{1}{\tau_{coulomb}} + \frac{1}{\tau_{ionization}} + \frac{1}{\tau_{adia}}. \quad (1.129)$$

The reacceleration times scale takes the form:

$$\tau_{reacc} = \frac{T^2}{K_{EE}} \quad (1.130)$$

We compare these different time scales in figure. 1.11 in the case of ^{12}C and ^{56}Fe for the MED model [Donato 2004](reminded in Appendix A.2.2).

The shortest timescale corresponds to the dominant process. For the example of ^{12}C it appears that the leakage at very low energies comes mainly from convection, then at intermediate energies from fragmentation and is limited by diffusion for very high energies (above dozens of GeV/nuc). The same behavior is featured for the energy losses, dominated by ionization under few 100 MeV/nuc and by adiabatic energy losses above this energy. The figure also shows that above a few GeV the leakage time is much shorter than the energy loss time and the reacceleration time. Thus, for such energies, the last two processes are negligible and will not impact the prediction of the flux.

As the reacceleration and the leakage processes depend on the propagation model, it is interesting to analyze their relative strength varying the propagation parameters consistent with the secondary over primary ratio. In figure 1.12, we focus on ^{12}C and vary the propagation parameter among the three benchmark models MIN, MED, MAX derived in [Donato 2004] and summarized in Appendix A.2.2. The transitions between the relevant processes do not appear very different from one model to another. This means that an approximation justified for one propagation model would probably still be valid for other models derived consistently from secondary to primary ratios.

This last decade, several teams have made strenuous efforts to numerically solve the propagation equation, using the most realistic inputs as possible. Although the relevance of this work is indisputable for some observables (e.g gamma rays), current uncertainties in the study of CR nuclei probably do not justify such refinements. In appendix A we give the analytical expressions of the solutions of the propagation equation for the nuclei case. First, we use the high energy approximation where the triangular system of the nuclear fluxes can be solved fully analytically. Second, we present the numerical way to solve the propagation equation including all the low energy effects.

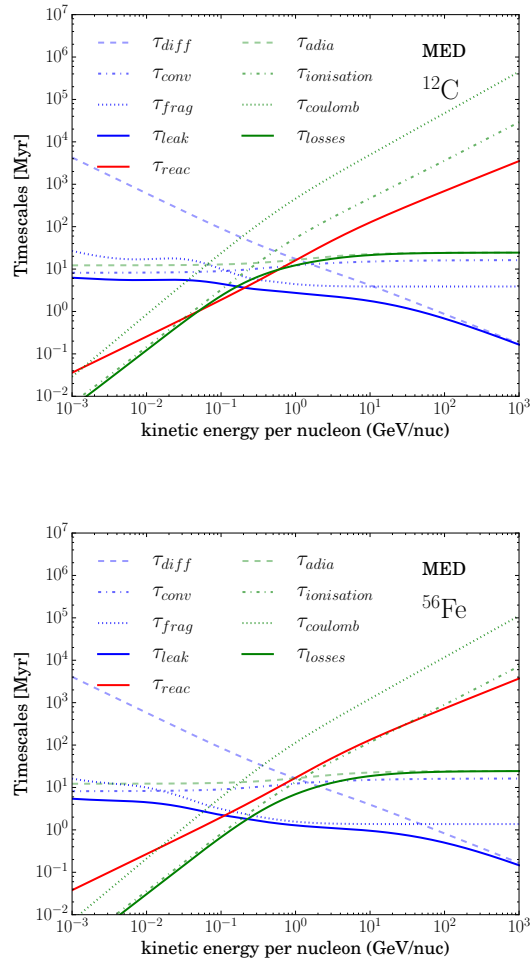


Figure 1.11: Timescale ratios for the two nuclei ^{12}C (top) and ^{56}Fe (bottom).

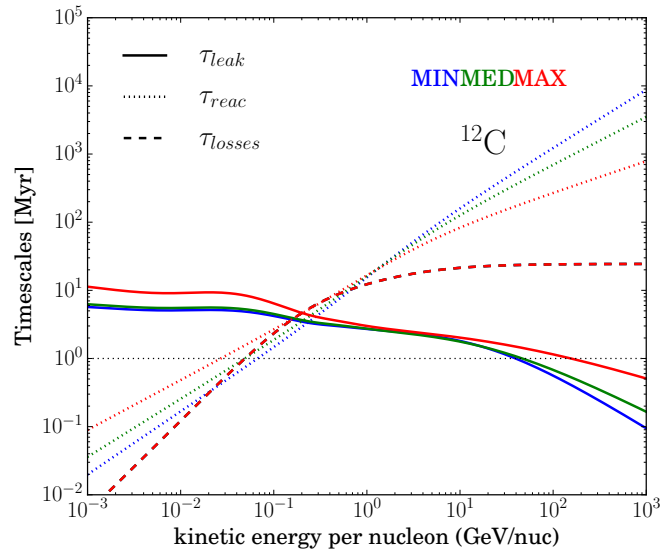


Figure 1.12: Timescale ratios for the propagation models MIN, MED, MAX in the case of ^{12}C .

Bibliography

- [Ahlers 2016] M. Ahlers and P. Mertsch. *Origin of Small-Scale Anisotropies in Galactic Cosmic Rays*. ArXiv e-prints, December 2016. (Not cited.)
- [Amato 2011] E. Amato. *The streaming instability: a review*. Mem. Soc. Astron. Italiana, vol. 82, page 806, 2011. (Not cited.)
- [Baade 1934] W. Baade and F. Zwicky. *Remarks on Super-Novae and Cosmic Rays*. Physical Review, vol. 46, pages 76–77, July 1934. (Not cited.)
- [Bauhoff 1986] W. Bauhoff. *Tables of Reaction and Total Cross Sections for Proton-Nucleus Scattering below 1 GeV*. Atomic Data and Nuclear Data Tables, vol. 35, page 429, 1986. (Not cited.)
- [Bell 1978] A. R. Bell. *The acceleration of cosmic rays in shock fronts. I*. MNRAS, vol. 182, pages 147–156, January 1978. (Not cited.)
- [Bell 2004] A. R. Bell. *Turbulent amplification of magnetic field and diffusive shock acceleration of cosmic rays*. MNRAS, vol. 353, pages 550–558, September 2004. (Not cited.)
- [Blandford 1987] R. Blandford and D. Eichler. *Particle acceleration at astrophysical shocks: A theory of cosmic ray origin*. Phys. Rep., vol. 154, pages 1–75, October 1987. (Not cited.)

- [Bradt 1950] H. L. Bradt and B. Peters. *The Heavy Nuclei of the Primary Cosmic Radiation*. Physical Review, vol. 77, pages 54–70, January 1950. (Not cited.)
- [Breitschwerdt 2000] D. Breitschwerdt and S. Komossa. *Galactic Fountains and Galactic Winds*. Ap&SS, vol. 272, pages 3–13, 2000. (Not cited.)
- [Cox 2015] Arthur N Cox. *Allen’s astrophysical quantities*. Springer, 2015. (Not cited.)
- [Donato 2004] F. Donato, N. Fornengo, D. Maurin, P. Salati and R. Taillet. *Antiprotons in cosmic rays from neutralino annihilation*. Phys. Rev. D, vol. 69, no. 6, page 063501, March 2004. (Not cited.)
- [Ekers 1977] R. D. Ekers and R. Sancisi. *The radio continuum halo in NGC 4631*. A&A, vol. 54, page 973, February 1977. (Not cited.)
- [Fermi 1949] E. Fermi. *On the Origin of the Cosmic Radiation*. Physical Review, vol. 75, pages 1169–1174, April 1949. (Not cited.)
- [Fermi 1954] E. Fermi. *Galactic Magnetic Fields and the Origin of Cosmic Radiation*. ApJ, vol. 119, page 1, January 1954. (Not cited.)
- [Ferrando 1988] P. Ferrando, W. R. Webber, P. Goret, J. C. Kish, D. A. Schrier, A. Soutoul and O. Testard. *Measurement of ^{12}C , ^{16}O , and ^{56}Fe charge changing cross sections in helium at high energy, comparison with cross sections in hydrogen, and application to cosmic-ray propagation*. Phys. Rev. C, vol. 37, pages 1490–1501, April 1988. (Not cited.)
- [Ferrière 2001] K. M. Ferrière. *The interstellar environment of our galaxy*. Reviews of Modern Physics, vol. 73, pages 1031–1066, October 2001. (Not cited.)
- [FLU] *Fluka website*. <http://www.fluka.org/fluka.php>. Accessed: 2017-01-30. (Not cited.)
- [Gaensler 2008] B. M. Gaensler, G. J. Madsen, S. Chatterjee and S. A. Mao. *The Vertical Structure of Warm Ionised Gas in the Milky Way*. PASA, vol. 25, pages 184–200, November 2008. (Not cited.)
- [Gaggero 2014] D. Gaggero, L. Maccione, D. Grasso, G. Di Bernardo and C. Evoli. *PAMELA and AMS-02 e^+ and e^- spectra are reproduced by three-dimensional cosmic-ray modeling*. Phys. Rev. D, vol. 89, no. 8, page 083007, April 2014. (Not cited.)
- [Garzón 2017] J. A. Garzón, J. Collazo, J. Cuenca-García, D. G. a Castro, J. Otero, M. Yermo, J. J. Blanco, T. Kurtukian, A. Morozova, M. A. Pais, A. Blanco, P. Fonte, L. Lopes, G. Kornakov, H. Álvarez-Pol, P. Cabanelas, A. Pazos, M. Seco, I. Riádigos, V. Pérez Muñuzuri, A. Gómez-Tato, J. C. Mouriño, P. Rey and J. Taboada. *TRAGALDABAS. First results on cosmic ray studies*

- and their relation with the solar activity, the Earth magnetic field and the atmospheric properties.* ArXiv e-prints, January 2017. (Not cited.)
- [GEA] *Geant 4 website.* <http://geant4.cern.ch/>. Accessed: 2017-01-30. (Not cited.)
- [Gleeson 1967] L. J. Gleeson and W. I. Axford. *Cosmic Rays in the Interplanetary Medium.* ApJ, vol. 149, page L115, September 1967. (Not cited.)
- [Gleeson 1968] L. J. Gleeson and W. I. Axford. *Solar Modulation of Galactic Cosmic Rays.* ApJ, vol. 154, page 1011, December 1968. (Not cited.)
- [Greisen 1966] K. Greisen. *End to the Cosmic-Ray Spectrum?* Physical Review Letters, vol. 16, pages 748–750, April 1966. (Not cited.)
- [Habe 1980] A. Habe and S. Ikeuchi. *Dynamical Behavior of Gaseous Halo in a Disk Galaxy.* Progress of Theoretical Physics, vol. 64, pages 1995–2008, December 1980. (Not cited.)
- [Hillas 2005] A. M. Hillas. *TOPICAL REVIEW: Can diffusive shock acceleration in supernova remnants account for high-energy galactic cosmic rays?* Journal of Physics G Nuclear Physics, vol. 31, pages R95–R131, May 2005. (Not cited.)
- [Iroshnikov 1964] P. S. Iroshnikov. *Turbulence of a Conducting Fluid in a Strong Magnetic Field.* Soviet Ast., vol. 7, page 566, February 1964. (Not cited.)
- [Israel 2005] M. H. Israel, W. R. Binns, A. C. Cummings, R. A. Leske, R. A. Mewaldt, E. C. Stone, T. T. von Rosenvinge and M. E. Wiedenbeck. *Isotopic Composition of Cosmic Rays: Results from the Cosmic Ray Isotope Spectrometer on the ACE Spacecraft.* Nuclear Physics A, vol. 758, pages 201–208, July 2005. (Not cited.)
- [Johnson 1971] H. E. Johnson and W. I. Axford. *Galactic Winds.* ApJ, vol. 165, page 381, May 1971. (Not cited.)
- [Kappl 2016] R. Kappl. *SOLARPROP: Charge-sign dependent solar modulation for everyone.* Computer Physics Communications, vol. 207, pages 386–399, October 2016. (Not cited.)
- [Kolmogorov 1941] A. Kolmogorov. *The Local Structure of Turbulence in Incompressible Viscous Fluid for Very Large Reynolds' Numbers.* Akademiia Nauk SSSR Doklady, vol. 30, pages 301–305, 1941. (Not cited.)
- [Kraichnan 1965] R. H. Kraichnan. *Inertial-Range Spectrum of Hydromagnetic Turbulence.* Physics of Fluids, vol. 8, pages 1385–1387, July 1965. (Not cited.)
- [Letaw 1983] J. R. Letaw, R. Silberberg and C. H. Tsao. *Proton-nucleus total inelastic cross sections - an empirical formula for E greater than 10 MeV.* ApJS, vol. 51, pages 271–275, March 1983. (Not cited.)

- [Longair 2011] Malcolm S Longair. *High energy astrophysics*. Cambridge University Press, 2011. (Not cited.)
- [Mannheim 1994] K. Mannheim and R. Schlickeiser. *Interactions of cosmic ray nuclei*. *A&A*, vol. 286, pages 983–996, June 1994. (Not cited.)
- [Maurin 2001] David Maurin. *Propagation des rayons cosmiques dans un modèle de diffusion: une nouvelle estimation des paramètres de diffusion et du flux d'antiprotons secondaires*. PhD thesis, Université de Savoie, 2001. (Not cited.)
- [Mertsch 2010] Philipp Mertsch. *Cosmic Ray Backgrounds for Dark Matter Indirect Detection*. PhD thesis, University of Oxford, 2010. (Not cited.)
- [Morlino 2016] G. Morlino. *High Energy Cosmic Rays From Supernovae*. ArXiv e-prints, November 2016. (Not cited.)
- [Nordgren 1992] T. E. Nordgren, J. M. Cordes and Y. Terzian. *The scale height of the galactic free electron cloud*. *AJ*, vol. 104, pages 1465–1471, October 1992. (Not cited.)
- [Nugaev 2015] E. Y. Nugaev, G. I. Rubtsov and Y. V. Zhezher. *Probing Milky Way's hot gas halo density distribution using the dispersion measure of pulsars*. ArXiv e-prints, September 2015. (Not cited.)
- [Parker 1965] E. N. Parker. *Dynamical Theory of the Solar Wind*. *Space Sci. Rev.*, vol. 4, pages 666–708, September 1965. (Not cited.)
- [Peters 2015] Thomas Peters, Philipp Girichidis, Andrea Gatto, Thorsten Naab, Stefanie Walch, Richard W \tilde{A} $\frac{1}{4}$ nisch, Simon C. O. Glover, Paul C. Clark, Ralf S. Klessen and Christian Baczynski. *Impact of supernova and cosmic-ray driving on the surface brightness of the galactic halo in soft X-rays*. *Astrophys. J.*, vol. 813, no. 2, page L27, 2015. (Not cited.)
- [Potgieter 2013] M. S. Potgieter. *Solar Modulation of Cosmic Rays*. *Living Reviews in Solar Physics*, vol. 10, page 3, December 2013. (Not cited.)
- [Putze 2010] A. Putze, L. Derome and D. Maurin. *A Markov Chain Monte Carlo technique to sample transport and source parameters of Galactic cosmic rays. II. Results for the diffusion model combining B/C and radioactive nuclei*. *A&A*, vol. 516, page A66, June 2010. (Not cited.)
- [Recchia 2017] S. Recchia, P. Blasi and G. Morlino. *Cosmic ray driven winds in the Galactic environment and the cosmic ray spectrum*. ArXiv e-prints, March 2017. (Not cited.)
- [Roberts 1991] D. A. Roberts and M. Goldstein. *Turbulence and waves in the solar wind*. *Reviews of Geophysics*, vol. 29, pages 932–943, 1991. (Not cited.)

- [Salem 2015] M. Salem, G. Besla, G. Bryan, M. Putman, R. P. van der Marel and S. Tonnesen. *Ram Pressure Stripping of the Large Magellanic Cloud's Disk as a Probe of the Milky Way's Circumgalactic Medium*. ApJ, vol. 815, page 77, December 2015. (Not cited.)
- [Schlickeiser 2013] Reinhard Schlickeiser. *Cosmic ray astrophysics*. Springer Science & Business Media, 2013. (Not cited.)
- [Sedov 1946] Leonid I Sedov. *Propagation of strong shock waves*. Journal of Applied Mathematics and Mechanics, vol. 10, pages 241–250, 1946. (Not cited.)
- [Seo 1994] E. S. Seo and V. S. Ptuskin. *Stochastic reacceleration of cosmic rays in the interstellar medium*. ApJ, vol. 431, pages 705–714, August 1994. (Not cited.)
- [Serpico 2015] P. Serpico. *Possible physics scenarios behind cosmic-ray anomalies*. In A. S. Borisov, V. G. Denisova, Z. M. Guseva, E. A. Kanevskaya, M. G. Kogan, A. E. Morozov, V. S. Puchkov, S. E. Pyatovsky, G. P. Shoziyoev, M. D. Smirnova, A. V. Vargasov, V. I. Galkin, S. I. Nazarov and R. A. Mukhamedshin, editors, 34th International Cosmic Ray Conference (ICRC2015), volume 34 of *International Cosmic Ray Conference*, page 9, July 2015. (Not cited.)
- [Shalchi 2005] A. Shalchi and R. Schlickeiser. *Evidence for the Nonlinear Transport of Galactic Cosmic Rays*. ApJ, vol. 626, pages L97–L99, June 2005. (Not cited.)
- [Shklovskii 1953] IS Shklovskii. *On the nature of the luminescence of the Crab Nebula*. In Doklady Akad. Nauk SSSR, volume 90, pages 1900–1975, 1953. (Not cited.)
- [Silberberg 1973a] R. Silberberg and C. H. Tsao. *Partial Cross-Sections in High-Energy Nuclear Reactions, and Astrophysical Applications. I. Targets With $z \geq 28$* . ApJS, vol. 25, pages 315–333, April 1973. (Not cited.)
- [Silberberg 1973b] R. Silberberg and C. H. Tsao. *Partial Cross-Sections in High-Energy Nuclear Reactions, and Astrophysical Applications. II. Targets Heavier than Nickel*. ApJS, vol. 25, pages 335–367, April 1973. (Not cited.)
- [Silberberg 1998] R. Silberberg, C. H. Tsao and A. F. Barghouty. *Updated Partial Cross Sections of Proton-Nucleus Reactions*. ApJ, vol. 501, pages 911–919, July 1998. (Not cited.)
- [Skilling 1975a] J. Skilling. *Cosmic ray streaming. I - Effect of Alfvén waves on particles*. MNRAS, vol. 172, pages 557–566, September 1975. (Not cited.)
- [Skilling 1975b] J. Skilling. *Cosmic ray streaming. II - Effect of particles on Alfvén waves*. MNRAS, vol. 173, pages 245–254, November 1975. (Not cited.)

- [Strong 1998] A. W. Strong and I. V. Moskalenko. *Propagation of Cosmic-Ray Nucleons in the Galaxy*. ApJ, vol. 509, pages 212–228, December 1998. (Not cited.)
- [Taylor 1955] J Lockwood Taylor. XXXVII. *An exact solution of the spherical blast wave problem*. The London, Edinburgh, and Dublin Philosophical Magazine and Journal of Science, vol. 46, no. 374, pages 317–320, 1955. (Not cited.)
- [Thornbury 2014] A. Thornbury and L. O. Drury. *Power requirements for cosmic ray propagation models involving re-acceleration and a comment on second-order Fermi acceleration theory*. MNRAS, vol. 442, pages 3010–3012, August 2014. (Not cited.)
- [Tripathi 1999] R. K. Tripathi, F. A. Cucinotta and J. W. Wilson. *Universal Parameterization of Absorption Cross Sections*. NASA STI/Recon Technical Report N, December 1999. (Not cited.)
- [Tsao 1995] C. H. Tsao, R. Silberberg, A. F. Barghouty and L. Sihver. *Energy Degradation in Cosmic-Ray Nuclear Spallation Reactions: Relaxing the Straight-ahead Approximation*. ApJ, vol. 451, page 275, September 1995. (Not cited.)
- [Verma 1999] M. K. Verma. *Mean magnetic field renormalization and Kolmogorov's energy spectrum in magnetohydrodynamic turbulence*. Physics of Plasmas, vol. 6, pages 1455–1460, May 1999. (Not cited.)
- [Völk 2014] H. J. Völk. *Cosmic-ray driven winds*. ArXiv e-prints, November 2014. (Not cited.)
- [Webber 1990] W. R. Webber, J. C. Kish and D. A. Schrier. *Formula for calculating partial cross sections for nuclear reactions of nuclei with $E > \sim 200$ MeV/nucleon in hydrogen targets*. Phys. Rev. C, vol. 41, pages 566–571, February 1990. (Not cited.)
- [Webber 1998a] W. R. Webber, J. C. Kish, J. M. Rockstroh, Y. Cassagnou, R. Legrain, A. Soutoul, O. Testard and C. Tull. *Production Cross Sections of Fragments from Beams of 400-650 MeV per Nucleon ^9Be , ^{11}B , ^{12}C , ^{14}N , ^{15}N , ^{16}O , ^{20}Ne , ^{22}Ne , ^{56}Fe , and ^{58}Ni Nuclei Interacting in a Liquid Hydrogen Target. II. Isotopic Cross Sections of Fragments*. ApJ, vol. 508, pages 949–958, December 1998. (Not cited.)
- [Webber 1998b] W. R. Webber, J. C. Kish, J. M. Rockstroh, Y. Cassagnou, R. Legrain, A. Soutoul, O. Testard and C. Tull. *Production Cross Sections of Fragments from Beams of 400-650 MeV per Nucleon ^9Be , ^{11}B , ^{12}C , ^{14}N , ^{15}N , ^{16}O , ^{20}Ne , ^{22}Ne , ^{56}Fe , and ^{58}Ni Nuclei Interacting in a Liquid Hydrogen Target. I. Charge Changing and Total Cross Sections*. ApJ, vol. 508, pages 940–948, December 1998. (Not cited.)

- [Webber 1998c] W. R. Webber, A. Soutoul, J. C. Kish, J. M. Rockstroh, Y. Cas-sagnou, R. Legrain and O. Testard. *Measurement of charge changing and isotopic cross sections at ~ 600 MeV/nucleon from the interactions of ~ 30 separate beams of relativistic nuclei from ^{10}B to ^{55}Mn in a liquid hydrogen target.* Phys. Rev. C, vol. 58, pages 3539–3552, December 1998. (Not cited.)
- [Webber 2003] W. R. Webber, A. Soutoul, J. C. Kish and J. M. Rockstroh. *Updated Formula for Calculating Partial Cross Sections for Nuclear Reactions of Nuclei with $Z \leq 28$ and $E > 150$ MeV Nucleon $^{-1}$ in Hydrogen Targets.* ApJS, vol. 144, pages 153–167, January 2003. (Not cited.)
- [Wellisch 1996] H. P. Wellisch and D. Axen. *Total reaction cross section calculations in proton-nucleus scattering.* Phys. Rev. C, vol. 54, pages 1329–1332, September 1996. (Not cited.)
- [Woltjer 1972] L. Woltjer. *Supernova Remnants.* ARA&A, vol. 10, page 129, 1972. (Not cited.)
- [XSC] *XSCRC2017 XSCRC2017: Cross sections for Cosmic Rays CERN.* <https://indico.cern.ch/event/563277/timetable/>. Accessed: 2010-09-30. (Not cited.)
- [Yusifov 2004] I. Yusifov and I. Küçük. *Revisiting the radial distribution of pulsars in the Galaxy.* A&A, vol. 422, pages 545–553, August 2004. (Not cited.)
- [Zatsepin 1966] G. T. Zatsepin and V. A. Kuz'min. *Upper Limit of the Spectrum of Cosmic Rays.* Soviet Journal of Experimental and Theoretical Physics Letters, vol. 4, page 78, August 1966. (Not cited.)
- [Zirakashvili 1996] V. N. Zirakashvili, D. Breitschwerdt, V. S. Ptuskin and H. J. Voelk. *Magnetohydrodynamic wind driven by cosmic rays in a rotating galaxy.* A&A, vol. 311, pages 113–126, July 1996. (Not cited.)

Refinements on primary species

Contents

2.1	On cosmic ray source discreteness in spacetime	52
2.2	Description of the problem	55
2.3	Technical aspects	59
2.3.1	Generalized central limit theorem: mathematical statement	59
2.3.2	Application of the theorem to the probability of measuring a Galactic CR flux	60
2.3.3	The case with an upper cut on the flux	64
2.3.4	Causality effect	65
2.3.5	Absence of very close and/or young sources	68
2.4	Comparison with numerical simulations	70
2.4.1	Simulation settings	72
2.4.2	Simulation results	73
2.5	Applications	76
2.6	Conclusions of the section	81
	Bibliography	84

Strictly speaking, *primary* cosmic rays refer to species present in the interstellar matter which are accelerated when supernova shocks sweep them. This definition is in fact loosened, since the name extends to species that are *mostly* primaries, in that no CR species is exempt of some secondary fraction coming from fragmentation of heavier species via interactions with the ISM. Neglecting this fraction, i.e. considering large enough energies, the understanding of primary CR fluxes closely relies on the one of their sources. In the standard framework of CR phenomenology, sources are assumed to be homogeneously distributed in space-time. In the following chapter we challenge this hypothesis and tackle the effects of the discreteness of the sources on the primary CR spectra. Although well realised by previous works, this problem never found a satisfactory statistical answer. After proposing a solution to this problem, we highlight that recent precision measurements of cosmic rays spectra can be sensitive to tiny fluctuations coming from the discreteness of the sources. This section is mainly based on [Genolini 2017], a paper written with Pierre Salati, Pasquale Serpico and Richard Taillet.

2.1 On cosmic ray source discreteness in spacetime

As mentioned in section 1.1.2.2, a striking property of the (Galactic) cosmic ray spectra is their power-law behavior over many decades in energy. We have shown in section 1.2.2 that the diffusion process is scale invariant through the power law dependance of the diffusion coefficient. Not surprisingly, then, the customary calculation of the cosmic ray flux at the Earth postulates a universal power-law source term, further assuming the limit of a continuous distribution of sources, both spatially and temporally, in a volume modelling the Galaxy: often, a simple cylinder or an effectively infinite slab. However, we believe the sources of CRs to be discrete, and having a glance at the typical scales of acceleration of cosmic rays by SNRs (10 kyr, 0.1 pc) compared with the propagation scales (10 Myr, 1 kpc) at 1 TeV justifies to consider SNRs as point-like sources in space-time. Thus the source term of a single SNR i at a position \mathbf{x}_i and of age t_i should write:

$$q_s(\mathbf{x}, t) = q_i \delta(\mathbf{x} - \mathbf{x}_i, t - t_i), \quad (2.1)$$

where q_i is the normalisation term which is assumed to be described by a power law in rigidity as shown in the left panel of figure 2.1. Considering the flux yielded by this source some time later at a given position in space-time, the right pannel of the same figure shows that it completely loses its power law shape, as a result from the sole diffusion process.

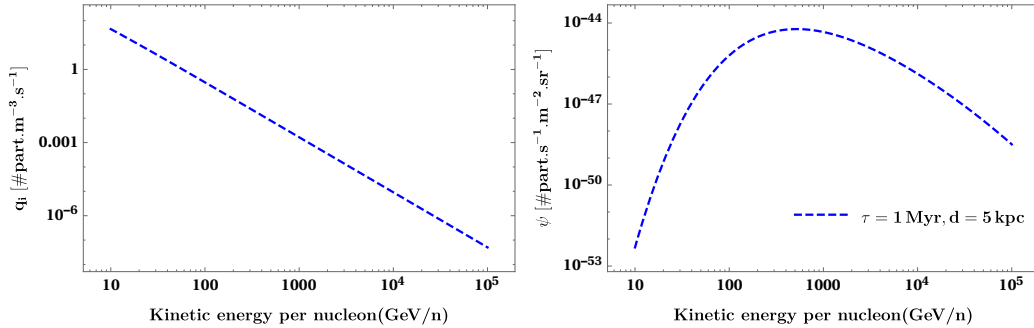


Figure 2.1: *Left:* power law injection spectrum. *Right:* propagated spectrum observed at a distance of 5 kpc and 1 Myr after its point-like injection in space-time.

Yet, with a large enough number of randomly distributed sources in a finite volume, one can show that the total flux retrieves a power-law shape. The figure 2.2 extracted from [Taillet 2004] shows in the Galactic case how the different generations of sources contribute to the actual shape of the flux, the oldest contributing mostly to the lowest part whereas the youngest dominate the higher flux.

The approximation of a homogeneous distribution of sources is thus motivated by the shape of the data, which implies that the distribution of sources is sufficiently dense in space and in time to be described as a continuum, much like in thermodynamics when the details of microscopic states corresponding to a given macroscopic

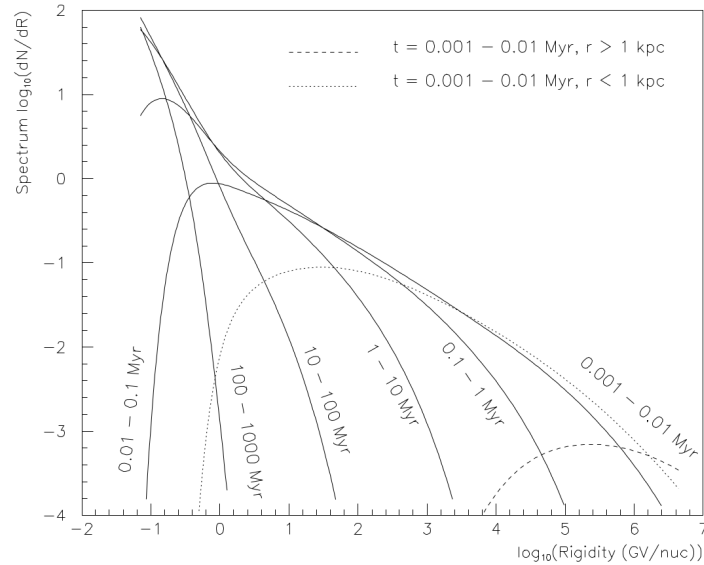


Figure 2.2: Contribution to the flux of sources with different ages. Plot extracted from [Taillet 2004]

state are ignored. This approximation is well-suited for describing the average expectations for the flux at Earth associated to a given hypothesis on propagation parameters, source spectra, and energetics. However, It is known that the discrete nature of cosmic ray sources should affect other observables, for instance, the time variation of the flux measured, as previously shown by simulations (see figure 2.3), which is nonetheless less important for all but a few phenomenological consequences.

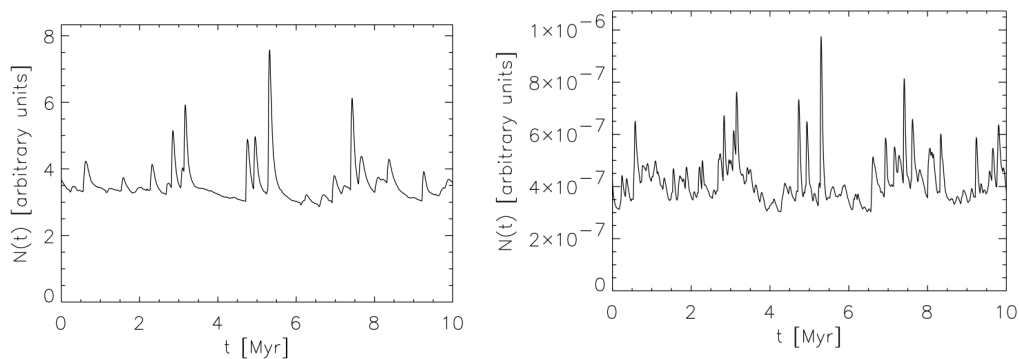


Figure 2.3: Time variation of the carbon flux. *Left:* at the energy of 10 GeV. *Right:* at the energy of 5 TeV. Plot extracted from [Büsching 2005]

Actually, several recent experiments have established that the cosmic ray spectrum, even within the three decades of energy probed by a single experiment such as AMS-02, cannot be satisfactorily described by a single power-law (for a recent review see Sec. 2 in [Serpico 2015]). This is observed for protons, helium nuclei, and

some heavier species. Several articles have attempted to explain this phenomenology as the result of the discrete nature of cosmic ray sources in space and time (as reviewed in Sec. 3.3 of [Serpico 2015] and also in [Bernard 2012]). While specific scenarios fitting the data can be found, the likelihood of these solutions, given our statistical knowledge of the source distribution and rate, is unknown. This is related to the conceptual difficulty that the probability distribution function p of a single source contributing a flux ψ at Earth is not a Gaussian function, but rather a heavy-tail/power law distribution (see [Bernard 2012], and arguments leading to Eqs. 21 and 24 in Sec. 3.2) which, if extrapolated to very large fluxes, does not even have a finite variance; the central limit theorem for the sum flux probability distribution $P(\Psi)$ cannot be applied. Ironically, the same mathematical property that makes a phenomenological description of the cosmic ray observables so simple (“power laws”) raises difficulties in theoretical probabilistic assessments starting from $p(\psi)$. While this problem has been overtly recognized [Lee 1979, Lagutin 1995], the quantitative consequences of this fact for cosmic ray physics are still a matter of debate. Far from being academic, the problem also has important implications for the theoretical limitations in the extraction of propagation parameters, as well as comparing theoretical models up to current experimental precision. Ultimately, barring an unrealistic, fully deterministic model of the sources of cosmic rays, theoretical predictions in this field are intrinsically statistical in nature. In fact, theoretical calculations concerning ultra-high energy cosmic ray observables have already routinely used ensemble techniques for estimating the flux and mass composition uncertainties (see e.g., Ahlers 2013). Important differences arise, however, due to the quasi-ballistic propagation and the non-negligible loss-effects ruling the extragalactic propagation regime.

Here, we aim at establishing a systematic theory to evaluate these effects for Galactic cosmic rays. Our main focus is on analytical treatment, but all major conclusions are validated by extensive numerical simulations. By itself, the numerical part of our work represents a major novel contribution to the understanding of the consequence of the discrete nature of sources for cosmic ray phenomenology. Also, novel when compared to previous publications in this domain, we analyze the effects of physical limitations on idealized mathematical extrapolations, such as the eventual failure of diffusion equations to cope with constraints such as causality or a priori knowledge about the discrete source distribution. Whenever a comparison with observations is performed, we refer to the proton flux, which is the best measured one due to high statistics, and for which the effects discussed here should be most prominent. Still, the same formalism can apply to any nuclear species, and could also be extended to leptons (at least qualitatively; for a pioneering earlier investigation of the lepton channel, see [Mertsch 2011]).

As an application, we then focus on the compatibility of several experimental results on interstellar protons (such as AMS-02, PAMELA, CREAM) with our current understanding of cosmic ray propagation, properly taking the theoretical uncertainty into account.

This chapter is organized as follows. In Sec. 2.2, we describe the problem and

introduce the main difficulties that make its solution challenging, as well as our strategy to approach them. Section 2.3 deals with the technical aspects of the analytical treatment proposed, including a discussion of the limitations of an overly naive approach. The reader uninterested by these subtleties and mostly interested in the validation of our description and the phenomenological implications of our work can quickly gloss over this part and focus on the following sections. In Section 2.4, we compare our theory with extensive simulations: this allows us to validate the theory, better defining its regimes of validity, also clarifying when one should be able to draw conclusions relying solely on analytical arguments without the need for long computing time. A few applications to cases of phenomenological interest are reported in Section 2.5. Finally, in Section 4.4.3, we conclude.

2.2 Description of the problem

Galactic cosmic rays are accelerated at discrete sources, the position and age of which is not known individually, only statistically. From the statistical distribution of these sources, we can infer the statistical distribution of the cosmic ray flux in the solar neighborhood. In this section, we describe the issues raised by this program. The cosmic ray (CR) flux Ψ obeys a diffusion equation which, in its simplest incarnation boils down to the form (energy dependence implicit):

$$\left[\frac{\partial}{\partial t} - K \nabla^2 \right] \Psi = \mathcal{Q}, \quad (2.2)$$

where K is the spatial diffusion coefficient supposed to be uniform in the diffusion volume and \mathcal{Q} is the source term. Additional terms accounting for convection, reacceleration, and energy losses are of little relevance for the species and the energy ranges of interest in the following and can be anyway dealt with at very least with standard techniques like the ones implemented in numerical codes such as GALPROP or DRAGON or semi-numerical ones such as USINE. The solution to this equation can be formally written as an integral over the Galactic volume and over the past Galactic history as:

$$\Psi(\mathbf{x}, t) = \int_{-t_{\text{MW}}}^t dt_S \int_{V_{\text{MW}}} d\mathbf{x}_S \mathcal{Q}(\mathbf{x}_S, t_S) \mathcal{G}_B(\mathbf{x}_S, t_S \rightarrow \mathbf{x}, t), \quad (2.3)$$

where V_{MW} is the volume of the Galaxy, given by $V_{\text{MW}} \simeq 2 h \pi R^2$ if the Galaxy is modeled as a cylinder of radius R and half-thickness h , of age t_{MW} , and \mathcal{G}_B is the Green function obtained by solving the analog of equation (2.2) with a temporal and spatial delta at the RHS, and the appropriate boundary conditions. As a reminder, the Green function of the pure diffusive problem (without boundary) with delta centered at spatial position \mathbf{x}_S and time t_S would simply write

$$\mathcal{G}(d = |\mathbf{x} - \mathbf{x}_S|, \tau = t - t_S) = \frac{1}{(4 \pi K \tau)^{3/2}} \exp\left(-\frac{d^2}{4 K \tau}\right). \quad (2.4)$$

There are a few issues related to the computation of the CR flux, which we now briefly describe.

First, the source term \mathcal{Q} is expected to be a sum of discrete injection points in space-time (the spatial and time scale of likely accelerators being assumed much shorter than propagation length and time), whose actual positions and epochs are unknown. This is the so-called myriad model approach [Higdon 2003] where cosmic rays are sourced by a constellation of point-like objects and not by a continuous jelly. It would then be formally correct to write

$$\mathcal{Q}(\mathbf{x}_S, t_S) = \sum_i^N q_i \delta(\mathbf{x}_i - \mathbf{x}_S) \delta(t_i - t_S), \quad (2.5)$$

leading to

$$\Psi(\mathbf{x}, t) = \sum_i^N \psi_i = \sum_i^N q_i \mathcal{G}_B(\mathbf{x}_i, t_i \rightarrow \mathbf{x}, t). \quad (2.6)$$

Commonly equation (2.2), sourced by a discrete sum, is replaced with a continuous proxy corresponding to its ensemble average. Specifically, the source term writes (for simplicity we assume a unique source term, i.e., $q_i = q$):

$$\begin{aligned} \langle \mathcal{Q}(\mathbf{x}_S, t_S) \rangle &= \left\langle \sum_i^N q_i \delta(\mathbf{x}_i - \mathbf{x}_S) \delta(t_i - t_S) \right\rangle \\ &\simeq \frac{q\nu}{V_{\text{MW}}} \times \begin{cases} \Theta(h - |z|) \Theta(R - r) & \text{in 3D, or} \\ 2h \delta(z) \Theta(R - r) & \text{in 2D,} \end{cases} \end{aligned} \quad (2.7)$$

where q is the single source spectrum (particles per unit energy) and ν the source rate per unit time. For example, assuming supernova remnants to be the sources of CRs, a rate of three explosions per century is reasonable. In the second equality, we assume a homogeneous distribution of sources lying within a cylindrical approximation of the Galaxy with radius R . Along the vertical direction, the sources are either uniformly distributed inside a disk with half-thickness h (3D case), or pinched inside an infinitesimally thick disk (2D case). The generalization to a different distribution is straightforward.

This source term leads to the theoretical average flux:

$$\langle \Psi(\mathbf{x}, t) \rangle = \int_{-t_{\text{MW}}}^t dt_S \int_{V_{\text{MW}}} d\mathbf{x}_S \langle \mathcal{Q}(\mathbf{x}_S, t_S) \rangle \mathcal{G}_B(\mathbf{x}_S, t_S \rightarrow \mathbf{x}, t). \quad (2.8)$$

This is only true on average. We expect the flux observed at the Earth to be ruled by a probability distribution function (pdf) $P(\Psi)$. This function also depends on the actual value of N of the underlying discrete sources. The average flux becomes

$$\langle \Psi \rangle = \int_0^\infty d\Psi \Psi P(\Psi). \quad (2.9)$$

Obtaining the probability $P(\Psi)$, entering, for example, in equation (2.9), requires a “change of variables”, from space-time location to flux space. To this end, we exploit the fact that there is a straightforward relation between $\{t_S, \mathbf{x}_S\}$ and the flux obtained by a single source, ψ_S , located at $\{t_S, \mathbf{x}_S\}$. For example, equation (2.9) can be rewritten in terms of the pdf for the flux from a single source, $p(\psi)$, as

$$\langle \Psi \rangle = \int_0^\infty d\Psi \Psi P(\Psi) = N \langle \psi \rangle = N \int_0^\infty d\psi \psi p(\psi). \quad (2.10)$$

Obtaining $p(\psi)$ (or rather its cumulative distribution) is the main subject of Sec. 2.3.2. Let us briefly note that the link is formally written as

$$p(\psi, \mathbf{x}, t) = \frac{\nu}{N V_{\text{MW}}} \int_{-t_{\text{MW}}}^t dt_S \int_{V_{\text{MW}}} d\mathbf{x}_S \delta(\psi - q \mathcal{G}_B(\mathbf{x}_S, t_S \rightarrow \mathbf{x}, t)). \quad (2.11)$$

Once $p(\psi)$ is known, the pdf for the sum flux $P(\Psi)$ can be computed thanks to the convolution of the individual probabilities $p(\psi_i)$ under the constraint $\sum_i^N \psi_i = \Psi$. The probability $P(\Psi)$ is formally written as

$$P(\Psi) = \int_{\psi_1} \int_{\psi_2} \dots \int_{\psi_N} p(\psi_1) p(\psi_2) \dots \quad (2.12)$$

$$\dots p(\psi_N) \delta \left(\sum_i^N \psi_i - \Psi \right) d\psi_1 d\psi_2 \dots d\psi_N. \quad (2.13)$$

This relation is based on the disputable yet natural assumption that the sources are not correlated with each other. The probability that two sources yield the fluxes ψ_1 and ψ_2 , respectively, is thus given by the product $p(\psi_1) p(\psi_2)$.

A second problem imposes itself as follows. If we try to use the generalization of equation (2.10) to compute, for example, the second moment of the flux, $\langle \Psi^2 \rangle$, and hence the expected variance of the flux, the expression formally diverges since the underlying $p(\psi)$ has a power-law tail, $p(\psi) \propto \psi^{-\alpha-1}$, with $1 < \alpha < 2$ (as derived e.g., in [Bernard 2012]). It turns out that despite the fact that (for instance) the variance of $p(\psi)$ is formally infinite, thanks to a so-called generalized central limit theorem, the resulting probability $P(\Psi)$, for large N , has a universal shape, a so-called stable law, only dependent on α and independent of N , but for a rescaling. More details on this are given in Sec. 2.3.1. Hence, this difficulty does not appear so severe, since meaningful statistical quantities (such as confidence levels or quantiles) can still be computed in this limit. A relatively minor complication is that the index α of the pdf $p(\psi)$ is in fact energy dependent and depends on the propagation model as well. We introduce two limiting behaviors of α in Sec. 2.3.2, which allow for a satisfactory description of the distribution over a wide range of fluxes.

The third issue is that some of the above-mentioned properties depend on the fact that the behavior $p(\psi) \propto \psi^{-\alpha-1}$ formally extends to infinity. Physically, however, there is no such thing as an infinite flux: an obvious cutoff is imposed, for instance, by the empirically established absence of a source that is too close and/or too recent; of course, this depends on the level of credibility attributed to independent

astrophysical information, such as available catalogs. In Sec. 2.3.3 and Sec. 2.3.5 we see the impact of this constraint on the maximum flux. A more subtle reason for having an effective cutoff to the domain of the probability distribution function $p(\psi)$ is the fact that equation (2.2) is non-relativistic, and does not automatically ensure that causality is fulfilled. Accounting exactly for this is outside of the scope of our study, but we show that this introduces an effective cutoff that is particularly relevant at high energies (see Sec.s 2.3.3 and 2.3.4). In either case, however, the conceptual problem that arises is that for a pdf $p(\psi)$, with a finite support, the asymptotic pdf for the sum of the fluxes variable Ψ is now a Gaussian due to the standard central limit theorem (moments are, in fact, finite). It turns out that stable laws still provide acceptable descriptions of the pdf $P(\Psi)$ up to the fluxes of phenomenological interest, and that for the values of N and Ψ of actual interest one is relatively far from the Gaussian limit and much closer to the stable law limit. This aspect is described in Sec. 2.3.3.

Before concluding this Section, a couple of comments are in order.

First, we shall limit ourselves to discussing the probabilities of departures of fluxes from their average only at a single energy. A natural generalization would be to discuss the probability that the flux at the Earth departs from its expected average value by more than a certain amount at two or more energies. Fluxes at different energies (especially near ones) are not expected to be independent, rather strongly correlated, which can be formally described, for instance, via the following inequality in the conditional probability

$$\begin{aligned} &P([\Psi(E_1) > \langle \Psi(E_1) \rangle] \cap [\Psi(E_2) > \langle \Psi(E_2) \rangle]) \\ &\neq P(\Psi(E_1) > \langle \Psi(E_1) \rangle) P(\Psi(E_2) > \langle \Psi(E_2) \rangle). \end{aligned} \quad (2.14)$$

A manifestation of this property if second moments are finite is

$$\langle \Psi(E_1)\Psi(E_2) \rangle \neq \langle \Psi(E_1) \rangle \langle \Psi(E_2) \rangle. \quad (2.15)$$

Estimating the probability of the most significant deviation among the different energy bins provides, however, an upper limit to the true probability of observing the actual flux excursion at different energy bins, the former being necessarily equal or lower due to the unitarity property of pdfs.

Second, while the effects discussed in this study are the result of replacing the true underlying discrete source distribution with a continuum space-time distribution that describes its smooth average, and are thus accounting for the partial (only “probabilistic”) knowledge we have on the sources frequency and position, this is different from what is usually intended by the “effects of the granularity” of the sources, in statistical mechanics, for example. These would typically manifest themselves in higher-order correlation functions (again, if finite, otherwise via conditional probabilities), like the correlations of fluxes measured at different times, or at the same time at different locations, etc. We emphasize that all source explosion models sharing the same time and volume average would give us the same flux $\langle \Psi \rangle$, while the above higher-order correlation observables could be different. In particular, in the

myriad model approach that we follow here, we assume point-like sources not to be correlated with each other. For example, a model where 20 SN explode at the same time in the Galaxy every 800 years does not satisfy this condition, and it will yield a different probability distribution function $P(\Psi)$ for the flux than a model where 1 SN explodes randomly in the Galaxy every 40 years. Both models have the same average flux but fluctuations around that mean do not follow the same law, and time correlations, for example, are different. On the other hand, our formalism can still provide a good approximation of strongly correlated source models: if the sources are strongly correlated in space and time (e.g., the 20 SN in the example above were to explode within a few pc distance of one another), simply downscaling ν and increasing q by a corresponding factor would provide a satisfactory approximation for all but very small scale correlations.

2.3 Technical aspects

2.3.1 Generalized central limit theorem: mathematical statement

The central limit theorem states that the sum Ψ of a large number N of independent, identical, and stochastic variables ψ is distributed according to a Gaussian law whose variance σ_Ψ^2 is N times larger than the variance σ_ψ^2 of each individual contribution ψ . In our case though, the pdf of ψ has a power-law tail $p(\psi) \propto \psi^{-\alpha-1}$ with $1 < \alpha < 2$. The average flux $\langle \psi \rangle$ from a single source is defined but its variance is not and the central limit theorem cannot be applied, at least in its mundane form.

A more general form of the theorem has been discussed in section 1.8 of [Nolan 2012], for example, and can be readily applied to our problem. We simply recall here the salient features of the version that can be adapted to the myriad model. Let ψ be a random variable with probability law $p(\psi)$ defined on \mathbf{R}_+ . The tail behavior can be captured by the cumulative distribution function (also called survival function) $C(\psi)$ such that

$$\forall \psi \geq 0, \quad C(\psi) \equiv \int_\psi^\infty p(\psi') \, d\psi'. \quad (2.16)$$

That function encodes the probability for the flux of a single source to be larger than ψ . As shown in what follows, its asymptotic behavior, which turns out to be an essential ingredient in the proof of the generalized theorem, has the simple power-law form

$$\lim_{\psi \rightarrow \infty} \psi^\alpha C(\psi) = \eta > 0. \quad (2.17)$$

We denote by $\Psi = \psi_1 + \dots + \psi_N$ the sum of N independent and identically p distributed random variables ψ_i . By introducing the rescaled flux

$$S_N = \frac{\Psi - \langle \Psi \rangle}{\sigma_N}, \quad \text{with} \quad \sigma_N = \left(\frac{\eta \pi N}{2\Gamma(\alpha) \sin(\alpha \pi/2)} \right)^{1/\alpha}, \quad (2.18)$$

the generalized central limit theorem states that the probability law P of S_N converges for large N toward the law $\mathbf{S}[\alpha, 1, 1, 0; 1]$ among the class of stable laws, in

the notation of [Nolan 2012]. Note that the spread parameter σ_N of the stable law depends on the constant η and increases as $N^{1/\alpha}$ instead of \sqrt{N} in the gaussian case. The general stable law function $\mathbf{S}[\alpha, \beta, \gamma, \delta; 1]$ also depends on additional arguments beyond the stability index α , notably a skewness parameter β , a scale parameter γ , and a location parameter δ . The last index sets the type of parameterization used, as several exist in the literature. For instance, the normal or Gaussian distribution centered around μ and with variance σ^2 is denoted in this notation as $\mathbf{N}(\mu, \sigma) = \mathbf{S}(2, 0, \sigma/\sqrt{2}, \mu; 1)$. We recall that a pdf that is invariant under the product of convolution is described as stable. This is the case for well-known examples such as the Gaussian, Cauchy, and Lévy distributions. But this class of functions is broad, as shown by Paul Lévy in his study of sums of independent identically distributed terms in the 1920s [Lévy 1925]. Most of the densities and distribution functions that it encompasses cannot be expressed analytically by closed-form expressions, although their Fourier transforms are tractable. That is why stable laws, such as the Pareto-Levy distribution $\mathbf{S}[\alpha, 1, 1, 0; 1]$, which we use hereafter, are not common in the field of astrophysics, but are relatively well known in finance for instance [Mandelbrot 1960, Uchaikin 1999]. Nowadays, computer programs such as Mathematica [Wolfram Research, Inc. 2016] can easily be used to compute these special functions. In the following we will show that the two relevant probability laws are $S[5/3, 1, 1, 0; 1]$ and $S[4/3, 1, 1, 0; 1]$. A brief comparison of their pdf and cumulative distributions with respect to the Gaussian is illustrated figure 2.4 for $\langle \Psi \rangle = 0$ and $\sigma_N = 1$. We notice the heavy tail behavior at large values of X of these peculiar stable laws.

2.3.2 Application of the theorem to the probability of measuring a Galactic CR flux

To compute the spread σ_N that comes into play in the stable law followed by the total flux Ψ_N , we need to determine the spectral index α so that $\lim_{\psi \rightarrow \infty} C(\psi) \psi^\alpha = \eta$. We recall that $C(\psi)$ is the survival probability to get a flux higher than ψ at the Earth. This probability can be obtained by integrating the density of a single source in space and time over the phase space region where it produces a flux larger than ψ .

As we are interested in the limit where the flux ψ is large, if not infinite, the source must be local and young. In that case, CR propagation is the same as if the magnetic halo was infinite and diffusion was dominating the other processes such as convection and spallation. The region in space and time that yields a flux ψ may be derived from the boundless propagator of equation (2.4), which we translate into:

$$\psi = \frac{a}{\tau_M^{3/2}} x^{-3/2} \exp\left(-\frac{d^2}{4K\tau_M x}\right), \quad \text{with} \quad a = \frac{q}{(4\pi K)^{3/2}}. \quad (2.19)$$

For simplicity, we have introduced the dimensionless time variable $x \equiv \tau/\tau_M$, where the timescale τ_M is defined as the maximal age for a source to provide a flux ψ . That

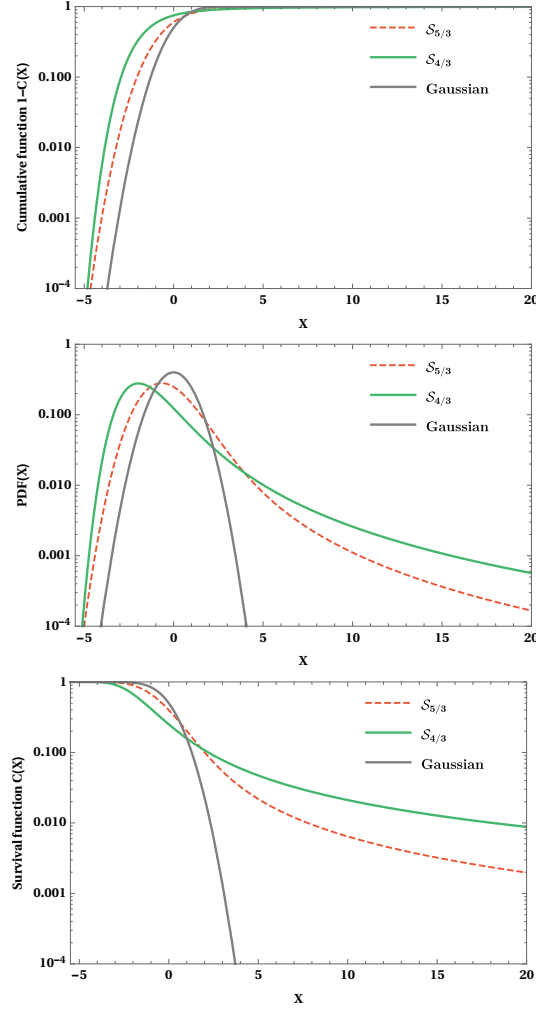


Figure 2.4: Qualitative comparison of the shape of the stables laws $S[5/3, 1, 1, 0; 1]$ and $S[4/3, 1, 1, 0; 1]$ with respect to the Gaussian. We use $\langle \Psi \rangle = 0$ and $\sigma_N = 1$.

value is reached when the source is located at $d = 0$ and is equal to $\tau_M = (a/\psi)^{2/3}$. It is straightforward to check that for a given value K of the diffusion coefficient, and hence at a given CR energy E , all space-time points in the plane (x, d^2) satisfying the condition

$$\frac{d^2}{6 K \tau_M} = -x \ln x \quad (2.20)$$

are characterized by the same flux $\psi \equiv \psi(r = 0, \tau = \tau_M)$. This corresponds to the thick blue line drawn in figure 2.5. Points below that curve yield a flux $\psi' > \psi(0, \tau_M)$, while points above it produce a flux $\psi' < \psi(0, \tau_M)$. One can thus compute the cumulative distribution $C(\psi)$ (sources with fluxes larger than ψ) by integrating the space and time density distribution of a single source $\rho(\mathbf{r}, t)$ (assumed constant in the following) over the region in phase space located below the blue line of figure 2.5. In the cylindrical approximation, N denoting the number of sources

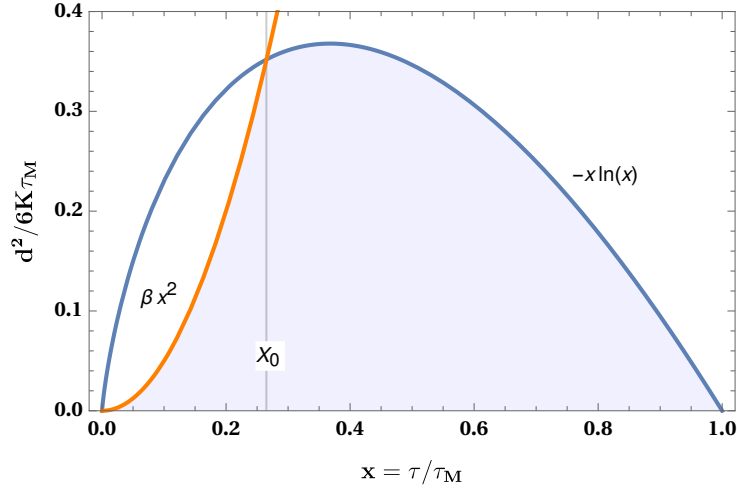


Figure 2.5: Below the thick line: space and time region where a source contributes a flux $\psi' > \psi = a/\tau_M^{3/2}$ in the diffusion approximation. Light blue shaded region: space and time domain that also respects the causal constraint.

contributing to the total flux Ψ allows us to write:

$$\rho(\mathbf{r}, t) = \frac{\nu}{2h\pi R^2} \frac{1}{N}. \quad (2.21)$$

There is no closed-form expression for $C(\psi)$ in general, but two relevant limiting situations can be discussed. Given ψ , if τ_M is such that the key length parameter $(6K\tau_M)^{1/2}$ is smaller than the typical thickness of the Galactic disk, h , the result will be equivalent to that of a uniform density in a 3D volume, hence

$$\begin{aligned} C_{3D}(\psi) &= \int_{\psi}^{\infty} p(\psi') d\psi' \\ &= \int_0^{\tau_M} dt \frac{4}{3} \pi d^3 \rho(\mathbf{r}, t) \Big|_{d^2 = -6K\tau_M x \ln(x)} \\ &= \underbrace{\frac{1}{\pi^{1/3}} \frac{3^{3/2}}{2^{1/3} 5^{5/2}} \frac{1}{N} \frac{R^{4/3} K^{2/3}}{h L^{5/3} \nu^{2/3}}}_{\eta_{3D}} \langle \Psi \rangle^{5/3} \psi^{-5/3} \propto \psi^{-5/3}. \end{aligned} \quad (2.22)$$

We highlight that the coefficient η depends on the space-time probability density to find a source lying in the neighborhood of the observer; as does the typical flux spread σ_N . We may nevertheless express it as a function of the average flux $\langle \Psi \rangle$ to demonstrate how the various CR parameters at stake come into play. For the sake of clarity, the value of $\langle \Psi \rangle$ has been derived here assuming that the Galactic disk is an infinitesimally thick slab. Taking the 2D model neglecting radial boundary conditions leads to the simple expression

$$\langle \Psi \rangle = \frac{hL}{K} Q = \frac{q\nu L}{2\pi R^2 K}, \quad (2.23)$$

whose numerical value is very close to the actual result, as shown in the Appendix. Qualitatively, we expect that the behavior outlined in equation (2.22) is always attained for sufficiently high fluxes, since those require very close sources, although when this regime is attained depends on the energy E via the diffusion coefficient K . Lower fluxes, however, are also yielded by sources located “far away” from us, with respect to the scale h . In the limit where these dominate, one can effectively model the Galaxy as an infinitesimally thick disk, so that the only quantity that matters is the 2D (surface) density $\mu(\mathbf{r}, t)$ which may be expressed as

$$\mu(\mathbf{r}, t) = \frac{\nu}{\pi R^2} \frac{1}{N}. \quad (2.24)$$

In this 2D limit, one gets:

$$\begin{aligned} C_{2D}(\psi) &= \int_0^{\tau_M} dt \pi d^2 \mu(\mathbf{r}, t) \Big|_{d^2 = -6K\tau_M x \ln(x)} \\ &= \underbrace{\frac{3}{2^{11/3} \pi^{2/3}} \frac{1}{N} \frac{K^{1/3} R^{2/3}}{\nu^{1/3} L^{4/3}} \langle \Psi \rangle^{4/3}}_{\eta_{2D}} \psi^{-4/3} \propto \psi^{-4/3}. \end{aligned} \quad (2.25)$$

We argue in the following that, depending on the regime of fluxes Ψ in which one is interested, either the 2D or the 3D distribution is relevant to the description of the problem. In any case, by virtue of the generalized version of the central limit theorem of Sec. 2.3.1, we know how to derive the pdf $P(\Psi)$ for both cases. It is sufficient to take an index $\alpha = 5/3$ (3D) or $\alpha = 4/3$ (2D) and to compute the spread σ_N from equation (2.18) via the corresponding coefficients η_{3D} and η_{2D} . The two probability laws at stake, namely $S[5/3, 1, 1, 0; 1]$ and $S[4/3, 1, 1, 0; 1]$ are displayed figure 2.4 for $\langle \Psi \rangle = 0$ and $\sigma_N = 1$. Notice that σ_N can be expressed as a function of the average flux $\langle \Psi \rangle$ and the various CR parameters. The number of sources N has cancelled out in the product ηN . When it is large enough, the asymptotic regime where the central limit theorem holds is reached and we expect

$$P(\Psi) \rightarrow \frac{1}{\sigma_N} S[\alpha, 1, 1, 0; 1] \left(\frac{\Psi - \langle \Psi \rangle}{\sigma_N} \right). \quad (2.26)$$

In order to comment upon the dependencies of the spread σ_N on the parameters of the problem, one may write

$$\frac{\sigma_N}{\langle \Psi \rangle} \propto \begin{cases} \frac{K^{2/5} R^{4/5}}{\nu^{2/5} h^{3/5} L} & \text{in the 3D case,} \\ \frac{K^{1/4} R^{1/2}}{\nu^{1/4} L} & \text{in the 2D case.} \end{cases} \quad (2.27)$$

As the reader may have noticed, the number N of sources has disappeared from the rescaled quantity $\sigma_N/\langle \Psi \rangle$. The latter encodes the statistical excursions of the total flux Ψ around its mean value $\langle \Psi \rangle$. Rescaled to the mean flux, the spread has the

same dependence on the height L of the diffusive halo ($\propto 1/L$) in both the 2D and 3D regimes. The thickness h of the Galactic disk only enters in the expression of η_{3D} . The relative spread $\sigma_N/\langle\Psi\rangle$ increases with CR energy through the diffusion coefficient K . It decreases as the rate ν of explosions is increased. Both K and ν enter through the ratio K/ν , with an exponent of 2/5 (3D) or 1/4 (2D).

2.3.3 The case with an upper cut on the flux

Strictly speaking, applying the generalized version of the central limit theorem requires that the cumulative distribution function $C(\psi)$ for a single source has a heavy-tail behavior up to an infinite flux ψ . This behavior should nevertheless break down since infinite fluxes, for example, are unphysical. However, one expects the stable law expression (2.26) for $P(\Psi)$ to still provide a good approximation of the actual distribution up to some value of the total flux Ψ , should the underlying power-law behavior of the single source pdf $p(\psi)$ be valid over a sufficiently large range. To quantify this, let us assume that the single source pdf follows the power-law behavior $p(\psi) \propto \psi^{-\alpha-1}$, with $1 < \alpha < 2$, up to some critical value ψ_{cut} above which it vanishes. There may be several reasons for this heuristic argument to hold, some to be explored in the following. Schematically, one can write the probability of measuring a flux ψ from a single source as:

$$p(\psi) = (1 + \varepsilon) p_{th}(\psi) \Theta(\psi_{cut} - \psi), \quad (2.28)$$

where $p_{th}(\psi)$ is the idealized pdf with an infinite power-law tail, discussed in section 2.3.1. Of course this may be too crude an approximation close to ψ_{cut} , but provided that ψ_{cut} is large compared to the fluxes of interest and the renormalization correction ε is small, it should not have a significant affect. In fact, given the Ansatz of equation (2.28), one can write the probability to measure a flux $\Psi = \sum_i^N \psi_i$ from N sources, among which N are located inside the light cone, as

$$P(\Psi) = \int_{\psi_1} \dots \int_{\psi_N} p(\psi_1) \dots p(\psi_N) \delta\left(\sum_i^N \psi_i - \Psi\right) d\psi_1 \dots d\psi_N, \quad (2.29)$$

$$\begin{aligned} &= (1 + \varepsilon)^N \int_{\psi_1} \dots \int_{\psi_N} p_{th}(\psi_1) \dots p_{th}(\psi_N) \Theta(\psi_{cut} - \psi_1) \dots \\ &\dots \Theta(\psi_{cut} - \psi_N) \delta\left(\sum_i^N \psi_i - \Psi\right) d\psi_1 \dots d\psi_N. \end{aligned} \quad (2.30)$$

For values of Ψ such as $\Psi < \psi_{cut}$ ¹, each individual value ψ_i must satisfy $\psi_i < \psi_{cut}$. Hence we get

¹This condition is denoted hereafter by a (\star)

$$P(\Psi) = (1 + \varepsilon)^N \int_{\psi_1} \dots \int_{\psi_N} p_{th}(\psi_1) \dots p_{th}(\psi_N) \delta \left(\sum_i^N \psi_i - \Psi \right) d\psi_1 \dots d\psi_N \text{ for } \Psi < \psi_{cut}. \quad (2.31)$$

Thus, for sufficiently large N , we expect

$$P(\Psi) \approx (1 + \varepsilon)^N \frac{1}{\sigma_N} S[\alpha, 1, 1, 0; 1] \left(\frac{\Psi - \langle \Psi \rangle_{th}}{\sigma_N} \right) \text{ for } \Psi < \psi_{cut} (\star), \quad (2.32)$$

where the average flux $\langle \Psi \rangle_{th}$ in the argument of the stable function corresponds to the uncut idealized pdf $p_{th}(\psi)$. The approximation of equation (2.32) is relatively general, but its actual usefulness depends on the precise values of ψ_{cut} and ε . For example, as long as $N\varepsilon \ll 1$, the result does not really depend on ε , with the subtlety that N is the number of causal sources. That condition turns out to be satisfied for the cases that are subsequently discussed. Furthermore note that in our case the correction is independent on the chosen value of N , as long as one can neglect the fraction of non-causal sources:

$$(1 + \varepsilon)^N = \left(\frac{1}{1 - \eta\psi_{cut}^{-\alpha}} \right)^N = \left(\frac{1}{1 - \frac{A}{N}\psi_{cut}^{-\alpha}} \right)^N \approx 1 + A\psi_{cut}^{-\alpha} \text{ for: } A\psi_{cut}^{-\alpha} \ll N, \quad (2.33)$$

A is a constant at a given energy (cf equation 2.25 and 2.22) and ψ_{cut} is considered in the high flux tail of the distribution. In the following subsections, we actually distinguish two evident physical reasons for imposing a cut on the tail of the pdf distribution.

2.3.4 Causality effect

To commence, propagation through diffusion should not violate causality, a condition which is not always satisfied by the propagator as defined in equation (2.4). Taking any finite age τ for a source leads to a non-zero value for \mathcal{G} , whatever the distance d . This will not cause any problems for far and young sources for which the flux is exponentially suppressed, but for young and close objects, which happen to dominate large positive fluctuations of Ψ with respect to the average value $\langle \Psi \rangle$, this can lead to much larger flux contributions than physically allowed.

A correction for this effect can be quantified with reference to the space-time diagram of figure 2.5 by removing the portion where causality is violated from the region of phase space that contributes to the flux. The domain to be withdrawn extends above the orange curve defined by the light cone condition $d^2 = c^2 x^2 \tau_M^2$, c being the speed of light in this case. The orange parabola allows us to carve away the domain in white that lies below the blue line, leaving only the light-blue

shaded region to contribute to fluxes larger than ψ . The intersection between the blue (diffusion) and orange (light cone) curves takes place at $x = x_0$ for which

$$-\beta x_0 = \ln(x_0) \quad \text{with} \quad \beta = \frac{c^2 \tau_M}{6K}. \quad (2.34)$$

The cumulative distribution function $C(\psi)$ has to be recalculated. It is given now by two different contributions corresponding to the integrals of the light-blue shaded area extending to the left (C_1) and to the right (C_2) of the vertical line at x_0 in figure 2.5. The 2D and 3D results may be expressed as:

$$\begin{aligned} C_{2D}^{causal}(\psi) &= \pi \mu_{(r,t)} 6K \left(\frac{a}{\psi}\right)^{4/3} \left\{ \left(\frac{1-x_0^2}{4}\right) + \frac{x_0^2}{2} \ln x_0 \right\} \\ &+ \pi \mu_{(r,t)} c^2 \left(\frac{a}{\psi}\right)^2 \frac{x_0^3}{3} \equiv C_1^{2D}(\psi) + C_2^{2D}(\psi), \end{aligned} \quad (2.35)$$

$$\begin{aligned} C_{3D}^{causal}(\psi) &= \frac{4}{3} \pi \rho_{(r,t)} (6K)^{3/2} \left(\frac{a}{\psi}\right)^{5/3} \int_{x_0}^1 \{-x \ln(x)\}^{3/2} dx \\ &+ \frac{4}{3} \pi \rho_{(r,t)} c^3 \left(\frac{a}{\psi}\right)^{8/3} \frac{x_0^4}{4} \equiv C_1^{3D}(\psi) + C_2^{3D}(\psi). \end{aligned} \quad (2.36)$$

The larger the flux ψ , the smaller the maximal age τ_M . In this limit, the coefficient $\beta \propto \tau_M$ vanishes. As the orange parabola of figure 2.5 opens, the value of x_0 tends to 1 and a large fraction of the space-time volume becomes causally disconnected. Thus, in the high flux limit, C_1 vanishes while C_2 increases. In the 2D regime, $C_{2D}(\psi) \propto \psi^{-2}$ whereas in the 3D regime, $C_{3D}(\psi) \propto \psi^{-8/3}$. As mentioned previously, the latter eventually takes over the former for very large values of the flux ψ for which the typical distances of the sources are smaller than the thickness h of the Galactic disk. As $8/3 > 2$, the variance associated to the pdf $p(\psi)$ is now finite. According to the central limit theorem, the probability $P(\Psi)$ converges toward a Gaussian when the number of sources N goes to infinity. We note, incidentally, that if the Galactic disk was infinitesimally thick, with $h = 0$, the 2D regime would apply with $\alpha = 2$. The variance is in that case divergent but the generalized central limit theorem can be applied, with the consequence that the total flux pdf $P(\Psi)$ also reaches a Gaussian form. Although causality arguments *per se* would allow arbitrarily large fluxes, we see that the whole discussion on stable laws loses its importance once a sizable fraction of the space-time volume is removed, since $p(\psi)$ is too steep. In practice, one can account for these effects by abruptly cutting the “standard” power-law distribution pdf above a transition flux $\psi_{cut} \equiv \psi_c$, which we may define for instance via the condition $C_1(\psi_c) = C_2(\psi_c)$. As we are interested in computing probabilities around the mean value $\langle \Psi \rangle$, let us compute ψ_c and compare it with $\langle \Psi \rangle$. To do so, we need to determine (ψ_c, x_c) by solving the two following equations:

$$C_1(\psi_c) = C_2(\psi_c) \quad \text{and} \quad -\beta_c(\psi_c) x_c = \ln(x_c), \quad (2.37)$$

which numerically yields $x_c \approx 0.6226$ in the 2D case and $x_c \approx 0.6424$ in the 3D case. Note that x_c (or equivalently β_c) does not depend on the cosmic ray energy, and is not very different between the 2D and 3D regimes. We can also define $y = \psi_c/\langle\Psi\rangle$, which can be written as

$$y = \frac{\psi_c}{\langle\Psi\rangle} = \frac{1}{46^{3/2}\sqrt{\pi}} \frac{1}{\beta_c^{3/2}} \frac{c^3 R^2}{K^2 L \nu}. \quad (2.38)$$

The estimate for y varies only by 14% between the 2D and 3D cases. As this difference is relatively small, we will take the average between these two values in the following discussion. Notice that y depends on energy through the diffusion coefficient K . Of course, for our discussion to be of any relevance, the stable law equation (2.32) should be valid for a total flux Ψ well in excess of its average $\langle\Psi\rangle$, that is, for values of y as large as possible. As an example, for the MED propagation model borrowed from Donato 2004, we find that $y \simeq 32$ at 10 TeV while it reaches $\sim 2 \times 10^4$ at 100 GeV.

The evolution of $\psi_c/\langle\Psi\rangle$ as a function of energy is displayed in gray in figure 2.6 for the three different benchmark propagation models discussed in Donato 2004, namely MIN, MED and MAX, and whose parameters are in table A.3 of the Appendix. That ratio is always larger than ten for cosmic ray energies below 10 TeV. To be conservative, the causality constraint could be forgotten below the TeV scale as long as we are interested in values of Ψ not exceeding a few times the average. However, depending on the propagation model, the light cone cut-off may seriously impair the use of equation (2.32) above a few tens of TeV, an energy range probed by calorimetric instruments such as CREAM or CALET.

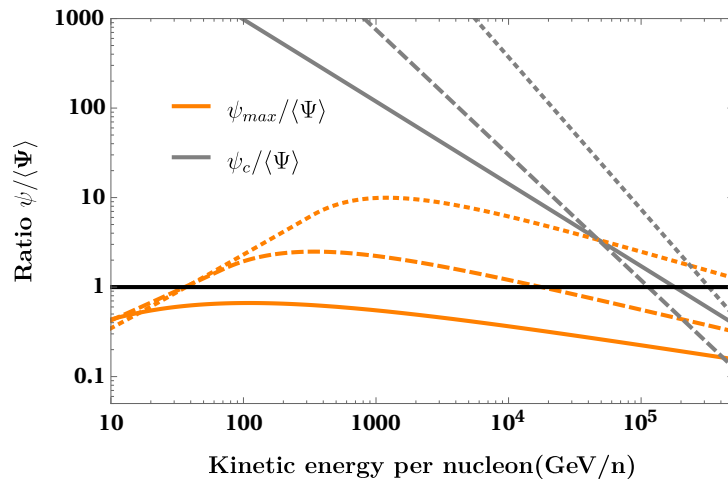


Figure 2.6: The causal cutoff flux $\psi_c/\langle\Psi\rangle$ (local environment cutoff flux $\psi_{max}/\langle\Psi\rangle$) as a function of energy is displayed in gray (orange) from top to bottom for the three propagation models MIN (dotted), MED (dashed) and MAX (solid).

2.3.5 Absence of very close and/or young sources

Another natural limitation to the maximum flux that a single source may contribute to the measured CR flux Ψ comes from some (partial) deterministic information on nearby sources; for example, one knows the sources within some distance one by one, but not the ones that are far away; or one only knows that no source exists within some distance. In a schematic way, one may split the flux into the sum of a local contribution from known sources and a remote component, on which the only information is of statistical nature, as considered above:

$$\Psi = \Psi_{\text{loc}} + \Psi_{\text{far}} . \quad (2.39)$$

The situation may be intermediate, for instance one has a catalog whose completeness decreases with distance and age of the source, but accounting for this complication is unnecessary for what follows. For a given catalog, which is assumed to be complete within a given region of space-time, from which the contribution Ψ_{loc} can be “exactly” computed, one could repeat the reasoning of the previous section to determine the pdf associated to Ψ_{far} . The cumulative distribution function $C(\psi)$ of a remote source can be computed by carving out the space-time region covered by the catalog.

Let us develop instead a slightly simpler argument by determining the maximal flux $\psi_{\text{cut}} \equiv \psi_{\text{max}}$ one can expect from a source located at the inner boundary of the phase space region filled by the catalog. We can use it to find the closest and youngest object, hence deriving plausible values for the minimal distance and age below which no cosmic ray injection takes place. A source located at distance d , which exploded at time τ in the past contributes the flux

$$\psi = \frac{q}{(4\pi K\tau)^{3/2}} \exp\left(-\frac{d^2}{4K\tau}\right) . \quad (2.40)$$

In the most general case, we want to put lower limits on the distance ($d > d_c$) and age ($\tau > \tau_c$) of remote sources in order to extract the cut-off, hereafter denoted by ψ_{max} , above which the pdf $p(\psi)$ vanishes. Constraining the distance d to be larger than d_c translates into the maximal flux

$$\psi_M = \frac{q}{(2\pi d_c^2/3)^{3/2}} \exp\left(-\frac{3}{2}\right) , \quad (2.41)$$

which is reached for an age $\tau_{\text{max}} = d_c^2/6K$. The flux ψ_M corresponds to the solid gray curve of figure 2.7. In this space-time diagram, the region below $d = d_c$ is excluded. From now on, two cases must be distinguished depending on the relative values of τ_{max} and τ_c . If $\tau_{\text{max}} > \tau_c$, the maximum flux that a remote source may provide is still ψ_M , a value reached at the space-time location (τ_{max}, d_c) . On the other hand, if $\tau_{\text{max}} < \tau_c$, the region to the left of the vertical line $\tau = \tau_c$ being excluded, remote sources can no longer yield the flux ψ_M . The solid gray line lies entirely in the excluded portion of the phase space diagram of figure 2.7. In this regime, the

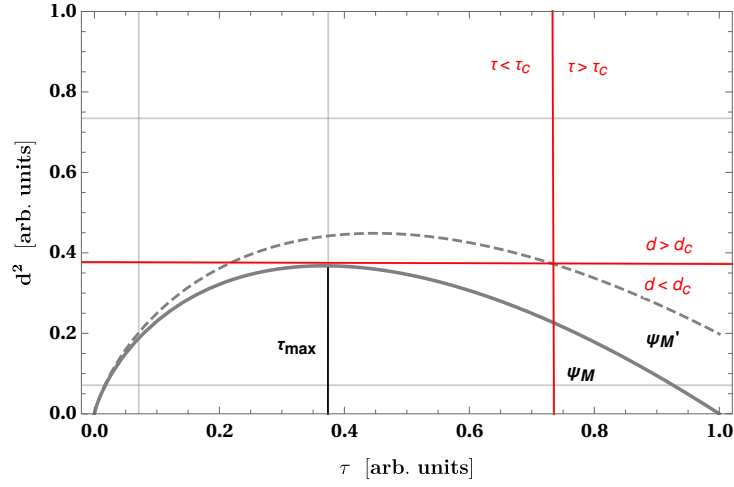


Figure 2.7: Solid gray line: locus of source ages and distances giving the same flux as the maximal one ψ_M yielded by a source located at distance d_c from the Earth, attained for $\tau = \tau_{max} = d_c^2/6K$. Dashed gray line: locus of source ages and distances giving the same flux ψ'_M as the one of a source of age τ_c and distance d_c . In the case shown ($\tau_{max} < \tau_c$), the flux ψ'_M is also the maximal flux from a source farther than d_c and older than τ_c .

maximal flux attainable by a remote source is $\psi'_M < \psi_M$. It corresponds to the dashed gray line that touches the allowed phase space region at location (τ_c, d_c) . In summary, imposing the constraint $\{d > d_c, \tau > \tau_c\}$ translates into $\psi < \psi_{max}$ with:

$$\psi_{max} = \begin{cases} \psi_M \equiv \frac{q}{(2\pi d_c^2/3)^{3/2}} \exp\left(-\frac{3}{2}\right), & \text{if } \underbrace{d_c^2/6K}_{\tau_{max}} > \tau_c, \\ \psi'_M \equiv \frac{q}{(4\pi K \tau_c)^{3/2}} \exp\left(-\frac{d_c^2}{4K\tau_c}\right), & \text{if } \tau_{max} < \tau_c. \end{cases} \quad (2.42)$$

This value may be compared to the mean flux $\langle \Psi \rangle$ taken as the theoretical average corresponding to the slab model and derived in Appendix B. The relations (2.42) readily translate into

$$\frac{\psi_{max}}{\langle \Psi \rangle} = \begin{cases} \frac{3R^2K}{\nu L d_c^3} \sqrt{\frac{3}{2\pi}} \exp\left(-\frac{3}{2}\right), & \text{if } \tau_{max} > \tau_c, \\ \frac{R^2}{4\nu L \sqrt{\pi K \tau_c^3}} \exp\left(-\frac{d_c^2}{4K\tau_c}\right), & \text{if } \tau_{max} < \tau_c. \end{cases} \quad (2.43)$$

As a conservative example of this procedure, we have taken $d_c = 0.06$ kpc as our lower limit on the distance, inspired by the closest known source G+276.5+19. In the same way, our lower boundary on the age comes from the youngest known source

J0855-4644 for which $\tau_c = 2.7$ kyr. These values are taken from the catalog compiled by [Delahaye 2010]. Using relations (2.43), we have derived the ratio $\psi_{max}/\langle\Psi\rangle$ and plotted it in orange in figure 2.6 to compare it with $\psi_c/\langle\Psi\rangle$. We observe a change of slope in the dependence of $\psi_{max}/\langle\Psi\rangle$ as a function of cosmic ray energy. This is particularly obvious in the MIN case (dotted orange curve) for which the diffusion coefficient is the smallest at low energies compared to the other propagation regimes MED and MAX. In the MIN configuration, the ratio $\psi_{max}/\langle\Psi\rangle$ increases with energy below 1 TeV. In this regime, K is small and the critical age $\tau_{max} = d_c^2/6K$ exceeds the lower bound τ_c . According to equation (2.43), the ratio $\psi_{max}/\langle\Psi\rangle$ scales as K and increases with cosmic ray energy. At approximately 1 TeV, a change of regime occurs when τ_{max} becomes smaller than τ_c , and the ratio $\psi_{max}/\langle\Psi\rangle$ scales as $1/\sqrt{K}$, decreasing with energy. The same trend is featured by the MED (dashed orange) and MAX (solid orange) curves, although in a milder way.

As clearly shown in figure 2.6, the cut-off ψ_{max} imposed by the catalog of local and recent sources is much more constraining than the value ψ_c yielded by the causality argument. The orange curves are basically always below the gray lines, which they intersect at energies in excess of 200 TeV, and for values of the ratio $\psi_{cut}/\langle\Psi\rangle$ of approximately 1. The use of approximation (2.32) is therefore possible below the orange curves. It is effectively interesting for values of the cut-off ψ_{max} larger than the average flux $\langle\Psi\rangle$. This is not the case for the MAX configuration. For the MIN and MED propagation models, the stable law (2.32) can still be applied on a fairly limited region in energy and total flux Ψ . As featured in figure 2.6, the ratio $\psi_{max}/\langle\Psi\rangle$ reaches a maximal value of ten at an energy of 1 TeV. The constraint from the catalog is therefore relatively strict. Most of the populations of sources that would otherwise lead to large values of the cosmic ray flux are excluded from the statistical analysis when the age and distance constraints are imposed. A word of caution is in order though since the completeness of a catalog is always questionable. Setting lower limits on the age and distance of nearby sources may be relatively subjective and eventually hazardous. That is why we have disregarded them in the Monte Carlo simulations that we discuss in the following section.

2.4 Comparison with numerical simulations

Until now, we have determined the range of fluxes Ψ for a given propagation setup over which the approximation described in section 2.3.3 holds. However, identically to how the combined pdf $P(\Psi)$ tends toward a Gaussian law when the conventional central limit theorem applies, the convergence to a stable law is only an asymptotic behavior. While exact results on the closeness to a stable law at finite N may exist in the mathematical literature, generic results are not useful in our case where a cut-off may be imposed on the individual flux pdf $p(\psi)$. We thus need to validate the reliability of the analytical theory via extensive numerical simulations. Our aim is to study how the total flux pdf $P(\Psi)$ converges to or departs from the stable law equation (2.26).

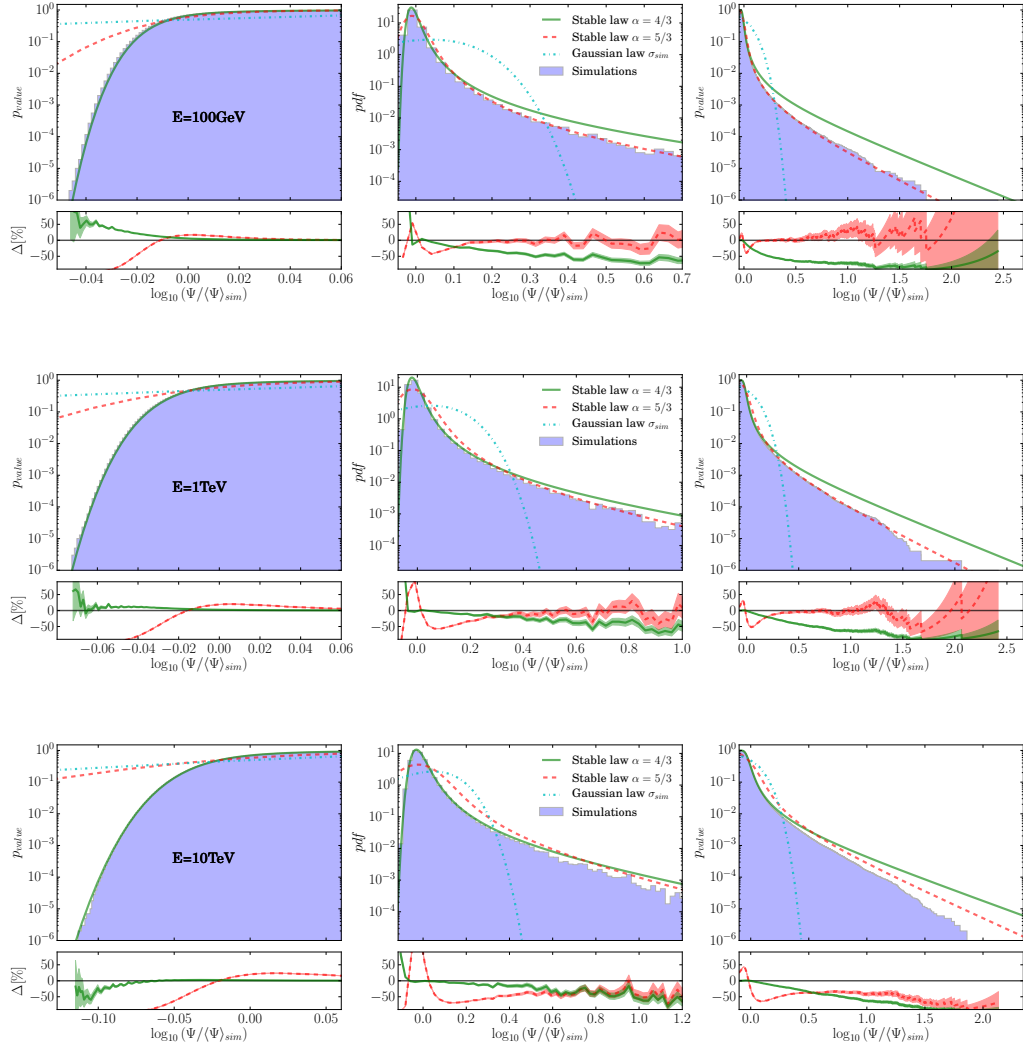


Figure 2.8: For each row, the left and right cumulative blue histograms of 10^6 Monte Carlo realizations of Galactic populations of CR sources are displayed in the left and right panels, respectively, whereas the pdf $P(\Psi)$ stands in the middle. The MED propagation model is used without taking into account convection, diffusive reacceleration and spallations. From top to bottom, the CR kinetic energy has been set equal to 100 GeV, 1 TeV, and 10 TeV. The solid green line indicates the theoretical prediction for the 2D model of the Galactic magnetic halo, whereas the dashed red curve corresponds to the 3D case. The residuals between theory and simulations are displayed below each histogram with their $1\text{-}\sigma$ Poissonian error.

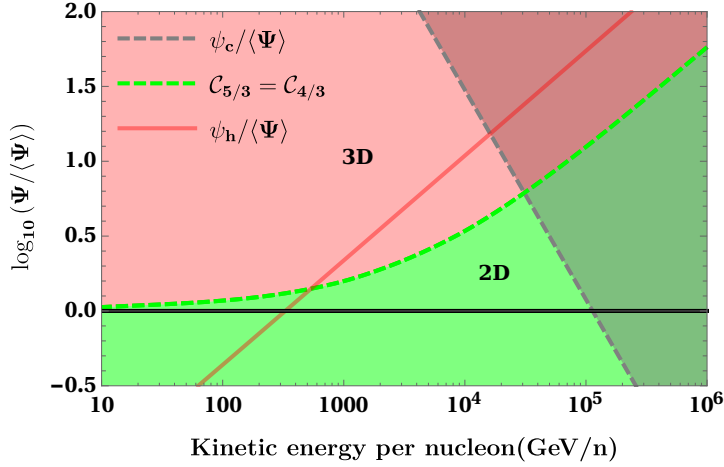


Figure 2.9: Regions in the flux versus energy plane where the 2D or 3D stable law is best suited to computing the probability of an excess above the mean (MED propagation model assumed). For a fluctuation lying in the light red (green) region, one should use the 3D (2D) approximation corresponding to the index $\alpha = 5/3$ ($\alpha = 4/3$). The dashed green curve signals the transition between these regimes as estimated from the equality of the cumulative distributions, $\mathcal{C}_{5/3} = \mathcal{C}_{4/3}$. The solid red line reports the alternative estimate of ψ_h following the argument developed in the text. In the shaded area in the upper-right corner of the diagram, causality is expected to generate deviations from the stable law behavior as a result of the light cone cut-off ψ_c it implies on the pdf.

2.4.1 Simulation settings

For each realization of Ψ , we simulate a Galactic population of sources in the framework of the 3D model of equation (2.7). Each source is generated at the random position \mathbf{x}_i within the Galactic disk, and with the random age τ_i . The positions \mathbf{x}_i are taken within an idealized cylindrical Milky Way Galaxy of radius R and half-thickness h , so that the spatial density of sources is homogeneous within the disk. The age of each source τ_i is taken between 0 and T , where T is the integration time of the simulation and is chosen to be $3\tau_0 = 3\pi L^2/4K$, that is, approximately three times the typical diffusion time within the magnetic halo. The peculiar choice of $3\tau_0$ is detail in appendix B. The number of sources of a realization is $N = T\nu$, with ν the rate of SN explosions, taken here to be three per century. Note that for a constant explosion rate of 3 SN/century and the chosen T , this means considering only sources younger than about 133 Myr at 100 GeV, so still much younger than the age of the Galaxy. In our model, this number reaches approximately 4×10^6 at a reference energy of 100 GeV. The spectrum of particles injected by each source is defined as

$$q = q_0 \left(\frac{\mathcal{R}}{1 \text{ GV}} \right)^{-2.2}, \quad (2.44)$$

where \mathcal{R} stands for the CR rigidity while the normalization q_0 is set equal to 1 GeV^{-1} . Notice that q does not come into play insofar as it can be factored out from our numerical results. The flux yielded by a source is computed assuming the CR propagation model MED, where we have safely neglected the effects of convection, diffusive reacceleration and spallations, which become negligible at the energies considered in our simulations. Without loss of generality, fluxes are derived for an observer placed at the radial and vertical centers of the Galactic disk, that is, at $r = z = 0$. The contributions ψ_i of the N sources of a given population are added to obtain one realization of Ψ . When the causality condition discussed in Sec. 2.3.4 is implemented, the contributions from sources lying outside the light cone of the observer are not included. We evaluated Ψ for each decade of energy between 100 GeV and 1 PeV. As we are interested in the pdf of the random variable Ψ , we simulated “only” 10^6 realizations of an idealized cylindrical Milky Way Galaxy, since we are not concerned with probabilities below the 10^{-5} level.

2.4.2 Simulation results

In figure 2.8, we show the results of the simulations that we carried out at 100 GeV, 1 TeV, and 10 TeV, with the light cone cut-off switched on. In each row, the left and right cumulative blue histograms of 10^6 realizations of Galactic populations of CR sources are displayed in the left and right panels, respectively, whereas the pdf $P(\Psi)$ stands in the middle. Once normalized to unity, the cumulative histograms on the left and on the right directly yield the probability of getting a population sourcing a flux smaller or larger, respectively, than the value $\Psi/\langle\Psi\rangle_{sim}$ read on the horizontal axis. Notice that $\langle\Psi\rangle_{sim}$ denotes the value of the flux averaged over the 10^6 realizations of our Monte Carlo. Due to finite sampling, results start to become unreliable for probabilities below 10^{-5} , and are obviously not even defined below 10^{-6} .

In each of the panels of figure 2.8, we also display the left and right cumulative distributions as well as the pdf corresponding to the theoretical predictions of Sec. 2.3.2. The dashed red line stands for the 3D case (i.e., $\alpha = 5/3$) whereas the solid green curve refers to the 2D case (i.e., $\alpha = 4/3$). In the argument of the stable distribution of equation (2.26), the average flux $\langle\Psi\rangle$ must be calculated exactly, assuming the same Milky Way magnetic halo as in the Monte Carlo simulations, namely a disk of radius 20 kpc and a maximal age for the SN explosions of T . Depending on whether the theoretical prediction is 2D or 3D, the sources are distributed along the vertical direction according to equation (2.7). As shown in the Appendix, the precise value of $\langle\Psi\rangle$ is slightly different from the approximation of equation (2.23). Once derived, the argument of the stable distribution (2.26) must be carefully rescaled to match the variable $\Psi/\langle\Psi\rangle_{sim}$ used on the horizontal axes of figure 2.8. For completeness, the residuals between the models (2D and 3D) and the histograms are also displayed below each panel. The shaded areas correspond to the one-sigma Poissonian uncertainty coming from the histogram binning. Finally, the dashed-dotted blue line depicts the results expected from a Gaussian distribution

with the same average and variance as given by the simulations. That variance is finite insofar as the light cone cut-off condition is implemented.

For energies not in excess of 10 TeV, the first noticeable result is the remarkable good convergence of the simulations toward the analytical model based on stable distributions. At low fluxes, the pdf and the left cumulative distribution of the simulations are very well matched by the theoretical 2D curve, and this holds whatever the energy considered. On the other hand, the theoretical prediction of the 3D model is always the closest to the simulations for large fluxes. Whatever the regime, all histograms reproduce the theoretical probability within $O(10\%)$ down to the 10^{-4} level, and even with the order of magnitude below 10^{-5} . Note that whatever the energy in the range extending from 100 GeV to 1 PeV, the simulations are not at all reproduced by the Gaussian law, featured by the dashed-dotted blue lines, which would be the limiting case for an infinite number N of sources according to the conventional central limit theorem. Stable laws are, on the contrary, an excellent approximation to our results, even though a cut has been imposed on the single source pdf $p(\psi)$ from causality considerations and one would naively expect $P(\Psi)$ to relax toward a Gaussian law.

At fixed CR energy, we observe a transition occurring at some critical value ψ_h of the flux Ψ , above which the 3D (i.e., $\alpha = 5/3$) stable law yields a better approximation than the 2D (i.e., $\alpha = 4/3$) distribution. In order to derive an estimate for ψ_h , we should keep in mind that stable laws tend to be dominated by the contribution from a single object. The transition between the 2D and 3D regimes of the total flux pdf $P(\Psi)$ should result from an evolution in the behavior of the individual flux pdf $p(\psi)$ with respect to ψ . This change is, in turn, related to a modification in the spatial distribution of the sources. We remark that the closer the object, the higher the flux it yields. Let us now make an educated guess and define ψ_h as the critical flux above which the dominant sources are statistically very close to the observer, at a distance less than the half-thickness h of the Galactic disk. As seen by the observer, they are isotropically distributed and the 3D model applies. As objects yielding a flux less than ψ_h are farther, their spatial distribution reflects the flatness of the Galactic disk and the 2D model is best suited to describe the simulations. In the phase space diagram of figure 2.7, the flux ψ_h corresponds to the solid gray iso-flux curve where d_c is replaced by h . A value can be derived from equation (2.41) and translates to the red solid line of figure 2.9 that depicts the behavior of the ratio $\psi_h/\langle\Psi\rangle$ as a function of CR kinetic energy. That curve features the same trend as our results. As the CR energy increases, the 2D to 3D transition occurs at higher values of the flux relative to the average $\langle\Psi\rangle$. At low CR energy, the agreement is not very good though. The transition flux ψ_h falls beneath the average flux for energies below 300 GeV, a trend that is not observed in our simulations. In the upper-left panel of figure 2.8, the left cumulative histogram is very well matched by the 2D stable law. Furthermore, defining ψ_h as the maximal flux yielded by sources located at a distance d_c exactly equal to h is somewhat arbitrary.

If we are interested in quantifying the probability of measuring a particular flux

excess with respect to the mean, as is the case for the applications discussed in Sec. 2.5, we can alternatively define ψ_h as the value for which the 2D and 3D right cumulative distributions $C(\psi)$ are equal. Following the notations of equation (2.16), the value of ψ_h is now given by the condition $\mathcal{C}_{4/3}(\psi_h) = \mathcal{C}_{5/3}(\psi_h)$. This leads to the dashed green line of figure 2.9 whose behavior with respect to CR energy exhibits the same trend as the red curve of the previous estimate. This time, the transition flux is always larger than the average $\langle\Psi\rangle$. The dashed green line separates the plot in two distinct regions. In the light green domain extending below the frontier, the simulations are well explained by the theoretical 2D stable law (i.e., $\alpha = 4/3$). In the light red part of the diagram, the 3D stable distribution (i.e., $\alpha = 5/3$) provides the best approximation. Above 1 TeV, our new value of the transition flux is smaller than the previous estimate derived from the Galactic disk half-thickness argument. Indeed, the cumulative distribution $C(\psi)$ is obtained via an integration of the pdf $p(\psi)$ from ψ upward. It contains information pertaining to the high-flux behavior of the pdf, and feels the 3D regime for smaller values of the flux compared to the other approach. Below 100 GeV, the 3D and 2D stable laws should be used above and beneath the mean flux, respectively, indicated in the plot by the solid black horizontal line.

The shaded area in the upper-right corner of figure 2.9 lies above the dashed gray curve featuring the ratio $\psi_c/\langle\Psi\rangle$. In this region, causality is expected to limit the statistical excursions of the flux toward high values, and the stable law should overestimate the actual pdf $P(\Psi)$. This trend is already present in the lower-right panel of figure 2.8, where the right cumulative blue histogram lies below the dashed red curve of the 3D stable law. For the simulations performed at 100 GeV and 1 TeV, the agreement is excellent. According to figure 2.9, the light cone cut-off starts to seriously affect the (not too large) fluctuations of the flux above an energy of 10 TeV. To illustrate this effect, we show the results of simulations realized at 100 TeV in figure 2.10, for which the causality constraint has been switched on (upper row) or off (lower row). The behavior of the pdf $P(\Psi)$ is very different between the two cases. In the upper row, sources lying outside the light cone of the observer are removed. The discrepancy between the simulated histograms and the stable law predictions is striking, even for fluctuations only 30% larger than the mean. If, now, all the sources are allowed to contribute to the flux Ψ , the agreement between the histograms and the stable laws is recovered. In the lower-right panel of figure 2.10, the 2D prediction $\mathcal{C}_{4/3}$ for the right cumulative distribution accounts well for the Monte Carlo results up to a flux approximately ten times larger than the mean. For larger fluctuations, the 3D function $\mathcal{C}_{5/3}$ is a good match to the histograms.

One last remark is in order. According to figure 2.9, the ratio $\psi_c/\langle\Psi\rangle$ drops below unity for energies above 100 TeV. In this energy range, we expect the effect of the causal cut to be so important that stable laws are poor representations of the actual pdf $P(\Psi)$, which they overshoot by a large margin. As discussed above, this occurs as soon as the flux exceeds its mean value. But for values of Ψ lower than the average $\langle\Psi\rangle$, the 2D stable law prediction (solid green curve) is still in excellent agreement with the histograms, whether the light cone cut-off condition is

implemented or not. In this regime, small fluxes are involved with two consequences. Distant sources dominate the faint signal received by the observer and their spatial distribution reflects the flatness of the Galactic disk, which is 2D in nature. Moreover, they yield a flux ψ well below the light cone cut-off ψ_c to which they are totally insensitive. Notice the excellent agreement between the simulations and the 2D stable law predictions in all the left panels of figure 2.8 and 2.10. We must finally conclude that for fluxes smaller than the mean, the pdf $P(\Psi)$ has asymptotically relaxed toward the (2D) stable distribution of equation (2.26), even though this is not the case in the high-flux regime. Stable laws seem to be robust descriptions of the pdf $P(\Psi)$ as soon as the condition of equation (2.17) is fulfilled over some range of values of ψ .

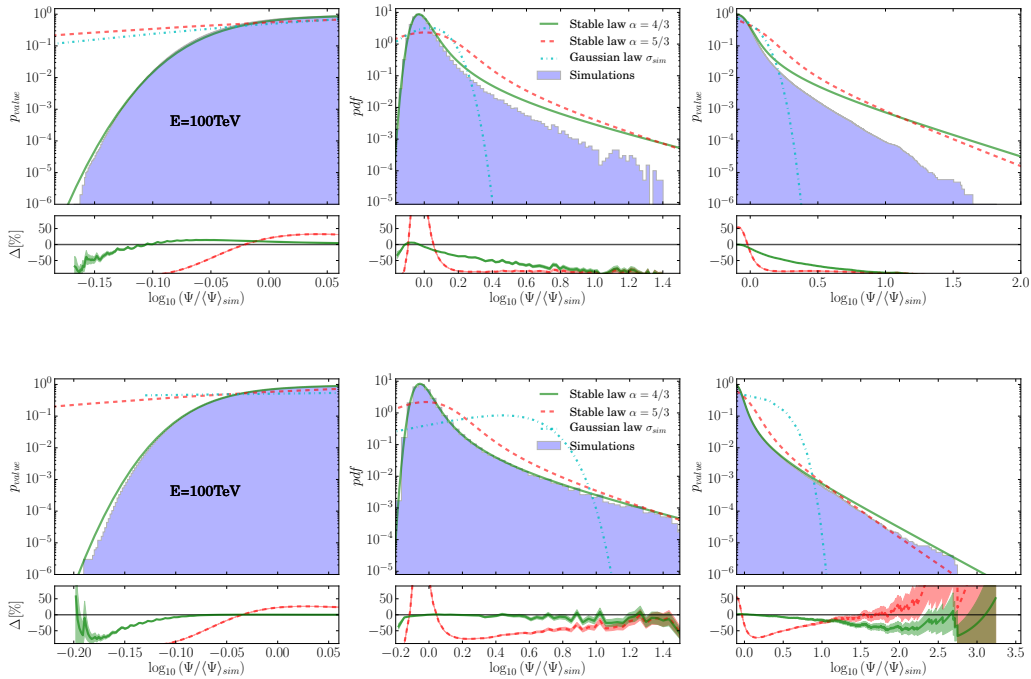


Figure 2.10: Same as in Fig 2.8 with a CR kinetic energy of 100 TeV. The upper row features the results of a simulation where the causality constraint is implemented whereas in the lower row, all sources are taken into account in the calculation of the flux Ψ , including those lying outside the light cone of the observer.

2.5 Applications

In this section we present some applications of the theory developed above. At first, we want to gauge if the present precision of experimental data is sufficient to be sensitive to a fluctuation of the flux coming from the discreteness of the

sources. To do so, we compute the probability that a source configuration leads to a 3σ fluctuation above and below the average flux assumed to follow a power law spectrum in energy. We actually calculate this probability for the proton flux measured by AMS-02 and PAMELA. The results are reported in Table 2.1 for the energies of 50 GeV and 1 TeV and for the three benchmark models MIN, MED and MAX. Each box of the table corresponds to the energy given at the top of its column. The upper value is the probability of getting a fluctuation above 3σ , and the value at the bottom corresponds to the probability of having a fluctuation below 3σ . The first noticeable feature is that the probability of seeing a 3σ fluctuation above the mean is always different than a 3σ fluctuation below. This is a consequence of the huge asymmetry of the stable distribution. Fluctuations below the mean are strongly prevented below the brutal fallout of the pdf. Furthermore, the probability of measuring a 3σ deviation from the mean is always larger at 50 GeV than at 1 TeV. This result means that the experimental uncertainty increases faster than the typical spread of the stable law with the energy. Thus, by improving data precision thanks to higher statistics or a new experiment, the probability of observing deviation from the mean flux at *low* energies (≈ 50 GeV) increases. Regarding the different propagation models, we notice that a fluctuation in the MAX model with a large halo height is much less expected than a fluctuation for small halo models, to which MIN belongs. In other words, the fact that AMS-02 proton data do not show any departure from a power law spectrum at relatively low energies can be interpreted as an independent hint for large halo size models. Finally, comparing PAMELA results with AMS-02, we notice that the latter has made a large step forward in reducing the experimental uncertainties, giving hope to chance of seeing deviation of the power law independently from the propagation models. We note that the effect of the stochasticity of the sources is expected to be smaller when dealing with secondary nuclei, since the interstellar gas on which they are produced is expected to be more smoothly distributed than Supernova remnants. Secondary to primary ratios are sensitive to this difference and may lead to biased results when extracting propagation parameters.

A positive large flux fluctuation corresponds to the situation where some of the sources are very near and very young. The extreme case for which a few sources (or even one source) dominate the contribution to the flux has been considered, for instance, in [Kachelrieß 2015]: the authors suggest explaining the low energy proton flux below $\sim \mathcal{O}(10)$ TeV by involving the major contribution of a local SNR (within a few hundreds of pc), which exploded approximately 2 Myr ago. According to figure 2.11 extracted from of this paper, this contribution would overcome the mean flux by a factor 2.86 at the energy of 10^3 GeV. In our myriad model, which assumes isotropic diffusion, the probability that a peculiar configuration of sources leads to a deviation comparable or larger to the one stated in this study, is given by:

Models	PAMELA		AMS02	
	50GeV	1TeV	50GeV	1TeV
Model	$p(\Psi > \langle \Psi \rangle + 3\sigma)$			
	$p(\Psi < \langle \Psi \rangle - 3\sigma)$			
MIN	0.15	0.083	0.28	0.26
	0.13	$< 10^{-6}$	0.63	0.51
MED	0.047	0.014	0.16	0.12
	$< 10^{-6}$	$< 10^{-6}$	0.26	0.0025
MAX	0.009	0.0018	0.045	0.016
	$< 10^{-6}$	$< 10^{-6}$	$< 10^{-6}$	$< 10^{-6}$

Table 2.1: Probability that a source configuration leads to a 3σ fluctuation above and below the flux measured by AMS-02 and PAMELA. The calculation is made for the three benchmark propagation models MIN, MED, and MAX, and for the two energies 50 GeV and 1 TeV.

$$\begin{aligned}
p_s &= \int_{2.86\langle\Psi\rangle}^{\infty} P(\Psi) d\Psi \\
&= 1 - \int_0^{2.86\langle\Psi\rangle} P(\Psi) d\Psi \\
&= 1 - \underbrace{(1 + \varepsilon)^N}_{\approx 1 \text{ (here)}} \int_0^{\frac{2.86\langle\Psi\rangle}{\sigma_N}} S[\alpha, 1, 1, 0; 1](X) dX . \quad (2.45)
\end{aligned}$$

Such a deviation corresponds to $\log_{10}(\psi/\langle\Psi\rangle) \approx 0.46$ at 10^3 GeV, for which figure 2.9 recommends the use of the 3D case corresponding to $\alpha = 5/3$. This conclusion holds for the MED model for which figure 2.9 was made, however we checked that it was actually also the case for the MIN and MAX cases. For the MIN case, $\psi/\langle\Psi\rangle$ also falls below the condition $\psi_{max}/\langle\Psi\rangle$ as shown in figure 2.6.

The probabilities for the three different benchmark propagation models are reported in table 2.2. For comparison, we also display the probabilities obtained by using a Gaussian law with the variance of the simulations. In the homogeneous diffusion framework, this result suggests that the chance probability for such an excursion is at most at the level of $\sim 0.1\%$, and even one order of magnitude smaller if the MAX model, apparently closer to the recent observations, is adopted. It would not be correct to discard the model in [Kachelrieß 2015] based on these considerations, however, since in that article the authors advocate a strongly anisotropic diffusion. Certainly, it emphasizes the importance of this ingredient in the plausibility of the scenario.

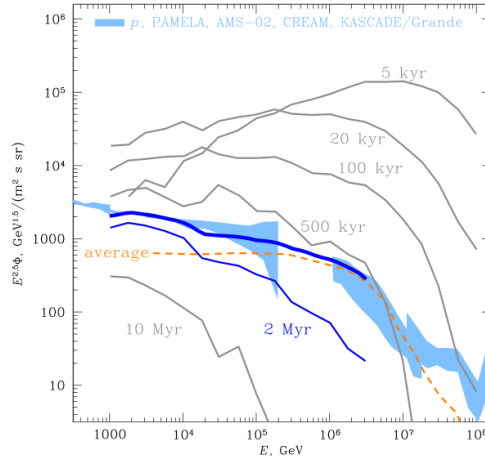


FIG. 1: Proton flux of the local source at different times. The average Galactic proton flux is shown as a thin orange line, the measured spectra of protons (light blue) from PAMELA [8], CREAM [9], KASCADE and KASCADE-Grande [11] as a band including experimental uncertainties. The sum of the average flux and the 2 Myr old source is shown by the blue thick line.

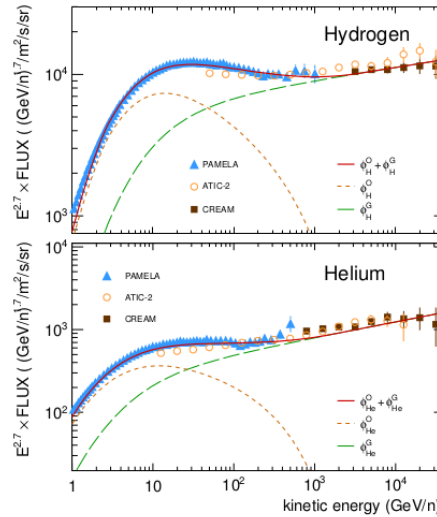


FIG. 2.— Energy spectra of H (top) and He (bottom) multiplied by $E^{2.7}$. The solid lines indicate the model calculations. The contribution arising from OSNR (short-dashed lines) and from GSNR (long-dashed lines) are shown. The data are from PAMELA (Adriani et al. 2011), ATIC-2 (Panov et al. 2009) and CREAM (Yoon et al. 2010).

Figure 2.11: Figures and legends extracted from [Kachelrieß 2015](*Top*) and [Tomassetti 2015](*Bottom*).

Another example is provided by the scenario discussed in [Tomassetti 2015]. Here the authors invoke a two components model for which the high energy CR spectrum is dominated by the average Galactic population, and the low energy part by one local old source, or, alternatively, a population of local old sources (see figure 2.11). In this case, homogeneous diffusion is assumed. The two different

Models	MIN	MED	MAX
Probabilities (Stable law 5/3)	0.0072	0.0012	0.00016
Probabilities (Gaussian law)	0.06	10^{-5}	0

Table 2.2: Probabilities of obtaining a flux larger than $2.86\langle\Psi\rangle$ at 1 TeV in the myriad model, calculated for three benchmark propagation models MIN, MED, and MAX. The Gaussian probability is extracted from the simulation and crucially depends on the integration time of the simulation.

energy dependences of these components would explain the break in the proton and helium flux above 200-300 GV. Once more, we can compute the probability for such a low-energy fluctuation of the flux in our myriad model, assuming the mean flux to be reached above the spectral break. From figure 2 of this paper, the proton flux at $E = 10$ GeV is dominated by some local sources, which yield a value of Ψ approximately 3.3 times the average $\langle\Psi\rangle$. Within their propagation model, one can show that the probability of such an excess must be treated with the 3D case. Making use of the formula in equation (2.45) of the previous example, we obtain a probability of 8.6×10^{-5} . Thus we can conclude that the only reasonable possibility for their scenario to be true is to assume a sum of two populations of sources, with the observed flux at the Earth being close to the sum of their average contributions rather than due to a local fluctuation.

Finally, one may consider the opposite possibility (advanced, for instance, in Bernard 2012, Bernard 2013) for which the high energy flux is a signature of the contribution of local sources, while the steeper flux at lower energies follows the Galactic average. In the left-hand panel of figure 2.12 we display the inferred mean proton flux in the range [45-200] GeV in this model, from which data depart more and more above the energies $\gtrsim 200$ GeV. To estimate the probability that such a discrepancy may occur, it is crucial to check the requirement for the applicability of the stable law, that is, $\Psi < \psi_c$. In the right-hand panel of figure 2.12, we plot the data divided by the mean above 45 GV, together with conditions $\psi_c/\langle\Psi\rangle$ and $\psi_{max}/\langle\Psi\rangle$ of figure 2.6 (solid for MAX model, dashed for MED, and dotted for MIN). If the data fall above the gray lines, it means that the observed excess cannot be provided by local sources in the diffusive regime. This is what happens to the two (three) highest energy CREAM data in the MED (MAX) propagation model. Strictly speaking, we can only conclude that our theory is inapplicable to those energies in the framework of these propagation models, since the diffusion approximation breaks down. However, it also means that the only way one or a few local sources might account for the measured flux in that range is to assume that CR propagate quasi-ballistically from the hypothetical source(s), which would qualitatively lead to $\mathcal{O}(1)$ anisotropy, in blatant contrast with the data, showing a dipole anisotropy in this energy range at or below the 0.1% level (see, e.g., the compilation in figure 2 of [Blasi 2012]). We also note that the data fall above the orange lines at all energies for the MAX model and already at 5 TeV for the MED

Models	MIN	MED	MAX
Probabilities(Stable law 4/3)	0.031	0.0082	0.0013

Table 2.3: Probabilities calculated for the most discriminating point of CREAM at 12.6TeV (the fourth one) and the three benchmark propagation models.

model. These lines correspond to the “maximal excursion” due to a source as young as $\tau < \tau_c = 2.7$ kyr and as close as $r < d_c = 0.06$ kpc, which is approximately the closest in space-time estimated on the basis of the available catalog. Although the available catalog may be incomplete, it is less and less likely the case for close and young/powerful sources. This is another independent argument suggesting that a local explanation for the high energy break of the type invoked in [Bernard 2012](#), [Bernard 2013](#) is unlikely in propagation scenarios of the MED or MAX type. If we discard all constraints from catalogs, our theory is applicable below 50 TeV to estimate the probability of such an excess within our myriad model. The probability is calculated as

$$p_{value} = \int_{\Psi_{exp}}^{\infty} d\psi_{exp} \int_0^{+\infty} d\psi p(\psi_{exp}|\psi) p(\psi|myriad), \quad (2.46)$$

where $p(\psi_{exp}|\psi)$ is a Gaussian law of spread, σ_{exp} the experimental variance, and $p(\psi|myriad)$ is the probability of achieving a theoretical flux ψ in the myriad model. We compute this probability for the most constraining data point, which lies at 12.6 TeV in the CREAM data. The fluctuation at this energy is $\psi/\langle\Psi\rangle \approx 1.73$, which justifies the use of the 2D case with the stable law $\alpha = 4/3$. The results are reported in [Table 2.3](#). We obtain a maximum of 3% within the MIN scenario. This probability is small but not vanishingly small. In fact, independent CR arguments disfavoring the MIN scenario (see for instance [[Lavalle 2014](#), [Giesen 2015](#), [Kappl 2015](#), [Evoli 2015](#)]) are probably even more capable of providing a killing blow to this model.

2.6 Conclusions of the section

Given the precision currently reached by cosmic ray measurements, it is more and more important to assess uncertainties associated with different theoretical predictions. The space-time discreteness of the cosmic ray sources is an important cause of theoretical uncertainty, given the the lack of information available on their precise epochs and locations, with the possible exception of the most recent and close ones.

In this article we have elaborated a statistical theory to deal with this problem, relating the composite probability $P(\Psi)$ to obtain a flux Ψ at the Earth and to the single-source probability $p(\psi)$ to contribute to a flux ψ . The main difficulty arises since $p(\psi)$ is a “heavy tail” distribution, characterized by power-law or broken power-law behavior up to very large fluxes for which the central limit theorem does

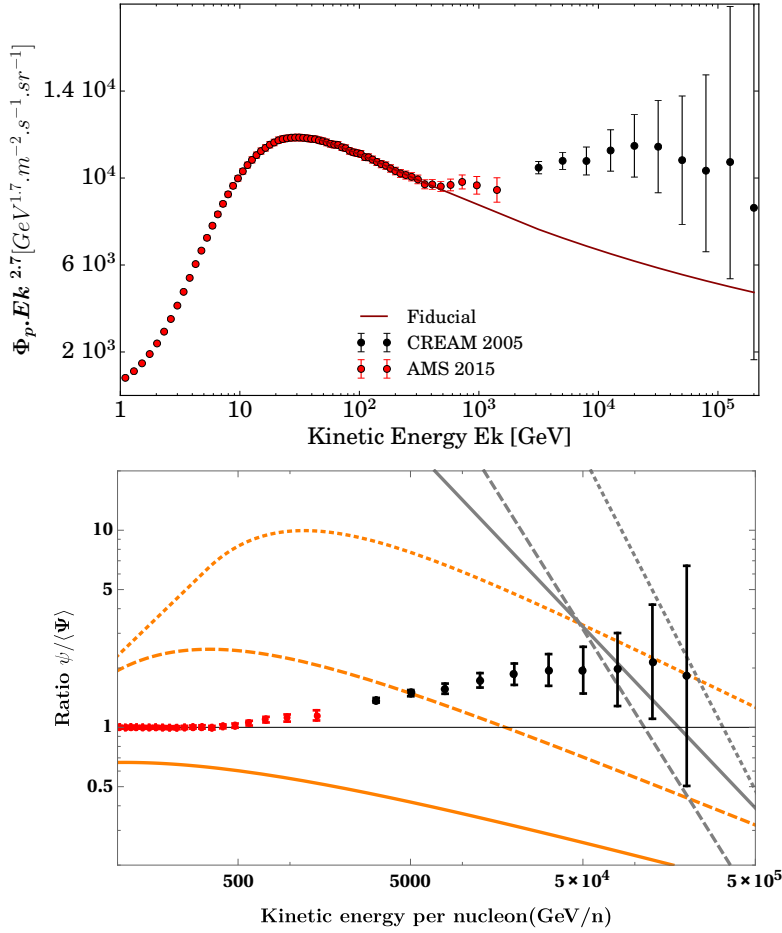


Figure 2.12: Left panel: proton flux from AMS-02 [Aguilar 2015] and CREAM [Yoon 2011], and a fit of the spectrum between 45 GeV and 200 GeV that we assume here to be the mean Galactic flux. Right panel: data divided by the theoretical mean above 45 GeV, together with conditions $\psi_c / \langle \Psi \rangle$ and $\psi_{max} / \langle \Psi \rangle$ of figure 2.6 (solid for MAX model, dashed for MED, and dotted for MIN).

not hold, and leading to peculiar function, stable under the convolution; namely stable laws different from the Gaussian distributions.

We have analytically discussed the regime of validity of the stable laws associated with the distributions arising in cosmic ray astrophysics for different propagation parameters and energy ranges, as well as the limitations to the treatment imposed by causal considerations and partial source catalog knowledge. We have also validated our results with extensive Monte Carlo simulations.

We find that relatively simple recipes provide a remarkably satisfactory description of the probability $P(\Psi)$. We also find that a naive Gaussian fit to simulation results would underestimate the probability of very large fluxes several times above

the average, while overestimating the probability of relatively milder excursions. At large energies, large flux fluctuations are prevented by causal considerations, while at low energies, a partial knowledge of the recent and nearby population of sources plays an important role.

We have applied our theory to some models recently discussed in the literature attempting to explain the spectral breaks as effects of a prominent nearby source. We showed that, at least within homogeneous and isotropic diffusion models, it is unlikely that this is the cause of the observed phenomenon, since the only case where this might happen with an appreciable probability is disfavored by independent arguments involving secondary tracers such as positrons, antiprotons, and/or the boron/carbon CR spectrum. We have also argued that the precision recently attained by cosmic ray measurements makes the observation of upward departures from the mean expectations more likely. Actually, the close agreement of recent AMS-02 at relatively low-energies with average expectations of continuous cosmic ray source models represents by itself a constraint on propagation models, which intriguingly goes in the same direction as those recently derived from secondary species. Diffusion models with a large halo and mild energy dependence appear favored. Another theoretically robust prediction is that no significant downward fluctuation with respect to average model expectations should be observed, a fact that, for the time being, seems to be confirmed by the data.

The formalism elaborated and validated in this article constitutes only a first step of a potentially much broader program. A trivial extension of the theory allows one to deal with several uncorrelated populations of sources, each one with its own distribution. One may also apply this formalism in a slightly modified form to deal with effects on secondary nuclei produced onto inhomogeneous medium with “heavy-tail” inhomogeneity distribution probability. A more subtle generalization would be required to deal with correlations of flux predictions at different energies. Even more challenging is to elaborate an analytical theory accounting for space and time correlations among the discrete sources of cosmic rays. Last but not least, it might be worth entertaining the possibility that some of the tools developed for applications to cosmic ray flux problems may find an application in other contexts of astroparticle physics, if not of physics in general.

Bibliography

- [Aguilar 2015] M. Aguilar, D. Aisa, B. Alpat, A. Alvino, G. Ambrosi, K. Andeen, L. Arruda, N. Attig, P. Azzarello, A. Bachlechner and et al. *Precision Measurement of the Proton Flux in Primary Cosmic Rays from Rigidity 1 GV to 1.8 TV with the Alpha Magnetic Spectrometer on the International Space Station*. Physical Review Letters, vol. 114, no. 17, page 171103, May 2015. (Not cited.)
- [Ahlers 2013] M. Ahlers, L. A. Anchordoqui and A. M. Taylor. *Ensemble fluctuations of the flux and nuclear composition of ultrahigh energy cosmic ray nuclei*. Phys. Rev. D, vol. 87, no. 2, page 023004, January 2013. (Not cited.)
- [Bernard 2012] G. Bernard, T. Delahaye, P. Salati and R. Taillet. *Variance of the Galactic nuclei cosmic ray flux*. A&A, vol. 544, page A92, August 2012. (Not cited.)
- [Bernard 2013] G. Bernard, T. Delahaye, Y.-Y. Keum, W. Liu, P. Salati and R. Taillet. *TeV cosmic-ray proton and helium spectra in the myriad model*. A&A, vol. 555, page A48, July 2013. (Not cited.)
- [Blasi 2012] Pasquale Blasi and Elena Amato. *Diffusive propagation of cosmic rays from supernova remnants in the Galaxy. II: anisotropy*. JCAP, vol. 1201, page 011, 2012. (Not cited.)
- [Büsching 2005] I. Büsching, A. Kopp, M. Pohl, R. Schlickeiser, C. Perrot and I. Grenier. *Cosmic-Ray Propagation Properties for an Origin in Supernova Remnants*. ApJ, vol. 619, pages 314–326, January 2005. (Not cited.)
- [Delahaye 2010] T. Delahaye, J. Laval, R. Lineros, F. Donato and N. Fornengo. *Galactic electrons and positrons at the Earth: new estimate of the primary and secondary fluxes*. A&A, vol. 524, page A51, December 2010. (Not cited.)
- [Donato 2004] F. Donato, N. Fornengo, D. Maurin, P. Salati and R. Taillet. *Antiprotons in cosmic rays from neutralino annihilation*. Phys. Rev. D, vol. 69, no. 6, page 063501, March 2004. (Not cited.)
- [Evoli 2015] Carmelo Evoli, Daniele Gaggero and Dario Grasso. *Secondary antiprotons as a Galactic Dark Matter probe*. JCAP, vol. 1512, no. 12, page 039, 2015. (Not cited.)
- [Genolini 2017] Y. Genolini, P. Salati, P. D. Serpico and R. Taillet. *Stable laws and cosmic ray physics*. A&A, vol. 600, page A68, March 2017. (Not cited.)
- [Giesen 2015] Gaij¹/₂lle Giesen, Mathieu Boudaud, Yoann Génolini, Vivian Poulin, Marco Cirelli, Pierre Salati and Pasquale D. Serpico. *AMS-02 antiprotons, at last! Secondary astrophysical component and immediate implications for Dark Matter*. JCAP, vol. 1509, no. 09, page 023, 2015. (Not cited.)

- [Higdon 2003] J. C. Higdon and R. E. Lingenfelter. *The Myriad-Source Model of Cosmic Rays. I. Steady State Age and Path Length Distributions*. ApJ, vol. 582, pages 330–341, January 2003. (Not cited.)
- [Kachelrieß 2015] M. Kachelrieß, A. Neronov and D. V. Semikoz. *Signatures of a Two Million Year Old Supernova in the Spectra of Cosmic Ray Protons, Antiprotons, and Positrons*. Physical Review Letters, vol. 115, no. 18, page 181103, October 2015. (Not cited.)
- [Kappl 2015] Rolf Kappl, Annika Reinert and Martin Wolfgang Winkler. *AMS-02 Antiprotons Reloaded*. JCAP, vol. 1510, no. 10, page 034, 2015. (Not cited.)
- [Lagutin 1995] AA Lagutin and Yu A Nikulin. *Fluctuations and anisotropy of cosmic rays in the Galaxy*. Soviet Journal of Experimental and Theoretical Physics, vol. 81, pages 825–830, 1995. (Not cited.)
- [Lavalle 2014] Julien Lavalle, David Maurin and Antje Putze. *Direct constraints on diffusion models from cosmic-ray positron data: Excluding the minimal model for dark matter searches*. Phys. Rev., vol. D90, page 081301, 2014. (Not cited.)
- [Lee 1979] MA Lee. *A statistical theory of cosmic ray propagation from discrete galactic sources*. The Astrophysical Journal, vol. 229, pages 424–431, 1979. (Not cited.)
- [Lévy 1925] Paul Lévy. *Calcul des probabilités*. Gauthier-Villars, 1925. (Not cited.)
- [Mandelbrot 1960] Benoit Mandelbrot. *The Pareto-Levy law and the distribution of income*. International Economic Review, vol. 1, no. 2, pages 79–106, 1960. (Not cited.)
- [Mertsch 2011] Philipp Mertsch. *Cosmic ray electrons and positrons from discrete stochastic sources*. JCAP, vol. 1102, page 031, 2011. (Not cited.)
- [Nolan 2012] John P Nolan. *Stable distributions*, volume 1177108605. ISBN, 2012. (Not cited.)
- [Serpico 2015] Pasquale D. Serpico. *Possible physics scenarios behind cosmic-ray "anomalies"*. In Proceedings, 34th International Cosmic Ray Conference (ICRC 2015), 2015. (Not cited.)
- [Taillet 2004] R. Taillet, P. Salati, D. Maurin, E. Vangioni-Flam and M. Cassé. *The Effects of Discreteness of Galactic Cosmic-Ray Sources*. ApJ, vol. 609, pages 173–185, July 2004. (Not cited.)
- [Tomassetti 2015] N. Tomassetti and F. Donato. *The Connection between the Positron Fraction Anomaly and the Spectral Features in Galactic Cosmic-ray Hadrons*. ApJ, vol. 803, page L15, April 2015. (Not cited.)

-
- [Uchaikin 1999] Vladimir V Uchaikin and Vladimir M Zolotarev. Chance and stability: stable distributions and their applications. Walter de Gruyter, 1999. (Not cited.)
- [Wolfram Research, Inc. 2016] Wolfram Research, Inc. *Mathematica 11.0*, 2016. (Not cited.)
- [Yoon 2011] Y. S. Yoon, H. S. Ahn, P. S. Allison, M. G. Bagliesi, J. J. Beatty, G. Bigongiari, P. J. Boyle, J. T. Childers, N. B. Conklin, S. Coutu, M. A. DuVernois, O. Ganel, J. H. Han, J. A. Jeon, K. C. Kim, M. H. Lee, L. Lutz, P. Maestro, A. Malinine, P. S. Marrocchesi, S. A. Minnick, S. I. Mognet, S. Nam, S. Nutter, I. H. Park, N. H. Park, E. S. Seo, R. Sina, S. Swordy, S. P. Wakely, J. Wu, J. Yang, R. Zei and S. Y. Zinn. *Cosmic-ray Proton and Helium Spectra from the First CREAM Flight*. *ApJ*, vol. 728, page 122, February 2011. (Not cited.)

Refinements on secondary species

Contents

3.1 Boron to carbon ratio and CR propagation	88
3.1.1 Parametric dependence	88
3.1.2 Dependence on theoretical hypotheses	94
3.1.2.1 Fitting procedure and benchmark values for this study	95
3.1.2.2 Primary boron?	99
3.1.2.3 Cross-section modelling	101
3.1.2.4 Systematics related to CR propagation modelling .	108
3.1.2.5 Conclusion and prospects of this study	111
3.2 Propagation parameters extraction and AMS-02 new release	113
3.2.1 A review of previous analyses	113
3.2.1.1 B/C analyses	113
3.2.1.2 Complementary constraints	118
3.2.2 AMS-02: preliminary analysis	120
3.2.2.1 Quality of the data	120
3.2.2.2 Preliminary tests	121
3.2.2.3 Cross-section effects	122
3.2.2.4 Evidence for a break in the diffusion coefficient . . .	125
Bibliography	127

As introduced in Chapter 1, we define secondary species those stemming from CR interactions with the ISM, in which they further propagate before reaching the Earth. Clearly, their fluxes have a different sensitivity to the propagation medium than the primary CRs, since their source terms already encode some information on the propagation. In the currently considered framework where injection and propagation are factorisable, a ratio of *secondary* to *primary* species is maximally sensitive to the propagation parameters, while at the same time it minimizes systematic uncertainties. Helium-4 is the lightest and most abundant (dominantly) primary species allowing for such a test, but its secondaries Deuterium ($Z = 1 A = 2$) and Helium-3 ($Z = 2 A = 3$) have to be singled out via an isotopic (i.e. mass) measurement against the significantly larger fluxes of protons ($Z = 1 A = 1$) and Helium-4 ($Z = 2 A = 4$). Carbon and Oxygen have the next more abundant CR fluxes, with Carbon ($Z = 6$) having the further advantage that a single-nucleon

spallation directly or indirectly yields Boron ($Z = 5$), whose abundance in the ISM is otherwise negligible. The situation with Oxygen is similar but slightly more complicated, since its main spallation byproduct is Nitrogen, whose abundance as primary ISM species is also sizable, and Oxygen only contributes one third or so (as opposed to roughly one half for Carbon) to the Boron flux. Since heavier primary species are less abundant and the needed charge resolution $\Delta Z/Z \sim 1/Z$ to separate the secondary from its primary species becomes more and more demanding, this justifies why the Boron to Carbon ratio (B/C) is one of the main targets of CR experiments for the understanding of cosmic ray propagation. In that sense, PAMELA and, more recently AMS-02, are ushering us into a new era of greatly reduced statistical uncertainties in experimental measurements. In particular, both of them recently published B/C data. Although one could question the pertinence of uniquely relying on this ratio—Oxygen is another excellent reference primary, and other species like Lithium or Beryllium also qualify as excellent secondaries—the availability of such high-quality data prompts the question of how best to exploit them to extract meaningful (astro)physical information. This section aims at covering this problem. We first focus on describing the sensitivity of the Boron to Carbon ratio to the propagation parameters. We also present our first estimates using AMS-02 data. Then, we argue that the current situation demands assessing theoretical uncertainties, which appear to be the limiting factor in the accuracy of parameter extraction.

3.1 Boron to carbon ratio and CR propagation

In this section we give the reader an idea of the sensitivity of B/C to the propagation parameters, first using analytical high energy approximation, then giving some clues of the numerical solution over a more extended energy range.

3.1.1 Parametric dependence

Here we focus on energies above 10 GeV/nuc which, according to figure 1.11, allows us to neglect continuous (ionisation and Coulomb) energy losses, electronic captures, and reacceleration. The simplest approach to model the transport of cosmic ray nuclei inside the Galaxy is to use the 1D model sketched in figure 1.7. We recall that it assumes that the CR production is confined inside an infinite plane of thickness $2h$, which is sandwiched inside an infinite diffusion volume of thickness $2L$, symmetric above and below the plane. The former region stands for the Galactic disk, which comprises the gas and the massive stars of the Milky Way, whereas the latter domain represents its magnetic halo. How to solve the simplified diffusion equation is addressed in detail in appendix A.1.1, let us just recall the general form of the flux for a stable species of charge Z_a :

$$\mathcal{J}_a(E_k) = \left\{ Q_a + \sum_{Z_b \geq Z_a}^{Z_{\max}} \sigma_{b \rightarrow a} \cdot \mathcal{J}_b \right\} / \{ \sigma^{\text{diff}} + \sigma_a \}, \quad (3.1)$$

$$(3.2)$$

$$\text{where } \sigma^{\text{diff}} = \frac{2K m_{\text{ISM}}}{\mu v L}.$$

The fluxes \mathcal{J}_b of the parent species are also taken at $z = 0$. We also recall that the cross-section for the production of the species a from the species b through its interactions with the interstellar medium (ISM) is denoted by $\sigma_{b \rightarrow a}$, whereas σ_a is the total inelastic interaction (destruction) cross-section of the species a with the ISM. More general formulas including radioactive species are given in appendix A.1.2. The fragmentation of the nucleus b takes place at constant energy per nucleon. So as $E_{kn} > 10 \text{ GeV/nuc}$, then $v \simeq c$ which here stands for the velocities of both parent (b) and child (a) nuclei. The surface mass density of the Galactic disk is denoted by μ , while m_{ISM} is the average mass of the atomic gas it contains. The fluxes \mathcal{J}_b of the parent species are also taken at $z = 0$. The source term Q_a is homogeneous to a flux times a surface and is expressed in units of particles $(\text{GeV/nuc})^{-1} \text{ s}^{-1} \text{ sr}^{-1}$. It is related to q_a through

$$Q_a = \frac{1}{4\pi} \cdot \frac{q_a}{n_{\text{ISM}}} \equiv N_a \left(\frac{\mathcal{R}}{1 \text{ GV}} \right)^\alpha, \quad (3.3)$$

where N_a is a normalisation constant that depends on the isotope a . We assume here an injection spectrum with the same spectral index α for all nuclei. We define the total flux of a nucleus of charge Z as the sum over all its isotopes a :

$$\mathcal{J}_Z = \sum_{\substack{\text{isotopes } a \\ \text{of same } Z}} \mathcal{J}_a. \quad (3.4)$$

The general form of the flux (equation 3.1) leads to two remarks in the limit where diffusion dominates over spallations (i.e $\sigma_{\text{diff}} \gg \sigma_a$):

- Pure primary species, are the byproducts of pure primary species. They are characterized by a vanishing Q_a , and their fluxes \mathcal{J}_a are also proportional to a power law of the rigidity, such that:

$$\mathcal{J}_a \propto \frac{Q_a}{K} \propto \mathcal{R}^{\alpha-\delta}. \quad (3.5)$$

- Pure secondary species byproducts of pure primary species—for which the first term of the numerator equation 3.1 cancels—have a flux \mathcal{J}_a also proportional to a power law of the rigidity, such that:

$$\mathcal{J}_a \propto \frac{Q_a}{K^2} \propto \mathcal{R}^{\alpha-2\delta}. \quad (3.6)$$

These cases are idealistic and, as mentioned previously in this thesis, in general cosmic ray species are a combination of primaries and secondaries. The resulting dependence of the flux can be written in the generic form:

$$\mathcal{J}_a \propto \varepsilon_1 \mathcal{R}^{\alpha-\delta} + \varepsilon_2 \mathcal{R}^{\alpha-2\delta} + \varepsilon_3 \mathcal{R}^{\alpha-3\delta} + \dots \quad (3.7)$$

In this expansion the two first terms usually dominate. At sufficiently high energy the first term eventually takes over the second which decreases faster. This simplified example, in the case $\sigma_{diff} \gg \sigma_a$, also gives an idea of the lower energy behavior of the fluxes. Assuming a universal injection index α , we expect the primary species to have different spectral shapes in the intermediate regime where the high order terms of the expansion are comparable to the first one. This fact is illustrated in figure 3.1, where we display the ratio of some *primary species* fluxes with respect to the Carbon flux. The slope difference Δ with respect to the carbon is also fitted in the regime [10 GeV, 1TeV]. At higher energies, extrapolating the trend shows that the ratios reach a constant value, which reflects the prominence of the first term of the expansion.

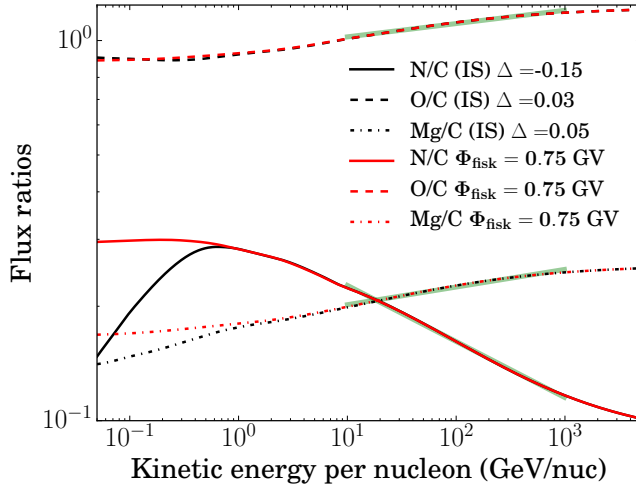


Figure 3.1: Illustration of the energy dependence of some *primary species* compared to carbon. A fit of the slope difference is shown between 10 GeV and 1TeV. The impact of solar modulation is also shown using $\Phi_{fisk} = 0.75\text{GV}$. These results depend on the chosen cross-section datasets.

The case of the B/C ratio is even simpler. Considering only the dominant contribution from stable nuclei, the B/C flux ratio can be written as

$$\frac{\mathcal{J}_B(E_k)}{\mathcal{J}_C(E_k)} = \left\{ \frac{Q_B}{\mathcal{J}_C} + \sigma_{C \rightarrow B} + \sum_{Z_b > Z_C}^{Z_{\max}} \sigma_{b \rightarrow B} \cdot \frac{\mathcal{J}_b}{\mathcal{J}_C} \right\} / \{ \sigma^{\text{diff}} + \sigma_B \}. \quad (3.8)$$

If we assume that there are no primary boron sources, i.e. $Q_B = 0$, this expression simplifies into

$$\frac{\mathcal{J}_B(E_k)}{\mathcal{J}_C(E_k)} = \frac{\sigma_{C \rightarrow B}}{\sigma_{diff} + \sigma_B} + \sum_{Z_b > Z_C}^{Z_{max}} \frac{\sigma_{b \rightarrow B}}{\sigma_{diff} + \sigma_B} \cdot \frac{\mathcal{J}_b}{\mathcal{J}_C}. \quad (3.9)$$

The impact of relaxing this hypothesis is explored in section 3.1.2.2 where the effect of a non-vanishing value for Q_B is considered. In the case where $\sigma_{diff} \gg \sigma_a$, stopping at the first term gives the well-known proportionality of the B/C ratio with the diffusion coefficient:

$$\frac{\mathcal{J}_B}{\mathcal{J}_C} \propto \frac{1}{K} \propto \frac{1}{K_0} \mathcal{R}^{-\delta}. \quad (3.10)$$

This decreasing power law behavior is actually present in the data, as illustrated in figure 3.2. Hence, the data and notably the latest release from AMS-02 are quite

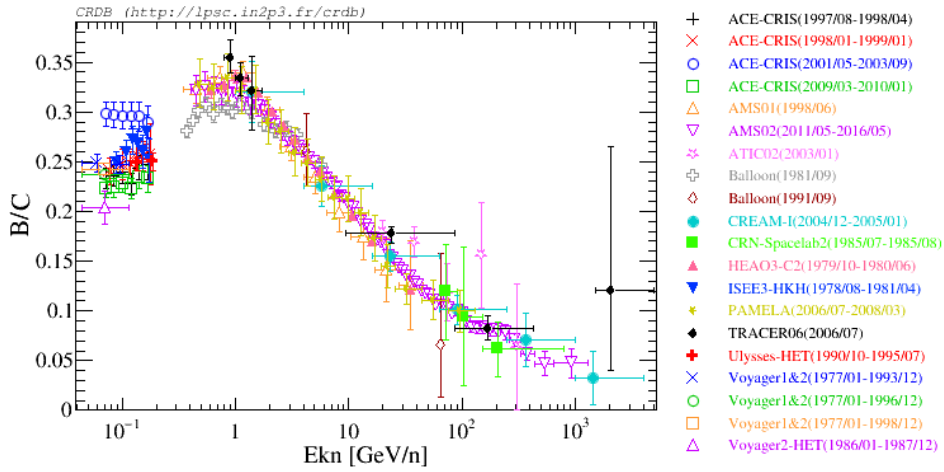


Figure 3.2: The B/C ratio as a function of the kinetic energy per nucleon, measured by several experiments (after 1980). Figure extracted from CRDB.

constraining for the diffusion coefficient. However, it is often believed that the high energy slope of the B/C ratio reflects the energy behaviour of the diffusion coefficient. Although this statement is completely true in the regime where $\sigma_{diff} \gg \sigma_a$, one can still expect to measure significant variation of the slope due to spallations. To convince the reader, we show in figure 3.3, two predictions of the B/C flux with (dashed line) and without (solid line) destruction of the species. The prediction including destructions of the species departs significantly from the diffusion power law spectrum, already for energies lower than 100 GeV, below which most of the data are available. Thus, accounting for destructions in the estimation of the spectral shape δ of the diffusion coefficient is essential. Once such an extraction is made, two remarks are in order about the obtained normalization K_0 of the diffusion coefficient:

- In all the theoretical formulas for the fluxes (appendix A.1.2), including stable and unstable species, K_0 is always degenerated with the density μ of the interstellar medium.

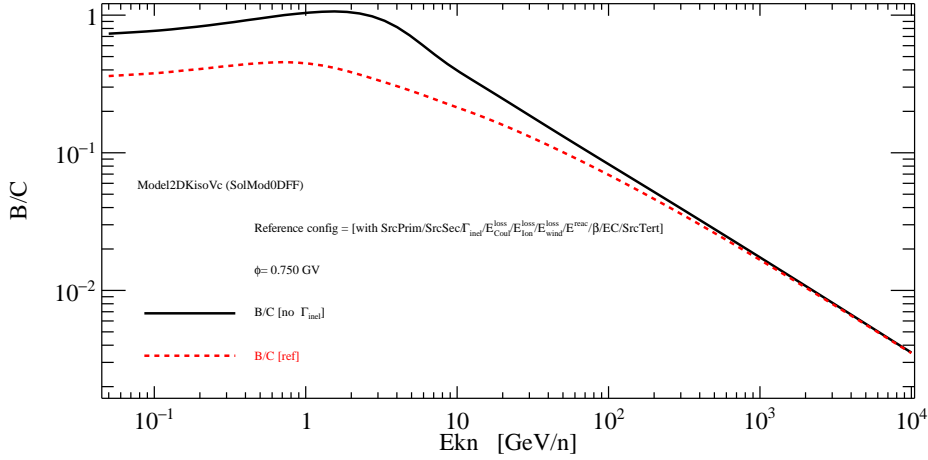


Figure 3.3: Prediction of the B/C ratio with (dashed red line) and without (black solid line) destructions, ruled by σ_a . Figure obtained with USINE.

- With the sole exception of unstable species, the normalization K_0 and the halo size L are always degenerated.

Extracting precise information from the normalization of the diffusion coefficient only makes sense if constraints on the density of the ISM and on the halo size can be obtained independently¹.

Whereas the high energy part of the B/C ratio is mostly sensitive to the diffusion coefficient, the low energies (from ~ 0.5 -10 GeV/nuc) are quite sensitive to the convective wind V_c , the reacceleration through Alfvénic speed V_A , but also the solar modulation parameterized by the Fisk potential Φ_f . As all these effects are quite degenerated, the interpretation of the B/C at low energies requires care.

As we saw in section 1.4, the prediction of the flux in all the energy range requires the resolution of a numerical equation, which reduces to one dimension after analytical simplifications. This task is achieved for example by the USINE code. The best way to visualize the effects of the different propagation parameters on the B/C ratio is to vary each of the parameters while keeping the others at a fixed value. Figure 3.4 shows the effects of a variation of the propagation parameters with respect to a fiducial model fitted with the AMS-02 data. We can readily check that the two parameters K_0 and δ are fixed by the high energy behavior, while V_c , V_a , Φ_f play a role at lower energies. The same remarks regarding the normalization K_0 extracted after a fit to the B/C data at high energy hold in all the energy range:

- From equation A.17, by neglecting coulomb energy losses (which is a fair approximation in the all energy range considered), we can show easily that

¹Actually a small fraction of the ^{10}B stems from radioactive decay of ^{10}Be which spectral shape breaks the degeneracy K_0/L . Nonetheless, this component is too small to be really constraining with the current precision of the data (see section 3.2.2).

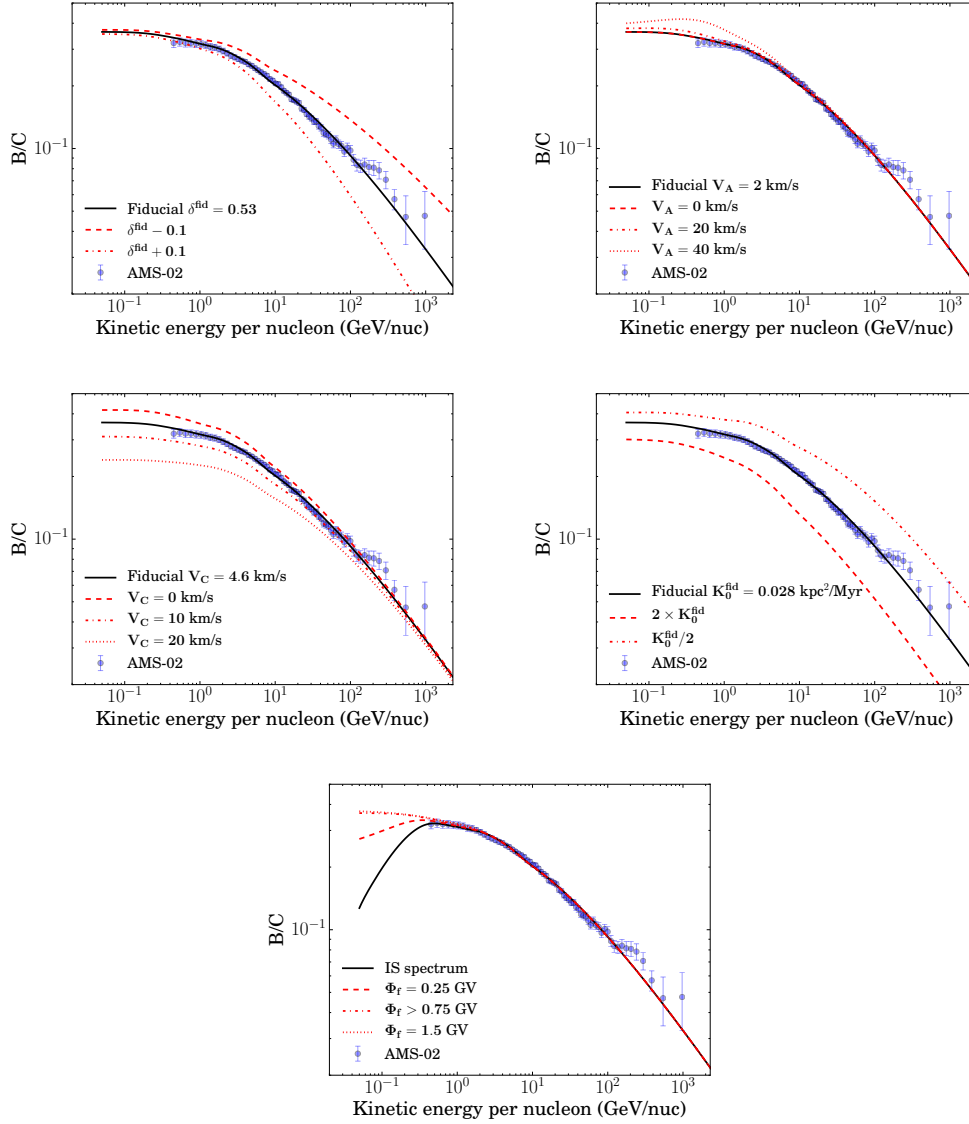


Figure 3.4: Effects of varying the propagation parameters (K_0 , Φ_{fisk} , δ , V_a , V_c) with respect to a fiducial model fitted to the AMS-02 data of the B/C ratio in kinetic energy per nucleon. Variations over L are not shown since this parameter is degenerated with K_0 .

the all propagation parameters— V_A , V_C , K —are degenerated with the density μ whose redefinition can be reabsorbed in the source term normalization.

- With the sole exception of unstable species, the normalization K_0 and the halo size L are always degenerated when radial boundaries are negligible (It simplifies thus the expression of S_i , equation A.2.1).

Once more, we reiterate that extracting information from the normalization of the

diffusion coefficient is only possible if constraints on the density of the ISM and on the halo size can be obtained independently.

3.1.2 Dependence on theoretical hypotheses

The newly available wealth of data demands reassessing theoretical uncertainties, which will probably be the limiting factor in the parameter extraction accuracy. As a preliminary work, preceding the actual data analysis, we revisit this issue to determine the relative importance of various effects: some have already been considered in the past, some were apparently never quantified. We also found that the main theoretical biases or errors are related to phenomena that can be described in a very simple 1D diffusive model. We thus adopt this model as a benchmark for our description, reporting the key formulae that thus have a pedagogical usefulness, too. In fact, we focus on determining the diffusion coefficient, which we parameterize as conventionally in the literature (see for example [Ptuskin 1997]):

$$D(\mathcal{R}) = D_0 \beta \left(\frac{\mathcal{R}}{\mathcal{R}_0 = 1 \text{ GV}} \right)^\delta, \quad (3.11)$$

where D_0^2 and δ are determined by the level and power-spectrum of hydromagnetic turbulences, \mathcal{R} is the rigidity, and the velocity $\beta = v/c \simeq 1$ in the high energy regime of interest here (kinetic energy/nucleon $\gtrsim 10 \text{ GeV/nuc}$). As seen for example in figure 1.11, at lower energies numerous effects, in principle of similar magnitude, are present, such as convective wind, reacceleration, and collisional losses. At high energy, there is a common consensus that only diffusion and source-related effects are important. We focus on the high energy region since it is the cleanest to extract diffusion parameters, that is the least subject to parameter degeneracies. While adding lower-energy data can lead to better constraints from a statistical point of view, the model dependence cannot but grow. Since our purpose is to compare theoretical with statistical uncertainties from observations, our choice is thus conservative: in a global analysis, the weight of the former with respect to the latter is probably larger. Nonetheless, we will explicitly compute the effect of adding a convective wind in the analysis, since this is the leading “low-energy” parameter still having an effect at the energies of interest, see figure 3.4. This study was published before AMS-02 last release of the B/C ratio [Aguilar 2016], and is based on preliminary AMS-02 data of the B/C ratio which were presented at [33rd Intern. Cosmic Ray Conf. 2013]. Reprocessing the results with the new data would only reinforce our conclusions, since statistical errors have shrank.

This study comes mainly from the paper [Genolini 2015] written in collaboration with Antje Putze, Pierre Salati and Pasquale Serpico. It is organised as follows. In section 3.1.2.1 we define our benchmark model based on the 1D diffusion geometry, we also recall the main statistical tools used for the analysis. In section 3.1.2.2 we

²Note that we have introduced the notation D_0 instead of K_0 , only to be consistent with the figures and comments of [Genolini 2015].

describe the main degeneracy affecting the analysis: the one with possible injection of boron at the sources. The next most important source of error is associated to cross-section uncertainties, to which we devote section 3.1.2.3. In section 3.1.2.4 we discuss relatively minor effects linked to modelling of the geometry of the diffusion volume, source distribution, or the presence of a convective wind. In section 4.4.3 we report our conclusions.

3.1.2.1 Fitting procedure and benchmark values for this study

Our focus on energies above 10 GeV/nuc allows us to neglect continuous (ionisation and Coulomb) energy losses, electronic capture, and reacceleration. These sub leading effects cannot be truly considered as theoretical uncertainties, since they can be introduced by a suitable upgrade of the model. However, taking them into account at this stage would imply a significant loss in simplicity and transparency. The solution of the equation in this high energy approximation are given in appendix A.2.2 ; it is also recalled section 3.1.1 for the precise case of the B/C ratio. Its expression depends on the source terms value N_a that should be adjusted by fitting the corresponding flux \mathcal{J}_a to the measurements performed at Earth. However, the values N_a scarcely contain information on the isotopic composition of cosmic rays. Nuclei with the same charge Z are in general collected together, irrespective of their mass. More isotopic observations would be necessary to set the values of the coefficients N_a for the various isotopes a of the same element.

In our analysis, we assumed solar system values [Lodders 2003] for the isotopic fractions f_a of the stable species a that were injected at the sources. We then proceeded by computing the flux \mathcal{J}_Z of each element Z at Earth. We fixed the normalisation N_Z for the total injection of all stable isotopes of the same charge Z by fitting the measured flux of that element. The normalisation entering in the calculation of Q_a is given by $N_a = f_a \cdot N_Z$, the sum of the fractions f_a corresponding to the same element Z amounting to 1. The actual isotopic composition of the material accelerated at sources might be different from the solar system one, as is the case for neon [Binns 2008]. Our method might introduce a theoretical bias in CR element flux calculations. However, our main focus here is to extract the propagation parameters thanks to the different sensitivities between primary carbon and (*a priori*) secondary boron. The only isotopes that come into play in the B/C ratio are the stable nuclei ^{12}C , ^{13}C , ^{10}B , and ^{11}B , unstable ^{14}C plays a very minor role. The isotopes of either carbon or boron have similar rigidities and destruction cross-sections. Varying the isotopic composition of carbon (and of boron, should it be partially primary) does not affect the ratio calculation. Furthermore, secondary boron is mainly produced by the fragmentation of one particular isotope of each heavier element. For example, the primary component of ^{12}C is two orders of magnitude larger than that of ^{13}C . This reduces the differences arising from the boron production cross-sections. Although most of the isotopes at stake are stable, radioactive nuclei were also taken into account in the calculation, and we obtained more complicated expressions for the fluxes, which are not displayed here for brevity. They are reported in appendix

A.1.2.

The values of the production cross-sections $\sigma_{b \rightarrow a}$ were calculated with the most recent formulae from [Webber 2003]. The destruction cross-sections σ_a were computed by the semi-empirical formulae of [Tripathi 1997, Tripathi 1999]. The high energy shapes of both cross-sections exhibit a plateau that allows one to approximate them as constants in this energy range.

Concerning the geometry, we use a simple 1D diffusion model providing our benchmark for the following analyses. This model certainly has pedagogical value, since it allows encoding the main dependences of the B/C ratio on input as well as astrophysical parameters in simple analytical formulae. At the same time, it provides a realistic description of the data, at least if one limits the analysis to sufficiently high energies.

We used the AMS-02 recent release of the B/C ratio [33rd Intern. Cosmic Ray Conf. 2013] to study the impact of systematics on the propagation parameters. As explained above, we limited ourselves to the high energy sub-sample, above 10 GeV/nuc. The set of Eqs. (3.1) is of triangular form. The heaviest element considered in the network, which in our case is ^{56}Fe , can only suffer destruction. No other heavier species b enters in the determination of its flux \mathcal{J}_a , which hence is proportional to the injection term Q_a . Once solved for it, the algebraic relation yields the solution for the lighter nuclei, down to boron. We evaluated the cascade down to beryllium to take into account its radioactive decay into boron.

The primary purpose of our analysis is to determine the diffusion parameters D_0 and δ from the B/C flux ratio $\mathcal{F} \equiv \mathcal{J}_B/\mathcal{J}_C$. Another parameter of the model is the magnetic halo thickness L . As shown in equation (3.1), D_0 and L are completely degenerate when only considering stable nuclei, which provide the bulk of cosmic rays. In the following, L is therefore fixed at 4 kpc for simplicity, although it should be kept in mind that, to a large extent, variations in D_0 can be traded for variations in L . Finally, the injection spectral index α also enters in the calculation of the B/C ratio through the source terms Q_a . How strong its effect is on the best-fit diffusion parameters D_0 and δ is one of the questions we treat in this section. To this purpose, we carried out a chi-square (χ^2) analysis of the B/C observations and minimised the function

$$\chi_{\text{B/C}}^2 = \sum_i \left\{ \frac{\mathcal{F}_i^{\text{exp}} - \mathcal{F}_i^{\text{th}}(\alpha, \delta, D_0)}{\sigma_i} \right\}^2, \quad (3.12)$$

where the sum runs over the data points i whose kinetic energies per nucleon are $E_{k,i}$, while $\mathcal{F}_i^{\text{exp}}$ and σ_i stand for the central values and errors of the measurements. The theoretical expectations $\mathcal{F}_i^{\text{th}}$ also depend on the normalisation constants N_a , which come into play in the source terms Q_a of the cascade relations (3.1). To determine them, we first fixed the spectral index α and the diffusion parameters D_0 and δ . We then carried out an independent χ^2 -based fit on the fluxes \mathcal{J}_Z of the various elements that belong to the chain that reaches from iron to beryllium. The measured fluxes

are borrowed from the cosmic ray database of [Maurin 2014] from which we selected the points above 10 GeV/nuc. As explained above, this method yields the constants N_Z and eventually the values of N_a once the solar system isotopic fractions f_a are taken into account. The overall procedure amounts to profile over the normalisation constants N_a to derive $\chi_{\text{B/C}}^2$ as a function of α , δ and D_0 . Minimisations were performed by MINUIT (<http://www.cern.ch/minuit>), a package interfaced in the ROOT programme (<https://root.cern.ch>).

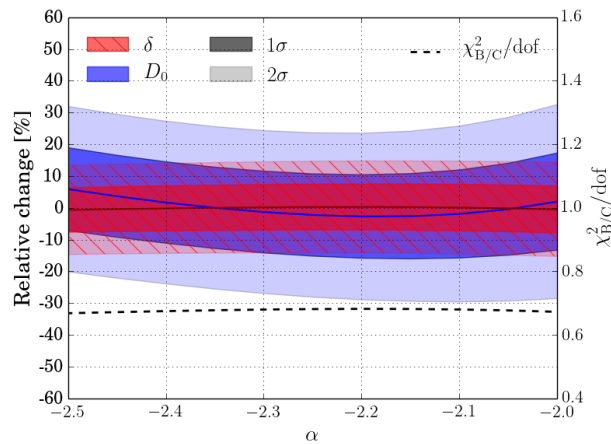


Figure 3.5: Relative variations of the best-fit propagation parameters (compared to the benchmark model of table 3.1) with respect to the injection spectral index α .

To check the accuracy and robustness of our fitting procedure, a preliminary test is in order. A commonly accepted notion is that the B/C ratio does not depend, to leading order, on the spectral index α . There is indeed no dependence on α in the cross-section ratios of equation (3.9) in the pure diffusive regime where $\sigma_{\text{B}} \ll \sigma^{\text{diff}}$. We have checked numerically that this behaviour holds by calculating the B/C best-fit values of the diffusion parameters at fixed spectral index α . The results are reported in figure 3.5, where D_0 and δ are plotted, with their confidence limits, as a function of α . We scanned over the physical range that extends from -2.5 to -2 and observed that the relative variations of D_0 and δ are 5% and 1%, respectively. The blue (D_0) and red (δ) bands are almost horizontal. An anti-correlation between D_0 and δ is marginally noticeable and can be understood by the interplay of these parameters inside the diffusion coefficient D , the only relevant parameter that the B/C fit probes. We attribute the small variation of D_0 with α to the different sensitivities of the normalisation constants N_Z of nitrogen and oxygen to the low-energy data points as compared to carbon. This could result in fluctuations of the $N_{\text{N}}/N_{\text{C}}$ and $N_{\text{O}}/N_{\text{C}}$ ratios with respect to the actual values. In any case, the extremely small dependence of the B/C ratio on α confirms the naive expectations and suggests that it is useless and simply impractical to keep α as a free parameter.

Nonetheless, there is a particular value of the injection index that best fits the

fluxes of the elements Z that come into play in the cascade from iron to beryllium. By minimising the χ^2 -function

$$\chi_{\mathcal{J}}^2 = \sum_{Z \geq Z_{\text{Be}}}^{Z_{\text{Fe}}} \sum_i \left\{ \frac{\mathcal{J}_{Z,i}^{\text{exp}}(E_{k,i}) - \mathcal{J}_{Z,i}^{\text{th}}(E_{k,i})}{\sigma_{Z,i}} \right\}^2, \quad (3.13)$$

we find $\alpha = -2.34$ as our benchmark value. Applying then our B/C analysis yields the propagation parameters D_0 and δ of the reference model of table 3.1 which we used for the following analyses. The corresponding B/C ratio is plotted in figure 3.6 as a function of kinetic energy per nucleon and compared to the preliminary AMS-02 measurements [33rd Intern. Cosmic Ray Conf. 2013]. In what follows, we study how D_0 and δ are affected by a few effects under scrutiny and gauge the magnitude of their changes with respect to the reference model. We could have decided to keep the injection index α equal to its fiducial value of -2.34, but we preferred to fix the spectral index $\gamma = \alpha - \delta = -2.78$ of the high energy fluxes \mathcal{J}_Z at Earth. Keeping α fixed would have little effect on the B/C ratio, but would degrade the goodness of the fits on absolute fluxes.

Reference parameter values	
α	-2.34
D_0 [kpc ² /Myr]	$(5.8 \pm 0.7) \cdot 10^{-2}$
δ	0.44 ± 0.03
$\chi_{\text{B/C}}^2/\text{dof}$	$5.4/8 \approx 0.68$
$\gamma = \alpha - \delta$ (fixed)	-2.78

Table 3.1: Benchmark best-fit parameters of the 1D/slab model, with respect to which comparisons are subsequently made.

Another crucial test of our fitting procedure is to check how the results depend on the low-energy cut-off E_{cut} above which we carried out our analysis. We set the flux spectral index γ to its benchmark value of table 3.1 and determined the B/C best-fit values of the diffusion parameters as a function of E_{cut} , which was varied from 5 to 30 GeV/nuc. The results are plotted in figure 3.7 with the 1σ and 2σ uncertainty bands. As expected, the statistical errors increase when moving from a low E_{cut} to a higher value. That is why the reduced χ^2 (dashed line) decreases steadily as the cut-off energy is increased. The higher the cosmic ray energy, the fainter the fluxes and the scarcer the events in the detector. The widths of the blue (D_0) and red (δ) bands at $E_{\text{cut}} = 10$ GeV/nuc, however, are not significantly larger than for a cut-off energy of 5 GeV/nuc. This suggests that our estimates for the statistical errors are slightly pessimistic, which is acceptable and consistent with our purpose.

The other trend that we observe in figure 3.7 is a shift in the preferred value of δ to increasingly lower values as we limit the analysis to increasingly higher energies.

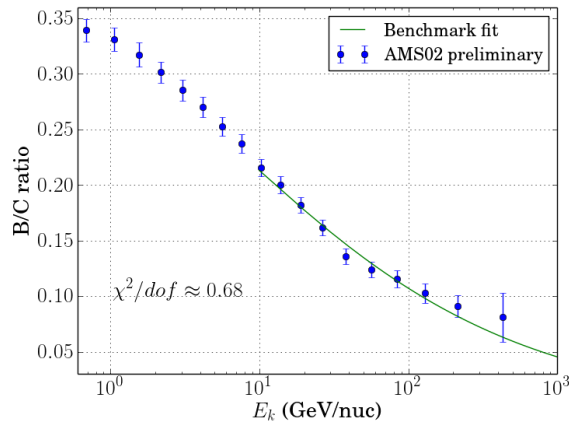


Figure 3.6: Preliminary AMS-02 measurements of the B/C ratio [33rd Intern. Cosmic Ray Conf. 2013] are plotted as a function of kinetic energy per nucleon. The theoretical prediction of the 1D/slab reference model of table 3.1 is also featured for comparison.

This is no limitation of our procedure. On the contrary, it is a real feature that the data exhibit, as is clear in figure 3.6, where the tail of the B/C points does look flatter above 50 GeV/nuc. The anti-correlation between δ and D_0 that we observe in figure 3.7 has already been explained by the interplay of these two parameters inside the diffusion coefficient D , to which the B/C ratio is sensitive. The increase of D_0 is then generic and does not signal any new effect. At that stage, the statistical uncertainties are still of the same order as the systematic uncertainties generated by using different energy cuts. Should the decrease of δ with E_{cut} be confirmed with higher statistics, some intrinsic explanation might be necessary for the failure of a power-law fit. See for instance section 3.1.2.2 for a possible explanation.

3.1.2.2 Primary boron?

Typical fits of the B/C ratio are based on the assumption that no boron is accelerated at sources, so that the term proportional to Q_B at the right-hand side of equation (3.8) vanishes. However, this is just an assumption that needs to be tested empirically. It is crucially linked to the hypothesis that the acceleration time is much shorter than the propagation time within the magnetic halo and that it occurs in a low-density environment. On the other hand, typical astrophysical accelerators such as supernova remnants might have the capability to accelerate up to TeV energies for $t_{\text{life}} \sim 10^5$ years in an interstellar medium with $n_{\text{ISM}} \sim 1 \text{ cm}^{-3}$, or greater when surrounded by denser circumstellar material. The corresponding surface density $n_{\text{ISM}} c t_{\text{life}} \sim 10^{23} \text{ cm}^{-2}$ easily leads to percent-level probabilities for nuclei to undergo spallation in the sources. A factor of only a few times higher than this would certainly have dramatic consequences on the information inferred

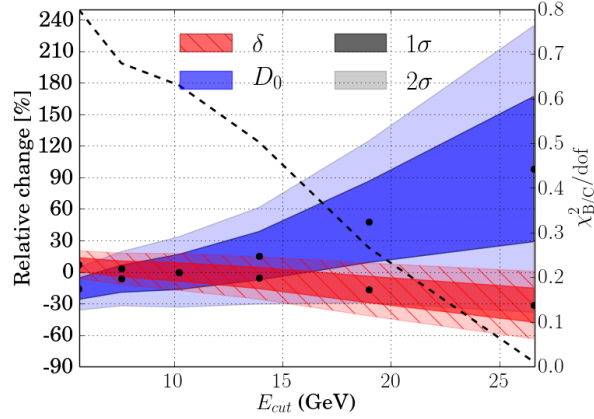


Figure 3.7: Relative variations of the best-fit propagation parameters, as compared to the benchmark model of table 3.1, with respect to the low-energy cut-off E_{cut} above which we carry out the B/C analysis.

from secondary-to-primary ratios. More elaborate versions of this idea and related phenomenology have also been detailed as a possible explanation of the hard spectrum of secondary positron data [Blasi 2009a, Blasi 2009b, Mertsch 2009], which was recently compared with the AMS-02 data [Mertsch 2014].

Apparently little attention has been paid to the bias introduced by the ansatz $Q_B = 0$. To the best of our knowledge, we quantify it here for the first time. As can be inferred from equation (3.8), in the presence of a primary source Q_B , the B/C ratio exhibits a plateau as soon as the cross-section ratio $\sigma_{C \rightarrow B}/(\sigma^{\text{diff}} + \sigma_B)$ becomes negligible with respect to the primary abundances ratio N_B/N_C . This happens at sufficiently high energy since σ^{diff} increases with the diffusion coefficient D . The height of this high energy B/C plateau is approximately given by the value of N_B/N_C . In the presence of this behaviour, the spectral index δ must increase to keep fitting the data at low energy, that is, here around 10 GeV/nuc. This also implies that D_0 decreases with N_B/N_C as a result of the above-mentioned anti-correlation between the diffusion parameters.

We have thus scanned the boron-to-carbon ratio at the source and studied the variations of the best-fit values of D_0 and δ with respect to the reference model of table 3.1. Our results are illustrated in figure 3.8, where the left panel features the confidence levels for δ (red) and D_0 (blue) as a function of the N_B/N_C ratio. The B/C fit is particularly sensitive to the last few AMS-02 points, notably the penultimate data point, around 214 GeV/nuc, for which the B/C ratio is found to be $\sim 9\%$. In the right panel, the theoretical expectation for that point is plotted (solid red curve) as a function of the primary abundances ratio, while the dashed black curve indicates how the goodness of fit varies. It is interesting to note that a minor preference is shown for a non-vanishing fraction of primary boron, around

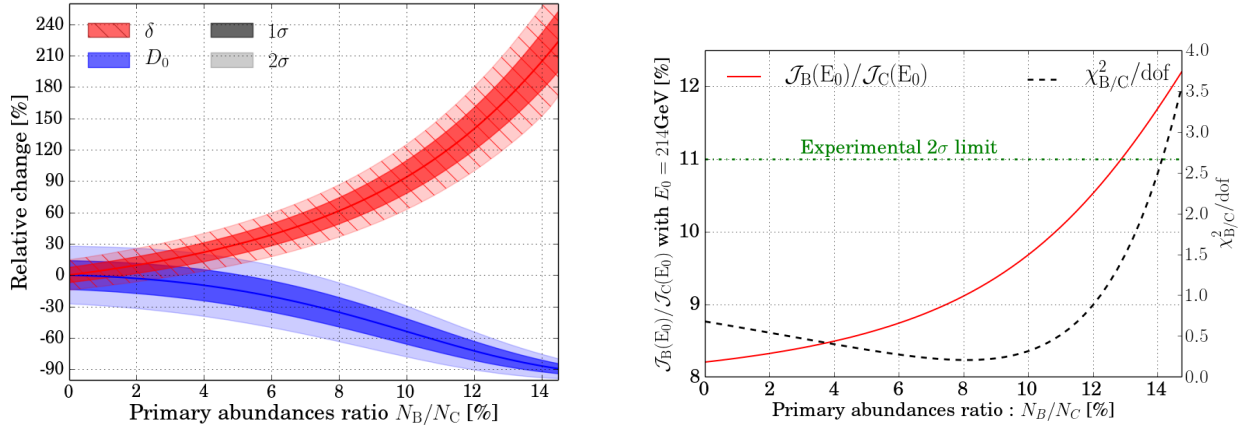


Figure 3.8: Left panel: variations of the best-fit propagation parameters D_0 (blue) and δ (red) relative to the benchmark values of table 3.1, as a function of the primary boron-to-carbon injection ratio. The reference model corresponds to the conventional no boron hypothesis for which N_B/N_C vanishes. Right panel: the theoretical value of the B/C ratio at 214 GeV/nuc (solid red curve) is plotted as a function of the primary boron-to-carbon injection ratio. The dashed black curve indicates the goodness of the B/C fit. As long as N_B/N_C does not exceed 13%, the theoretical B/C ratio is within 2 σ from the AMS-02 measurement (dashed-dotted green curve).

8%, due to the marginal preference for a flattening of the ratio already mentioned in the previous section. The N_B/N_C ratio is only loosely constrained to be below 13%. Such a loose constraint would nominally mean that a spectral index δ more than three times larger than its benchmark value would be allowed, with a coefficient D_0 one order of magnitude smaller than indicated in table 3.1. In fact, such changes are so extreme that they would clash with other phenomenological or theoretical constraints and should probably be considered as unphysical. A spectral index δ in excess of 0.9, corresponding to a relative increase of 100% with respect to our benchmark model, is already so difficult to reconcile with the power-law spectrum of nuclei and the present acceleration schemes that it would probably be excluded. The message is quite remarkable however. The degeneracy of the diffusion parameters with a possible admixture of primary boron is so strong that it dramatically degrades our capability of determining the best-fit values of D_0 and δ , and beyond them the properties of turbulence, unless other priors are imposed.

3.1.2.3 Cross-section modelling

The outcome of cosmic ray propagation strongly depends on the values of the nuclear production $\sigma_{b \rightarrow a}$ and destruction σ_a cross-sections with the ISM species,

mainly protons and helium nuclei. Some of these are measured, albeit in a limited dynamical range, while a significant number of them rely on relatively old semi-empirical formulae, calibrated to a few available data points. In this section, we discuss how parametric changes in these inputs reflect on the B/C ratio. The effect of cross-section systematics was already studied by [Maurin 2010], who parameterized it in terms of a systematic shift with respect to the energy. Since we consider here only the high energy limit, we simply allowed for a rescaling of the cross-sections. However, we distinguished between two cases: a correlated ($\nearrow \nearrow$) or anti-correlated ($\nearrow \searrow$) rescaling between the production $\sigma_{b \rightarrow a}$ and the destruction σ_a cross-sections. These in fact are not affected by the same uncertainties. It is often the case that the latter are known to a better precision than the former since they rely on a richer set of data. A priori, it is conceivable that several relevant production cross-sections might be varied independently. It is worth noting, however, that only a few nuclei – notably oxygen and carbon ($\sim 80\%$), and to a lesser extent nitrogen ($\sim 7\%$) – are in fact responsible for most of the produced boron, as shown in figure 3.9.

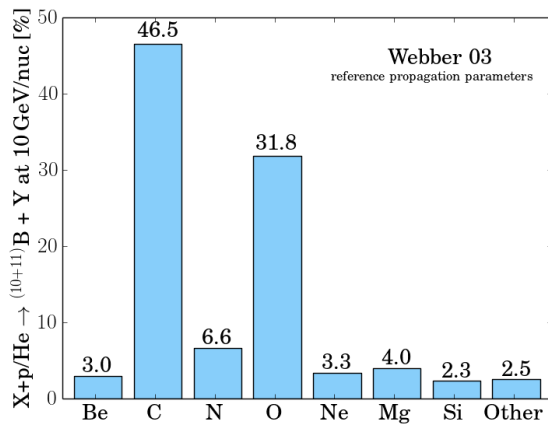


Figure 3.9: Contribution of the various primary nuclear species to the secondary boron flux at 10 GeV/nuc, as estimated with the semi-empirical code of Webber 03.

First, we need to assess the reasonable range over which the various cross-sections of the problem are expected to vary. For this, we compared our reference models for the destruction and production cross-sections with those used in popular numerical propagation codes such as GALPROP [Strong 2001] and DRAGON [Evoli 2008]³. The database implemented in these two codes traces back to the GALPROP team work and is based on a number of references including – but not limited to – Nuclear Data Sheets and Los Alamos database [Mashnik 1998] (see [Moskalenko 2001] and [Moskalenko 2003] for a more complete list of references). In this work we compare the values given directly by the default cross-section parameterizations without any renormalisation (which can be implemented however).

³Updated version of these two codes can be found at: <https://sourceforge.net/projects/galprop> and <http://www.dragonproject.org/Home.html>, respectively.

In the case of the destruction cross-sections σ_a , we compared our reference model [Tripathi 1997] with the parameterizations of [Barashenkov 1994], [Letaw 1983] and [Wellisch 1996]. The last case only applies to elements with $Z > 5$, while the [Letaw 1983] modelling is conserved for lighter nuclei. Figure 3.10 shows the relative differences between our reference model and the three other semi-empirical approaches and allows deriving an indicative lower limit on the systematic uncertainties for the destruction cross-sections of roughly 2 to 10% for the B/C ratio. The systematic difference is at the 3% level for the channels (CNO) that contribute most to secondary boron production. The difference to our reference model is stronger for larger charges ($Z > 10$), but these nuclei have a negligible contribution to the B/C ratio.

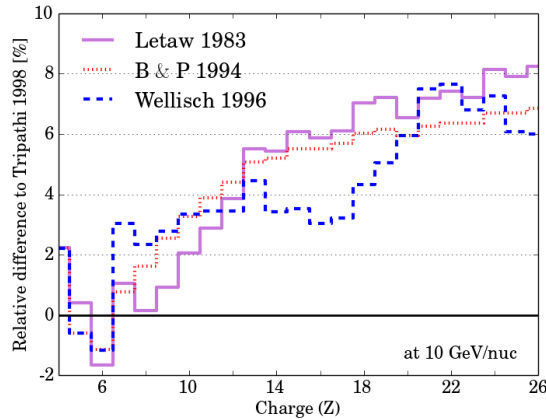


Figure 3.10: The relative differences between our reference model [Tripathi 1997] for the destruction cross-sections σ_a and the other parameterizations by Letaw 1983 [Letaw 1983], Wellisch 1996 [Wellisch 1996] and B&P 1994 [Barashenkov 1994] are displayed as a function of the nucleus charge, at an energy of 10 GeV/nuc. Each bin is characterised by a given charge Z and encodes the arithmetic mean over the corresponding isotopes. Only the elements involved in the cascade from iron to beryllium are displayed.

For the production cross-sections $\sigma_{b \rightarrow a}$, one may choose between the semi-empirical approach proposed by [Silberberg 1998], subsequently revised in 2000 and called here S&T 00, and the parameterization provided by [Webber 1990] (hereafter Webber 93) and its updates of 1998 [Webber 1998] and 2003 [Webber 2003]. We selected the last set of values as our reference model, to which we have compared the other parameterizations to gauge the uncertainties that affect, on average, the values of $\sigma_{b \rightarrow a}$. The relative differences between Webber 93, Webber 98, and S&T 00 with respect to Webber 03 are plotted in the form of the three histograms of figure 3.11. The charges of the parent and child nuclei are given on the vertical and horizontal axes. The most important reactions, whose cross-sections are higher, correspond to a change of charge ΔZ not in excess of 3 during the fragmentation

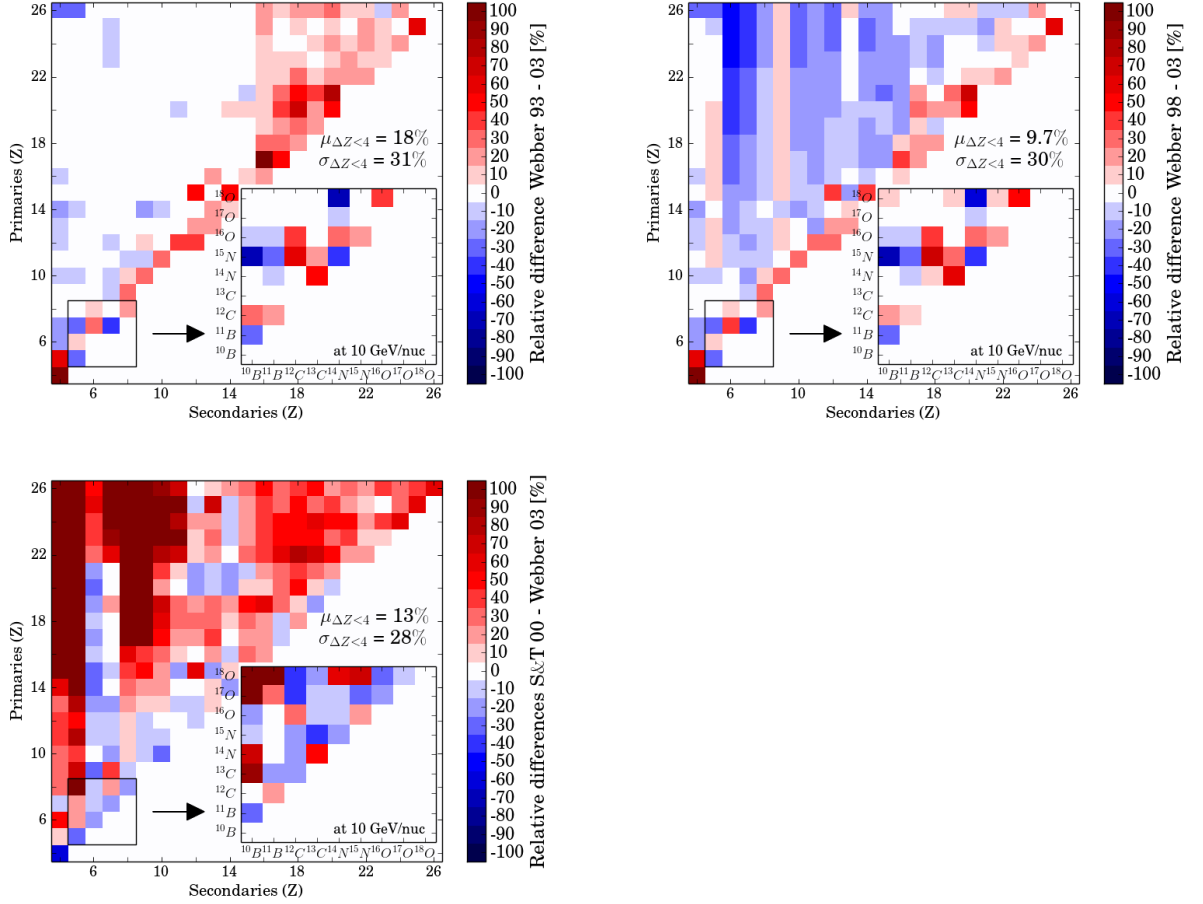


Figure 3.11: 2D histograms feature the relative differences between various semi-empirical models currently used to calculate the production cross-sections $\sigma_{b \rightarrow a}$. Our reference model is [Webber 2003] (Webber 03), and we compare it to the parameterizations from [Webber 1990] (Webber 93), [Webber 1998] (Webber 98) and [Silberberg 1998] (S&T 00). The charges of the parent and child nuclei are given on the vertical and horizontal axes, respectively. The relative difference in each bin is given by the arithmetic mean over the various isotopes of each element. A detailed view provides the most important channels for the B/C ratio studies. For a fragmentation of $\Delta Z < 4$, we also give the means and the variances of the uncertainty distributions.

process and are located close to the diagonals of the 2D-grids of figure 3.11. We first note that the Webber 93 and 98 production cross-sections are on average larger than the values of the Webber 03 reference model. Most of the pixels on the diagonals of the corresponding histograms are red, and we measured a mean excess μ on the reactions for which $\Delta Z < 4$ of 18% and 9.7% for Webber 93 and Webber 98 as compared to Webber 03. Furthermore, in both cases the dispersion of these differences is quite large and amounts to 31% for Webber 93 and 30% for Webber 98. A rapid comparison between S&T 00 and Webber 03 would also leave the impression that in the former case, the reactions in the upper left corner of the histogram have cross-sections exceedingly larger than for the Webber 03 parameterization. A close inspection along the diagonal indicates, on the contrary, that the S&T 00 values for $\Delta Z < 4$ are on average 13% higher than for the reference model, with a dispersion σ of 28% similar to the other cases. The main production channels of secondary boron are listed in table 3.2 and are also displayed in the expanded views of the small square regions that sit in the lower right corners of the histograms of figure 3.11. The most relevant reactions involve the stable isotopes of carbon, nitrogen, and oxygen fragmenting into ^{10}B and ^{11}B , and are indicated in boldface in table 3.2. The largest contributor to secondary boron is ^{12}C . The three semi-empirical models with which we compared our Webber 03 reference parameterization tend to predict production cross-sections that are 15% for S&T 00 to 25% for Webber 93 larger. In contrast, those models underpredict the spallation of ^{16}O by 10% in the case of Webber 93 and 98 to 18% for S&T 00. In the latter case, the production cross-section of ^{10}B from ^{14}N is 68% larger than for Webber 03. But nitrogen only contributes $\sim 7\%$ of the secondary boron, and this has no significant impact. To summarise, the production cross-sections $\sigma_{b \rightarrow a}$ can be varied up or down by a factor of order 10-20% with respect to Webber 03.

Main production channels	Webber 03 reference model (RM) [mb]	S&T 00 rel. difference to RM [%]	Webber 98 rel. difference to RM [%]	Webber 93 rel. difference to RM [%]
$\sigma_{\text{CNO} \rightarrow \text{B}}$ at 10 GeV/nuc				
$\sigma({}_6^{12}\text{C} \rightarrow {}_5^{10}\text{B})$	14.0	-2.14	21.8	25.4
$\sigma({}_6^{12}\text{C} \rightarrow {}_5^{11}\text{B})$	47.0	15.3	14.8	18.4
$\sigma({}_6^{13}\text{C} \rightarrow {}_5^{10}\text{B})$	4.70	92.0	-2.06	-0.03
$\sigma({}_6^{13}\text{C} \rightarrow {}_5^{11}\text{B})$	40.0	-20.6	2.21	4.20
$\sigma({}_7^{14}\text{N} \rightarrow {}_5^{10}\text{B})$	9.90	68.1	0.14	1.01
$\sigma({}_7^{14}\text{N} \rightarrow {}_5^{11}\text{B})$	27.2	1.33	-8.86	-11.0
$\sigma({}_7^{15}\text{N} \rightarrow {}_5^{10}\text{B})$	9.20	-6.55	-70.9	-70.7
$\sigma({}_7^{15}\text{N} \rightarrow {}_5^{11}\text{B})$	28.0	-0.33	-27.4	-27.9
$\sigma({}_8^{16}\text{O} \rightarrow {}_5^{10}\text{B})$	10.7	-18.0	-7.67	-8.85
$\sigma({}_8^{16}\text{O} \rightarrow {}_5^{11}\text{B})$	24.0	2.94	-9.36	-10.9
$\sigma({}_8^{17}\text{O} \rightarrow {}_5^{10}\text{B})$	3.60	124	0.27	-1.00
$\sigma({}_8^{17}\text{O} \rightarrow {}_5^{11}\text{B})$	19.7	27.3	1.42	-0.09
$\sigma({}_8^{18}\text{O} \rightarrow {}_5^{10}\text{B})$	0.70	545	4.43	4.48
$\sigma({}_8^{18}\text{O} \rightarrow {}_5^{11}\text{B})$	12.0	113	2.20	0.77

Table 3.2: Comparison between different cross-section parameterizations for the main production channels of secondary boron. The reference model used in our calculations is adapted from [Webber 2003] (Webber 03) and is compared to previous releases by [Webber 1990] (Webber 93) and [Webber 1998] (Webber 98) as well as to the work from [Silberberg 1998] (S&T 00). The dominant production channels, which involve the stable isotopes of carbon, nitrogen, and oxygen, are listed in boldface.

Varying the various production and destruction cross-sections has an effect on the calculation of the B/C ratio and thus affects the determination of the propagation parameters D_0 and δ . Before gauging this effect, we remark that secondary boron is essentially produced by CNO nuclei, as indicated in figure 3.9. These are essentially primary species for which \mathcal{J}_b is approximately given by the ratio $Q_b/(\sigma^{\text{diff}} + \sigma_b)$ and is proportional to the injection normalisation N_b . Furthermore, the relevant destruction cross-sections σ_C , σ_N and σ_O being approximately equal to each other, with an effective value ranging from 290 to 317 mb, we conclude that the flux ratios $\mathcal{J}_b/\mathcal{J}_C$ are given by the corresponding ratios N_b/N_C of the injection normalisation constants, with the consequence that relation (3.9) simplifies to

$$\frac{\mathcal{J}_B(E_k)}{\mathcal{J}_C(E_k)} \simeq \sum_{Z_b \geq Z_C}^{Z_{\text{max}}} \frac{\sigma_{b \rightarrow B}}{\sigma^{\text{diff}} + \sigma_B} \cdot \frac{N_b}{N_C}. \quad (3.14)$$

As mentioned at the beginning of this section, we first rescaled in our code all production $\sigma_{b \rightarrow a}$ and destruction σ_a cross-sections by the same amount κ , which ranges from 0 to 2, to study how D_0 and δ are affected by this change. The results are summarised in the left panel of figure 3.12.

The diffusion index δ does not suffer any change, whereas the diffusion normalisation D_0 increases linearly with the rescaling factor κ . Multiplying both $\sigma_{b \rightarrow B}$ and σ_B by the same factor κ in equation (3.14) amounts to dividing the diffusion cross-section σ^{diff} by κ . The B/C ratio depends then on the ratio $\sigma^{\text{diff}}/\kappa$, which scales as D_0/κ . The theoretical prediction on the B/C ratio is not altered as long as D_0/κ is kept constant, hence the exact scaling of D_0 with κ displayed in the left panel of figure 3.12. The energy behaviour of the B/C ratio is not sensitive to the rescaling factor κ , which has been absorbed by D_0 , and the fit yields the same spectral index δ irrespective of how much the cross-sections have been changed. Despite the relatively modest alterations, the effect discussed here has two qualitatively interesting consequences. To commence, a systematic uncertainty on the central value of D_0 at the 5 to 10% level seems unavoidable due to the current uncertainty level of about 10% on the nuclear cross-sections. Then, fully correlated changes in both production and destruction cross-sections can break the degeneracy between D_0 and δ .

We now analyse the effects of an anti-correlated change of the production $\sigma_{b \rightarrow a}$ and destruction σ_a cross-sections. Surprisingly, this has never been considered before, as far as we know, although the potential effect of this rescaling clearly is very strong. Multiplying $\sigma_{b \rightarrow B}$ by a factor κ while rescaling σ_B by a complementary factor of $(2 - \kappa)$ leads to the B/C ratio

$$\frac{\mathcal{J}_B(E_k)}{\mathcal{J}_C(E_k)} = \sum_{Z_b \geq Z_C}^{Z_{\text{max}}} \left\{ \frac{\sigma_{b \rightarrow B}}{(\sigma^{\text{diff}} + 2\sigma_B)/\kappa - \sigma_B} \right\} \frac{N_b}{N_C}. \quad (3.15)$$

Keeping the B/C ratio constant while increasing κ at a given energy translates into keeping the ratio

$$\frac{\sigma^{\text{diff}} + 2\sigma_B}{\kappa} = \frac{CE^\delta + 2\sigma_B}{\kappa} \quad (3.16)$$

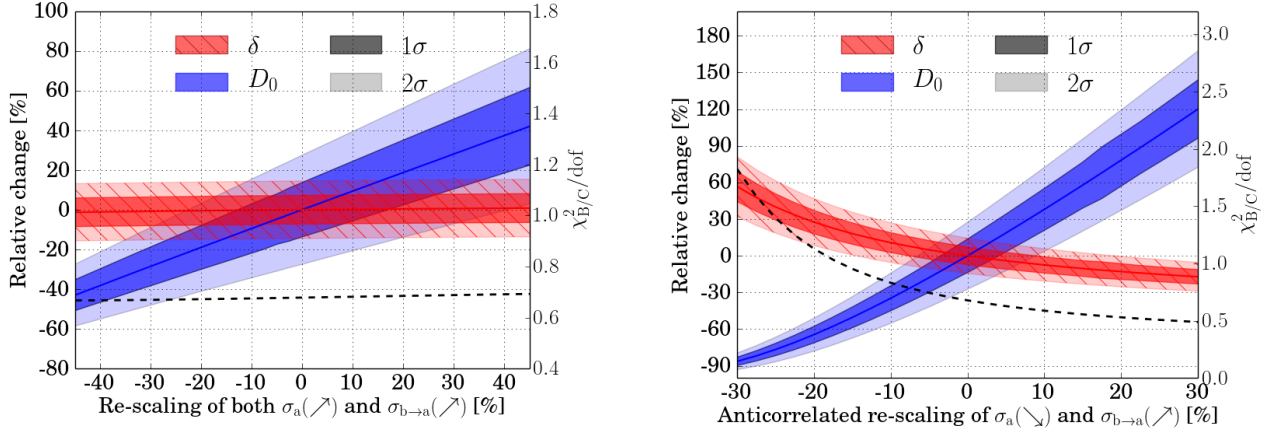


Figure 3.12: Effect of rescaling nuclear cross-sections for boron production channels and destruction ones: the left and right panels assume respectively correlated and anti-correlated rescalings.

roughly constant, where C is a constant directly proportional to D_0 . It can be immediately inferred that, when κ increases, C and D_0 have to increase and thus δ has to decrease. This trend is confirmed in the right panel of figure 3.12. From realistic assessments of the minimum systematic uncertainties of about 10% derived from the different cross-section models, we estimate a systematic uncertainty of 10% on δ and of 40% on D_0 .

3.1.2.4 Systematics related to CR propagation modelling

A significant effort has been made in recent years to provide increasingly sophisticated modelling of the CR diffusion environment, source distribution, and alternative forms of CR transport. In this section we discuss a perhaps surprising conclusion: these effects are less relevant for the prediction of B/C than the effects discussed previously (which are instead usually neglected)! The message is: although the efforts invested by the community in refining CR propagation modelling could have and have had important implications for other observables, for the mere purpose of fitting B/C to infer diffusion propagation parameters they are to a large extent unnecessary complications, until one can significantly reduce the biases previously discussed.

Geometric effects

The crude modelling of the diffusive halo as an infinite slab may appear too simplistic. In this section, we estimate the effects of a 2D cylindrical diffusion box, modelled as in figure 1.7. Furthermore, we assess the effect of adding a radial

dependence in the injection term, as opposed to the uniform hypothesis. These can be seen as upper limits to reasonable systematics due to simplified description of the spatial dependence of the diffusion medium or source term: given our limited knowledge on this subject, even the most detailed modelling of the propagation medium and source term, in fact, may not be fully realistic.

The formalism in such a situation is well known and we do not repeat it here (it has been summarised for instance in [Putze 2010a]). It suffices to say that to take advantage of the cylindrical symmetry, equation(1.121) can be projected on the basis of the zero order Bessel functions $J_0^i(r) = J_0\left(\xi_i \frac{r}{R_{gal}}\right)$ ensuring that the density vanishes on the edge of the cylinder of radius $R_{gal} = 20$ kpc. The flux of an isotope is then the sum over all its harmonic components

$$\mathcal{J}_a(E_k, R_\odot) = \sum_i^\infty J_0\left(\xi_i \frac{R_\odot}{R_{Gal}}\right) \mathcal{J}_a^i(E_k). \quad (3.17)$$

The results, reported in table 3.3, allow us to draw a few conclusions:

- the presence of a new escape surface at $R_{gal} \simeq 20$ kpc is basically irrelevant: the best-fit δ and its error remain the same, with a statistically insignificant, 2% modification of the best-fit value of D_0 ;
- perhaps more surprisingly, even the replacement of a uniform source distribution with a commonly assumed donut distribution of the form [Yusifov 2004]

$$q(r) \propto \left(\frac{r + 0.55}{R_\odot + 0.55}\right)^{1.64} \exp\left(-4.01 \left(\frac{r - R_\odot}{R_\odot + 0.55}\right)\right) \quad (3.18)$$

has minor effects, a mere 1% modification in the best-fit determination of δ , and a $\sim 13\%$ lowering of the best-fit value of D_0 , still statistically insignificant (roughly a 1σ effect);

- since the goodness of fit is similar, the B/C observable is essentially insensitive to these improvements. Unless they are justified by the goal of matching or predicting other observables, the complication brought by the 2D modelling of the problem are unnecessary in achieving a good description of the data.

Convective wind

Although the high energy CR propagation is mostly diffusive, the advection outside the Galactic plane (for instance due to stellar winds) has a non-negligible effect, which we now quantify. We adopted the simplest model of constant velocity wind, directed outside the galactic plane, with magnitude u . Taking this effect into account, the 1D stationary propagation equation can be written as

$$\begin{aligned} & -\frac{\partial}{\partial z} \left(D \frac{\partial}{\partial z} \psi_a \right) + \frac{\partial}{\partial z} (u \psi_a) - \frac{\partial}{\partial E} \left(\frac{1}{3} \frac{du}{dz} E_k \frac{(E_k + 2m)}{E_k + m} \psi_a \right) \\ & + \delta(z) \sigma_a v \frac{\mu}{m_{ISM}} \psi_a = 2h\delta(z)q_a + \delta(z) \sum_{\substack{Z_b \geq Z_a \\ Z_b \leq Z_{max}}} \sigma_{b \rightarrow a} v \frac{\mu}{m_{ISM}} \psi_b. \end{aligned} \quad (3.19)$$

Geometry	Plane – 1D	Cylindrical – 2D homogeneous source distribution	Cylindrical – 2D realistic source distribution
D_0 [kpc ² /Myr]	$(5.8 \pm 0.7) \cdot 10^{-2}$	$(5.7 \pm 0.7) \cdot 10^{-2}$	$(5.0 \pm 0.6) \cdot 10^{-2}$
$\Delta D_0^{1D}/D_0^{1D}$	N/A	–2%	–13%
δ	0.441 ± 0.031	0.439 ± 0.031	0.445 ± 0.032
$\Delta \delta^{1D}/\delta^{1D}$	N/A	0%	+1%
$\chi_{B/C}^2/\text{ndof}$	$5.4/8 \approx 0.68$	$5.4/8 \approx 0.68$	$5.5/8 \approx 0.69$

Table 3.3: Results on the propagation parameters fitted on the B/C for different geometries.

The two new terms (second and third one on the LHS) account for the advection of the cosmic ray density and the adiabatic losses, respectively. A characteristic time of these two processes can be estimated inside the thin disk of matter:

$$\begin{aligned} \tau_{\text{advection}} &= \frac{h}{u} = \frac{0.1 \text{ kpc}}{20 \text{ km/s}} \\ &= 5 \cdot \left(\frac{h}{0.1 \text{ kpc}} \right) \cdot \left(\frac{20 \text{ km/s}}{u} \right) \text{ My}, \end{aligned} \quad (3.20)$$

and

$$\begin{aligned} \tau_{\text{adiabatic}} &= \left(\frac{1}{3} (\nabla u) \right)^{-1} \simeq 3 \frac{h}{u} \\ &\approx 15 \cdot \left(\frac{h}{0.1 \text{ kpc}} \right) \cdot \left(\frac{20 \text{ km/s}}{u} \right) \text{ My}. \end{aligned} \quad (3.21)$$

This means that adiabatic losses can be safely neglected compared to the typical diffusion time of

$$\begin{aligned} \tau_{\text{diffusion}}(\mathcal{R} > 10 \text{ GV}) &< \tau_{\text{diffusion}}(10 \text{ GV}) = \frac{h L}{D(10 \text{ GV})} \\ &= 0.4 \cdot \left(\frac{h}{0.1 \text{ kpc}} \right) \cdot \left(\frac{L}{4 \text{ kpc}} \right) \cdot \left(\frac{0.16 \text{ kpc}^2/\text{My}}{D} \right) \text{ My}. \end{aligned} \quad (3.22)$$

It is clear that our previous results provide a suitable first-order approximation at least at high energy, with the leading correction at energies near 10 GeV/n given especially by the advection. The adiabatic energy loss, instead, is several times smaller and can be safely ignored in the following.

The solution of equation (3.19) neglecting adiabatic losses has the same form of equation (3.1) for the flux of stable species, modulo the change

$$D \rightarrow D' = \frac{L u}{1 - \exp\left(-\frac{L u}{D}\right)}, \quad (3.23)$$

so that the behaviour of the solution smoothly interpolates between the convective timescale at low energy and the diffusive one at high energy: this can be simply

checked by neglecting the exponential with respect to unity for a high value of its argument, or Taylor-expanding it to first order in the opposite limit. This formula also suggests that, if one fits the data by neglecting the convective wind, one biases its result toward a lower value of δ , and a corresponding higher value of D , so to reproduce a flatter dependence with energy at low-energy as for the case described by equation (3.23), as illustrated in figure 3.13. Quantitatively, a variation of 15 km/s in u is roughly similar to a 1σ shift in the benchmark parameters. Note, however, that the goodness of the fit worsens, or in other words, high energy data are better described by a pure diffusive behaviour than by a convective-diffusive one. Overall, we conclude that these effects appear still somewhat less important in determining the diffusion parameters from high energy data than the role of primary boron or even cross-section uncertainties. While convection, adiabatic losses, reacceleration, etc. are important to account for when extending the analysis down to very low energies (sub-GeV/nuc) or in global analyses, they do not currently constitute the main limitations to the determination of D_0 or δ from high energy data.

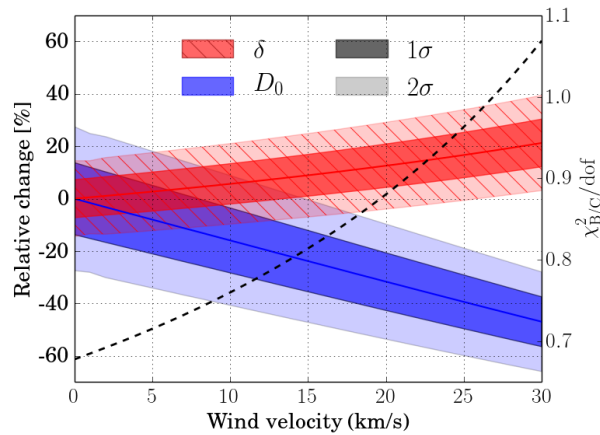


Figure 3.13: Variations of the best-fit propagation parameters with respect to the velocity of the convective wind.

3.1.2.5 Conclusion and prospects of this study

The high-precision measurements of cosmic ray fluxes that have become available in recent years prompt the question of the theoretical uncertainties inherent to the models used to interpret them. We have compared the effect of different theoretical biases with statistical uncertainties in the determination of diffusion parameters from the boron-to-carbon flux ratio, or B/C. This is representative of a much broader class of observables, involving ratios of secondary to primary species, which have been recognised as key tools for diagnostics in cosmic ray astrophysics. We adopted a pedagogical approach, showing and interpreting the results whenever possible within simple analytical models. We also used preliminary AMS-02 data

	Wind	1D/2D geometry	Cross-sections	Primary boron
$\Delta D_0/D_0$	-40%	-2 to -13%	$\pm 60\%$	0 to -90%
$\Delta\delta/\delta$	+15%	0 to +1%	$\pm 20\%$	0 to +100%

Table 3.4: Summary of the main systematics found in current analyses in determining the propagation parameters by fitting the B/C ratio.

and limited the analysis to energies above 10 GeV/nuc, which gives a pessimistic—hence conservative—estimate of the statistical uncertainties that will eventually be available.

Our main results, summarised in table 3.4, are the following:

- The single most important effect that we quantified (to the best of our knowledge, for the first time) is the degeneracy between diffusion parameters and a small injection of primary boron at the source, finding at present even a statistically insignificant preference for a small but finite value for a primary boron flux. This degeneracy cannot be removed by high-precision measurements of B/C, but probably requires multi-messenger tests and certainly demands further investigations, in particular if data should manifest a significant preference for a high energy flattening of secondary-to-primary ratios.
- The second most important theoretical uncertainty is associated to cross-sections. In particular, anti-correlated modifications in the destruction and production cross-sections with respect to reference values may also have an effect on the determination of the diffusion index δ , another effect discussed here for the first time. This should be kept in mind when comparing the outcome of data analyses relying on different databases for cross-sections. The good news is that this problem is not due to intrinsic limitations in the astrophysical modelling or the lack of astrophysical data, but to the scarce laboratory measurements available. For the case of boron, measurements of production cross-sections via spallation of oxygen, carbon and, to a minor extent, nitrogen, are essentially what would be needed to set the predictions on much firmer grounds. A motivated wish-list for such measurements is presented in section 3.2.2.3.
- The other effects which we tested are typically less important and are similar to or smaller than statistical uncertainties: effects such as those of convective winds, certainly important in more complete analyses including low-energy data, appear unlikely to bring uncertainties large enough to compete with the above-mentioned ones. We also showed how the geometry of the diffusive box and the distribution of sources is virtually irrelevant, at least if only a B/C data analysis is concerned. More or less realistic radial distribution of sources, while it may marginally affect the determination of D_0 , is still indistinguishable from the goodness-of-fit point of view. Another outcome of

this exercise is that at least at the 10% level, D_0 is degenerate with a choice of geometry and source distribution, in addition to the already well-known degeneracy with the diffusive halo height L .

In conclusion, we found that the main uncertainties in inferring diffusion parameters from B/C (and we expect from other secondary-to-primary ratios, too) depend on theoretical priors on sources (linked to sites and mechanisms of acceleration) and, to a lesser extent, to nuclear cross-sections. While exploring more complicated schemes and geometries for the diffusion may thus be important, we can anticipate that sensitivity to such effects will probably require fixing more mundane questions first. A multi-messenger strategy, coupled to a new measurement campaign of nuclear cross-sections, appears to be a next crucial step in that direction.

3.2 Propagation parameters extraction and AMS-02 new release

3.2.1 A review of previous analyses

In this section we briefly review former phenomenological studies extracting propagation parameters from a B/C ratio analysis. We also mention some other observables used both to check the consistency of the parameters found and to add other constraints.

3.2.1.1 B/C analyses

In the literature one can distinguish two kinds of analyses based either on a numerical resolution of the propagation, or on the chosen method of this thesis which uses a semi-analytical resolution. We restrict this review to homogeneous diffusion, and place more emphasis on the different methodologies rather than on the actual results.

Numerical approaches

Here we focus on two examples from recent studies. The first one was made by the DRAGON Team [Evoli 2015], while the other one is from GALPROP Team [Jóhannesson 2016]. These numerical codes deal with propagation by defining a discrete grid in phase-space. They are thus able to treat spatial dependent energy losses, convection, diffusion and, reacceleration, whereas the semi-analytical approach needs simplifications.

These two analyses do not have the same final goal: while the first was made to reestimate the antiproton astrophysical background, the other intends to challenge the homogeneous diffusion in the Galaxy. The methodologies to derive the propagation parameters are quite different and illustrate well the hypotheses commonly made. The main parameters we are interested in are related to the diffusion

coefficient whose generic form is the following:

$$K(\mathcal{R}) = K_0 \beta^\eta \left(\frac{\mathcal{R}}{\mathcal{R}_0} \right)^\delta. \quad (3.24)$$

In hindsight, we have summarized the important points of both of the analyses in a single table 3.5. Hereafter, we stress some similarities and differences between the two studies:

- One of the main difference between the two studies relies on the propagation model used: [Jóhannesson 2016] uses a pure diffusion-reacceleration model (so without convective wind), whereas [Evoli 2015] adds convection, and more precisely a convective gradient as a free parameter.
- In both analyses, the B/C ratio is not fitted alone, but in combination with other observables, notably the fluxes of some elements. Indeed, computing the B/C prediction requires to resolve the spallation network of heavier nuclei whose relative contributions are directly linked to the abundances of each element. The latter is fixed by a comparison to a chosen dataset, which can be included in the calculation of the goodness of fit. This approach is chosen by [Jóhannesson 2016], while [Evoli 2015] includes such a comparison in the fitting procedure but does not take the quality of this fit into account in the extraction of the propagation parameters from the B/C ratio. Surprisingly, in [Evoli 2015] the authors seem to neglect the production of boron from beryllium beta decay, which we find to be non-negligible in the overall production of boron.
- The two analyses are diverging on a crucial hypothesis: while [Jóhannesson 2016] assumes a universal injection power law for all the species (governed by the power law indexes $\gamma_0, \gamma_1, \gamma_2$), [Evoli 2015] lets the element slopes to vary freely. As we can guess with the simple expansion, equation 3.7, the two cases can lead to significant differences in the energy dependence of the species, and thus, of the B/C ratio.
- The CR injection spectrum is modeled as a broken power law, with different indexes below and above the breaks. The lowest rigidity break is known to be necessary in numerical diffusion-reacceleration models in order to compensate for the large bump at low rigidities, a consequence of the large Alfvén velocities needed to fit the B/C ratios below 1 GeV.
- Both analyses rely on the GALPROP cross-section dataset.
- Notice that in [Jóhannesson 2016], the halo size L is let free to vary. While we have seen that the B/C ratio cannot constrain this parameter, the isotopic ratio $^{10}\text{Be}/^9\text{Be}$ is able to do so since typical decay time of ^{10}Be is of the order of the propagation time. However, with the current precision of this ratio,

[Jóhannesson 2016] is not very conclusive in constraining L . In [Evoli 2015], the authors claim that the observables they use are not sensitive to the halo size. Hence, they fix its value to 2 kpc, and give a renormalization law to deduce the value K_0 , once L is chosen.

- Concerning the numerical method used for the minimization, the neural network implemented in [Jóhannesson 2016] is much more costly in CPU time than the random sampling of [Evoli 2015], since its goal is to access the uncertainties of the parameters and not only the best fit.

A last remark interesting for the following, [Evoli 2015] provides us with a propagation model consistent with preliminary AMS-02 data: $(K_0, \delta, dV_c/dz, V_A) = (1.5 \times 10^{28} \text{cm}^2 \cdot \text{s}^{-1}, 0.42, 14 \text{km} \cdot \text{s}^{-1} \cdot \text{kpc}^{-1}, 27 \text{km} \cdot \text{s}^{-1})$.

Semi-analytical approaches

An alternative—which is also the option chosen in this thesis—consists in a semi-analytical treatment of the propagation. The main difference between this approach and the numerical one lies on the modelling of convection, reacceleration, and on the gas distribution. In the semi-analytical approach, the gas distribution is homogeneously spread inside the Galactic disk considered to be infinitesimally thin. Thus, all the energy losses are pinched inside the disk. Furthermore, the analytical simplifications require that convection is discontinuous across the disk, and that reacceleration is limited within the disk.

We focus on two studies: [Putze 2010b] is a dedicated Monte Carlo study which aims at providing the best propagation parameters and their uncertainties and, [Kappl 2015] whose final goal is, once more, the reevaluation of the antiproton background. As previously done, we report their main characteristics in table 3.6, and give some comments about similarities and differences.

- These two studies are using the same geometry (Slab) which does not take into account the radial boundary of the Galaxy. This approximation is fair for relatively small halo heights compared to their radius.
- The choice of these two analyses is to fit only the B/C ratio, while the other nuclei are fixed independently.
- In fact, the main difference in the method comes from whether or not the hypothesis of universal injection for the nuclei is invoked. In [Putze 2010b], where this hypothesis is used, the only free parameter for each element spectrum is the normalization. The latter is fixed at the value of one single HEAO-3 data point. Instead, in [Kappl 2015] where such an hypothesis is not used, the nuclei fluxes are fitted first and demodulated to obtain their actual values in the interstellar medium.

Paper	[Evoli 2015]	[Jóhannesson 2016]
Code	DRAGON	GALPROP
Minimization method	Random sampling of the parameter space	Neural network
Cross-section dataset	GALPROP XS (option ?)	GALPROP XS (option ?)
Fitted data	PAMELA for B/C, C and H	ACE/HEAO3/CREAM for B/C + [B,Si] + ISOMAX for $^{10}\text{Be}/^9\text{Be}$
Nuclei data	CREAM data, $M_i \geq M_C$, $E_{kn} > 10\text{GeV/nuc}$, (γ_i, q_i)	Fitted
Solar Modulation	HelioProp	HelMod
Spectrum for nuclei (injection)	$\mathcal{Q}^p \propto q_i \left(\frac{\mathcal{R}}{\mathcal{R}_0}\right)^{-\gamma_i}$	$\mathcal{Q}^p \propto q_i \left(\frac{\mathcal{R}}{\mathcal{R}_1}\right)^{-\gamma_0} \mid \left(\frac{\mathcal{R}}{\mathcal{R}_1}\right)^{-\gamma_1} \mid \left(\frac{\mathcal{R}}{\mathcal{R}_2}\right)^{-\gamma_2}$
Spectrum for protons	$\mathcal{Q}^p \propto q_i \left(\frac{\mathcal{R}}{\mathcal{R}_0}\right)^{-\gamma_p} \mid \left(\frac{\mathcal{R}}{\mathcal{R}_1}\right)^{-\gamma_p+\delta_p}$	NA
Free parameters	$\eta, K_0, \delta, dV_c/dz, V_A$	$K_0, \delta, V_A, \gamma_0, \gamma_1, \gamma_2, \mathcal{R}_1, L$
Parameters' units	$(-, 10^{28}\text{cm}^2.\text{s}^{-1}, -, \text{km}.\text{s}^{-1}.\text{kpc}^{-1}, \text{km}.\text{s}^{-1})$	$(10^{28}\text{cm}^2.\text{s}^{-1}, -, \text{km}.\text{s}^{-1}, -, -, \text{GV}, \text{kpc})$
Fixed parameters	$L = 2\text{kpc}, \mathcal{R}_0 = ?\text{GV}$	$\eta = 1, \mathcal{R}_0 = 4\text{GV}, \mathcal{R}_2 = 220\text{GV}$
Best fit parameters	$(-, 1.6, 0.41, 1.6, 8.5)$	$(9.0, 0.38, 30, 2.02, 2.55, 2.20, 16.7, 10.3)$
Uncertainties of the fit	NA	Provided
Best $\chi^2/ndof$	not given	not given

Table 3.5: Summary of recent B/C analyses using a numerical resolution of the propagation equation. The exponents p and E for the injection spectrum specify if it is given in units of momentum or energy. The vertical bars | between the different parts of the source term mean that the function is piecewise defined.

- As mention previously, a probable caveat of [Kappl 2015], is not to account for the production of boron through beryllium beta decay, which is relatively important at low energies compared with the current precision of the data.

Paper	[Putze 2010b]	[Kappl 2015]
Code	USINE	Mathematica Program
Minimization method	Monte Carlos Markov Chain	Random sampling
Cross-section dataset	WEBBER 2003	WEBBER 2003
Fitted data	CREAM, ACE, HEAO-3 for B/C	Preliminary B/C AMS-02 data
Nuclei data	HEAO-3 data [Be to Si] at $E_{kn} = 10.6\text{GeV/nuc}$, (γ_i, q_i)	Preliminary fit of [C, N, O, Ne, Mg, Si] ACE, PAMELA, HEAO3, CREAM-II
Solar Modulation	Force field	Force field
Spectrum for nuclei (injected propagated)	$Q^E \propto q_i \beta^{-1} \left(\frac{\mathcal{R}}{\mathcal{R}_0}\right)^{2.65-\delta}$	$\psi^E \propto a_i E_k^{-\gamma_i} \left(\frac{E_k}{E_k + b_i}\right)^{c_i}$
Spectrum for protons	NA	NA
Free parameters	K_0, δ, V_A, V_C	K_0, δ, V_A, V_C, L
Parameters' units	(kpc ² .Myr ⁻¹ , -, km.s ⁻¹ , km.s ⁻¹ , kpc)	(kpc ² .Myr ⁻¹ , -, km.s ⁻¹ , km.s ⁻¹ , kpc)
Fixed parameters	$L = 4, \eta = 1, \mathcal{R}_0 = 1\text{GV}$	$\eta = 1, \mathcal{R}_0 = 1\text{GV}$
Best fit parameters	(0.0048, 0.86, 38, 18.8)	(0.0967, 0.408, 31.9, 0.2, 13.7)
Uncertainties of the fit	Provided	NA
Best $\chi^2/ndof$	1.47	1.2

Table 3.6: Summary of recent B/C analyses using semi-analytical resolution of the propagation equation. The exponent E for the injection spectrum specify that it is given in units of energy.

In this case study, beyond the numerical vs semi-analytical division, we see that there is no unified approach to the problem. This reveals our still partial understanding of the physics of production and propagation of CRs, and results in different analysis choices and hypotheses. To start with, it is not yet clear which mechanism dominates the propagation, and if some ingredients (e.g. including or not convective wind) should be neglected. Whether or not a universal injection law

should be used is not consensual, either. In that sense strong differences in the chosen source term are observed. Concerning the inputs, the number of available data is large, but the B/C analysis needs to combine the datasets of several experiments to be complete. Including all or part of the data in the overall goodness of fit, is one of the choices of the analysis. Finally, another very important ingredient is the cross-section dataset, on which secondary predictions crucially depends.

Obviously, all these differences result in different outcomes, sometimes incompatible within the error bars while using the same dataset. This last statement is even truer, as the precision of the data is increasing. Eventually, we believe that a systematic comparison of the different techniques, notably between the two methods of resolution (numerical and semi analytical), taking care of using the same physical inputs, would be a useful task to reveal their limits and their areas of agreement.

3.2.1.2 Complementary constraints

In this section we give a short overview of other observables also used to constrain the propagation parameters. As stressed in the introduction, these observables must be secondary particles.

Antiprotons:

Although they are one of the preferred target to look for new physics, CRs antiprotons are, in the energy range probed by current experiment, mostly secondary particles. As boron and carbon, antiprotons can give us clues about propagation scenarios, if their study is combined with the one of some primary particles, for example protons, their main progenitors. For instance, in [Jóhannesson 2016], the authors assume antiprotons to be pure secondary particles and include the quality of the fit of proton and helium nuclei in the overall goodness of fit. Then, they use the same algorithm as for the B/C case, to find the best propagation parameters and their uncertainties. Their study reveals some incompatibilities with respect to the propagation parameters derived with the B/C ratio, giving hints for non-homogeneous diffusion. Indeed, light nuclei (as antiprotons, protons and, helium) are probing a larger diffusion volume than heavier species which fragment earlier in their trip because of their larger destruction cross-section. This fact was studied for example in [Taillet 2003] from which figure 3.14 is extracted. Note that the volume of the sources accounting for 99% of the CR protons detected at Earth is much wider than the one of CR iron sources⁴. The conclusions of this study are corroborated by a more recent paper [Korsmeier 2016].

Positrons:

⁴Incidentally, this illustrates that CRs detected at the Earth come from sufficiently far sources that can be considered at first approximation as homogeneous. Furthermore, as a corollary of the finite scope of diffusion and source homogeneity, this figure gives a qualitative argument to extend the disk geometry to an infinite plane.

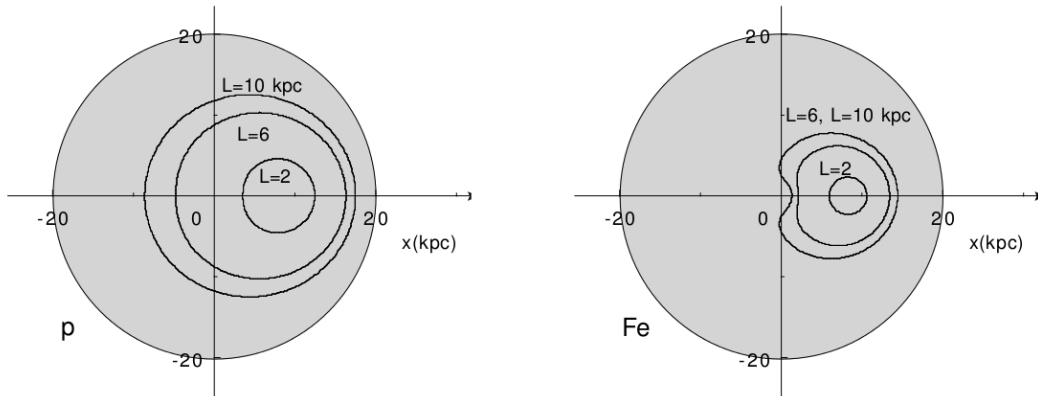


Figure 3.14: Contours containing the sources accounting for 99% of the CRs detected at the Earth. Several values of the magnetic halo size L are considered. The cases of protons (left) and iron (right) are displayed. Extracted from [Taillet 2003].

Until the discovery of a high energy excess, positrons have been thought for a long time as being pure secondary particles. Although its secondary component tends to be forgotten behind the excitement of such discovery, positrons still carry a wealth of information on propagation properties. In fact, as noticed in Lavalley 2014, in many propagation models compatible with the B/C ratio (especially those with a small halo size), pure secondary predictions of the flux at the lowest energies (typically below 4 GeV) are not in deficit but rather *in excess* with respect to measurements. This observation has been shown to yield a useful complementary constraint on the propagation parameters. Indeed, since the flux of secondary positrons scales as the ratio of the production volume over the diffusion one, leading to $1/\sqrt{K_0}$ dependency, the well-known degeneracy K_0/L introduced by secondary-to-primary ratio studies can be lifted. However, in order to use this complementarity, one needs in practice to be able to compute accurately the positron spectrum at the lowest energies, despite the presence of DR, convection, and disc energy losses. In Lavalley 2014, a qualitative trick is used: it is argued that the inclusion of DR would lead to the formation of a bump around 1 GeV which tends to *increase* the flux with respect to cases in which it is neglected, thus leading to a predicted flux in excess of the data.

In the recent study [Boudaud 2016], we devise a new semi-analytical method to take into account transport processes so far neglected, but important below a few GeV. It is essentially based on the pinching of inverse Compton and synchrotron energy losses from the magnetic halo, where they take place, inside the Galactic disc. The corresponding energy loss rate is artificially enhanced by the so-called pinching factor which needs to be calculated at each energy. Armed with this method, we recompute the constraints of Lavalley 2014 with i) our full resolution method at low energy, and ii) updated fluxes measured by AMS-02. This leads to more robust and more stringent constraints on the propagation parameters. For example we are able

to rule out conservatively 1569 models out of the 1623 selected by the B/C analysis of [Maurin 2001]. We find that only models with large diffusion coefficients (and so large halo size L) are selected by this test, thus excluding small halo sizes. This is discussed in details in section 4.3.

In relation with the points highlighted in the previous section, such analyses may also care about the variable diffusion volume probed by positrons with respect to their energy.

The two examples of positrons and antiprotons are not the only observables that can deliver complementary information about the propagation scenarios. The measurement of peculiar radioisotopes (so-called CR clocks, see section 1.1.2.1), or light isotopes (e.g. [Coste 2012]), could also provide constraints that can lift intrinsic degeneracies of the B/C analysis. On the electromagnetic side, synchrotron radio emission [Fornengo 2014, Orlando 2013, Bringmann 2012, Di Bernardo 2013] and gamma rays [Ackermann 2012] are also frequently invoked as a probe of the Galactic distribution of the CR density. A comprehensive analysis of the propagation should take into account those different constraints.

3.2.2 AMS-02: preliminary analysis

In this section we present the first steps of an analysis for the latest release of the B/C ratio by AMS-02 [Aguilar 2016]. This analysis uses the semi-analytical code USINE whose general description can be found for example in [Putze 2010b]. As previously noticed, one of the underlying default hypotheses of this code is to assume that all the primary species are injected with the same power law: the so-called universality hypothesis.

3.2.2.1 Quality of the data

In its publication, the AMS-02 collaboration provides two sets of data for the B/C ratio. The first in units of rigidity and the second in unit of kinetic energy per nucleon. As the detector actually measures the rigidity of the particles, the kinetic energy per nucleon needs to be reconstructed from an estimate of the isotopic abundances. Hence in [Aguilar 2016], the fraction of ^{13}C and ^{14}C is neglected, the fraction of ^{11}B is estimated to be 0.7 ± 0.1 of the total abundance of boron (made of ^{10}B and ^{11}B). The latter uncertainty is propagated in the systematic uncertainty, and reaches a level of 36% of the total uncertainty at the energy of 12 GeV, and 20% in average. We readily conclude that the best constraints will be obtained by adjusting the B/C ratio on the data given in rigidity. To test the actual effect of the two datasets on the propagation parameter extraction, we use USINE to fit the B/C ratio, setting $L = 5$ kpc, and $\Phi_{fisk} = 0.699$ GV, inspired by [Ghelfi 2016] as the average fisk potential over the data taking period. For this test, systematic and statistic uncertainties are added in quadrature. The results of these fits are displayed in table 3.7. Two remarks are in order: i) The fit using the B/C ratio in

units of kinetic energy per nucleon gives a much better χ_{ndof}^2 than the one using the data in rigidity, ii) The parameters δ and K_0 are incompatible within their error bars. While the first result is well understood because of the larger uncertainties of the data, the latter is less clear, and could stem from the existing correlations at different energies of this new uncertainty. In any case, in the light of this simple fit, we strongly advocate to use the data in units of rigidity, which is what actually measures the AMS-02 experiment.

Fit in:	χ_{ndof}^2	δ	K_0 [kpc ² /Myr]	V_a [km/s]	V_c [km/s]	Φ_{fisk} [GV]
R	103.0/(67 - 4) \approx 1.63	0.60 ^{+0.017} _{-0.016}	0.0188 ^{+0.0015} _{-0.0016}	2.17 ^{+5.49} _{-2.17}	6.7 ^{+0.68} _{-0.72}	0.699
Ek/n	54.0/(67 - 4) \approx 0.86	0.53 ^{+0.021} _{-0.020}	0.0285 ^{+0.003} _{-0.003}	0.1 ⁺²¹ _{-0.1}	4.5 ^{+1.1} _{-0.9}	0.699

Table 3.7: Best fit of the AMS-02 B/C data in rigidity and in kinetic energy per nucleon obtained by USINE. The free parameters are (K_0, δ, V_a, V_c)

3.2.2.2 Preliminary tests

Before lending any credibility to the benchmark model fitted in table 3.7 on the B/C data in rigidity, some tests are necessary. In particular one may wonder if the chosen universal injection slope has an impact on the outcome, or not. Having a look at the high energy general formulae of the flux (equation 3.1), it is straightforward to infer that the dependence in \mathcal{R}^α is factorisable, and so disappears in the B/C ratio. Thus, different choices for α should not affect too much the determination of the *high energy* parameters. However, the solution at lower energy stemming from the differential equation 1.123, may influence the best choice for the *low energy* parameters with the present precision of the data. Figure 3.15, displays the best fit values of the propagation parameters for three different values of α . The error bars show the statistical error coming from the uncertainty of the data. As these latter are always larger than the drift of the parameters with α , we conclude that the results of a B/C analysis under the universality hypothesis are insensitive to the chosen value of α .

A similar study, about the dependence on the halo size L , is also performed. Indeed, the choice of $L = 5$ kpc could bias the resulting values of the parameters, since a small fraction of radioisotopes could lift the degeneracy K_0/L already discussed. The results displayed in figure 3.16 show the variation of the parameters for different values of L . Once more, the error bars enclose the mild variations of the best fit values, provided that $L > 3$ kpc. Actually, we have seen that lower values of L are excluded by low energy positrons Lavalley 2014 (or gamma rays [Ackermann 2012]), thus we conclude that the physical value chosen for L does not affect the outcome, either.

Other tests on the fitting procedure itself (notably on the normalization of the element fluxes), but also other dependencies (such as solar modulation) will be performed to check the robustness of our results.

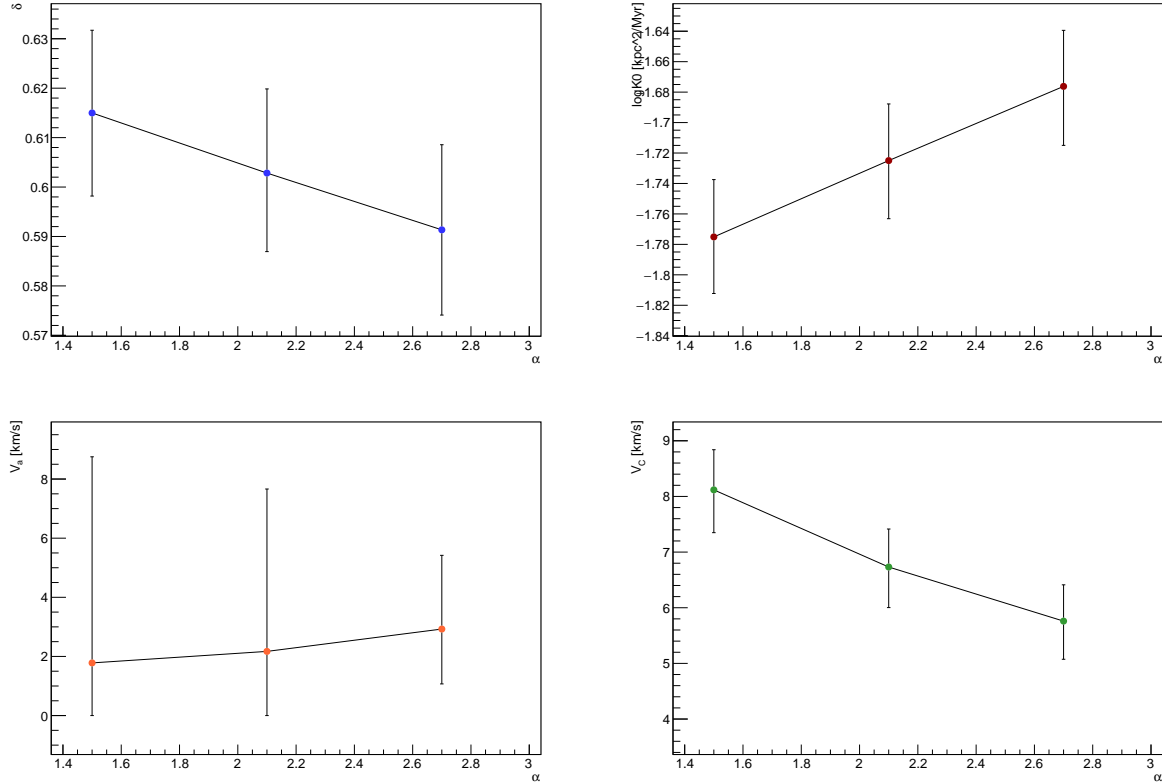


Figure 3.15: Best fit values resulting from the fit of the AMS-02 B/C ratio in rigidity for several values of the universal injection index α . Error bars show the associated statistical uncertainties.

3.2.2.3 Cross-section effects

Cross-section datasets and AMS-02 release

As argued previously, one of the most important ingredients in the prediction of the B/C ratio is the adopted production cross-section datasets which can dramatically impact the result of the fit (see e.g. [Maurin 2010]). The reader should see this part as an application of section 3.1.2.3, using up to date data from AMS-02. As mentioned in the introduction, several cross-section datasets are publicly available. For the sake of clarity, we select three of them and compare the differences in the outcomes. The chosen datasets are the following:

- **Webber 2003:** extracted from [Webber 2003]. This set is the default choice

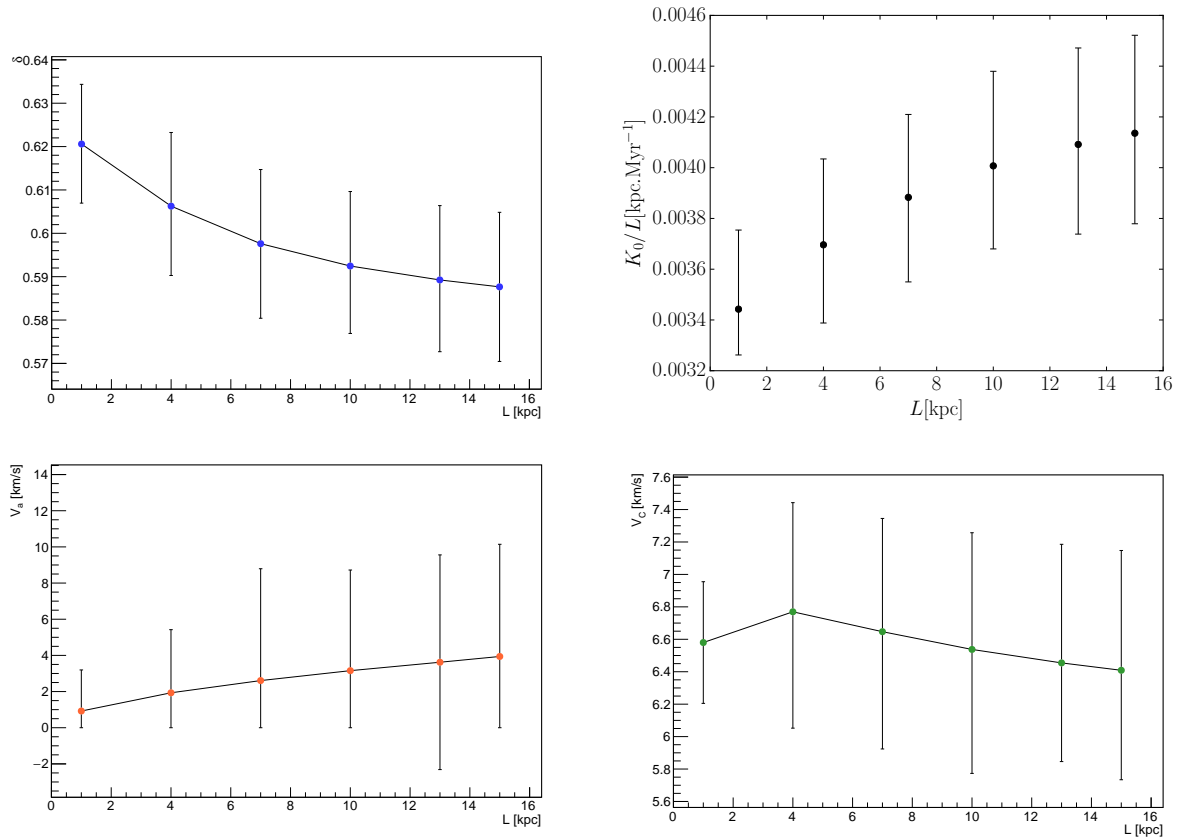


Figure 3.16: Best fit values resulting from the fit of the AMS-02 B/C ratio in rigidity for several values of the magnetic halo size L . Error bars show the associated statistical uncertainties.

of USINE.

- **Galprop 12:** option of the Galprop code which uses numerical tables first, then if no data are available, it uses a custom fit of cross-section data, otherwise it uses the code of Webber 1993 [Knott 1993] as default, and renormalized to the available data.
- **Galprop 22:** basically the same option as the previous one, except that it uses the code of Silberberg and Tsao [Silberberg 1998] as default instead of Webber 1993.

The results of the best fit parameters are shown in table 3.8. The different datasets of Webber 2003 and Galprop lead, after the fit, to incompatible propagation parameters within their one sigma confidence intervals. However, no real difference is seen for the propagation parameters extracted from the two Galprop datasets. They are compatible at the level of one sigma for all the parameters except K_0 and V_C . Thus, the effective effect of changing from one to the other, is close to a simple

renormalization of the B/C ratio. To illustrate this fact, we show in figure 3.17 the effect of changing the cross-section dataset among the chosen ones, while fixing the propagation parameter values to the result of the fit using Webber 2003.

XS set :	χ^2_{ndof}	δ	K_0 [kpc ² /Myr]	V_a [km/s]	V_c [km/s]	Φ_{fisk} [GV]
Webber 2003	103.0/(67 - 4) \approx 1.63	0.60 ^{+0.017} _{-0.016}	0.0188 ^{+0.0015} _{-0.0016}	2.17 ^{+5.49} _{-2.17}	6.7 ^{+0.68} _{-0.72}	0.699
Galprop 12	89.1/(67 - 4) \approx 1.41	0.55 ^{+0.003} _{-0.007}	0.0292 ^{+0.0006} _{-0.0007}	2.1 ^{+5.0} _{-2.1}	6.8 ^{+0.44} _{-0.45}	0.699
Galprop 22	83.7/(67 - 4) \approx 1.33	0.54 ^{+0.015} _{-0.015}	0.0326 ^{+0.0027} _{-0.0025}	2.6 ^{+5.7} _{-2.6}	2.1 ⁺¹ ₋₁	0.699

Table 3.8: Fit of the AMS-02 B/C data in rigidity obtained by USINE, for several cross-section datasets

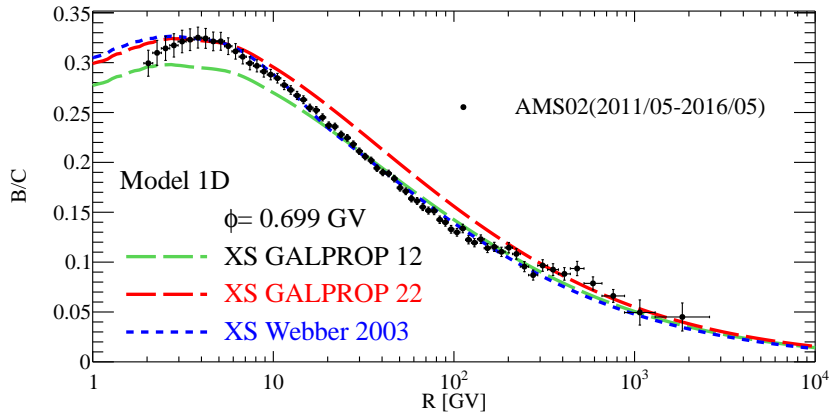


Figure 3.17: Boron to carbon ratio calculated by USINE with the propagation parameters of Webber 2003 table 3.8. The different colors correspond to the prediction using different production cross-section datasets.

The most important cross-sections

A precise measurements of spallation cross-sections is thus an inevitable task for whom wants to derive powerful constraints from these data. The aim of the conference *XSCRC2017: Cross-sections for Cosmic Rays* held at CERN last March, was to trigger the interest of the high energy physics community on this point, and hopefully, to initiate new measurement campaigns. Having a glance at the spallation network, this looks an extremely challenging goal since hundreds of reactions are involved, for example, in the production of boron. We have initiated a project with David Maurin to rank these cross-sections by decreasing contributing order, showing that only few dozens are actually accounting for *most* of the boron production. Table 3.9 shows such a ranking, and displays the reactions whose contributions

Energy	1 GeV/nuc		10 GeV/nuc	
1 step	74.6%		80.6%	
2 steps	19.4%		15.9%	
>2 steps	6%		3.5%	
>1%	$^{11}\text{B} \leftarrow ^{12}\text{C}$	33%	$^{11}\text{B} \leftarrow ^{12}\text{C}$	32.4%
	$^{11}\text{B} \leftarrow ^{16}\text{O}$	15.9%	$^{11}\text{B} \leftarrow ^{16}\text{O}$	18.8%
	$^{10}\text{B} \leftarrow ^{12}\text{C}$	10.3%	$^{10}\text{B} \leftarrow ^{12}\text{C}$	10.4%
	$^{10}\text{B} \leftarrow ^{16}\text{O}$	7.4%	$^{10}\text{B} \leftarrow ^{16}\text{O}$	9.0%
	$^{10}\text{B} \leftarrow ^{11}\text{B} \leftarrow ^{12}\text{C}$	3.0%	$^{10}\text{B} \leftarrow ^{11}\text{B} \leftarrow ^{12}\text{C}$	2.3%
	$^{11}\text{B} \leftarrow ^{12}\text{C} \leftarrow ^{16}\text{O}$	2.3%	$^{11}\text{B} \leftarrow ^{24}\text{Mg}$	1.8%
	$^{11}\text{B} \leftarrow ^{15}\text{N} \leftarrow ^{16}\text{O}$	2.2%	$^{11}\text{B} \leftarrow ^{12}\text{C} \leftarrow ^{16}\text{O}$	1.7%
	$^{10}\text{B} \leftarrow ^{11}\text{B} \leftarrow ^{16}\text{O}$	1.5%	$^{11}\text{B} \leftarrow ^{15}\text{N} \leftarrow ^{16}\text{O}$	1.6%
	$^{11}\text{B} \leftarrow ^{24}\text{Mg}$	1.4%	$^{11}\text{B} \leftarrow ^{14}\text{N}$	1.5%
	$^{11}\text{B} \leftarrow ^{14}\text{N}$	1.3%	$^{11}\text{B} \leftarrow ^{28}\text{Si}$	1.4%
	$^{11}\text{B} \leftarrow ^{14}\text{N} \leftarrow ^{16}\text{O}$	1.2%	$^{11}\text{B} \leftarrow ^{20}\text{Ne}$	1.4%
	$^{11}\text{B} \leftarrow ^{13}\text{C} \leftarrow ^{16}\text{O}$	1.1%	$^{10}\text{B} \leftarrow ^{11}\text{B} \leftarrow ^{16}\text{O}$	1.3%
	$^{11}\text{B} \leftarrow ^{20}\text{Ne}$	1.1%		
	$^{11}\text{B} \leftarrow ^{28}\text{Si}$	1.0%		
		# of reactions	Total	# of reactions
[0.1%, 1%]	28	7.2%	28	8.8%
[0.01%, 0.1%]	89	3.3%	90	3.5%
< 0.01%	276	0.7%	277	0.7%

Table 3.9: Ranking of the main contributing reactions to the boron amount in CRs using Webber 2003 cross-section dataset [Webber 2003]. One-step reactions correspond to the direct fragmentation of a nuclei into boron (either ^{11}B or ^{10}B), whereas n step reactions involve $n - 1$ intermediate species. Calculations made with USINE.

are above 1% of the total amount of boron. Such a ranking depends of course on the prior cross-section dataset used (in case of table 3.9, Webber 2003) and on the underlying propagation model. Using the latest AMS-02 B/C release, we have shown that, when the propagation model is derived consistently with the chosen cross-section dataset, the ranking is quite stable amongst the three datasets previously used. This result will soon be published in order to be included in high energy experiment proposals. We further argue that few percent uncertainties on these *most important cross-sections* are sufficient to obtain predictions reaching the level of the data uncertainties.

3.2.2.4 Evidence for a break in the diffusion coefficient

As noticed before, using the new B/C data from AMS-02 yields a low quality fit with a $\chi^2_{\text{ndof}} \approx 1.63$ and a p -value of 1.1×10^{-3} . Although this result could be interpreted as a lack of realism in the model used compared to the high quality

of the new data, one could hope that adding minimal ingredients may enhance significantly the quality of the fit.

As reminded in the introduction chapter, it has been recognized during the last decade that the CR spectra—of proton and helium, first—above the TeV energy were significantly harder than the ones computed within the 10 to 100 GeV range. Early hints of this change of behaviour were given by ATIC-2 [Panov 2009] and especially by CREAM [Yoon 2011], also extending to heavier nuclei, and seemingly confirmed by the new release of CREAM-III flight [Yoon 2017]. PAMELA [Adriani 2011] was the first experiment able to probe the transition between the two shapes, suggesting that the change of slope in protons and helium was not due to different detection technologies (and mutual systematics) between low and high energies. After the contradictory results in the preliminary AMS-02 proton data presented at the ICRC 2013, also AMS-02 has eventually confirmed—and greatly improved over—the results of the former experiments in [Aguilar 2015]. Phenomenologically, the high energy proton flux can be fit by a broken power law of the form:

$$\mathcal{J}_p \propto R^\gamma \left(1 + \left(\frac{R}{R_c} \right)^{-\Delta\gamma/s} \right)^s \quad (3.25)$$

Amongst the hypotheses suggested to explain this hardening, a change of slope in the diffusion coefficient is well motivated theoretically (see for example [Blasi 2012, Aloisio 2015]). Introducing the inverse of the second term of equation 3.25 (fixed by the AMS-02 proton flux) as a correction the diffusion coefficient, results in a much better quality of fit as shown table 3.10. The comparison between the two cases implies a $\Delta\chi^2 \approx 39$, with a *p-value* going from 1.1×10^{-3} (without break) to 0.41 (including the break). The computation of the χ^2 presented here, assumes that systematic uncertainties behave like statistical ones (gaussians and uncorrelated) and are thus summed in quadrature with these latter. A careful description of the errors will be soon released in a forthcoming paper to check quantitatively these differences.

This change of slope is actually well hidden by spallation effects in the quasi featureless tail of the B/C ratio. Indeed spallation is still an efficient process below ~ 200 GV (see figure 3.3), while above, the B/C tail follows the trend of the inverse of the diffusion coefficient. Although the presence of a break seems to be clearly hinted to by the data, its interpretation and actual value is no yet clear, as it could be the result of nested propagation effects. A dedicated discussion will be included in the forthcoming paper.

Form of $K(\mathcal{R})$:	χ_{ndof}^2	δ	K_0 [kpc ² /Myr]	V_a [km/s]	V_c [km/s]	Φ_{fisk} [GV]
$K_0 \mathcal{R}^\delta$	$103.0/(67 - 4) \approx 1.63$	$0.60^{+0.017}_{-0.016}$	$0.0188^{+0.0015}_{-0.0016}$	$2.17^{+5.49}_{-2.17}$	$6.7^{+0.68}_{-0.72}$	0.699
$K_0 \frac{R^\delta}{\left(1 + \left(\frac{R}{R_c}\right)^{-\Delta\gamma/s}\right)^s}$	$65.1/(67 - 4) \approx 1.03$	$0.705^{+0.003}_{-0.007}$	$0.0123^{+0.0006}_{-0.0007}$	$0.0^{+5.0}_{-0.0}$	$8.74^{+0.44}_{-0.45}$	0.699

Table 3.10: Fit of the AMS-02 B/C data in rigidity obtained by USINE, for two different dependences of the diffusion coefficient.

Bibliography

- [33rd Intern. Cosmic Ray Conf. 2013] Proc. 33rd Intern. Cosmic Ray Conf., editor. Precision Measurement of the Cosmic Ray Boron-to-Carbon Ratio with AMS [AMS collaboration], 2013. (Not cited.)
- [Ackermann 2012] M. Ackermann *et al.* *Fermi-LAT Observations of the Diffuse γ -Ray Emission: Implications for Cosmic Rays and the Interstellar Medium.* *Astrophysical Journal*, vol. 750, page 3, May 2012. (Not cited.)
- [Adriani 2011] O. Adriani, G. C. Barbarino, G. A. Bazilevskaya, R. Bellotti, M. Boezio, E. A. Bogomolov, L. Bonechi, M. Bongi, V. Bonvicini, S. Borisov, S. Bottai, A. Bruno, F. Cafagna, D. Campana, R. Carbone, P. Carlson, M. Casolino, G. Castellini, L. Consiglio, M. P. De Pascale, C. De Santis, N. De Simone, V. Di Felice, A. M. Galper, W. Gillard, L. Grishantseva, G. Jerse, A. V. Karelin, S. V. Koldashov, S. Y. Krutkov, A. N. Kvashnin, A. Leonov, V. Malakhov, V. Malvezzi, L. Marcelli, A. G. Mayorov, W. Menn, V. V. Mikhailov, E. Mocchiutti, A. Monaco, N. Mori, N. Nikonov, G. Osteria, F. Palma, P. Papini, M. Pearce, P. Picozza, C. Pizzolotto, M. Ricci, S. B. Ricciarini, L. Rossetto, R. Sarkar, M. Simon, R. Sparvoli, P. Spillantini, Y. I. Stozhkov, A. Vacchi, E. Vannuccini, G. Vasilyev, S. A. Voronov, Y. T. Yurkin, J. Wu, G. Zampa, N. Zampa and V. G. Zverev. *PAMELA Measurements of Cosmic-Ray Proton and Helium Spectra.* *Science*, vol. 332, page 69, April 2011. (Not cited.)
- [Aguilar 2015] M. Aguilar, D. Aisa, B. Alpat, A. Alvino, G. Ambrosi, K. Andeen, L. Arruda, N. Attig, P. Azzarello, A. Bachlechner and et al. *Precision Measurement of the Proton Flux in Primary Cosmic Rays from Rigidity 1 GV to 1.8 TV with the Alpha Magnetic Spectrometer on the International Space Station.* *Physical Review Letters*, vol. 114, no. 17, page 171103, May 2015. (Not cited.)
- [Aguilar 2016] M. Aguilar, L. Ali Cavasonza, G. Ambrosi, L. Arruda, N. Attig, S. Aupetit, P. Azzarello, A. Bachlechner, F. Barao, A. Barrau and et al. *Precision Measurement of the Boron to Carbon Flux Ratio in Cosmic Rays*

- from 1.9 GV to 2.6 TV with the Alpha Magnetic Spectrometer on the International Space Station. *Physical Review Letters*, vol. 117, no. 23, page 231102, December 2016. (Not cited.)
- [Aloisio 2015] R. Aloisio, P. Blasi and P. D. Serpico. *Nonlinear cosmic ray Galactic transport in the light of AMS-02 and Voyager data*. *A&A*, vol. 583, page A95, November 2015. (Not cited.)
- [Barashenkov 1994] V S Barashenkov and A Polanski. *Electronic guide for nuclear cross-sections: version 1994*. Technical report E2-94-417. JINR-E2-94-417, Joint Inst. Nucl. Res., Dubna, Oct 1994. (Not cited.)
- [Binns 2008] W. R. Binns, M. E. Wiedenbeck, M. Arnould, A. C. Cummings, G. A. de Nolfo, S. Goriely, M. H. Israel, R. A. Leske, R. A. Mewaldt, E. C. Stone and T. T. von Rosenvinge. *The OB association origin of galactic cosmic rays*. *New A Rev.*, vol. 52, pages 427–430, October 2008. (Not cited.)
- [Blasi 2009a] Pasquale Blasi. *The origin of the positron excess in cosmic rays*. *Phys.Rev.Lett.*, vol. 103, page 051104, 2009. (Not cited.)
- [Blasi 2009b] Pasquale Blasi and Pasquale D. Serpico. *High-energy antiprotons from old supernova remnants*. *Phys.Rev.Lett.*, vol. 103, page 081103, 2009. (Not cited.)
- [Blasi 2012] P. Blasi, E. Amato and P. D. Serpico. *Spectral Breaks as a Signature of Cosmic Ray Induced Turbulence in the Galaxy*. *Physical Review Letters*, vol. 109, no. 6, page 061101, August 2012. (Not cited.)
- [Boudaud 2016] M. Boudaud, E. F. Bueno, S. Caroff, Y. Genolini, V. Poulin, V. Poireau, A. Putze, S. Rosier, P. Salati and M. Vecchi. *The pinching method for Galactic cosmic ray positrons: implications in the light of precision measurements*. ArXiv e-prints, December 2016. (Not cited.)
- [Bringmann 2012] T. Bringmann, F. Donato and R. A. Lineros. *Radio data and synchrotron emission in consistent cosmic ray models*. *J. Cosmology Astropart. Phys.*, vol. 1, page 049, January 2012. (Not cited.)
- [Coste 2012] B. Coste, L. Derome, D. Maurin and A. Putze. *Constraining Galactic cosmic-ray parameters with $Z \leq 2$ nuclei*. *A&A*, vol. 539, page A88, March 2012. (Not cited.)
- [Di Bernardo 2013] G. Di Bernardo, C. Evoli, D. Gaggero, D. Grasso and L. Maccione. *Cosmic ray electrons, positrons and the synchrotron emission of the Galaxy: consistent analysis and implications*. *J. Cosmology Astropart. Phys.*, vol. 3, page 036, March 2013. (Not cited.)
- [Evoli 2008] C. Evoli, D. Gaggero, D. Grasso and L. Maccione. *Cosmic Ray propagation in the Galaxy and diffuse gamma-ray emission*. In F. A. Aharonian,

- W. Hofmann and F. Rieger, editors, American Institute of Physics Conference Series, volume 1085 of *American Institute of Physics Conference Series*, pages 380–383, December 2008. (Not cited.)
- [Evoli 2015] C. Evoli, D. Gaggero and D. Grasso. *Secondary antiprotons as a Galactic Dark Matter probe*. *J. Cosmology Astropart. Phys.*, vol. 12, page 039, December 2015. (Not cited.)
- [Fornengo 2014] N. Fornengo, R. A. Lineros, M. Regis and M. Taoso. *The isotropic radio background revisited*. *J. Cosmology Astropart. Phys.*, vol. 4, page 008, April 2014. (Not cited.)
- [Genolini 2015] Y. Genolini, A. Putze, P. Salati and P. D. Serpico. *Theoretical uncertainties in extracting cosmic-ray diffusion parameters: the boron-to-carbon ratio*. *A&A*, vol. 580, page A9, August 2015. (Not cited.)
- [Ghelfi 2016] A. Ghelfi, F. Barao, L. Derome and D. Maurin. *Non-parametric determination of H and He interstellar fluxes from cosmic-ray data*. *A&A*, vol. 591, page A94, June 2016. (Not cited.)
- [Jóhannesson 2016] G. Jóhannesson, R. Ruiz de Austri, A. C. Vincent, I. V. Moskalenko, E. Orlando, T. A. Porter, A. W. Strong, R. Trotta, F. Feroz, P. Graff and M. P. Hobson. *Bayesian Analysis of Cosmic Ray Propagation: Evidence against Homogeneous Diffusion*. *ApJ*, vol. 824, page 16, June 2016. (Not cited.)
- [Kappl 2015] R. Kappl, A. Reinert and M. W. Winkler. *AMS-02 antiprotons reloaded*. *J. Cosmology Astropart. Phys.*, vol. 10, page 034, October 2015. (Not cited.)
- [Knott 1993] C. N. Knott, S. Albergo, Z. Caccia, C. X. Chen, S. Costa, H. J. Crawford, M. Cronqvist, J. Engelage, P. Ferrando, I. Flores, R. Fonte, L. Greiner, T. G. Guzik, A. Insolia, F. C. Jones, S. Ko, C. Kuo, P. J. Lindstrom, J. Mazzotta, J. W. Mitchell, R. Potenza, J. Romanski, G. V. Russo, A. Soutoul, T. J. M. Symons, O. Testard, C. E. Tull, C. Tuve, C. J. Waddington, W. R. Webber, J. P. Wefel, L. Wu and X. Zhang. *Systematics elemental Production Cross Sections from Neon to Nickel*. *International Cosmic Ray Conference*, vol. 2, page 187, 1993. (Not cited.)
- [Korsmeier 2016] M. Korsmeier and A. Cuoco. *Galactic cosmic-ray propagation in the light of AMS-02: Analysis of protons, helium, and antiprotons*. *Phys. Rev. D*, vol. 94, no. 12, page 123019, December 2016. (Not cited.)
- [Lavalle 2014] J. Lavalle, D. Maurin and A. Putze. *Direct constraints on diffusion models from cosmic-ray positron data: Excluding the minimal model for dark matter searches*. *Phys. Rev. D*, vol. 90, no. 8, page 081301, October 2014. (Not cited.)

- [Letaw 1983] J. R. Letaw, R. Silberberg and C. H. Tsao. *Proton-nucleus total inelastic cross sections - an empirical formula for E greater than 10 MeV*. ApJS, vol. 51, pages 271–275, March 1983. (Not cited.)
- [Lodders 2003] K. Lodders. *Solar System Abundances and Condensation Temperatures of the Elements*. Apj, vol. 591, pages 1220–1247, July 2003. (Not cited.)
- [Mashnik 1998] S. G. Mashnik, A. J. Sierk, K. A. Van Riper and W. B. Wilson. *Production and Validation of Isotope Production Cross Section Libraries for Neutrons and Protons to 1.7 GeV*. ArXiv Nuclear Theory e-prints, December 1998. (Not cited.)
- [Maurin 2001] D. Maurin, F. Donato, R. Taillet and P. Salati. *Cosmic Rays below $Z=30$ in a Diffusion Model: New Constraints on Propagation Parameters*. ApJ, vol. 555, pages 585–596, July 2001. (Not cited.)
- [Maurin 2010] D. Maurin, A. Putze and L. Derome. *Systematic uncertainties on the cosmic-ray transport parameters. Is it possible to reconcile B/C data with $\delta = 1/3$ or $\delta = 1/2$?* A&A, vol. 516, page A67, June 2010. (Not cited.)
- [Maurin 2014] D. Maurin, F. Melot and R. Taillet. *A database of charged cosmic rays*. A&A, vol. 569, page A32, September 2014. (Not cited.)
- [Mertsch 2009] Philipp Mertsch and Subir Sarkar. *Testing astrophysical models for the PAMELA positron excess with cosmic ray nuclei*. Phys.Rev.Lett., vol. 103, page 081104, 2009. (Not cited.)
- [Mertsch 2014] P. Mertsch and S. Sarkar. *AMS-02 data confront acceleration of cosmic ray secondaries in nearby sources*. Prd, vol. 90, no. 6, page 061301, September 2014. (Not cited.)
- [Moskalenko 2001] I. V. Moskalenko, S. G. Mashnik and A. W. Strong. *New calculation of radioactive secondaries in cosmic rays*. International Cosmic Ray Conference, vol. 5, pages 1836–1839, August 2001. (Not cited.)
- [Moskalenko 2003] I. V. Moskalenko and S. G. Mashnik. *Evaluation of Production Cross Sections of Li, Be, B in CR*. International Cosmic Ray Conference, vol. 4, page 1969, July 2003. (Not cited.)
- [Orlando 2013] E. Orlando and A. Strong. *Galactic synchrotron emission with cosmic ray propagation models*. MNRAS, vol. 436, pages 2127–2142, December 2013. (Not cited.)
- [Panov 2009] A. D. Panov, J. H. Adams, H. S. Ahn, G. L. Bashinzhagyan, J. W. Watts, J. P. Wefel, J. Wu, O. Ganel, T. G. Guzik, V. I. Zatsepin, I. Isbert, K. C. Kim, M. Christl, E. N. Kouznetsov, M. I. Panasyuk, E. S. Seo, N. V. Sokolskaya, J. Chang, W. K. H. Schmidt and A. R. Fazely. *Energy spectra of*

- abundant nuclei of primary cosmic rays from the data of ATIC-2 experiment: Final results.* Bulletin of the Russian Academy of Sciences, Physics, vol. 73, pages 564–567, June 2009. (Not cited.)
- [Ptuskin 1997] V. S. Ptuskin, H. J. Voelk, V. N. Zirakashvili and D. Breitschwerdt. *Transport of relativistic nucleons in a galactic wind driven by cosmic rays.* A&A, vol. 321, pages 434–443, May 1997. (Not cited.)
- [Putze 2010a] A. Putze, L. Derome and D. Maurin. *A Markov Chain Monte Carlo technique to sample transport and source parameters of Galactic cosmic rays: II. Results for the diffusion model combining B/C and radioactive nuclei.* Astron.Astrophys., vol. 516, page A66, 2010. (Not cited.)
- [Putze 2010b] A. Putze, L. Derome and D. Maurin. *A Markov Chain Monte Carlo technique to sample transport and source parameters of Galactic cosmic rays. II. Results for the diffusion model combining B/C and radioactive nuclei.* A&A, vol. 516, page A66, June 2010. (Not cited.)
- [Silberberg 1998] R. Silberberg, C. H. Tsao and A. F. Barghouty. *Updated Partial Cross Sections of Proton-Nucleus Reactions.* ApJ, vol. 501, pages 911–919, July 1998. (Not cited.)
- [Strong 2001] A. W. Strong and I. V. Moskalenko. *Models for galactic cosmic-ray propagation.* Advances in Space Research, vol. 27, pages 717–726, 2001. (Not cited.)
- [Taillet 2003] R. Taillet and D. Maurin. *Spatial origin of Galactic cosmic rays in diffusion models. I. Standard sources in the Galactic disk.* A&A, vol. 402, pages 971–983, May 2003. (Not cited.)
- [Tripathi 1997] R. K. Tripathi, F. A. Cucinotta and J. W. Wilson. *Universal Parameterization of Absorption Cross Sections.* Technical report, January 1997. (Not cited.)
- [Tripathi 1999] R. K. Tripathi, F. A. Cucinotta and J. W. Wilson. *Accurate universal parameterization of absorption cross sections III - light systems.* Nuclear Instruments and Methods in Physics Research B, vol. 155, pages 349–356, September 1999. (Not cited.)
- [Webber 1990] W. R. Webber, J. C. Kish and D. A. Schrier. *Formula for calculating partial cross sections for nuclear reactions of nuclei with $E > \sim 200$ MeV/nucleon in hydrogen targets.* Phys. Rev. C, vol. 41, pages 566–571, February 1990. (Not cited.)
- [Webber 1998] W. R. Webber, A. Soutoul, J. C. Kish, J. M. Rockstroh, Y. Casagnou, R. Legrain and O. Testard. *Measurement of charge changing and isotopic cross sections at ~ 600 MeV/nucleon from the interactions of ~ 30*

- separate beams of relativistic nuclei from ^{10}B to ^{55}Mn in a liquid hydrogen target.* Phys. Rev. C, vol. 58, pages 3539–3552, December 1998. (Not cited.)
- [Webber 2003] W. R. Webber, A. Soutoul, J. C. Kish and J. M. Rockstroh. *Updated Formula for Calculating Partial Cross Sections for Nuclear Reactions of Nuclei with $Z \leq 28$ and $E > 150 \text{ MeV Nucleon}^{-1}$ in Hydrogen Targets.* ApJS, vol. 144, pages 153–167, January 2003. (Not cited.)
- [Wellisch 1996] H. P. Wellisch and D. Axen. *Total reaction cross section calculations in proton-nucleus scattering.* Phys. Rev. C, vol. 54, pages 1329–1332, September 1996. (Not cited.)
- [Yoon 2011] Y. S. Yoon, H. S. Ahn, P. S. Allison, M. G. Bagliesi, J. J. Beatty, G. Bigongiari, P. J. Boyle, J. T. Childers, N. B. Conklin, S. Coutu, M. A. DuVernois, O. Ganel, J. H. Han, J. A. Jeon, K. C. Kim, M. H. Lee, L. Lutz, P. Maestro, A. Malinine, P. S. Marrocchesi, S. A. Minnick, S. I. Mognet, S. Nam, S. Nutter, I. H. Park, N. H. Park, E. S. Seo, R. Sina, S. Swordy, S. P. Wakely, J. Wu, J. Yang, R. Zei and S. Y. Zinn. *Cosmic-ray Proton and Helium Spectra from the First CREAM Flight.* ApJ, vol. 728, page 122, February 2011. (Not cited.)
- [Yoon 2017] Y. S. Yoon, T. Anderson, A. Barrau, N. B. Conklin, S. Coutu, L. Derome, J. H. Han, J. A. Jeon, K. C. Kim, M. H. Kim, H. Y. Lee, J. Lee, M. H. Lee, S. E. Lee, J. T. Link, A. Menchaca-Rocha, J. W. Mitchell, S. I. Mognet, S. Nutter, I. H. Park, N. Picot-Clemente, A. Putze, E. S. Seo, J. Smith and J. Wu. *Proton and Helium Spectra from the CREAM-III Flight.* ApJ, vol. 839, page 5, April 2017. (Not cited.)
- [Yusifov 2004] I. Yusifov and I. Küçük. *Revisiting the radial distribution of pulsars in the Galaxy.* A&A, vol. 422, pages 545–553, August 2004. (Not cited.)

Dark Matter searches in cosmic ray antiparticles

Contents

4.1	A short story of dark matter evidences	134
4.1.1	Observing the present sky	134
4.1.1.1	At galactic scales	134
4.1.1.2	At galaxy cluster scales	139
4.1.2	Observing the primordial sky	140
4.1.2.1	Cosmological paradigm	140
4.1.2.2	Independent hints for dark matter	142
4.2	The quest of dark matter particles	144
4.2.1	Necessary dark matter properties	144
4.2.1.1	Some particle physic models	145
4.2.1.2	Macroscopic dark-matter and modified gravity	149
4.2.2	Indirect detection of dark matter and constraints	150
4.3	Exotic production of positron cosmic rays	153
4.3.1	Revisiting the DM hypothesis with the pinching method	154
4.3.1.1	Propagation of cosmic ray positrons with the pinching method	155
4.3.1.2	Implications for secondary positrons and the dark matter signal	162
4.3.1.3	Constraining propagation parameters with AMS-02 data	166
4.3.1.4	Dark matter interpretation of the AMS-02 data	169
4.3.1.5	Robustness of the results	173
4.3.1.6	Conclusion	176
4.3.2	Pulsars as astrophysical sources of positrons	178
4.3.2.1	Selection of possible pulsars: the five survivors of the ATNF catalogue	179
4.3.2.2	Results for the five pulsars	181
4.3.2.3	What happens when we get more statistics?	182
4.3.2.4	Conclusion	184
4.4	Refined constraints on dark matter using the antiproton flux	185
4.4.1	Re-evaluation of the astrophysical antiproton background	186

4.4.2 Updated constraints on Dark Matter	192
4.4.3 Final remarks	195
Bibliography	197

The twentieth century was a very fruitful age for fundamental physics. While completing successfully our understanding of microscopic physics, it also stressed its limits. One of the greatest mystery raised at this epoch, and which is still unresolved nowadays, is the dark matter (DM) problem. Hints for a new form of matter, based on gravitational phenomena happened at a similar epoch in astronomy and in the newly born field of cosmology. From the end of the twentieth century till now a vast community of researchers has been trying to find a common origin for these phenomena within some particle physics framework. In this section we will first discuss the observational evidences for DM, trying to highlight the historical milestones. Then, we will address quickly the particle physics framework which motivates a possible imprint in ordinary matter, and we will expose the different detection strategies. Finally we will detail the indirect detection technique based on cosmic rays. They have been used in this thesis to derive constraints on dark matter, thanks to new experimental data.

4.1 A short story of dark matter evidences

This section has been written with the help of the lessons of Pierre Salati and Pasquale Serpico, as well as informations gathered on the websites of Richard Taillet [RT] and Yann Mambrini [YM].

4.1.1 Observing the present sky

4.1.1.1 At galactic scales

The pioneers

Chronologically, Poincare was the first to introduce the word *dark matter* referring to the dead stars in [Poincare 1906]. By applying the kinetic theory of gas recently elaborated to the Galaxy, he derived a theoretical number of stars in the Galaxy comparable to the observed one in order to reproduce the Sun velocity. Hence, he wrote “*..the total number of stars including the dark ones[...]/is comparable to that which the telescope gives, then there is no dark matter, or at least not so much as there is of shining matter*”. Soon afterwards, the two Dutch astronomers Jacobus Kapteyn and Jan Oort highlighted in turn, that there should be part of the Galactic mass which is not shining. Jacobus Kapteyn, a pioneer of galactic dynamic observations, made the first statistical analysis in astronomy to determine the density of stars and of their magnitudes in the Galaxy. In one of his most important studies [Kapteyn 1922], he found the first hints of the corotational motion of the

stars around the Galactic center, formerly thought to have uncorrelated motions like in a gas. He also mentioned that the mass of the stars he derived, as the ratio of the total mass over the number of stars observed, is the apparent mass of the stars since it enclosed a *dark matter* part. He also add that *“this mass cannot be excessive. If it were otherwise, the average mass as derived from binary stars would have been very much lower than what has been found for the effective mass”*. According to Jan Oort, this fraction is significant, since only one third of the dynamically inferred mass should be present in bright visible stars [Oort 1932]. However, for both astronomers, the origin of this missing mass was not problematic and only due to the limitations of our means of observation of cold matter. The first work who underlined that this missing mass could be problematic was [Zwicky 1933] from the Swiss astronomer Fritz Zwicky studying galaxy clusters, a field described in more details in the next section. Staying at the galactic scale, the first measurements of a galactic rotation curve was made by Horace Babcock during his PhD thesis [Babcock 1939] in which he concluded for Andromeda that the *“constant angular velocity discovered for the outer spiral arms is hardly to be anticipated from the current theories of galactic rotation.”* From these measurements, and assuming the mass of the Galaxy to be distributed in spheroids, he inferred the total mass of Andromeda and that *“the ratio of mass to luminosity, in solar units, is about 50. This last coefficient is much greater than that for the same relation in the vicinity of the Sun.”* As its predecessor, Babcock did not make a big case of this problem, and attributed it to light absorption in the Galaxy or peculiar dynamics in spiral arms.

Babcock’s discovery is still quite puzzling with the current understanding of galactic dynamics. From the classification made by Edwin Hubble in the thirties [Hubble 1936], we learn that the Universe contains several types of galaxies, notably elliptical and spiral galaxies. In both cases we believe that the near infrared luminosity profile is a good tracer of the matter density essentially for two reasons: first, these galaxies are stellar systems; second, the color and metallicity gradients are quite small in each individual galaxy. Given a mass to light ratio, it is then possible to convert the luminosity profile into a mass profile, or surface density profile that in most of the cases will look like,

$$\Sigma^d(r) = \Sigma_0^d \exp\left(-r/r_0^d\right), \quad (4.1)$$

for disk morphologies (outer part of spiral galaxies), while for bulge like morphologies (bulge of spiral galaxies and elliptical galaxies in the whole) it takes the form:

$$\Sigma^b(r) = \Sigma_0^b \exp\left(\left(-r/r_0^b\right)^{1/4}\right). \quad (4.2)$$

Applying Newton’s laws on a test particle (i.e. a star) rotating at a distance r around the galactic center, one finds in both cases a typical Keplerian decrease as $1/\sqrt{r}$ of the orthoradial velocity provided that $r \gg r_0^d$ or $r \gg r_0^b$. This prediction is at odds with Babcock’s observation of the rotation of the spiral galaxy Andromeda.

The precision era

The advent of radioastronomy marked a watershed in galactic rotation observation. The pioneer of this new kind of astronomy was Karl Jansky. Engineer of the Bell society, Karl Jansky was employed to study crackling thunderstorm noise which interfered with radio-telephone conversations over trans-Atlantic short-wave links of the Bell system. To that purpose he designed and built a huge radio antenna which let him detect this thunderstorm noise, as well as another component with a period of one sidereal year over which he concluded in [Jansky 1933] that *“the direction of arrival of this disturbance remains fixed in space, that is to say, the source of this noise is located in some region that is stationary with respect to the stars.”*. This noise is known today as the synchrotron radiation from relativistic electrons from the inner Galaxy. In 1951, Van Hulst [Van de Hulst 1957], but also Ewen and Purcell [Ewen 1951] in Harvard, used this idea to look for the 21cm line from the hyperfine transition of neutral hydrogen suggested some years before by Casimir and Jan Oort as a probe of the interstellar medium. After the work of Hulst, Louise Volders at Dwingeloo [Volders 1959], Vera Rubin and Kent Ford [Rubin 1970] at the Carnegie Institute, but also many PhD students in the seventies (like A. Bosma [Bosma 1981], figure 4.1) were making use of this method and confirmed with high precision the flatness of the rotation curves in many galaxies as well as large mass over light ratios.

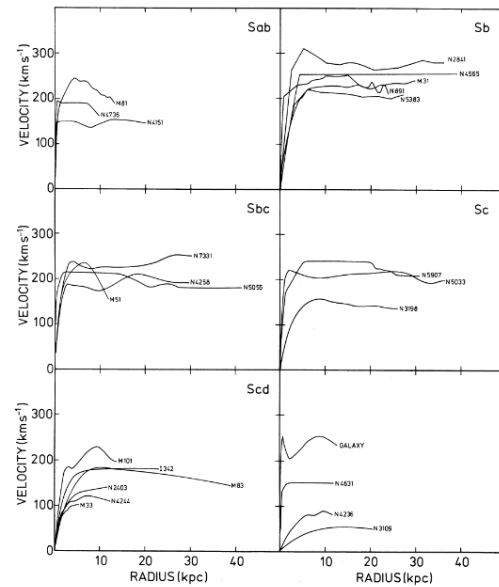


Figure 4.1: Measurements of the rotation curve of 25 galaxies observed by A. Bosma and published in [Bosma 1981]. These galaxies are classified according to their Hubble sequence.

The halo paradigm

While the observational techniques were improving significantly, the seventies were also a turning point with respect to computational physics. With the optimization of the transistor it was now possible to simulate N-body interactions and so to try to mimic galactic behavior. The first study of that kind was by Franck Hohl [Hohl 1971], who simulated the motion of a rotating disk of stars and noticed that the stability was not reproduced after two revolutions. The system became an ellipsoid dominated by kinetic pressure. Starting from the observation that in spiral-like galaxies the stars do have a global motion, i.e. $\sigma^2/\langle v^2 \rangle < 1$, Peebles and Ostriker noticed that galaxies seemed to be dominated by a cold gravitational component and not a kinetic pressure dominated one. Let us discuss an energetic argument: Being \mathcal{T} the kinetic energy sum of the rotational \mathcal{T}_{rot} and the random motion \mathcal{T}_{rand} components and \mathcal{U} the gravitational energy, the virial theorem states that:

$$2\mathcal{T} + \mathcal{U} = 0 \quad \Leftrightarrow \quad 2\mathcal{T}_{rand} + 2\mathcal{T}_{rot} + \mathcal{U} = 0 \quad \Leftrightarrow \quad r + t = \frac{1}{2} \quad (4.3)$$

$$\text{with: } r = -\frac{\mathcal{T}_{rand}}{\mathcal{U}}, \quad \text{and } t = -\frac{\mathcal{T}_{rot}}{\mathcal{U}}.$$

When $r(t)$ is equal to $1/2$ the system is supported by random (rotation) motion. Thanks to numerical N-body simulations, Peebles and Ostriker showed that if $t > 0.14$ the rotating disk is unstable and becomes elongated. It is actually the case for the Galaxy with $t \approx 0.49$. To restore the stability, Peebles and Ostriker had the idea to add a gravitational mass –dark halo– dominated by kinetic pressure and which would sufficiently decrease the value of t . Since then, different halo models have been designed with the first requirement to explain the flatness of rotation curves, leading to an evolution of the density profile as $\rho \propto 1/r^2$. Such a density profile density profile is also obtained with a self-gravitating gas at constant temperature and is thus called isothermal profile. In the central part of the Galaxy the rotation curves changes behavior, it is dominated by the observable Bulge. Since no major extra component is truly needed, it is common to regularize the above isothermal “dark matter” profile via add a (poorly constrained) constant term. The density profile then writes:

$$\rho_{iso}(r) = \frac{\rho_0}{1 + \left(\frac{r}{r_c}\right)^2}. \quad (4.4)$$

Later in the nineties, Navarro, Frenk and White ran more precise N-body simulations from which they extracted the by now famous dark-matter profile known as the NFW law [Navarro 1996], that is actually used in the dark matter analyses of this thesis. This distribution is:

$$\rho_{NFW}(r) = \frac{\rho_0}{\frac{r}{r_c} \left(1 + \frac{r}{r_c}\right)^2}. \quad (4.5)$$

One can notice the cuspy shape of this profile. More general parameterizations always from N-body simulations lead to distributions of the form:

$$\rho(r) = \rho_s \left(\frac{r}{r_c}\right)^\gamma \left[\left(1 + \frac{r}{r_c}\right)^\alpha \right]^{(\beta-\gamma)/\alpha} \quad (4.6)$$

To avoid the cusp at the center, Einasto [Einasto 1965] introduced the profile:

$$\rho_{Ein}(r) = \rho_s \exp\left(-\frac{2}{\alpha} \left[\left(\frac{r}{r_c}\right)^\alpha - 1 \right]\right), \quad (4.7)$$

which better fits recent numerical simulations [Navarro 2010]. Another category of profile, based on the observed rotation curves shapes, was introduced by Burkert [Burkert 1995]. These profiles are given by:

$$\rho_{Bur}(r) = \frac{\rho_s}{\left(1 + \frac{r}{r_c}\right) \left(1 + \frac{r}{r_c}\right)^2}. \quad (4.8)$$

All these profiles are thus determined by two normalization parameters usually calibrated on the local dark matter density at the position of the Sun, which, as used in [Cirelli 2011], is of 0.3 GeV/cm^3 at $r_\odot = 8.33 \text{ kpc}$, complemented by the total mass of dark matter within a given sphere centered on the Milky Way center. A mass $M_{60kpc} = 4.7 \times 10^{11} M_\odot$ leads to the profiles displayed in figure 4.2:

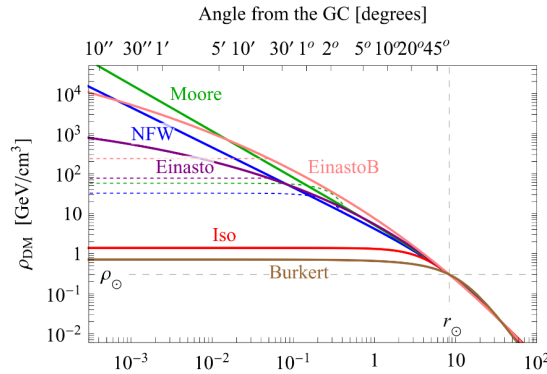


Figure 4.2: Dark matter density profiles obtained in [Cirelli 2011] after normalization to the local dark matter density. In dotted line: modified profile by the same authors to avoid the cusp problem.

As one can see in figure 4.2, the uncertainty of the dark matter profiles is huge toward the central region. The Galactic center is dominated by baryonic matter, i.e.

dust and stars, whose observational mass estimation is in addition made difficult by the poorly known dust absorption.

Remark on elliptical galaxies:

All the previous considerations are related to spiral galaxies, which before Kapteyn's work, were thought to behave like a gas of stars, dominated by the kinetic energy of their random motion. Actually, similar galaxies exist, being identified as elliptical galaxies in Hubble's classification. Apart from their morphology, the main kinematic difference between ellipticals and spirals is the ratio of the velocity dispersion over the average velocity of stars. For ellipticals $\sigma^2/\langle v^2 \rangle \gg 1$ whereas it is of the order 1 for spirals. Hence, while the equilibrium of spiral galaxies comes from the balance between their rotational and potential energies, in ellipticals it is due to the balance of gravitation via velocity dispersion. Thus, ellipticals are not commonly used for rotation curve measurements, but rather for the estimation of mass-to-light ratios thanks to the virial theorem. This technique is actually used to derive the dark matter mass in galaxy clusters, and it will be detailed in the following section. Let us just mention that ellipticals usually contain a very small fraction of gas, with quite old stars (PopII) and are very good candidates to probe dark matter. Their associated mass to light ratios are of order 10.

4.1.1.2 At galaxy cluster scales

Let us move to a larger scale view of the gravitational structures, focusing on the few Mpc scale where one finds gravitationally linked ensembles of galaxies ($\sim 10^3$), in so-called clusters of galaxies¹.

The astronomer Fritz Zwicky is actually one of the first to apply the virial theorem to such an astronomical system. In his (nowadays famous) paper [Zwicky 1933], he calculated the velocity spread of the galaxies inside the Coma Cluster, a highly regular gravitationally bound system of thousands of objects at a distance of about 60 Mpc. The virial theorem gives the velocity dispersion of a homogeneous sphere (radius R and mass M) of particles interacting gravitationally:

$$\sigma^2 = \frac{3}{5} \frac{GM}{R}. \quad (4.9)$$

Using an estimate of the Coma Cluster mass, he found a velocity dispersion of 80 km/s whereas the observed spread reaches ~ 1000 km/s. On which Zwicky concluded: *In order to obtain the observed value of an average Doppler effect of 1000 km/s or more, the average density in the Coma system would have to be at least 400 times larger than that derived on the grounds of observations of luminous matter. If this would be confirmed we would get the surprising result that dark*

¹Instead, the Milky Way is enclosed in a much less prominent family, known as Local Group and composed by 25 galaxies, and in which we also count Andromeda (M31) and the Triangulum Galaxy (M33). This group is enclosed in a wider group, the Virgo Supercluster which seems to be only a lobe of a greater supercluster, Laniakea, centered on the Great Attractor [Tully 2014].

matter is present in much greater amount than luminous matter.

Today we know that most of the mass of galaxy clusters is in the form of a hot intergalactic gas component extending widely outside the surrounding galaxies (see figure 4.3). Thanks to X-ray telescopes it is possible to observe the bremsstrahlung emission of this gas and to assess both its mass profile and the gravitational potential it feels [Lewis 2003]. Despite this progress in the understanding, we still confirm that the known mass is not sufficient to explain the gravitational potential well in which it is trapped. For the Coma Cluster an additional dark matter mass, seven times higher than the hot gas one, is needed.

Recent techniques are based on gravitational lensing for mapping the gravitational potential. General relativity predicts that the light observed at Earth is deviated from its straight path trajectory by the gravitational potential of any massive object on its way. Thus, the observed deformations of background objects are used to infer the gravitational potential of foreground objects. The most spectacular evidence for dark matter is given by the collisions of galaxy clusters [Clowe 2006] as seen figure 4.3. Indeed when two galaxy clusters collide, the baryonic hot gas (in pink in the figure) is dragged by ram pressure, while the masses causing the gravitational lensing effect (as well as the subdominant component of galaxies) cross each other (in bluish in the figure). The most obvious interpretation is that most of the mass is not the collisional gas, as it would happen if the law of gravity were altered. We have already observed more than 70 collisions of that kind and they are now used to derive upper bounds on dark matter self interaction. For example in the case of the bullet cluster the conservative bound is found to be [Randall 2008]:

$$\frac{\sigma_{\chi}}{m_{\chi}} < 1.25 \text{ cm}^2 \text{ g}^{-1} \quad (4.10)$$

4.1.2 Observing the primordial sky

While people were observing the rotation curves of galaxies, a faint cold microwave radiation (roughly corresponding to a black-body with a temperature of 3.5 K, according to the estimates at the time), filling the whole sky was discovered by Penzias and Wilson, two Bell Laboratories engineers [Penzias 1965]. Predicted earlier by Gamow [Gamow 1946], the so-called cosmic microwave background (CMB) is one of the pillars of modern cosmology, and still provides a wealth of information on the evolution of the Universe, independently suggesting the need for a *non-baryonic* matter component, among others.

4.1.2.1 Cosmological paradigm

The current paradigm is based on the cosmological principle first stated by Einstein in 1917, according to which the Universe is homogeneous and isotropic. From this principle, one can derive the Friedmann-Lemaître-Robertson-Walker equations

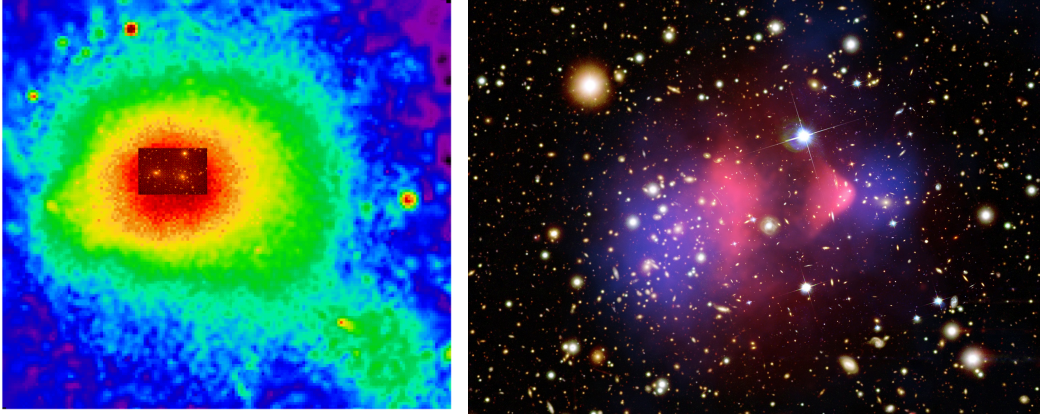


Figure 4.3: Left: the Coma Galaxy cluster in X-Rays as observed by ROSAT [Briel 1992], with superimposed the optical channel by Hubble. Right: The bullet cluster

obtained by inserting the generic metric of a curved space with the corresponding symmetries

$$ds^2 = dt^2 - a^2(t) \left[\frac{dr^2}{1 - kr^2} + r^2 d\theta^2 + r^2 \sin^2 \theta d\phi^2 \right], \quad (4.11)$$

into Einstein's equations of general relativity. Here, the whole additional information is encoded in a time dependent scale factor $a(t)$ and in the coefficient k , which—modulo a rescaling of $a(t)$ —can only assume the three discrete values $+1, 0, -1$, characterizing the space curvature of this geometry. As the chosen form of the metric implies that the energy-momentum tensor is isotropic, for a fluid of energy density ρ and pressure P , these equations become:

$$H^2 \equiv \left(\frac{\dot{a}}{a} \right)^2 = \frac{8\pi G_N}{3} \rho - \frac{k}{a^2} + \frac{\Lambda}{3}, \quad (4.12)$$

$$\frac{\ddot{a}}{a} = -\frac{4\pi G}{3} (\rho + 3P) + \frac{\Lambda}{3}, \quad (4.13)$$

where H is defined as the (time-dependent) Hubble expansion rate and Λ is the cosmological constant. This system of equations can be closed only if an equation of state for the fluid is provided, relating P to ρ . Matter and radiation are defined by their equation of state $P = 0$ and $P = \rho/3$ respectively. Renormalized to the critical density $\rho_c = 3H_0^2/8\pi G_N^2$ corresponding to a spatially flat Universe, one can define the cosmological parameters:

$$\Omega_i = \frac{\rho_i}{\rho_c}, \quad (4.14)$$

²The parameter H_0 is the current value of the expansion rate. It is estimated by CMB analyses to $H_0 = 67.27 \pm 0.66 \text{ km s}^{-1} \text{ Mpc}^{-1}$, but also thanks to cepheid stars $H_0 = 72 \pm 3 \text{ km s}^{-1} \text{ Mpc}^{-1}$. The difference between these two values (as well as its significance) is strongly debated.

which give the energy density fraction of each component i . Equation 4.13 readily yields:

$$\Omega_k \equiv -\frac{k}{H_0^2 a_0^2} = 1 - \Omega_m - \Omega_r - \Omega_\Lambda, \quad (4.15)$$

with Ω_m , Ω_r , and Ω_Λ being the fractions of matter, radiation and dark energy, respectively. Introducing the Hubble time $\tau = H_0 t$ and $x \equiv a(t)/a_0$, the equation 4.12 becomes:

$$\left(\frac{dx}{d\tau}\right)^2 + V(x) = \Omega_k \quad \text{with:} \quad V(x) = -\frac{\Omega_r}{x^2} - \frac{\Omega_m}{x} - x^2 \Omega_\Lambda, \quad (4.16)$$

which is simply the equation for the 1D evolution of a fictive point with energy Ω_k in a potential $V(x)$. Hence, the evolution of $a(t)$ depends on the actual matter content at time t of the Universe.

4.1.2.2 Independent hints for dark matter

Constraining these cosmological parameters has been achieved with strenuous experimental efforts. The measured CMB emission fixes $\Omega_r \sim 4 \times 10^{-53}$. In the concordance model or Λ CDM model, a number of probes suggests that the Universe is flat ($\Omega_k = 0$), with $\Omega_\Lambda = 1 - \Omega_m \simeq 0.7$, and the only dimensional parameter is then H_0 . In turn, Ω_m splits in Ω_{DM} for the dark matter part and Ω_b for the baryonic part. In this model we further assume that, *at least* after the recombination era when the CMB was emitted, the different components do not interfere with each other but gravitationally. Among few notable probes, we list here:

- *Big bang nucleosynthesis*: The theory of nucleosynthesis predicts the abundances of light elements produced in the early Universe, when the energy density was of order $\sim (1\text{MeV})^4$. Their predicted abundances depends only on the baryonic abundance Ω_b . Primordial deuterium and ^4He abundances can be fixed by spectroscopy in old gas clouds and stars, respectively, assuming those have not yet been significantly affected by stellar nucleosynthesis. This fixes the baryon abundance to $\Omega_b = 0.020 \pm 0.002$.
- *Standard candles*: Cepheids stars were found to exhibit a universal relation between period and luminosity. Therefore, after calibration with the closest ones, they were used by Hubble as the first probes of the luminosity distance-redshift relation, showing that the Universe is not static, but is expanding. Later, a relation between the absolute magnitude and the luminosity decay rate in supernovae of type Ia was found as universal too. In the same way, SNIa were used to extend the measurements at high redshift (of order one or two), because they are much more luminous than Cepheids. The observations form

³Note that this estimate should also take into account the neutrino background, whose contribution is supposed to be lower than 6.2×10^{-3}

the *Supernova Cosmology Project Collaboration* revealed first that $\Omega_\Lambda > 0$ and that the Universe is actually undergoing an accelerated expansion. Assuming a flat Universe, the collaborations SDSS-II and SNLS [Betoule 2014] found $\Omega_m = 0.295 \pm 0.034$ using the data from 740 SNIa.

Form these two observations we conclude that baryons only account for about 20 % of the matter in the Universe, and so that cosmology strongly suggests the need for a non baryonic matter component. Confirmations came once we were able to measure and to interpret inhomogeneities in the CMB and in the distribution of galaxies.

- *Cosmic microwave background*: The first light of the Universe is not only the most perfect black body radiation in nature ($T = 2.72548 \pm 0.00057K$ [Fixsen 2009]), ⁴, but it presents tiny relative temperature fluctuations at the level of 10^{-5} whose origin is currently believed to be of quantum nature. The statistical properties of these fluctuations can be predicted by perturbation theory, and correspond to acoustic oscillations in the primordial plasma resulting from the competition between gravity pull, and photon pressure. Thus, the angular power spectrum of the cosmic microwave background (CMB) anisotropies is a rich observable, encoding a strong dependence on the all cosmological parameters. First measured by COBE, the latest release of the temperature power spectrum measured by PLANCK satellite [Planck Collaboration 2014] is shown in figure 4.4. Combining the temperature and polarization power spectrum, the PLANCK Collaboration derived the following parameters [Planck Collaboration 2016]: $\Omega_\Lambda = 0.6844 \pm 0.0091$, $\Omega_m = 0.3156 \pm 0.0091$, the latter split in $\Omega_b h^2 = 0.02225 \pm 0.00016$ and $\Omega_{DM} h^2 = 0.1198 \pm 0.0015$, with $H_0 = 67.27 \pm 0.66 \text{ km.s}^{-1}.\text{Mpc}^{-1}$.
- *Galaxy correlation function*: In the Λ CDM model the fluctuations yielding the anisotropies in the CMB also seed the formation of structures on all scales in the Universe today. The last decades, astronomers were able to build very large three-dimensional maps of the galaxy distribution (see for example [Tegmark 2006] or more recently [Anderson 2012]). The power spectrum of the galaxy correlation function, at least at large scales, can be compared with predictions of gravitational perturbation theory and thus can be used to constrain cosmological parameters. By the way, it is noteworthy that the same baryon acoustic oscillations imprinted in the CMB have a clearly detected residual imprint in the correlation function of matter. The results are in perfect agreement with the CMB constraints, which is one of the successes of the Λ CDM model. In particular the mere shape of the spectrum could not be explained with a sole baryonic component (see figure 4.4), and calls for dark matter [Dodelson 2011].

⁴Its observation is also one of the main motivations of the "Big Bang" paradigm for which there is a time where all the species were at thermal equilibrium.

Other cosmological observations such as *cosmic shear* or analyses of *Lyman- α forests in the spectra of quasars* are also supporting the concordance model, but are not discussed here. Notice that as long as the model is not challenged by the data, constraints combining several observables are more stringent, and so often used in cosmology. In addition to these constraints, N-body simulations (like e.g. [Springel 2005]) require that DM is non-relativistic (at least by the time $T \sim 1\text{keV}$) or cold (CDM), to account for structure formation. This supports the bottom-up scenario where galaxies or, in general, smaller clumps are formed first, before clustering. However, at Galactic scales the ΛCDM paradigm seems to suffer of some inconsistencies between simulations and observations. Here is a list of the problems, often referred by their nicknames:

- The “missing satellite” problem: the simulations predict more dwarf satellite galaxies than what is actually observed (see for example [Moore 1999]).
- The “too big to fail” problem: N-body simulations show that the majority of the most massive sub-haloes of the Milky Way are too dense to host any of the known satellites.
- The “cusp vs. core” problem: the simulations predict cuspy DM profiles at the galaxy centers, with $\rho \propto 1/r$. This is at odds with observations which prefer core profiles with central constant densities.

These problems all arise in a deeply non-linear gravitational regime, in addition for systems where phenomena involving baryonic feedback are known to be important. At the moment, it is unclear if some (if not all) of these problems can be overcome by a more precise modelling. Not surprisingly, however, effects like baryonic feedback, the stripping of DM satellite haloes by the galactic one, have been proposed as possible solutions, together with more radical modification of the cosmological model, such as introducing a warm DM component, i.e. with non-negligible velocity dispersion at formation [Boylan-Kolchin 2011, van den Bosch 2001].

4.2 The quest of dark matter particles

4.2.1 Necessary dark matter properties

In the previous section, we have seen that the pieces of evidence for DM are only based on its gravitational interactions with luminous matter. In the particle physics framework, based on quantum field theory, one would like to attribute a fundamental particle to DM, and to characterize its quantum numbers specifying its interactions with the other particles of the standard model (SM). Summarizing the astrophysical and cosmological constraints previously stated, plus some additional ones coming from other observations (see e.g. [Taoso 2008]), we need the DM to be:

- stable on cosmological timescales.

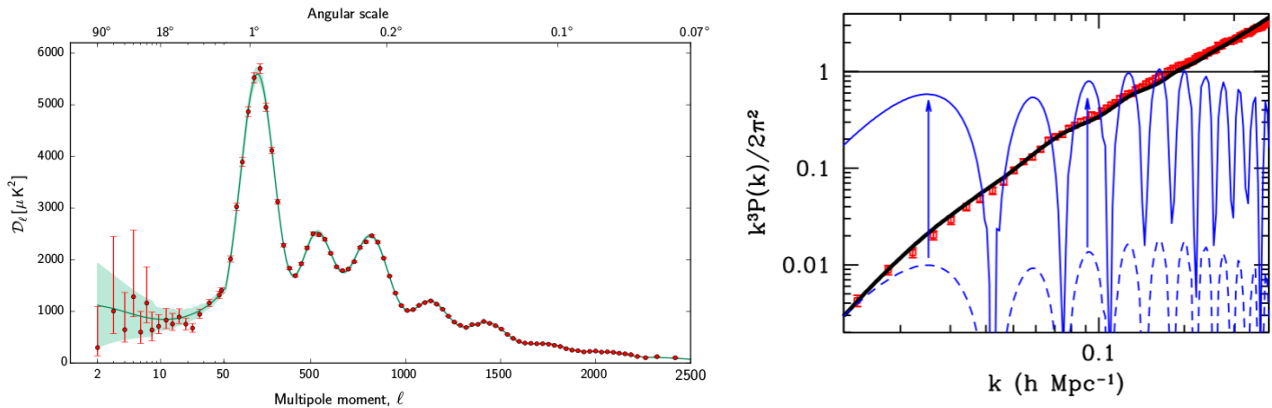


Figure 4.4: *Left*: The temperature power spectrum measured by PLANCK satellite, adapted from [Planck Collaboration 2014]. *Right*: The difference of the matter spectrum in real space, taking into account or not the dark matter component, black solid curve and blue dashed curves, respectively. The solid blue curve shows an hypothetical modified gravity effect where baryons are simply sourcing a stronger pull, as to match the normalization of the matter power spectrum: the wavenumber dependence is nonetheless completely off. The data from SDSS are shown in red. Extracted from [Dodelson 2011]

- almost collisionless.
- transparent and dissipationless.
- at most weakly interacting with ordinary matter.
- cold, so with non-relativist distribution function at decoupling.

When the penultimate condition bans all charged particles, the last one excludes standard model neutrinos since at least one mass eigenstate is relativistic today. Hence, none of the SM particles can accommodate for these constraints, and it pushes to look for extensions of the standard model of particle physics where a dark matter species embeds new degrees of freedom. Interestingly, many models trying to address the short-comings of the standard model (like the origin of mass, the strong CP problem, neutrino oscillations, or the matter-antimatter asymmetry), also provide us with DM particle candidates. Hereafter we list some of these particles and point out the motivations.

4.2.1.1 Some particle physic models

WIMP miracle

If such a DM particle χ exists, in the Big-Bang paradigm when the temperature of the Universe exceeds the mass m_χ of the particle, the particle should be in

abundance and in thermal equilibrium with the primordial plasma. Let us assume that the mass of the particle is above 1 GeV, as long as the Universe temperature is above this value, the reaction

$$\chi + \chi \rightleftharpoons f\bar{f},$$

is at equilibrium, thanks to strong coupling with the thermal bath⁵. As the Universe cools down, the temperature decreases below m_χ , and the probability that the center of mass energy involved in the reaction $f\bar{f} \rightarrow \chi + \chi$ is higher than $2m_\chi$ becomes lower and lower. Hence, the equilibrium quantity $n_\chi^{eq} \propto \exp(-m_\chi/T)$ is Boltzmann suppressed. If the Universe was always in thermal equilibrium, there would not be any more dark matter particles left today. However, the Universe is not static, and as it expands, the dilution of the DM particles freezes the annihilation since the probability that two DM particles meet becomes too low. A rough estimate of the remaining quantity of DM is given by equating the expansion rate H with the annihilation rate Γ , yielding the so-called relic cosmological abundance. Physically, $\Gamma = \langle\sigma v\rangle n_\chi$, where $\langle\sigma v\rangle$ is the mean over the velocity distribution, of the relative velocity v times the annihilation cross-section. Denoting T_f the temperature of *freeze-out*, one finds in a radiation dominated Universe, using typical electroweak coupling, that $x = m_\chi/T_f \approx 20$ (see e.g. [Jungman 1996]). A more precise estimation of that value relies on the numerical resolution of the Boltzmann equation:

$$\frac{dn_\chi}{dt} + 3Hn_\chi = -\langle\sigma v\rangle[n_\chi^2 - (n_\chi^{eq})^2], \quad (4.17)$$

where n_χ^{eq} is the equilibrium density. Nevertheless, using the conservation of the entropy of the Universe, one can estimate the relic density as:

$$\Omega_\chi h^2 = \frac{3 \times 10^{-27} \text{cm}^3 \text{s}^{-1}}{\langle\sigma v\rangle}, \quad (4.18)$$

h denotes the Hubble constant in units of $100 \text{ km.s}^{-1}.\text{Mpc}^{-1}$. We notice that choosing the value $\langle\sigma v\rangle \sim \alpha^2(100\text{GeV})^{-2} \sim 10^{-25} \text{cm}^3 \text{s}^{-1}$, with $\alpha \sim 10^{-2}$, can lead to the observed cosmological abundance of $\Omega_\chi h^2 \approx 0.1198$ inferred from CMB, for values of $\alpha \sim 10^{-2}$ close to the electroweak coupling. Hence, using the weak coupling and the electro-weak scale mass, there is a striking coincidence which suggests that if there is a stable particle associated with new physics at the electroweak scale, it would probably be the dark matter. Therefore this remarkable result was dubbed the *weakly interacting massive particle (WIMP) miracle*. Although this result can be regarded as a coincidence, it is very powerful in constraining the interactions of DM with SM particles and thus DM particle models.

Supersymmetric WIMPs

⁵Here we assume that dark-matter and its antiparticle are identical, which can be either fermion (then Majorana fermion) or boson.

While strenuous experimental efforts have been made to detect the WIMP, its identity remains a mystery. Theoretically, perhaps the most well-motivated and certainly the most theoretically well-developed WIMP candidate is the lightest supersymmetric particle (LSP). The supersymmetry theory (SUSY) was developed in the seventies as an extension of the standard model. The basic idea is to define a super-algebra by adding new generators to the Poincaré algebra originally associated with the translation and Lorentz symmetries in the Minkowski space-time. These new generators transform like a spin $1/2$, and are defined by specific anticommutation relations. Hence new degrees of freedom emerge. In particular, to each standard model particle corresponds a supersymmetric partner of same mass, but differing by a half unit of spin. Then, to each fermion would correspond a boson and *vice versa*, and this is precisely what is needed to solve the problem of hierarchy, a strong plus for this theory. Thus, SUSY implies a particle content at least twice as big as the standard model one. However, since no such particles are known to exist, the new symmetry must be broken under the electroweak scale. An important defect of supersymmetry is that proton becomes unstable because the baryon and lepton numbers are not conserved anymore. To cure that problem a new conservation law of the so-called R-parity ($R = (-1)^{3B-3L+2s}$), can be introduced. Since for each standard model particle $R = +1$ and for each supersymmetric partner $R = -1$, the latter rule forbids supersymmetric particle to decay into SM species only.

Interestingly, one of the consequences is that the lightest supersymmetric partner (LSP) is stable. In most theories, the LSP is the neutralino, a linear combination of the supersymmetric partners of the photon, Z boson, and Higgs bosons. In some models, the neutralino may also be a pure photino or higgsino, but in general it is some arbitrary linear combination. Nevertheless, it appears that in broad regions of parameter space in minimal supersymmetric extensions of the standard model, the cosmological abundance of the LSP is $\mathcal{O}(1)$ and suitable for solving the dark matter problem, independent of the specific composition of the LSP [Jungman 1996].

Extra dimensions

In supersymmetric models, the hierarchy problem is solved by adding an intermediate scale between the electroweak scale and the Plack mass $M_P = \sqrt{\frac{\hbar c}{8\pi G}} \approx 2 \times 10^{18} \text{GeV}$. Actually this problem can also be handled by adding δ spatial extra dimensions to the usual three ones, bringing the number of space-time dimensions to $D = 4 + \delta$. These new dimensions are compactified on a scale R . As gravity has a geometrical origin, it feels all the geometrical dimensions, and as a result of the Gauss theorem, we can relate the Planck mass in D -dimensions to the one in 4-dimensions:

$$M_P = (2\pi R)^{\delta/2} M_D^{\frac{2+\delta}{2}} . \quad (4.19)$$

Hence, by tuning the parameters δ and R , $M_D \sim 1 \text{TeV}$ could be enough to reach the Planck scale. This solves the hierarchy problem. A key element of the theory is the

conservation of momentum in the extra dimensions. In the simplest version where $\delta = 1$, the momentum of the particles propagating within the compact dimension is quantified. For each SM field X^0 , new particles – so-called Kaluza-Klein particles [Klein 1926]– are attributed to each excitation of the field, with a mass spectrum given at tree level by:

$$m_{X^n} = \sqrt{\left(\frac{n}{R}\right)^2 + m_{X^0}^2}. \quad (4.20)$$

The excitations of the field X^n have the same quantum numbers as X^0 . In the sub category of models named universal extradimension models (UED), as for the case of supersymmetry, a new conservation rule for the K -parity is introduced to protect the results from electroweak precision tests. This K symmetry also predicts the existence of a lightest particle which is stable, dubbed Lightest Kaluza-Klein Particle (LKP). The Kaluza-Klein parity is not an *ad-hoc* condition, but stems from topological arguments [Cacciapaglia 2010]. More information about these theories applied to the dark matter problem can be found in [Appelquist 2001] and [Cheng 2002].

Sterile neutrinos

Sterile neutrinos refer to neutrinos with right-handed chirality, which would naturally complement the SM. They should correspond to singlet representations with respect to the strong and weak interactions, without any charge so that they would only interact through gravity. Their name *sterile* distinguishes them from the known *active* neutrinos of the SM, which have weak charges. Thus this particle would be extremely difficult to detect. Although, due to their Yukawa interactions with ordinary leptons and Higgs bosons, they would contribute to all the processes involving ordinary neutrinos, to which they are mixed via the Higgs mechanism. However constraints from neutrino oscillations indicate that this angle is tiny. Sterile neutrino models are often invoked to solve the mystery of neutrino masses in the SM, via the seesaw mechanism. The number of sterile neutrino types, as well as their masses remains unknown, and in general the latter can be within the broad range $\sim[1\text{eV}, 10^{15}\text{GeV}]$ [Drewes 2013]. Since sterile neutrinos are collisionless and can be very long lived, they are an obvious DM candidate. In this case, the mass range shrinks because of cosmological and astrophysical constraints: the upper bound is given by X-rays for a value around 5 keV (see e.g [Riemer-Sorensen 2009]), the lowest bound ensures that structure formation is not spoiled and is of few keV too [Adhikari 2017]. These observations leave little room for sterile neutrinos as DM candidates.

Axions

Axions were first introduced to solve the strong CP problem. Indeed, experimentally, the strong interaction conserves parity (P) and charge-parity (CP) symmetries,

although there are terms in the Lagrangian of the strong interaction that can naturally violate them. The relative importance of those terms in the Lagrangian is parameterized by the effective angle $\bar{\Theta}$, which experimentally is constrained to be lower than 10^{-10} from measurements of the magnetic moment of the neutron. An attempt to explain such a low value was made in [Peccei 1977], where the authors introduced a new $U(1)$ global chiral symmetry, spontaneously broken under an energy scale f_a . As for the Higgs mechanism, the broken symmetry gives birth to pseudo Nambu-Goldstone boson, which under Λ_{QCD} gets a dynamical mass of m_π^2/f_a :

$$m_a \approx 0.6 \text{ eV} \times \frac{10^7 \text{ GeV}}{f_a} . \quad (4.21)$$

The low vacuum expectation value (vev) value of the axion potential solves the strong CP problem. Thus, nowadays, the axion particles would behave like cold DM, with a contribution to the relic density of:

$$\Omega_a h^2 \approx 0.5 \left(\frac{f_a}{10^{12} \text{ GeV}} \right) . \quad (4.22)$$

Because of its couplings with other SM particles, there is a variety of constraints on the axion mass, from collider searches to astrophysics. The viable mass range is currently $\sim [10 \mu\text{eV}, 10 \text{ meV}]$.

4.2.1.2 Macroscopic dark-matter and modified gravity

It is not excluded that DM is made of dark macroscopic objects or is the observable consequence of a modified version of gravity laws at Galactic scales. Many searches have been performed in these directions. Hereafter is a brief summary of the most studied possibilities that could account for part (if not all) of the DM amount.

Neutral gas

The total quantity of molecular hydrogen H_2 in the interstellar medium is much harder to determine than for neutral hydrogen, as the former does not emit any specific spectral line. Although, in some cases, its thermal infrared emission can be used to estimate its abundance. Thus, it was shown that in some spiral galaxies, notably NGC 891 [Valentijn 1999], the H_2 component could be sufficient to solve the problem of the missing mass. However, at least in the case of the Milky Way, observations of diffuse gamma-ray emission stemming from CR interaction with the gas, constrain its maximal contribution at $\sim 20\%$ of the total Galactic mass (see e.g. [Salati 1996, Kalberla 1999]).

Compact objects

It has been thought that DM could be baryonic matter hidden inside low radiating compact object, so-called (Massive Halo Compact Objects). This generic term includes neutron stars, brown dwarves, planets and even black holes. Through microlensing effects, it is possible to test whether these object contribute significantly to the dark matter mass [Paczynski 1986]. Several collaborations (notably MACHO, EROS, and OGLE) have launched programs to observe such objects by monitoring the luminosity of millions of stars in the Large and Small Magellanic Clouds for several years. The EROS collaboration showed that MACHOs with masses in the range $[0.6 \times 10^{-7}M_{\odot}, 15M_{\odot}]$ cannot contribute more than 8% to the mass of the galactic halo [Tisserand 2007]. In the cases of the MACHO experiment, a signal was observed at 0.4 solar mass and an upper limit of 40% was set [Alcock 2000]. Recently, the LIGO collaboration observed twice the passage of gravitational waves, corresponding to the merging of black holes with masses above $15 M_{\odot}$ [Abbott 2016]. These observations have been triggering a lot of excitement in the community as a tiny window is still left to explain the DM abundance with such massive objects. Possible production mechanisms from quantum primordial fluctuations are presently being discussed. A comprehensive review can be found in [García-Bellido 2017].

Modified gravity

General relativity has been tested with high accuracy at the scale of the solar system, however it is not yet clear if variations exist at Galactic and cosmological scales. The modification of Newton's law as a function of the acceleration was first introduced by M. Milgrom as an *ad-hoc* condition to reproduce the rotation curves of galaxies (for a review see [Milgrom 2015]). Deeper investigations extended this *empirical* law as modifications of the Einstein-Hilbert action. However it was stressed (for example in [Dodelson 2011]) that these theories do still need another component of matter at cosmological scales to account for the power spectrum of the galaxy correlation function. Intriguingly, it can also be shown in some cases [Calmet 2017], that the apparent difference at the classical level between modification of the gravitational force and additional DM component, stems from the various interpretations of the new degree of freedom introduced at the quantum level.

4.2.2 Indirect detection of dark matter and constraints

Dazzled by overwhelming evidences for DM in the last decades, the physics research programs have mobilized an important community to track the putative DM particle. A myriad of experiments were built trying to unveil an observable imprint of dark matter interaction with SM particles. Three complementary ways are presently explored. First, *the production in accelerators*, where one look for producing DM particles by colliding SM particles with a center-of-mass energy above the DM mass threshold and looking at missing energy within well-known processes. The most promising outcomes in this domain are from the LHC experiments. Secondly, *direct-*

detection experiments in which the dark matter species are expected to collide on the nuclei of a terrestrial instrument and to deposit a detectable amount of energy⁶. Finally, in *indirect-detection*, DM is expected to annihilate in pairs or decay within the galactic halo and to produce visible radiations such as high energy photons or neutrinos as well as rare antimatter cosmic rays. In the WIMP paradigm, dark matter species are expected to annihilate through one or several particles,

$$\chi + \chi \longrightarrow q\bar{q}, l^+l^-, W^+W^-, ZZ, \gamma\gamma, HH \longrightarrow e^\pm, p\bar{p}, N\bar{N}, \gamma, \nu,$$

which finally decay in stable SM particles. Hence, numerous channels of detection are opened. The careful determination of the astrophysical background is the common feature of these different channels which aim at maximizing their sensitivity to any unknown deviation that could be attributed to DM. The latter could be calculated or inferred from observation when it is possible. The different observation channels for dark-matter annihilation indirect detection are briefly reviewed in the following for some wavelengths.

Neutral radiations

As we have seen before, generic WIMP annihilations may generate high energy neutral particles i whose energy distribution at sources is described by the function $g(E_i) \equiv dN_i/dE_i$. The corresponding flux at the Earth, from the direction toward which the unit vector \mathbf{u} is pointing, is given by the product

$$\Phi_\gamma^{\text{DM}}(E_i, \mathbf{u}) = \frac{\eta}{4\pi} \left\{ \frac{\langle \sigma_{\text{ann}} v \rangle g(E_i)}{m_\chi^2} \right\} \times \int_{\text{los}} \rho^2(\mathbf{x}) ds. \quad (4.23)$$

This formula is often seen as the emblem of particle astrophysics insofar as it exhibits two distinct pieces. The first part is related to particle physics and encodes informations on the WIMP properties such as its mass and annihilation cross-section. The second term is clearly astrophysical in nature and deals with the distribution of DM along the line of sight (los) toward which \mathbf{u} is pointing.

As the DM density is expected to increase toward the center of galaxies, these are interesting targets to look for DM byproducts, to start with our own: the Milky Way. A careful comparison of the fluxes toward and outward the galactic center region, is one of the preferred methods of detection. Focusing at the extragalactic sky, the studies of DM dominated objects such as dwarf spheroidal galaxies (dSphs), are currently giving the best constraints as well as hopes for new discoveries. Although it was shown in [Bonnivard 2015, Bonnivard 2016], that large uncertainties are affecting the calculation of the J-factor – the right hand side term in equation 4.23 – of these systems.

Of course the detection threshold crucially depends on the form of the assumed spectrum $g(E_i)$, which in the most optimistic case of a complete annihilation in $\gamma\gamma$ would yield a spectral line centered on the DM mass. For other cases, a smoother

⁶These experiments are settled deep underground in order to be protected from CRs noise.

spectrum is expected, with a sharp cut-off at the DM mass. Hereafter we recall interesting results from some wavelengths under scrutiny.

- *Gamma-rays*: The last decade has been fruitful for gamma astronomy thanks to ground based Cherenkov detectors (VERITAS, MAGIC, HESS), and also with the FERMI-LAT which scans every three hours the entire sky. The gamma-ray emission of the Galactic bulge has been studied in detail since a possible excess around ~ 70 GeV has been detected (see e.g. [Goodenough 2009, Calore 2015] and references therein). The hot topic is currently to now whether this excess is coming from point sources or has a diffuse pattern, this distinction could help disentangling the astrophysical hypothesis (notably the contribution of milipulsars) from the DM one. A dedicated survey with the radio-telescope MeerKAT TRAPUM will be launched in 2018. Notice that this excess is not observed in dwarf galaxies, which have provided the best constraints for DM annihilation in quarks so far (see e.g. [Rico 2015]). At energies above the TeV, Cherenkov telescopes are producing the most stringent constraints. The future telescope CTA will improve the current constraints by one order of magnitude, which will reach the level of the thermal cross-section.
- *Neutrinos*: The last decade celebrates also the birth of neutrino astronomy, thanks to huge neutrino telescopes like Antares and IceCube. Interestingly, the PeV-energy neutrinos detected by IceCube, and the broken power-law shape of the resulting spectrum can be interpreted as a dark matter signal [Esmaili 2014]⁷. Looking at DM annihilation inside the Sun, these experiments provide the most stringent bounds on spin-dependent scattering cross-sections in the 10 GeV to multiple TeV range.
- *X-rays*: In 2014 a X-ray spectral ray at 3.55 keV was first identified in 73 stacked and de-redshifted nearby galaxy clusters (central parts) with XMM-Newton data [Bulbul 2014]. This observation would coincide with a sterile neutrino interpretation of DM. A large number of follow-up studies focused on the Galactic center, dwarf galaxies and stacked galaxies, and this excess was not systematically confirmed (see e.g. Malyshev 2014). There were actually some debates about the eventual origin from potassium emission line [Jeltema 2015], but thanks to a dedicated campaign of observation of Draco (A dSphs), the same authors are now able to rule out the DM origin of this excess [Jeltema 2016]. In the keV energy range, the analysis of dwarf galaxies can be very constraining.

The track for dark matter also extends to radio wavelength (since production of electrons leads to radio synchrotron emission) and visible light, which for concision are not detailed here. A review of these constraints can be found for example in

⁷Note that it will take ten years to collect enough data to have a 3-sigma evidence based on the anisotropy of the signal.

[Cirelli 2015].

Cosmic ray antiparticles

As mentioned in the introduction chapter, antimatter cosmic rays are thought to be secondary species and their relatively low flux makes them the perfect target to look for rare processes, such as dark matter annihilation. The main difference with *neutral radiations* is, not surprisingly, that these particles are charged particles, hence they undergo the effects of the tangled galactic magnetic field and lose the information of the direction of their production. In this case, the source term does not only depend on the line-of-sight integral of the DM (squared) density, but is averaged over the DM content within the diffusive galactic halo. As a result, the derived constraints do not have the same dependence on the DM profile.

The two preferred channels of detection are positrons and antiprotons, because there are the most abundant antiparticles. Recently, the GAPS project received NASA support to measure galactic antideutons, which is a very promising channel to look for DM too, because of the very low secondary background. As regards positrons and antiprotons, AMS-02 has a very efficient rejection power of the proton background and can identify these antiparticles in the GeV to TeV energy range.

In the following sections, we fully benefit from these advances and we address i) the *positron excess* problem, and ii) refresh the DM annihilation constraints from antiproton. The works presented here were achieved within the fruitful Cosmic Rays Alpine Collaboration (CRAC), involving both experimentalists and theorists.

4.3 Exotic production of positron cosmic rays

The cosmic ray (CR) positron flux has been measured with unprecedented accuracy by the AMS-02 collaboration [Aguilar 2014]. This observation is of paramount importance in several respects. To start with, it provides an insight into the mechanisms that create positrons inside the Milky Way. For a long time, CR positrons have been thought to be exclusively secondary species originating from the spallation of the gas lying in the Galactic disc by high energy nuclei. The first experimental hints for a deviation from the conventional scenario came from the data collected by the High energy Antimatter Telescope (HEAT) collaboration [Barwick 1997, DuVernois 2001, Beatty 2004], but the existence of a positron anomaly has been firmly established by [Adriani 2009] who reported an excess in the positron fraction measured up to 100 GeV by the Payload for Antimatter Matter Exploration and Light-nuclei Astrophysics (PAMELA) satellite (see figure 4.5). Recently, AMS-02 has released high-quality data on the positron fraction [Aguilar 2013a, Accardo 2014] and positron flux [Aguilar 2014] up to 500 GeV. The AMS-02 observations definitely confirm that, in addition to the secondary component, a new ingredient is at play in the cosmic positron radiation.

The observed anomaly in the positron flux and fraction, triggered a lot of ex-

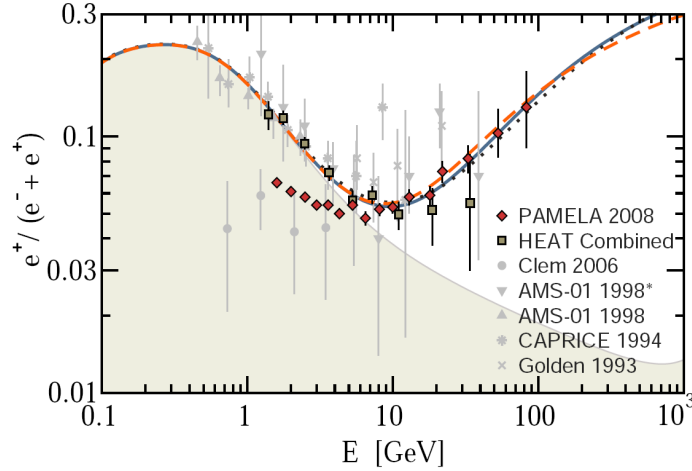


Figure 4.5: Data from pre-AMS-02 experiments, confirming the excess of positrons with respect to their secondary production (Shaded area computed by [Moskalenko 1998]). Figure adapted from [Yüksel 2009].

citement, as it could be interpreted as an indirect signature of the presence of dark matter species in the Galaxy, the so-called weakly interacting massive particles or WIMPs. Alternatively, it could be produced by nearby sources, such as pulsars.

In the following we revisit these two explanations, relying on two studies ([Boudaud 2015a] and [Boudaud 2016]) achieved within the Cosmic Rays Alpine Collaboration (CRAC).

4.3.1 Revisiting the DM hypothesis with the pinching method

Many investigations explored whether or not WIMPs might be the source of that anomaly. We refer the reader to the analyses by [Di Mauro 2014a, Di Mauro 2016, Lin 2015, Boudaud 2015a] and references therein. The vast majority of these studies are focused on the high energy part of the positron spectrum, above 10 GeV. Below this energy, solar modulation comes into play and complicates the interpretation of the data. Moreover, Galactic convection, diffusive re-acceleration, and positron annihilation on interstellar gas must be taken into account in addition to space diffusion. Finally, energy losses, which play a key role in the propagation of positrons, are mostly concentrated inside the Galactic disc whereas they extend all over the magnetic halo at high energy.

In this section, we present a new semi-analytical tool to take into account transport processes so far neglected, but important below a few GeV. It is essentially based on the pinching of inverse Compton and synchrotron energy losses from the magnetic halo, where they take place, inside the Galactic disc. The corresponding energy loss rate is artificially enhanced by the so-called pinching factor which needs to be calculated at each energy.

Thus this new tool allows us to reinvestigate the problem of the positron anomaly over the entire energy range covered by the AMS-02 data. In order to test the DM hypothesis, we have computed the interstellar positron flux yielded at the Earth by (i) the spallation of interstellar gas by CR protons and helium nuclei and (ii) WIMP annihilation.

4.3.1.1 Propagation of cosmic ray positrons with the pinching method

In this section, we recall the basics of the propagation of positrons in the Galaxy. We first present the transport equation and its semi-analytical resolution. We then introduce the *pinching method*, to solve semi-analytically the transport equation for electrons and positrons when *all* propagation effects are simultaneously taken into account.

The transport equation of positrons

The propagation of positrons and electrons is governed by the same propagation equation as for nuclei (equation 1.117), with the sole exception of the expression of different energy losses. Indeed, in addition to Coulomb interactions and ionisation losses, electrons and positrons (loosely dubbed electrons hereafter except when explicitly mentioned) lose energy by bremsstrahlung, synchrotron emission as well as inverse Compton (IC) scattering when they interact with the interstellar radiation field (ISRF), at respective rates b_{brem} , b_{sync} , and b_{IC} . Following the procedure described in [Delahaye 2010], we consider IC scattering in the relativistic regime and make use of the mean value of the GMF $\langle B \rangle = 1 \mu\text{G}$ [Ferrière 2001]. The total energy loss rate $b(E) \equiv dE/dt$ is then simply the sum of all the loss processes (their explicit expression can be found in [Strong 1998] and [Moskalenko 1998]).

Following the work of [Maurin 2001] (and reference therein), we assume the Galaxy to be axisymmetric and describe it by a two-zone model. The first, within which ISM is homogeneously distributed, represents the Galactic disc of half-height $h = 100 \text{ pc}$. Atomic densities are taken to be $n_{\text{H}} = 0.9 \text{ cm}^{-3}$ and $n_{\text{He}} = 0.1 \text{ cm}^{-3}$. It is embedded inside a much larger region, namely the magnetic halo (MH), of half-height L lying between 1 and 15 kpc. Both zones share the radius $R = 20 \text{ kpc}$. In practice, we assume space diffusion, as well as energy losses from synchrotron emission and IC scattering, to lie in the whole magnetic halo. On the other hand, DR, bremsstrahlung, Coulomb interaction, ionisation, and destruction take place only in the Galactic disc where the matter of the ISM is concentrated [Ptuskin 1997]. Hence, we split the energy losses $b(E, z)$ into a disc component $b_{\text{disc}} \equiv b_{\text{coul}} + b_{\text{brem}} + b_{\text{ioni}} + b_{\text{adia}}$ that includes the mechanisms taking place only in the thin disc, and a halo component $b_{\text{halo}} \equiv b_{\text{IC}} + b_{\text{sync}}$ for those taking place in the whole magnetic halo (including the disc). We impose a vanishing density of CRs outside the MH of the Galaxy.

Under a steady state and thin disc approximation, the density of CRs per unit

of space and energy $\psi \equiv dN/d^3x dE$ obeys the transport equation

$$\begin{aligned} & \vec{\nabla} \cdot \left[\vec{V}_c \psi(E, r, z) - K(E) \vec{\nabla} \psi(E, r, z) \right] \\ & + \partial_E [b(E, z) \psi(E, r, z) - 2h \delta(z) D(E) \partial_E \psi(E, r, z)] + 2h \delta(z) \Gamma \psi = Q(E, r, z), \end{aligned} \quad (4.24)$$

where Q represents the injection rate of CRs in the Galaxy. The CR flux at the Earth is here written as $\Phi(E, \odot) = v/4\pi \psi(E, \odot)$ where $r_\odot = 8.5$ kpc.

In the case of electrons, the semi-analytical resolution of the transport equation, *as it is*, is not possible. Indeed, the difficulty comes from the fact that electrons lose energy in the Galactic disc as well as in the whole magnetic halo. In the thin disc approximation, the energy loss rate can be written $b(E, z) = 2h \delta(z) b_{\text{disc}}(E) + b_{\text{halo}}(E)$, but the presence of the term b_{halo} prevents direct semi-analytical resolution of equation (4.24). Therefore, numerical codes have been adopted to predict the flux of electrons at the Earth. An alternative way, often used in literature, is to focus only on high energy electrons ($E > \text{few GeV}$). In this case, as shown in [Delahaye 2009], the dominant propagation processes are the space diffusion and the halo energy losses (b_{sync} and b_{IC}). The high energy approximation consists thus in neglecting the DR, the convection, the disc energy losses b_{disc} , and the destruction of CRs. Hence, the high energy transport equation can be written

$$-K(E) \Delta \psi + \partial_E [b(E) \psi] = Q(E, r, z), \quad (4.25)$$

where $b = b_{\text{halo}}$. equation (4.25) can be solved analytically using the pseudo-time method introduced by [Baltz 1999] and its solution can be expressed in term of Bessel functions [Delahaye 2008], where the Bessel coefficients evaluated at $z = 0$ are given by

$$P_i(E, 0) = \frac{-1}{b(E)} \int_E^{+\infty} dE_S B_i(E, E_S), \quad (4.26)$$

where

$$B_i(E, E_S) = \sum_{n=2m+1}^{+\infty} Q_{i,n}(E_S) \exp[-C_{i,n} \lambda_D^2]. \quad (4.27)$$

The function $Q_{i,n}$ is the Fourier transform of $Q_i(E, z)$ defined as

$$Q_{i,n}(E) = \frac{1}{L} \int_{-L}^L dz \varphi_n(z) Q_i(E, z), \quad (4.28)$$

where $\varphi_n(z) = \cos(nk_0 z)$ with $k_0 = \pi/2L$. The coefficient $C_{i,n}$ is defined as

$$C_{i,n} = \frac{1}{4} \left[\left(\frac{\alpha_i}{R} \right)^2 + (nk_0)^2 \right]. \quad (4.29)$$

Finally, the diffusion length λ_D is related to the space diffusion coefficient K and the energy loss rate b by the expression

$$\lambda_D^2(E, E_S) = 4 \int_{E_S}^E dE' \frac{K(E')}{b(E')}. \quad (4.30)$$

Note that the density ψ at the Earth can be written as

$$\psi(E, \odot) = \frac{-1}{b(E)} \int_E^{+\infty} dE_S \mathcal{I}(\lambda_D) Q(E_S, \odot), \quad (4.31)$$

where the halo integral \mathcal{I} is defined as

$$\mathcal{I}(\lambda_D) = \sum_{i=1}^{+\infty} J_0 \left(\alpha_i \frac{r}{R} \right) \frac{B_i(E, E_S)}{Q(E_S, \odot)}. \quad (4.32)$$

The flux at the Earth can then be computed for secondary electrons from proton and helium spallation [Delahaye 2009, Boudaud 2015a], as well as for primary electrons produced by DM annihilation [Delahaye 2008, Boudaud 2015a] and astrophysical objects like pulsars [Boudaud 2015a]. One can then perform comparisons with data, which have led to the discovery of a high energy positron excess requiring the presence of a dominant primary component above approximately 10 GeV. The high energy approximation is often used in the literature to derive conclusions for energies above that value. However, it is not obvious that the low-energy propagation effects (DR, convection, and energy losses in the Galactic disc) can be safely neglected, especially in the era of the AMS-02 high-accuracy measurements. Furthermore, due to high statistics, the region below 10 GeV is affected by the lowest experimental uncertainties and could thus provide the strongest constraints. These considerations led us to develop a new theoretical solution for the propagation of electrons over the energy range covered by AMS-02. This method dubbed *pinching method* is described in the following section.

The pinching method

At first sight, it seems that the semi-analytical method cannot be used to solve equation (4.24) when energy losses take place simultaneously in the MH and in the Galactic disc. The trick to overcome this issue is to impose the halo energy losses to take place, in an effective way, only in the Galactic disc. In other words, it consists in replacing the term b_{halo} in the transport equation (4.24) with an effective term $2h \delta(z) b_{\text{halo}}^{\text{eff}}$ while keeping the same solution ψ . By doing so, it will be possible to rewrite equation (4.24) in the form of equation (A.14) and to apply the Crank-Nicholson algorithm to solve it. This procedure consists thus in *pinching* the halo energy losses inside the disc, hence the name *pinching method*.

The function $b_{\text{halo}}^{\text{eff}}$ depends on all propagation effects electrons undergo. Nevertheless, from few GeV to 1 TeV, halo energy losses and space diffusion are the dominant propagation processes [Delahaye 2009]. Hence, at first order, we can reasonably neglect other processes and determine $b_{\text{halo}}^{\text{eff}}$ using the high energy approximation, i.e., equation (4.25). This approximation may not be completely valid for energies below a few GeV where other effects come into play and are expected to affect the calculation of $b_{\text{halo}}^{\text{eff}}$. But the more dominant these processes are, the less important halo energy losses turn to be, so that the precise value of the pinching factor does not matter at low energies.

Let us start with the pedagogical case of a monochromatic source of electrons $Q(E, r, z) = \delta(E - E_S) Q(r, z)$. In order to determine $b_{\text{halo}}^{\text{eff}}$, we compute first the exact high energy solution ψ^h using the pseudo-time method described above. The index h means that ψ^h is solution of equation (4.25) where IC and synchrotron energy losses are distributed in the whole MH. In that case, the electron density ψ^h at $z = 0$ is given by

$$\psi^h(E, r, 0) = \sum_{i=1}^{+\infty} J_0\left(\alpha_i \frac{r}{R}\right) P_i^h(E, 0), \quad (4.33)$$

where $P_i^h(E, 0)$ is given by the expression (4.26).

In a second step, we introduce ψ^d , solution of the high energy equation

$$-K(E) \Delta \psi^d + 2h \delta(z) \partial_E \left[b_{\text{halo}}^{\text{eff}} \psi^d \right] = Q(E, r, z), \quad (4.34)$$

where IC and synchrotron energy losses are confined to the disc. The condition $\psi^h(E, r, 0) = \psi^d(E, r, 0)$ enables then to determine the function $b_{\text{halo}}^{\text{eff}}$ such that

$$b_{\text{halo}}^{\text{eff}}(E, E_S, r) = \xi(E, E_S, r) b_{\text{halo}}(E), \quad (4.35)$$

where we introduced the pinching factor $\xi(E, E_S, r)$, given by the expression

$$\xi(E, E_S, r) = \frac{1}{\psi^h(E, r, 0)} \sum_{i=1}^{+\infty} J_0\left(\alpha_i \frac{r}{R}\right) \xi_i(E, E_S) P_i(E, 0), \quad (4.36)$$

with

$$\xi_i(E, E_S) = \frac{1}{B_i(E, E_S)} \left[J_i(E_S) + 4k_i^2 \int_E^{E_S} dE' \frac{K(E')}{b_{\text{halo}}(E')} B_i(E', E_S) \right]. \quad (4.37)$$

The coefficient J_i and k_i are given by

$$k_i^2 = \frac{S_i}{8h} \coth\left(\frac{S_i L}{2}\right). \quad (4.38)$$

and

$$J_i(E_S) = \frac{1}{h} \int_0^L dz_S \mathcal{F}_i(z_S) Q_i(E_S, z_S), \quad (4.39)$$

where $S_i \equiv 2\alpha_i/R$ and

$$\mathcal{F}_i(z) = \sinh \left[\frac{S_i}{2}(L - z) \right] / \sinh \left[\frac{S_i L}{2} \right]. \quad (4.40)$$

Once the effective term $b_{\text{halo}}^{\text{eff}}$ has been computed, it is possible to switch on low-energy effects and to solve equation (4.24) with *all* propagation processes using the usual Crank-Nicholson algorithm.

In practice, the electron source term is not a Dirac function but follows a continuum distribution in energy, which depends on the actual source considered (e.g. spallation in the disc, DM, pulsars). We therefore have to compute the pinching coefficients $\xi_i(E, E_S)$ for each electron energy at source E_S , which requires a very long computational time. However, an alternative way consists in averaging the quantity $\xi_i(E, E_S)$ over electron energies at source E_S . We show in Sec.4.3.1.1 that the effect arising from this simplification is kept below 0.2% over the whole energy range. We describe in the following how to perform such averaging.

Let $\mathcal{P}_i(E, E_S) = p_i(E, E_S) dE_S$ be the probability that an electron, injected with energy in the range $[E_S, E_S + dE_S]$ and measured at the Earth with an energy E , contributes to the i^{th} Bessel order of the Bessel transform $P_i^h(E, 0)$. The associated probability density p_i is then given by

$$p_i(E, E_S) = \frac{B_i(E, E_S)}{\int_E^{+\infty} dE_S B_i(E, E_S)}. \quad (4.41)$$

Therefore, the mean value of the pinching coefficients $\xi_i(E, E_S)$ is given by the expression

$$\bar{\xi}_i(E) = \frac{\int_E^{+\infty} dE_S \left[J_i(E_S) + 4k_i^2 \int_E^{E_S} dE' \frac{K(E')}{b(E')} B_i(E', E_S) \right]}{\int_E^{+\infty} dE_S B_i(E, E_S)}, \quad (4.42)$$

and

$$\bar{\xi}(E, r) = \frac{1}{\psi^h(E, r, 0)} \sum_{i=1}^{+\infty} J_0(\alpha_i \frac{r}{R}) \bar{\xi}_i(E) P_i(E, 0). \quad (4.43)$$

The mean pinching factor $\bar{\xi}(E)$ of secondary positrons is represented in figure 4.6 for the MIN, MED and MAX sets of propagation parameters. As it is expected the pinching factor is larger in the case of MAX, that corresponds to the larger value of K_0 and L , where the effect of the pinching must be more important.

Testing the pinching method

We wish to assess the theoretical uncertainty of the pinching method used to compute the positron flux. We focus our study on the energy range probed by AMS-02 i.e. the rough interval [100 MeV, 1 TeV]. To this aim, we compare the analytical

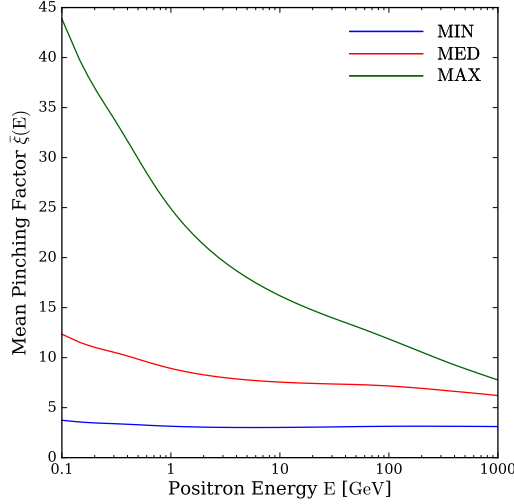


Figure 4.6: The mean pinching factor of secondary positrons computed for the MIN (blue), MED (red), and MAX (green) models as a function of the positron energy.

solution of equation (4.25) to the semi-analytical solution arising from the pinching method equation (4.34). Thus, we switch off the low-energy processes (DR, disc energy losses, convection, and destruction) and consider only halo energy losses and space diffusion processes (high energy approximation).

We represent in the left panel of figure 4.7 the secondary positron flux at the Earth computed in the high energy approximation scheme with the MED model. The red solid line represents the analytical solution whereas the blue dotted line represents the semi-analytical solution obtained when IC scattering and synchrotron energy losses are pinched in the Galactic disc. The relative error arising from the pinching method, is shown in the right panel of Figs. 4.7 for MIN (blue), MED (red), and MAX (green). Furthermore, we plot in the left panels of figure 4.8 and figure 4.9 the solutions for the primary positron flux produced respectively by a 350 GeV DM particle annihilating into $\mu^+\mu^-$ and a 1 TeV DM particle annihilating into $b\bar{b}$. The cross-section is taken to be $\langle\sigma v\rangle = 3 \times 10^{-26} \text{ cm}^3 \text{ s}^{-1}$. The relative error corresponding is represented in the right panels of figure 4.8 and figure 4.9.

For secondary positrons, this error is always kept below 0.1 %. Our method is therefore very accurate at computing positrons produce by p and He spallation onto the ISM. Regarding the primary contribution from DM annihilations, as long as the positron energy is well under the DM particle mass m_χ , the error is also very small, always below 0.2%. Close to m_χ , the steep decrease of the positron flux (which eventually vanishes at $E \geq m_\chi$) induces a fast increase of the relative error. However, the error is above 0.2% only for energies at which the positron flux is highly suppressed. Therefore, we can safely consider that our technique will not introduce any sizeable bias in the analysis.

Given its generality, expression (4.43) enables us to pinch IC and synchrotron

energy losses in the Galactic disc regardless of their origins, i.e. whether they are secondary or primary CRs. Thus, we can predict for the first time the electron flux at the Earth, including all propagation effects, using the semi-analytical resolution of the transport equation. In the following sections, we will apply our method to both secondary and primary CRs from DM annihilation to illustrate important differences with previous treatments. Our goal is now to recompute in the most accurate way propagation constraints from positron flux at the Earth and then reinvestigate the DM explanation of the excess.

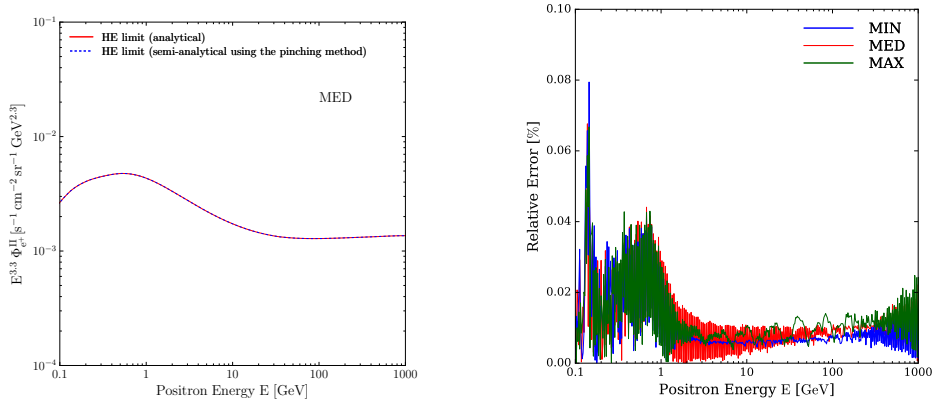


Figure 4.7: **Left panel:** IS secondary positron flux (multiplied by $E^{3.3}$) in the high energy approximation scheme for the MED model. **Right panel:** relative error using the pinching method for secondary positrons.

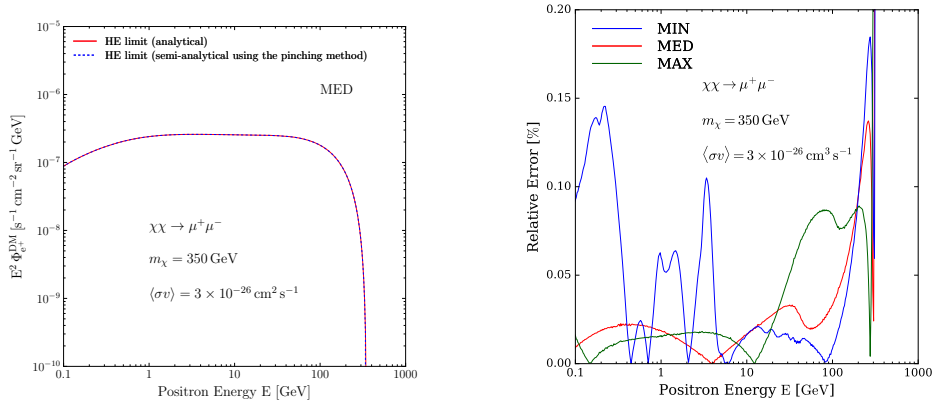


Figure 4.8: **Left panel:** IS positron flux (multiplied by E^2) produced by a 350 GeV DM particle annihilating into $\mu^+\mu^-$ pairs with $\langle\sigma v\rangle = 3 \times 10^{-26} \text{ cm}^3 \text{ s}^{-1}$ in the high energy approximation scheme for the MED model. **Right panel:** relative error using the pinching method.

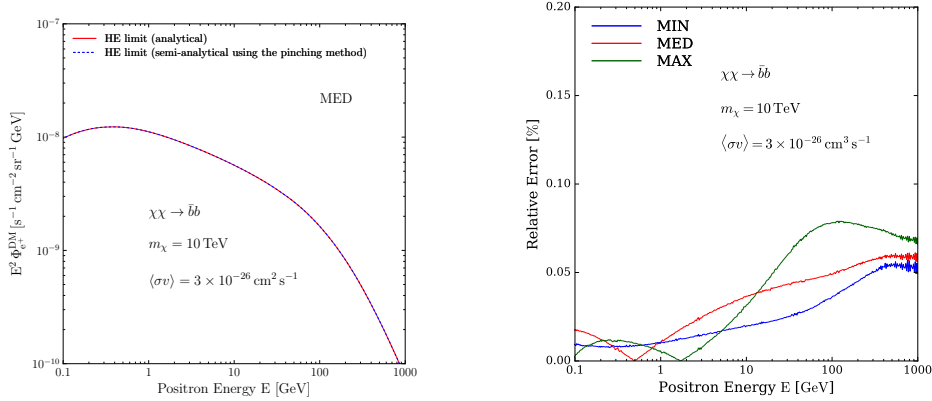


Figure 4.9: Same as figure 4.8 with a 1 TeV DM particle annihilating into $b\bar{b}$ pairs.

4.3.1.2 Implications for secondary positrons and the dark matter signal

In this section, we compute the source term of secondary positrons with the up-to-date primary proton and helium fluxes. The interstellar flux of secondary positrons is derived semi-analytically with the pinching method presented in section 4.3.1.1. We then focus on the DM signal coming, as an illustration, from a 10 TeV WIMP annihilating into $b\bar{b}$ quark pairs. These secondary and primary fluxes, computed including all the propagation processes, are compared with the ones derived previously with the high energy approximation.

Astrophysical background of secondary positrons

Secondary positrons originate from the decay of pions, kaons, and delta baryons produced by inelastic collisions of primary CR protons and helium nuclei on the ISM. The injection rate of secondary positrons reads:

$$Q^{\text{II}}(E, r, z) = 4\pi \sum_{j=p, \text{He}} \sum_{i=H, \text{He}} n_i \int dE_j \frac{d\sigma_{ji}}{dE}(E_j \rightarrow E) \Phi_j(E_j, r, z), \quad (4.44)$$

where n_i labels the atomic density of the nucleus i in the ISM, $d\sigma_{ji}/dE$ indicates the positron differential production cross-section, and Φ_j stands for the CR proton and helium fluxes. We use the parameterization of the proton-proton interaction differential cross-section derived by [Kamae 2006]. For proton-helium interactions, we take the parameterization from [Norbury 2007]. To obtain the proton and helium fluxes everywhere in the Galaxy, we apply the retro-propagation method introduced by [Maurin 2001], which requires as an input the TOA flux. This work is based on the latest measurements by AMS-02 [Aguilar 2015b, Aguilar 2015a] and CREAM [Yoon 2011]. The proton and helium fluxes are fitted using a model introduced in [Aguilar 2015b, Aguilar 2015a], where a single power law in rigidity R^γ exhibits a smooth transition to $R^{\gamma+\Delta\gamma}$ above the rigidity R_b . The smoothness of the spectral

index transition is described by the parameter s . An additional effective parameter α is used to fit the low-rigidity part of the proton flux. The interstellar (IS) primary fluxes can be described as follows:

$$\Phi_p^{\text{IS}}(R) = C \beta (1 - e^{\alpha R}) R^\gamma \left[1 + \left(\frac{R}{R_b} \right)^{\Delta\gamma/s} \right]^s, \quad (4.45)$$

and

$$\Phi_{\text{He}}^{\text{IS}}(R) = C \beta R^\gamma \left[1 + \left(\frac{R}{R_b} \right)^{\Delta\gamma/s} \right]^s, \quad (4.46)$$

with β the particle velocity. The force-field approximation [Fisk 1971] is used to obtain the relation between Φ_{IS} and Φ_{TOA} , i.e. respectively the IS and TOA fluxes. The value $\phi_F = 724$ MV determined by [Ghelfi 2016] is used hereafter unless explicitly stated. This model has been fitted to the measured fluxes, as it is shown in

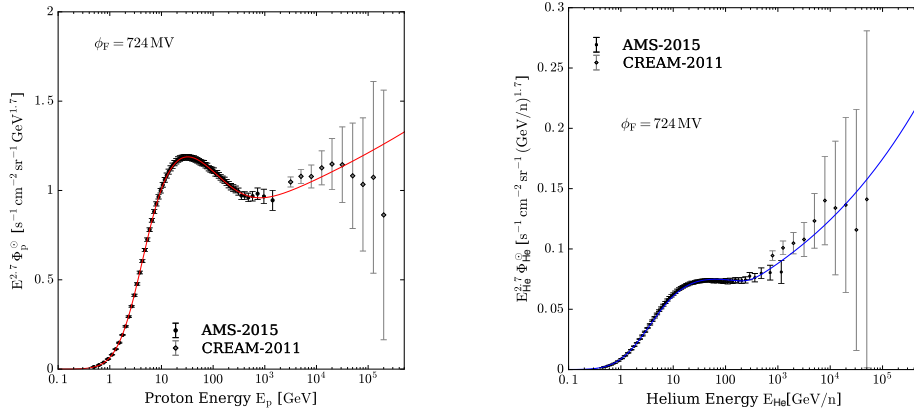


Figure 4.10: Proton (**left panel**) and helium (**right panel**) fluxes (multiplied by $E^{2.7}$) as a function of kinetic energy for AMS-02 [Aguilar 2015b, Aguilar 2015a] and CREAM [Yoon 2011] data. The red and blue curves are the fitted proton and helium fluxes corresponding respectively to Eqs. (4.45) and (4.46). We use the value from [Ghelfi 2016] of 724 MV for the Fisk potential ϕ_F .

figure 4.10, yielding the parameter values reported in Table 4.1.

Table 4.1: Values of the proton and helium flux parameters resulting from a fit to the AMS-02 [Aguilar 2015b, Aguilar 2015a] and CREAM [Yoon 2011] data assuming $\phi_F = 724$ MV.

	C [$\text{m}^{-2} \text{s}^{-1} \text{sr}^{-1} \text{GV}^{-1}$]	α [GV^{-1}]	γ	R_b [GV]	$\Delta\gamma$	s
Proton	$(2.71 \pm 0.02) \times 10^4$	-0.512 ± 0.012	-2.88 ± 0.01	424 ± 158	0.242 ± 0.056	0.156 ± 0.072
Helium	$(3.56 \pm 0.04) \times 10^3$	-	-2.77 ± 0.01	543 ± 163	0.213 ± 0.045	0.047 ± 0.018

The interstellar flux of secondary positrons, computed with the pinching method including all propagation effects, is represented in the left panel of figure 4.11 by

the solid lines for MIN (blue), MED (red), and MAX (green). The high energy approximation, where only diffusion and halo energy losses are taken into account, is featured by the dotted lines. It is henceforth possible to assess the error made when applying the high energy approximation often used in the literature to compute the positron flux above 10 GeV. This error is defined as $(\Phi_{\text{HE}}^{\text{II}} - \Phi^{\text{II}})/\Phi^{\text{II}}$ where the index HE stands for high energy. This quantity is plotted in the right panel of figure 4.11, and a few numerical values are displayed in Table 4.2. As already noticed by [Delahaye 2009], the high energy approximation tends to largely underestimate the amount of positrons below 5 GeV. Interestingly, we find on the other hand that above that value, the high energy approximation overshoots the exact result. Indeed, although convection and disc energy losses are subdominant with respect to halo energy losses and space diffusion, they still have a sizeable effect and tend to reduce the positron flux above 10 GeV. Moreover, the relative error strongly depends on the propagation parameters, the maximum value being reached for the MIN configuration. This can be understood by the fact that the convection velocity decreases along the sequence MIN, MED, MAX. Therefore, we observe that the discrepancy with the high energy approximation increases with higher values of the convection.

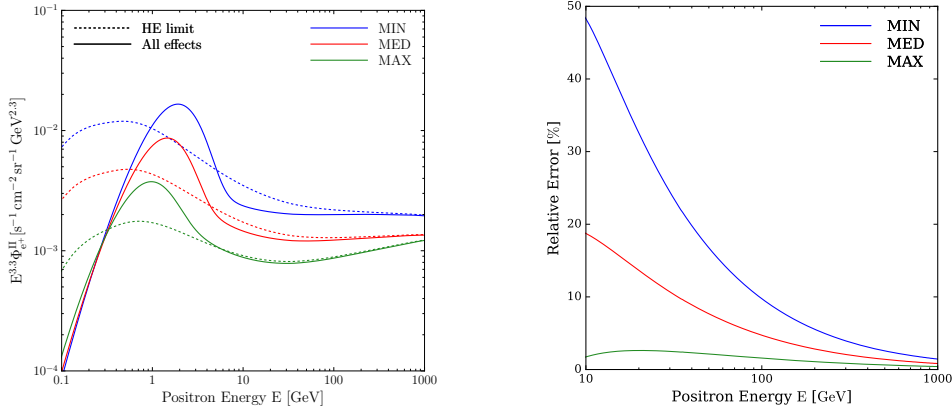


Figure 4.11: **Left panel:** interstellar flux (multiplied by $E^{3.3}$) of secondary positrons computed with all propagation effects (Φ^{II} , solid lines) and with the high energy approximation ($\Phi_{\text{HE}}^{\text{II}}$, dotted lines) for the MIN (blue), MED (red), and MAX (green) models. **Right panel:** relative error $(\Phi_{\text{HE}}^{\text{II}} - \Phi^{\text{II}})/\Phi^{\text{II}}$ above 10 GeV of the high energy approximation for secondary positrons compared to the exact result.

Primary positrons from the annihilation of dark matter particles

The source term of positrons produced by the annihilation of DM particles reads

$$Q^{\text{DM}}(E, \vec{x}) = \eta \langle \sigma v \rangle \frac{\rho_\chi^2(\vec{x})}{m_\chi^2} \left\{ g(E) \equiv \sum_i^N b_i \frac{dN}{dE} \Big|_i \right\}, \quad (4.47)$$

Table 4.2: Typical values of the relative error $(\Phi_{\text{HE}}^{\text{II}} - \Phi^{\text{II}})/\Phi^{\text{II}}$ (%) of the high energy approximation for secondary positrons compared to the exact result.

Positron energy (GeV)	10	50	100	500	1000
MIN	48	17	9.7	2.5	1.4
MED	19	7.7	4.7	1.4	0.8
MAX	1.7	2.0	1.5	0.6	0.4

where m_χ is the DM particle mass and $\langle\sigma v\rangle$ its average annihilating cross-section. The value of η depends on whether the DM particle is Majorana-type ($\eta = 1/2$) or Dirac-type ($\eta = 1/4$). We use the DM density profile introduced by [Navarro 1997], hereafter denoted NFW, with the local DM density $\rho_\odot = 0.3 \text{ GeV cm}^{-3}$ [Bovy 2012]. The energy distribution of positrons $g(E)$ at the source is obtained by summing over the individual contributions $dN/dE|_i$ for each annihilating channel i weighted by the branching ratio b_i . The individual energy distributions $dN/dE|_i$ are computed with the micrOMEGAs_3.6 package [Bélanger 2011, Bélanger 2014].

For illustrative purposes, we consider throughout this section a Majorana-type DM species with a mass m_χ of 10 TeV annihilating into $\bar{b}b$ quark pairs with the thermal cross-section $\langle\sigma v\rangle = 3 \times 10^{-26} \text{ cm}^3 \text{ s}^{-1}$. The IS flux of primary positrons computed with all propagation processes taken into account is featured by the solid lines in the left panel of figure 4.12. The high energy approximation corresponds to the dotted lines. The relative error $(\Phi_{\text{HE}}^{\text{DM}} - \Phi^{\text{DM}})/\Phi^{\text{DM}}$ is plotted in the right panel whereas a few numerical values are displayed in Table 4.3. We notice differences in the magnitude of this error, depending on the CR propagation configuration. We attribute them to the different values of the convective velocity V_c . Actually, positrons produced by DM annihilating throughout the MH are more sensitive to convection than secondary positrons, which originate from the Galactic disc. As a consequence, the error associated to the high energy approximation tends to be larger for primary positrons than for secondary ones. In the former case, it is significantly large in the MIN model for which V_c is the highest.

Table 4.3: Typical values of the relative error $(\Phi_{\text{HE}}^{\text{DM}} - \Phi^{\text{DM}})/\Phi^{\text{DM}}$ of the high energy approximation for primary positrons compared to the exact result.

Positron energy (GeV)	10	50	100	500	1000
MIN	74	18	10	2.6	1.4
MED	22	6.2	3.8	1.1	0.6
MAX	4.4	1.3	0.7	0.5	0.4

In summary, we have computed the flux of positrons including all the propagation effects for the secondary component as well as the DM signal. We have shown that low-energy effects modify drastically the shape of the positron spectrum. In

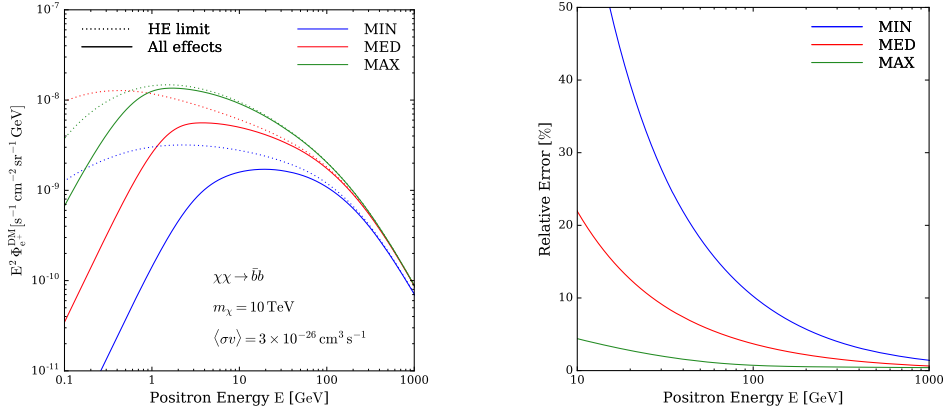


Figure 4.12: **Left panel:** interstellar flux (multiplied by E^2) of primary positrons computed with all propagation effects (Φ^{DM} , solid lines) and with the high energy approximation ($\Phi_{\text{HE}}^{\text{DM}}$, dotted lines) for a 10 TeV WIMP annihilating into $\bar{b}b$ pairs with $\langle\sigma v\rangle = 3 \times 10^{-26} \text{ cm}^3 \text{ s}^{-1}$, for the MIN (blue), MED (red), and MAX (green) models. **Right panel:** relative error $(\Phi_{\text{HE}}^{\text{DM}} - \Phi^{\text{DM}})/\Phi^{\text{DM}}$ above 10 GeV of the high energy approximation for primary positrons compared to the exact result.

addition, these effects could have a sizeable importance above 10 GeV, in contrast to what has been assumed in the literature. At 10 GeV, they modify the prediction up to 48% for the secondary component, and up to 74% for the DM signal, in the MIN configuration. Therefore, neglecting the low-energy CR propagation processes could lead to misleading interpretations when attempting to compare the theoretical predictions to the high-accuracy data provided by the AMS-02 collaboration. All the results presented in the following of this paper are obtained using the pinching method to solve the *full* transport equation equation (4.24).

4.3.1.3 Constraining propagation parameters with AMS-02 data

Secondary positrons and propagation models

In section 3.2.1.2, we have argued that low energy secondary positrons can be used, in addition to the B/C ratio, for constraining the propagation scenarios. Indeed, as we have shown in section 4.3.1.2, the competition between DR, convection, and disc energy losses, tends to the formation of a bump around 2 GeV, which can overshoot the data. This argument was first used qualitatively in [Lavalle 2014]. However, already above 5 GeV, there might be parts of the $\{V_c, V_a\}$ parameter space that actually lead to a *decrease* of the flux. This is particularly pronounced in the MIN model as shown in figure 4.11. We will therefore recompute the constraints of Lavalle 2014 with i) our full resolution method at low energy, and ii) updated fluxes measured by AMS-02. This will lead to more robust and more stringent constraints on the propagation parameters.

Skimming method for the propagation models

We compute the secondary positron flux for the 1,623 propagation parameter sets selected by the B/C ratio analysis of [Maurin 2001]. These parameters are sorted from a uniform linear grid in the propagation parameter space, namely $(\delta, K_0, L, V_c, V_a)$, and are in agreement with the HEA03 B/C ratio within 3 standard deviations. The secondary positrons are calculated including all the effects described in section 4.3.1.1 and recalled hereafter: diffusion, convection, reacceleration, high energy losses (IC, synchrotron), low-energy losses (adiabatic, ionisation, coulombic, bremsstrahlung), retro-propagation of the proton and helium fluxes, annihilation, and solar modulation. One may worry that our constraints highly depend on solar modulation modelisation. Although no extensive study of solar modulation for positrons during the period for which AMS-02 has been taking data is available, this modulation is commonly assumed to affect equally particles of same rigidity and same sign of charge. This assumption will soon be tested by the forthcoming AMS-02 measurements of the variations of the positron-to-proton ratio over the last solar cycle. Therefore, within the force-field approximation, we can rely on studies of the proton solar modulation such as in [Ghelfi 2016] and make use of the Fisk potential derived therein. In a conservative approach, we lower the secondary prediction as much as possible using the 3σ *highest* Fisk potential which was found by [Ghelfi 2016] to be 830 MV. The constraints derived with this high value might not be optimal. They already provide quite strong conclusions as discussed in the following sections.

In order to quantify, for a given propagation model, the deviations of the predicted flux from the data, and any potential overshooting, we follow the criterion advocated in [Lavalle 2014], and first define, for each energy bin, the quantity

$$Z_i = \frac{\Phi_{e^+}^{\text{II}}(E_i) - \Phi^{\text{data}}(E_i)}{\sigma^{\text{data}}(E_i)}, \quad (4.48)$$

where $\Phi_{e^+}^{\text{II}}(E_i)$ is the predicted secondary positron flux in a given energy bin, $\Phi^{\text{data}}(E_i)$ is the corresponding experimental flux, and $\sigma^{\text{data}}(E_i)$ its experimental uncertainty. A propagation model is allowed provided that Z_i does not exceed 3 whatever the energy bin. In other words, for selected models, we allow predictions to overshoot the data by at most 3 standard deviations in each energy bin. Note that, unlike Lavalle 2014, we do not combine the values of Z_i at different energies into a single statistical test. To do so, one would need to know correlations of experimental uncertainties between different energies, but those are not provided by the AMS-02 collaboration. One could assume uncorrelated uncertainties, but this would be only true for the statistical ones. We therefore consider bins separately, making our test a conservative choice over which there could be room for some improvement.

Results and discussion

An illustration of the selection method is presented in the left panel of figure 4.13. In this figure, we display the AMS-02 positron flux and superimpose a colored band whose edges correspond to the envelope of the 1,623 predictions for the secondary positrons. The red colored region represents predictions that overshoot the data according to our definition and therefore contains the excluded models. On the other hand, the yellow colored region contains all allowed models. As an example, we display in dashed green a model that fulfills the Z-score constraint defined as $Z_s = \max_{E_i \in \text{data}} (Z_i) < 3$, and in dashed red two models that do not respect it. The right panel of figure 4.13 illustrates the allowed propagation models that remain *after* the selection process: only 54 propagation sets out of 1,623 survive the criterion. Interestingly, one can see that the positron excess measured by AMS-02 seems to start already above 2 GeV, and not 10 GeV as often advocated. This will reveal itself very complicated to explain in terms of a single primary component. Selected models are those which minimize the secondary production over the whole energy range. Figure 4.14 compares ranges of selected parameters with respect to their initial ones. One can see that our new method enables us to drastically reduce the allowed parameter space with respect to former B/C analysis. Furthermore, we confirm the lifting of the degeneracy between K_0 and L , as one can see from the top-left panel of figure 4.14, as well as the high sensitivity to parameters that (mainly) control propagation at low energies, namely V_a and V_c . Practically, common characteristics of these models are i) a large halo size L (ranging from 8.5 to 15 kpc) together with relatively high K_0 , typically $\geq 0.06 \text{ kpc}^2 \text{ Myr}^{-1}$, ii) a slope of the diffusion coefficient δ equal to 0.46, the minimal value allowed by the B/C analysis used in this study, iii) small values of the convective wind $V_c \leq 6 \text{ km s}^{-1}$ accompanied by large values of the Alfvén waves velocity $V_a \geq 100 \text{ km s}^{-1}$. The fact that, in our analysis, δ is confined to the edge of the range indicates that even smaller values are likely to be favoured by positron data. This affirmation is indeed confirmed since, during the writing of this article, AMS-02 published the value of $\delta = 0.333 \pm 0.015$ from a power law fit of the high rigidity pure diffusive regime of their B/C data [Aguilar 2016b].

These features can be readily understood. As reminded above, the secondary positron flux scales with $1/\sqrt{K_0}$. Hence, models with larger K_0 result in lower density of positrons at Earth compared to models with small diffusion coefficient. Given that secondary-to-primary ratios mostly constrain the K_0/L ratio, selected models have a relatively high L , as well as a small value of δ , the former being anti-correlated with K_0 . Finally, values of the selected couples $\{V_a, V_c\}$ minimize the bump at low energies and are therefore favored by the analysis. Interestingly, in the recent literature, models with a large halo size have been suggested by other observables. Especially, the study of the antiproton-to-proton [Aguilar 2016a] and boron-to-carbon [Aguilar 2016c] ratios measured by AMS-02 point as well toward MAX-like propagation model [Giesen 2015, Korsmeier 2016]. Radioactive species such as $^{10}\text{Be}/^9\text{Be}$ [Strong 2001, Putze 2010] hint also at similar models although the dependence of this observable on the local density (local bubble) may bias the

result. At other wavelengths (e.g. radio) [Di Bernardo 2013] and in diffuse gamma ray analyses [Ackermann 2012a], a high value of L also seems to be preferred. Even more recently, it has been shown that, as far as the stochastic injection of cosmic rays is concerned, the regularity of the proton spectrum could arise from a large magnetised halo size [Genolini 2016]. Our results are in very good agreement with all these different observables, which therefore all underline the need for a primary positron component in order to explain data above a few GeV. In the next section, we investigate the consequences of our updated propagation constraints on the hypothesis of dark matter annihilations as the source of this primary component.

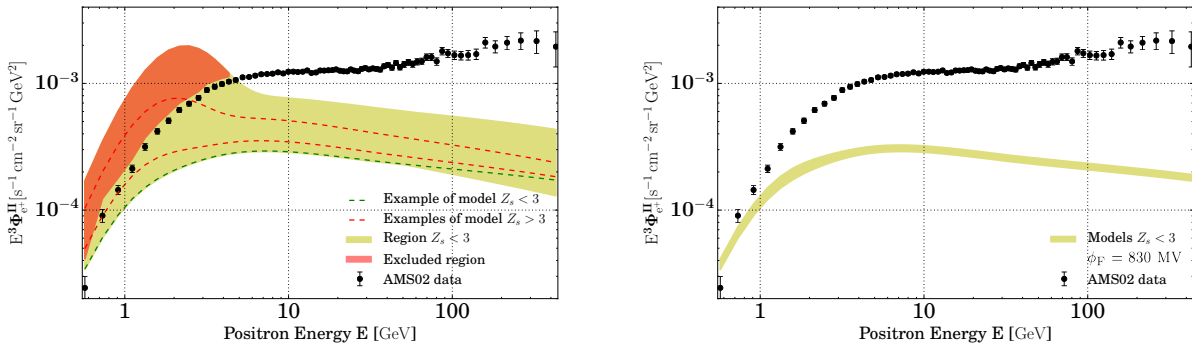


Figure 4.13: **Left panel:** positron flux (multiplied by E^3) from the AMS-02 data compared to the envelope of the 1,623 flux predictions for the secondary positrons (colored band). The red colored region is the domain which is crossed by all the excluded models. The dashed red lines show two examples of models that do not fulfill the constraints $Z_i < 3$ for all energy bins i (i.e. the Z-score constraint defined as $Z_s = \max(Z_i) < 3$). The dashed green line represents an example of a model that fulfills the constraints $Z_i < 3$ for all energy bins i . **Right panel:** positron flux (multiplied by E^3) from the AMS-02 data compared to the envelope of the 54 models fulfilling $Z_i < 3$ for all energy bins i .

4.3.1.4 Dark matter interpretation of the AMS-02 data

Dark matter fitting procedure

The most striking feature of the positron flux data is the high energy gap with respect to the secondary prediction. Filling this gap with a dark matter component has been the concern of many studies, but semi-analytical methods were always restricted above 10 GeV (see for example [Boudaud 2015a]). Hereafter, we use the resolution method of section 4.3.1.1 to compute the positron flux resulting from dark matter annihilation over all the energy range covered by AMS-02 data. Due to the important statistics of data below 10 GeV, constraints based only on the quality of the fit become more stringent.

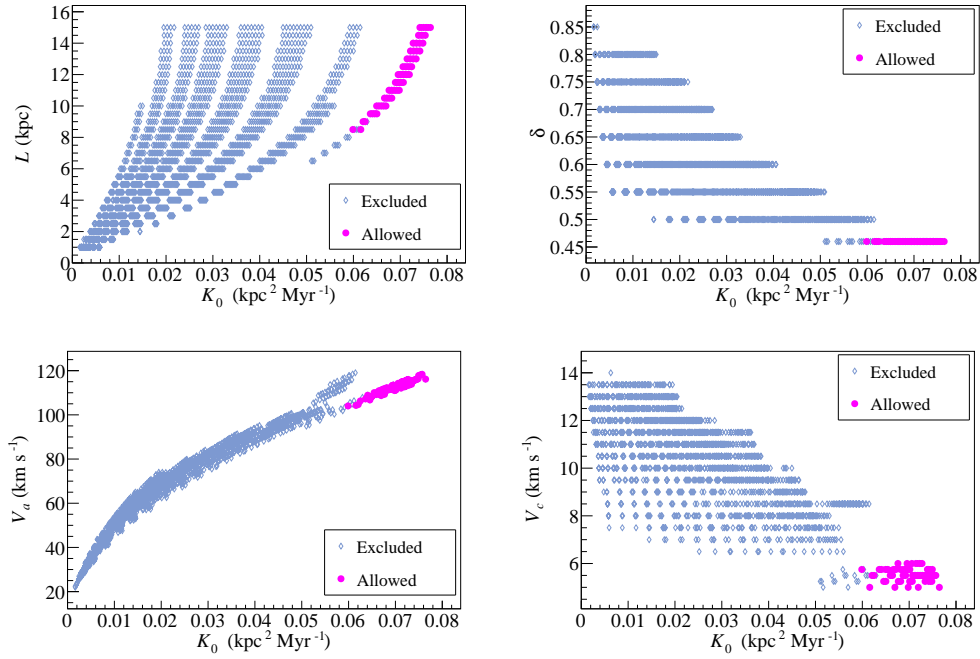


Figure 4.14: Projection of the 1,623 propagation parameter sets selected by the B/C ratio [Maurin 2001] in the $K_0 - L$, $K_0 - \delta$, $K_0 - V_a$, and $K_0 - V_c$ planes. The light blue diamonds show the propagation parameter values which are excluded, whereas the magenta circles denote the values which are allowed by this analysis.

Technically, we use the 54 propagation models selected in section 4.3.1.3 to compute the theoretical prediction of the positron flux, which is the sum of a primary component coming from dark matter annihilation and the secondary component,

$$\Phi_{e^+}^{\text{th}} = \Phi_{e^+}^{\text{DM}} + \Phi_{e^+}^{\text{II}}. \quad (4.49)$$

We consider two different cases: DM particle annihilating into a general final state composed of quarks, leptons, and bosons, and the case of a leptophilic DM which annihilates into a combination of leptonic channels through a light mediator.

In a similar vein as [Boudaud 2015a], we make no assumptions about the underlying DM model and consider the possibility that DM annihilates into a combination of channels, namely $b\bar{b}$, W^+W^- , e^+e^- , $\mu^+\mu^-$, and $\tau^+\tau^-$, with a branching ratio free to vary. The limited choice of these channels relies on the fact that they describe relatively well the various spectral shapes, and avoids introducing too many free parameters. For example, the $b\bar{b}$ channel typically describes the spectra of the different quark and gluon final states. To a certain extent positron spectra following Higgs decay are also similar to the $b\bar{b}$ case, since the Higgs decays dominantly into hadrons. Finally, the W^+W^- channel is chosen to describe positron spectrum from gauge bosons decay. On the other hand, given the high dependence of the

spectra on the lepton flavour, we allow non-universal lepton contributions. The DM annihilation spectra of all these channels are calculated using `micrOMEGAs_3.6` [Bélanger 2011, Bélanger 2014].

Concerning the case of a leptophilic DM species, only three branching ratios are introduced as free parameters. They correspond to the three leptonic channels ($\phi\phi \rightarrow 2e^+2e^-$, $\phi\phi \rightarrow 2\mu^+2\mu^-$, $\phi\phi \rightarrow 2\tau^+2\tau^-$), where ϕ is a light scalar mediator. In this case the annihilation spectra are taken from the PPC4DMID [Cirelli 2011, Ciafaloni 2011].

For both cases, the DM component thus depends on the branching ratios, on the DM mass m_χ , and on $\langle\sigma v\rangle$ the velocity averaged annihilation cross-section, henceforth loosely dubbed "the cross-section".

The search for the best fit to the positron data is led in the following way: for twenty DM masses logarithmically distributed in the range [100 GeV ; 1000 GeV], we perform a fit to the AMS-02 measurements of the positron flux using MINUIT. We determine the minimum value of the χ^2 defined as

$$\chi^2 = \sum_i \left\{ \frac{\Phi^{\text{data}}(E_i) - \Phi^{\text{th}}(E_i)}{\sigma^{\text{data}}(E_i)} \right\}^2. \quad (4.50)$$

In the case of the five annihilation channels, the parameter space is of dimension six: two corresponding to m_χ and $\langle\sigma v\rangle$, and four to the branching ratios b_i given the constraint $\sum_i b_i = 1$. In the case of the leptophilic DM, the parameter space is of dimension four. To remain conservative, for each propagation model, we perform the fit seven times, varying the Fisk potential in the 3σ range [647 MV ; 830 MV] where 724 MV corresponds to the nominal value of the potential [Ghelfi 2016]. In the following, we first discuss results for DM annihilation into the five channels $b\bar{b}$, W^+W^- , e^+e^- , $\mu^+\mu^-$, and $\tau^+\tau^-$, then for the leptophilic DM case.

Results of the analysis

We plot in figure 4.15 the main result of our analysis, namely the evolution of the χ^2 per degrees of freedom χ_{dof}^2 , as a function of the DM mass m_χ . The two plots correspond to DM annihilating into a fitted combination of $b\bar{b}$, W^+W^- , e^+e^- , $\mu^+\mu^-$, and $\tau^+\tau^-$ channels (left panel) and $\phi\phi \rightarrow 2e^+2e^-$, $\phi\phi \rightarrow 2\mu^+2\mu^-$, and $\phi\phi \rightarrow 2\tau^+2\tau^-$ channels (right panel). The results are displayed for different values of the Fisk potential (nominal value, and $\pm 3\sigma$). In the direct annihilation case, as one can see from figure 4.15, we find a global best fit corresponding to a minimal $\chi_{\text{dof}}^2 = \chi^2/\text{ndof} = 100/66 = 1.5$. It is obtained for a DM mass of $m_\chi = 264$ GeV annihilating into $b\bar{b}$, e^+e^- , and $\mu^+\mu^-$ with branching ratios of 0.92, 0.05, and 0.03 respectively (the branching ratios for the channels W^+W^- and $\tau^+\tau^-$ are found to be zero). The associated annihilation cross-section is ~ 272 times larger than the thermal cross-section. It means that a peculiar enhancement mechanism is required, as it has been found in many former studies.

Similarly, in the leptophilic case, we find a global best fit associated to a $\chi_{\text{dof}}^2 = 1231/68 = 18$. It corresponds to a DM mass m_χ of 183 GeV annihilating into

$\phi\phi \rightarrow 2e^+2e^-$ and $\phi\phi \rightarrow 2\tau^+2\tau^-$ with respective branching ratios of 0.09 and 0.91. The branching ratio of the channel $\phi\phi \rightarrow 2\mu^+2\mu^-$ is chosen as zero by the fit.

Interestingly, values of the minimal χ_{dof}^2 are high, especially in the leptophilic case. To understand results of the fitting procedure, we plot on figure 4.16 the theoretical positron fluxes obtained using the best fit models, together with the data. In the direct annihilation case, one can note the remarkably good agreement of the fit with the data up to 300 GeV. However, the prediction is in discrepancy with the last two data points at two to four sigma. These two points (and marginally the first one) are responsible for the low quality of the fit yielding a $\chi_{\text{dof}}^2 = 1.5$ or equivalently a p -value of 0.4%. From left panel of figure 4.15, we observe that imposing the DM mass to be above 450 GeV in order to explain the last two points of the positron flux would yield an even poorer χ_{dof}^2 , above 2. In the leptophilic case, the picture is even worse: no single part of the spectrum can be accurately described when one tries to fit the whole energy range. Thus, the resulting minimal χ_{dof}^2 is extremely bad.

Let us now discuss the evolution of χ_{dof}^2 with respect to the DM mass. First of all, we observe that, whatever is the solar modulation, the evolution of the χ_{dof}^2 is similar: with increasing DM mass, the χ_{dof}^2 first decreases, reaching a minimal value around a few hundred GeV, and then increases. Low DM masses cannot account for the high energy part of the positron flux since no positrons with energy above the DM mass can be emitted. Thus, at first, the goodness of the fit is improving (i.e. the χ_{dof}^2 decreases) with the DM mass. Interestingly, above a peculiar DM mass, none of the channels can produce low-energy positrons in a sufficient amount to explain the low energy part of the data. Consequently the goodness of fit degrades, i.e. the χ_{dof}^2 increases. As a result, there is a “middle ground” at a peculiar mass (the value changes with annihilation channels and Fisk potential) which corresponds to the best possible attempt to fulfill similarly high- and low-energy constraint. Somehow, the flatness of the spectrum is such that it is not possible to accommodate it entirely with a single primary component. We also note the drift of the best fit toward lower DM masses as the solar modulation increases. This is simply because the low energy part of the fluxes is more and more suppressed with an increasing Fisk potential. Hence, additional low-energy positrons are needed (i.e. lighter DM) to fit the data. However increasing the Fisk potential is not necessarily associated with an improving χ_{dof}^2 : the actual shape of the annihilation spectrum matters, as it can be seen by comparing the upper and lower panels of figure 4.16. Indeed, in the direct annihilation case increasing the Fisk potential tends to improve the fit, whereas in the case of annihilation through light mediators it worsens it.

In summary, we find challenging to interpret the excess in terms of pure DM annihilations, since our conservative analysis always leads to low-quality fits of the data. It is remarkable that the shape of the positron excess, with respect to the pure secondary prediction, cannot be captured by annihilations of a single DM species. This feature is due to: i) the high precision of the AMS-02 data; ii) the possibility to fit the whole data range thanks to our new semi-analytical resolution method. It is reasonable to believe that a fit above 10 GeV would not have had this

issue. Similarly, we expect multi-component models, with e.g. one heavy and one light DM species to be able to fit the excess. In the next section, we discuss how robust this conclusion is against a relaxation of our selection criterion of propagation parameters, as well as the inclusion of theoretical uncertainties in the modelling.

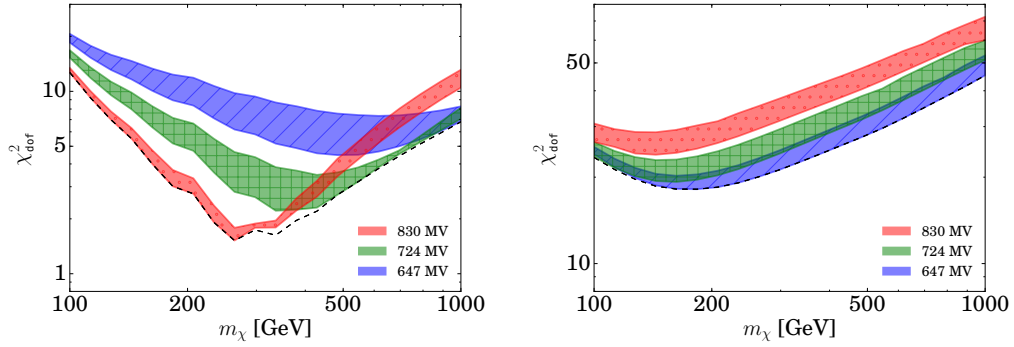


Figure 4.15: Evolution of the χ_{dof}^2 as a function of the DM mass m_χ in the case of direct annihilation into standard model particles (**left panel**) and annihilation into four leptons through light mediators (**right panel**). The results of the analysis are displayed using a Fisk potential of 830 MV, 724 MV, and 647 MV in red, green, and blue, respectively. The black dashed line represents the minimal χ_{dof}^2 among the seven Fisk potentials and 54 propagation models. The thickness of the colored band is obtained by scanning over the 54 propagation models.

4.3.1.5 Robustness of the results

In this section, we assess the robustness of the conclusions drawn above, under changes in the skimming method and source term modelisation. Since our selection criterion does not combine information of data points together but makes use of them separately, we will investigate first whether a specific data point of the positron flux can be leading the constraints, eventually biasing the results. Indeed, one can see on figure 4.13 that the position of the first data point measured by AMS-02 is very low with respect to the expected trend from the predicted secondary positron flux. Secondly, we evaluate uncertainties of the secondary component source term in order to attest that they can be safely neglected in our analysis. These uncertainties come from the experimental measurement of the AMS-02 primary fluxes, as well as the choice of p and He spallation cross-sections onto the ISM.

To check whether the first data point is more discriminating than the higher energy ones, we repeat the skimming method presented in section 4.3.1.3 discarding this peculiar point from the analysis. The comparison between the results of the analysis with and without the first point is reported in the first two lines of Table 4.4. Not surprisingly, the number of selected models do increase. However, in a much striking way than expected, we notice that it increases more than twelve

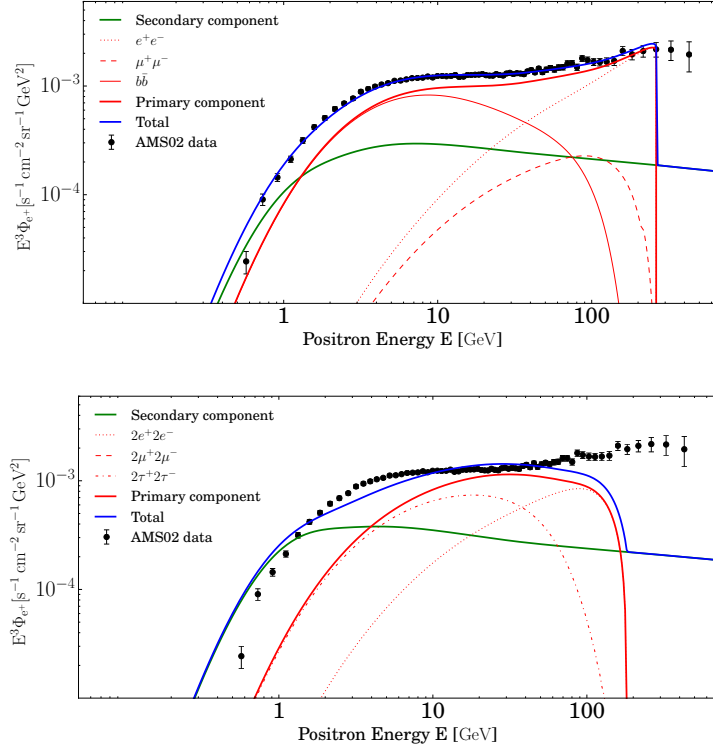


Figure 4.16: Global best fit for the direct annihilation into standard model particles (**upper panel**) and annihilation into four leptons through light mediators (**lower panel**). The DM (resp. secondary) component is displayed in thick red (resp. thick green) while the total flux, the sum of these two components, is shown in thick blue. In the case of direct annihilation, the electron, muon, and b quark channels are displayed in dotted, dashed, and solid red line respectively. In the case of annihilations through light mediators, the electron and τ channels are displayed in dotted and dot-dashed red line respectively. The AMS-02 positron flux, including experimental uncertainties, is superimposed with black dots.

times. The parameter space counts now 623 allowed models. We conclude that, within our skimming method, the first point of the flux has indeed a very strong discriminating power. To check that it was a peculiarity of the first data point, we repeat successively the skimming method discarding up to the three first data points. The results are reported in Table 4.4 and confirm the singularity of the first point: the number of allowed models never exceeds 692. Let us emphasize that even without its first point, the positron flux provides stringent constraints on propagation parameters: it enables to rule out two thirds of the parameter space allowed by former boron-over-carbon analysis. To check the impact of a bigger parameter space on our DM analysis (see section 4.3.1.4), we repeat it with the 623 propagation models selected without the first point of the positron flux. In the case

of DM annihilating directly into a combination of $b\bar{b}$, W^+W^- , e^+e^- , $\mu^+\mu^-$, and $\tau^+\tau^-$ channels, the χ_{dof}^2 of the best fit is now of 1.1, which corresponds to a p -value of 26%. Such a value might indicate that DM annihilation can still explain the positron excess. However, the associated DM mass is 336 GeV, causing a cut-off of the primary positron flux at this energy, not observed in AMS-02 data. Hence, with improving statistics in this last two bins, it is likely that the χ_{dof}^2 will quickly degrade. On the other hand, imposing the DM mass to be above the energy of the last data point increases the χ_{dof}^2 to a value above 2, synonym of a bad quality fit. In the hypothesis of leptophilic DM annihilating into $\phi\phi \rightarrow 2e^+2e^-$ and $\phi\phi \rightarrow 2\tau^+2\tau^-$ through a light mediator, the best fit has a χ_{dof}^2 larger than 10. Thus, the conclusion remains unaltered. We now turn to assessing the impact of uncertainties associated

	Allowed propagation models	δ	K_0 (kpc ² Myr ⁻¹)	L (kpc)	V_c (km s ⁻¹)	V_a (km s ⁻¹)
All data points	54	0.46	0.0599 – 0.0764	8.5 – 15	5 – 6	104.0 – 118.3
First point excluded	623	0.46 – 0.7	0.0240 – 0.0764	4.5 – 15	5 – 12	70.9 – 119.0
First two points excluded	623	0.46 – 0.7	0.0240 – 0.0764	4.5 – 15	5 – 12	70.9 – 119.0
First three points excluded	692	0.46 – 0.7	0.0215 – 0.0764	4 – 15	5 – 12	70.4 – 119.0

Table 4.4: Number of propagation models allowed after the analysis of section 4.3.1.3, and associated parameter ranges. We present results of the skimming method discarding successively up to the three first data points.

to the source term of the secondary component on our conclusions. A key ingredient of the secondary positron prediction is an accurate measurement of the flux of their progenitors, mainly proton and helium nuclei. In section 4.3.1.2, we gave the parameterization used to describe these fluxes, as well as the best-fit value of the parameters. Given the finite precision of AMS-02 measurements, uncertainties in the determination of these parameters can affect our secondary positron prediction. To estimate the uncertainty associated to the fitting procedure, we developed an original method that takes into account both systematic and statistical uncertainties of the measured primary fluxes. We proceed in the following way: we first generate mock data of the primary fluxes within their total uncertainties, fit them with our parameterisation and compute a new secondary positron flux. Repeating this process 10,000 times allows us to determine the distribution of the secondary positron flux in each energy bin. The mock data for the primary fluxes are generated according to the following strategy: for each data point a new random value is computed as $\bar{\Phi}^{\text{data}}(E_i) + \delta\Phi^{\text{stat}}(E_i) + \delta\Phi^{\text{syst}}(E_i)$, where $\bar{\Phi}^{\text{data}}$ is the mean value of the flux in the energy bin E_i , $\delta\Phi^{\text{stat}}$ is drawn from a Gaussian distribution with standard deviation $\sigma^{\text{stat}}(E_i)$ and $\delta\Phi^{\text{syst}}$ is drawn from a uniform distribution of size $2\sigma^{\text{syst}}(E_i)$. These two uncertainties σ are provided by the AMS-02 collaboration in [Aguilar 2015b] and [Aguilar 2015a]. Results are displayed in figure 4.17. On the left panel is shown the distribution of our prediction in each energy bin, compared to the fiducial value

calculated with the MED propagation model. The relative uncertainty displayed on the right panel is found to increase with energy, with a maximum of 7% at 500 GeV. The experimental uncertainties of the positron flux are respectively of 6% and 30%, much larger than the theoretical uncertainty yielded by the primary fluxes. We thus conclude that the precision in the measurement of the primary fluxes is sufficiently small not to alter our analysis.

A second major ingredient entering the source term for secondary positrons are the cross-sections adopted for the p and He interaction with the ISM. In our studies, we used proton-proton cross-section from [Kamae 2006]. We recall that any other nucleus-nucleus cross-section can be obtained by rescaling this one with an empirical factor, which we took from [Norbury 2007]. The choice of proton-proton cross-section from [Kamae 2006] is motivated by the fact that, at low energy, this model produces *less* positrons than the commonly used [Moskalenko 1998], which includes the parameterisation of the Lorentz invariant obtained by [Tan 1983b] and [Badhwar 1977]. We therefore adopt a strategy similar to our treatment of solar modulation, which minimizes as much as possible the positron flux below 10 GeV by using a very high Fisk potential, on the edge of current allowed values. Although there is an uncertainty associated to the cross-section and solar modulation modelling, our choices lead to conservative results and thus robust conclusions.

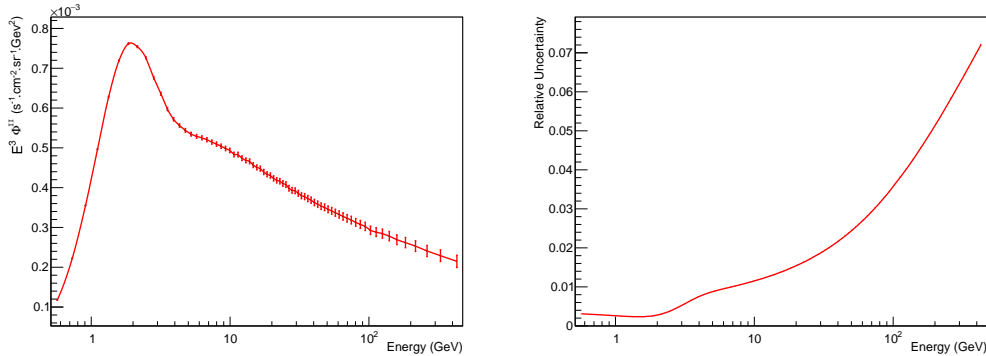


Figure 4.17: **Left panel:** secondary positron flux (multiplied by E^3) as a function of the positron energy. The error bars represent the uncertainty due to the experimental uncertainty on the proton and helium fluxes. **Right panel:** relative uncertainty on the secondary positron flux, as a function of the positron energy.

4.3.1.6 Conclusion

Three years ago, the AMS-02 collaboration released the most precise measurement of the positron flux in the energy range 0.5 to 500 GeV, confirming the high energy excess with respect to pure secondary predictions. Until now, most of the studies trying to explain this excess in terms of DM annihilations restricted themselves to energies above 10 GeV by prejudice and to simplify computations. Indeed,

below this energy, several mechanisms taking place in the halo, namely diffusive reacceleration and convection, as well as energy losses in the disc, make the resolution of the propagation equation much more involved. However, a consistent model should be able to explain the positron flux over the entire energy range covered by the AMS-02 data.

We have therefore reinvestigated the problem of the positron anomaly with a new semi-analytical resolution method enabling us to take into account transport processes so far neglected but important below a few GeV. The key idea is to pinch energy losses occurring in the whole magnetic halo, namely inverse Compton and synchrotron, inside the Galactic disc. The corresponding energy loss rate is artificially enhanced by a so-called pinching factor which is calculated for each energy. This allows us to solve the CR propagation equation using a Bessel expansion and the Cranck-Nicholson scheme.

With this procedure, we recover the correct high energy positron flux at the per mille level and extend the computation to low energies, with the main advantage of a very fast resolution technique compared to fully numerical methods. We have re-evaluated both primary and secondary components of the positron flux, finding as expected that they are significantly affected at low energies by the incorporation of the so far neglected CR transport mechanisms. Surprisingly, we also find that modifications are still substantial at a few tens of GeV, depending on the CR propagation parameters. As pointed out in [Delahaye 2009] and [Lavalley 2014], we confirm that the secondary prediction of the positron flux at low energies can be in large excess compared to AMS-02 data, even for propagation models compatible with the B/C analysis from [Maurin 2001].

Motivated by this result, we have carried out a scan over the CR propagation parameters of [Maurin 2001], applying an original skimming method which leads to severe constraints on the propagation parameters: out of the 1,623 models, only 54 survive the procedure. In particular, the benchmark MIN and MED configurations are excluded. On the other hand, MAX-like propagation models, i.e. with large $\{K_0, L\}$ and small δ , are favored by the data. Those models are very close to the best configuration found in [Kappl 2015] by fitting the preliminary B/C data of AMS-02. This needs to be confirmed with the newest B/C published recently by AMS-02 [Aguilar 2016b]. We do not expect major changes in our conclusions.

To overcome the difficulty arising from solar modulation, we have made use of a very high Fisk potential, 3σ above the mean value obtained by [Ghelfi 2016]. This choice minimizes the flux at low energies and makes our skimming procedure of the CR parameter space conservative, leading us to keep models that should be disregarded.

In a similar way, we have made use of the p and He spallation cross-sections from [Kamae 2006] since they lead to the lowest amount of positrons. Furthermore, we have checked that uncertainties in the measurements of the p and He fluxes do not alter our result. Finally, given that our skimming method makes use of information from data points separately, we have investigated whether a specific data point could drive the constraints. We found that this is indeed the case: the first data point

has a much higher discriminating power than the others. Discarding it from the analysis, our skimming method selected 623 models, which still corresponds to a rejection of about two thirds of the parameter space. We can therefore conclude that the positron flux is a very useful and independent probe of CR propagation, to be used in synergy with other tracers such as the B/C ratio. Our results also indicate that the positron excess is already present at GeV energies, typically starting above 2 GeV.

We have finally re-investigated the explanation of the positron anomaly in terms of annihilations of a single DM species, in the WIMP framework, over the whole energy range of the AMS-02 data. We have performed a scan over WIMP mass and explored the possibility of: i) direct annihilation into a combination of channels; ii) leptophilic DM annihilating into four leptons through a light mediator. For a given WIMP mass and propagation model (selected by our skimming method), we have obtained the best-fit values of the annihilation cross-section and branching ratios. Our most striking result is that no good fit to the data is obtained for both cases i) and ii). Indeed, in case i), the best fit is found for a mass of 264 GeV that does not allow to reproduce the highest-energy data points. Hence, the associated p -value is as low as 0.4%. On the other hand, requiring the DM mass to be larger than 500 GeV yields $\chi^2_{\text{dof}} > 3$, since the low-energy part of the data cannot be consistently accommodated. Case ii) turns out to be even worse, the best-fit χ^2_{dof} being as high as 15. We have checked the robustness of our conclusions against a few possible loopholes.

We are thus led to the conclusion that annihilations of a single DM species should be disregarded as the sole origin of the positron excess, on the basis of the positron data themselves, irrespective of other observables such as the antiproton flux or CMB anisotropies. It is likely that more ad-hoc multi-species models, with e.g. one heavy and one light DM particle, will be able to accommodate the excess, although a strong statement would require a dedicated study. It is probable that such an analysis with a unique pulsar as the source of the anomaly would lead to similar conclusions, requiring in the future more realistic multi-component studies.

4.3.2 Pulsars as astrophysical sources of positrons

This part is mostly based on sections 4 and 5 of [Boudaud 2015a] for which I contributed. This study, older than the one previously presented, relies on the interpretation of the positron fraction which was the first observable released by the AMS-02 collaboration. Note that the study is restricted to positron energies above 10 GeV, since the pinching method is of no use to deal with the time dependent equation. Some remarks in the conclusion have been added to comment upon more recent studies.

Pulsars are astrophysical sources known to exist. They were first detected in 1967 and a few of them have been observed in the Earth vicinity. They correspond to highly-magnetised neutron stars which emit electromagnetic radiation as they

spin [Shapiro 1983]. At their surfaces, the very strong electric fields extract and accelerate charged particles, which subsequently interact with the magnetic field or the thermal emission of the pulsar to trigger an electromagnetic cascade [Rees 1974]. This yields an electron-positron plasma which, for a pulsar wind nebula, drifts away from the star to form a shock on the surrounding medium. Acceleration takes place there until the reverse shock from the supernova explosion releases in the ISM the positrons and electrons confined so far. Recently, [Linden 2013] and [Cholis 2013] concluded that either Geminga or Monogem, two well-known nearby pulsars, could account for the rise of the positron fraction measured by AMS-02 [Aguilar 2013b]. The aim of this section is to re-investigate if a single pulsar is enough to explain the positron anomaly. Indeed, if the single pulsar hypothesis is viable, the whole of pulsars is capable of reproducing the experimental data.

The positron spectrum at the source is parameterized by

$$g(E) = Q_0 \left(\frac{E_0}{E} \right)^\gamma \exp(-E/E_C). \quad (4.51)$$

The normalization constant Q_0 is determined by requiring that the total energy provided by the pulsar to the positrons above an energy E_{\min} is a fraction f of the initial spinning energy W_0 . This leads to

$$\int_{E_{\min}}^{+\infty} E_S g(E_S) dE_S = fW_0. \quad (4.52)$$

When pulsars form, they initially rotate with a period as small as a few milliseconds. The initial kinetic energy of a 3 ms pulsar is of order 10^{51} ergs, or equivalently 10^{54} GeV, which sets the natural unit in which we will express the energy fW_0 carried out by positrons. The energy E_C in relation (4.51) is a cut-off in the injection spectrum. It has been set equal to 1 TeV throughout our analysis. The exact value does not matter much, since the high energy cut-off of the positron spectrum at the Earth comes from the age t_\star of the pulsar and not from a cut-off at the source [Malyshev 2009].

4.3.2.1 Selection of possible pulsars: the five survivors of the ATNF catalogue

The contribution of a single pulsar is calculated using the injection spectrum given equation 4.51 in the time dependent solution which are recalled in [Boudaud 2015a]. The free parameters are the spectral index γ and the energy released by the pulsar through positrons fW_0 , which are related to the spectral shape and normalisation, respectively. In our analysis, we assume a fictional source placed at a distance d from the Earth and of age t_\star . We then estimate the parameters γ and fW_0 , which give the best fit to the positron fraction. We allow the spectral index γ to vary from 1 to 3 and we fix the upper limit of fW_0 to 10^{54} GeV. Since only close and relatively young single pulsars reproduce the experimental data well,

we repeat this procedure for 2500 couples of (d, t_*) with $d < 1$ kpc and $t_* < 1$ Myr. We perform our analysis with the benchmark set of propagation parameters MED.

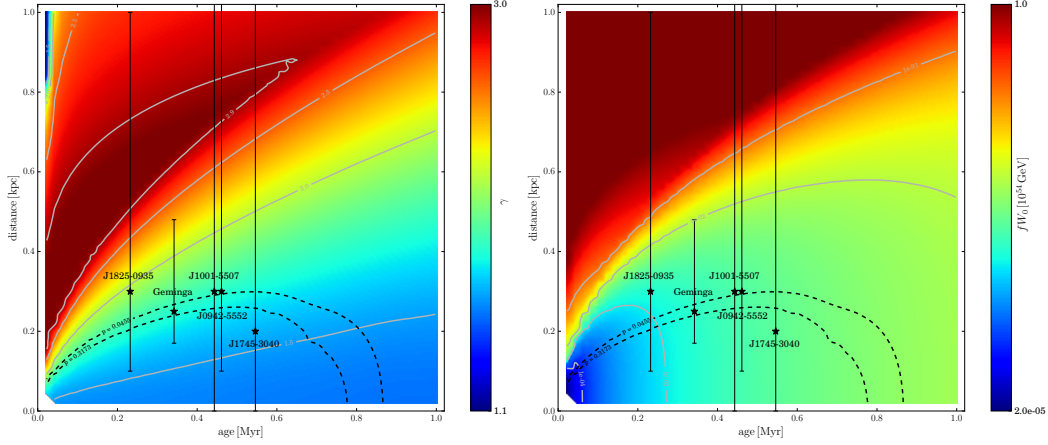


Figure 4.18: Best-fit values of the spectral index γ (left panel) and the total energy carried by positrons fW_0 (right panel) for each point of the plane (age, distance) with the benchmark propagation model MED. The grey lines display the iso-contours for given values of γ (left) and fW_0 (right). The black dashed lines represent the iso-contours of the critical p -values. The five selected pulsars with their associated uncertainty on their distance are indicated by the black stars.

The results are shown in figure 4.18 where the colour scale indicates the value of γ (left panel) and fW_0 (right panel). The grey lines highlight the iso-contours for given values of γ and fW_0 . We observe a positive (negative) correlation between the distance (age) of the pulsar and its injection spectral index γ . This can be explained by the fact that the free parameters of the pulsar (γ, fW_0) are predominantly determined by the well-measured low-energy shape of the positron fraction. Indeed, the positron flux between 10 and ~ 100 GeV can be approximated by $\Phi_{e^+}(E) \propto \exp(-d^2/\lambda_D^2)$, with the positron sphere radius $\lambda_D^2 \simeq 4K_0 t_* (E/E_0)^\delta$. We can hence define a lower energy limit $E_{\min} = E_0 (d^2/4K_0 t_*)^{1/\delta}$ below which the positron flux becomes negligible since the positrons have not had enough time to reach the Earth. Given a pulsar age, lengthening the distance implies, on the one hand, an increase of E_{\min} , i.e. the spectrum becomes harder and the best-fit value of γ larger. On the other hand, the positron flux decreases exponentially and the value of fW_0 increases consequentially. In the same way, for a fixed pulsar distance, an older source yields at the Earth positrons at lower energies and needs a smaller γ and fW_0 to reproduce the experimental data. In the special case of a very close pulsar ($d \lesssim 0.3$ kpc), the shape of the injected positron flux mildly depends on the pulsar distance and varies like $\Phi_{e^+}(E) \propto \lambda_D^{-3} \propto t_*^{-3/2}$. In this situation, fW_0 and the age are positively correlated.

In the same figures, the two iso-contours of the critical p -values corresponding to a 1 ($p > 0.3173$) and 2 ($p > 0.0455$) standard deviation (σ) significance level for a normal distribution (black dashed lines) are also represented. Those define the good-fit region with $\gamma \lesssim 2$ and fW_0 within the range of $[10^{49}, 10^{52}]$ GeV. These value ranges are consistent with previous studies [Hooper 2009, Malyshev 2009, Delahaye 2010, Linden 2013, Di Mauro 2014a]. We select the pulsars from the ATNF catalogue that fall into this good-fit region. The pulsar distance suffers from large uncertainties, which are taken into account for the pulsar selection. The uncertainty on the pulsar age is negligible due to a precise measurement of its spin and spin-down. Only five pulsars from the ATNF catalogue fulfil the goodness-of-fit criteria. The chosen pulsars and their distance uncertainties are indicated in figure 4.18 by black stars with error bars.

4.3.2.2 Results for the five pulsars

For each of these five selected pulsars we estimate the values of γ and fW_0 that best reproduce the experimental data. The results are listed in Table 4.5 with the corresponding χ^2 and p -values. The nominal age and distance (bold line) are taken from the ATNF catalogue. We also perform this procedure for their minimal (first line) and maximal distances (third line) according to the experimental uncertainty, which is not taken into account in the minimisation procedure. A further study will include this uncertainty, but it is beyond the scope of this study. Finally, we study the contribution to the positron fraction of the well-known pulsars Monogem and Vela, and present these results in the Table.

As can be seen in figure 4.18, for their nominal distances, the pulsar J1745–3040 (J1825–0935) reproduces best (worst) the AMS-02 positron fraction. This is well reflected in their respective p -values. In contrast, Monogem and Vela cannot adjust the data. Because of their very young age, they are not able to contribute to the low-energy positron fraction between 10 and 50 GeV where the error bars are the smallest. For all studied pulsars, the p -values increase with decreasing distance. This can be explained by the above mentioned low-energy cut-off E_{\min} , which is significantly lowered and allows hence the pulsar to cover a larger part of the positron fraction. An example is given in figure 4.19 where the contribution of Geminga is studied for its nominal (left) and minimal (right) ATNF distance. In the case of most pulsars the fit does not converge for the maximal distance and reaches the defined limits of the free parameters. The associated χ^2 and p -values are hence not meaningful. The resulting positron fractions of the pulsars J1745–3040 (solid line), Geminga (dashed-dotted line), and Monogem (dotted line) are shown in figure 4.20 for their nominal distances. Because of the large error bars at high energies the contribution of J1745–3040 reproduces well the experimental data, reflected by the good p -value, even though it does not reach the highest energy data points. As mentioned in the introduction, increasing E_C neither changes our conclusions nor modifies our list of selected pulsars.

Name	Age [kyr]	Distance [kpc]	fW_0 [10^{54} GeV]	γ	χ^2	χ^2_{dof}	p
J1745–3040	546	0	$(2.95 \pm 0.07) \cdot 10^{-3}$	1.45 ± 0.02	23.4	0.57	0.99
		0.20	$(3.03 \pm 0.06) \cdot 10^{-3}$	1.54 ± 0.02	33.6	0.82	0.79
		1.3	1	2.54	9902	241	0
J0633+1746 <i>Geminga</i>	342	0.17	$(1.48 \pm 0.03) \cdot 10^{-3}$	1.56 ± 0.02	26.8	0.65	0.96
		0.25	$(1.63 \pm 0.02) \cdot 10^{-3}$	1.68 ± 0.02	49.6	1.21	0.17
		0.48	$(1.01 \pm 0.06) \cdot 10^{-2}$	2.29 ± 0.02	332	8.10	0
J0942–5552	461	0.10	$(2.28 \pm 0.05) \cdot 10^{-3}$	1.48 ± 0.02	21.7	0.53	0.99
		0.30	$(2.61 \pm 0.04) \cdot 10^{-3}$	1.69 ± 0.02	61.0	1.49	0.02
		1.1	1	2.65	7747	189	0
J1001–5507	443	0	$(2.13 \pm 0.05) \cdot 10^{-3}$	1.46 ± 0.02	19.8	0.48	0.99
		0.30	$(2.49 \pm 0.03) \cdot 10^{-3}$	1.70 ± 0.02	62.4	1.52	0.02
		1.4	1	2.46	13202	322	0
J1825–0935	232	0.1	$(0.80 \pm 0.02) \cdot 10^{-3}$	1.52 ± 0.02	21.0	0.51	0.99
		0.30	$(1.45 \pm 0.03) \cdot 10^{-3}$	1.94 ± 0.02	126	3.07	0
		1.0	1	2.64	12776	312	0
J0659+1414 <i>Monogem</i>	111	0.25	$(1.06 \pm 0.05) \cdot 10^{-3}$	2.18 ± 0.02	216	5.27	0
		0.28	$(2.53 \pm 0.16) \cdot 10^{-3}$	2.37 ± 0.02	316	7.71	0
		0.31	$(7.96 \pm 0.61) \cdot 10^{-3}$	2.58 ± 0.02	444	10.8	0
J0835+4510 <i>Vela</i>	11.3	0.26	$(2.53 \pm 0.08) \cdot 10^{-1}$	3	14316	349	0
		0.28	$(3.90 \pm 0.14) \cdot 10^{-1}$	3	14982	365	0
		0.3	$(6.00 \pm 0.26) \cdot 10^{-1}$	3	15446	377	0

Table 4.5: Results for the pulsar parameters fW_0 and γ for the best fits in the single pulsar approach. Only pulsars with a p -value > 0.0455 , taking their distance uncertainty into account, are listed, besides the well-known pulsars Monogem and Vela. The bold lines correspond to the nominal distance value.

4.3.2.3 What happens when we get more statistics?

We can now investigate how the list of selected pulsars would change if AMS-02 publishes a positron fraction in ten years with more statistics. To estimate the new error bars, we assume that the number of events follows a Gaussian distribution in each bin. This is a reasonable assumption since the last bin already contains 72 positrons. Therefore, the statistical uncertainty σ_{stat} decreases with time t as $\sigma_{\text{stat}} \propto 1/\sqrt{t}$. The systematic uncertainty σ_{syst} is here assumed to be constant with time. The uncertainty on the lepton flux is expected to follow the same variation with time as that on the positron fraction. Accordingly, the total uncertainty in each energy bin is multiplied by the reduction factor $RF(t)$ defined as:

$$RF(t) = \sqrt{\frac{\sigma_{\text{stat, AMS}}^2 \frac{t_0}{t} + \sigma_{\text{syst, AMS}}^2}{\sigma_{\text{stat, AMS}}^2 + \sigma_{\text{syst, AMS}}^2}}, \quad (4.53)$$

where $\sigma_{\text{stat, AMS}}$ and $\sigma_{\text{syst, AMS}}$ are the statistical and systematic uncertainties, while $t_0 = 2.47$ yr stands for the data taking time of the published AMS-02 data, to be

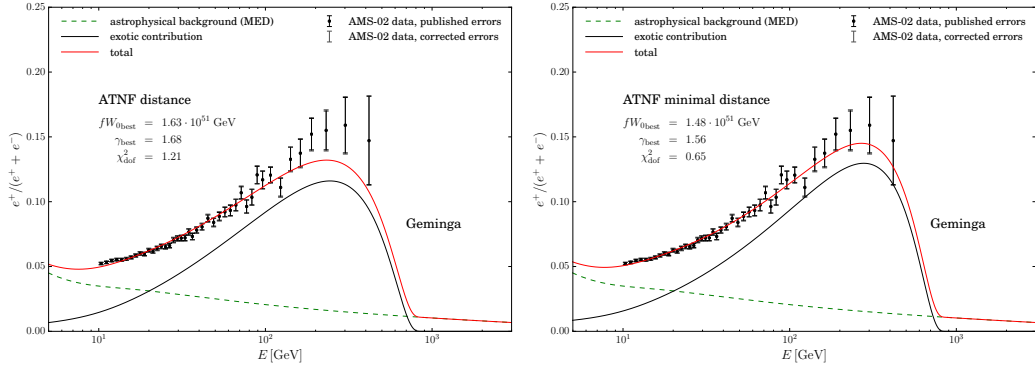


Figure 4.19: Positron fraction for the best fits for the pulsar Geminga considering the nominal (left panel) and minimal (right panel) distances. The spectral index γ at the source decreases with the pulsar distance. The positron flux becomes harder and better fits the highest-energy data points.

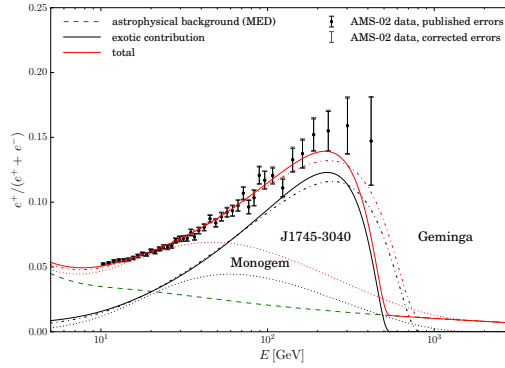


Figure 4.20: Positron fraction for the best fits for the pulsars J1745-3040 (solid line), Geminga (dashed-dotted line), and Monogem (dotted line) with the propagation model MED.

compared to the time t of the assumed data collection (10 years).

In figure 4.21 the same analysis as in section 4.3.2.1 and figure 4.18 is performed. Since the mean value of the positron fraction does not change, the colour variations of figure 4.18 and 4.21 are the same. However, the good-fit regions defined by the iso-contours of the p -values drastically shrink. Thus, if the tendency of the positron fraction remains similar, the single pulsar hypothesis would be excluded by our criterion. The currently allowed five pulsars benefit from the large statistical uncertainties of the last bins.

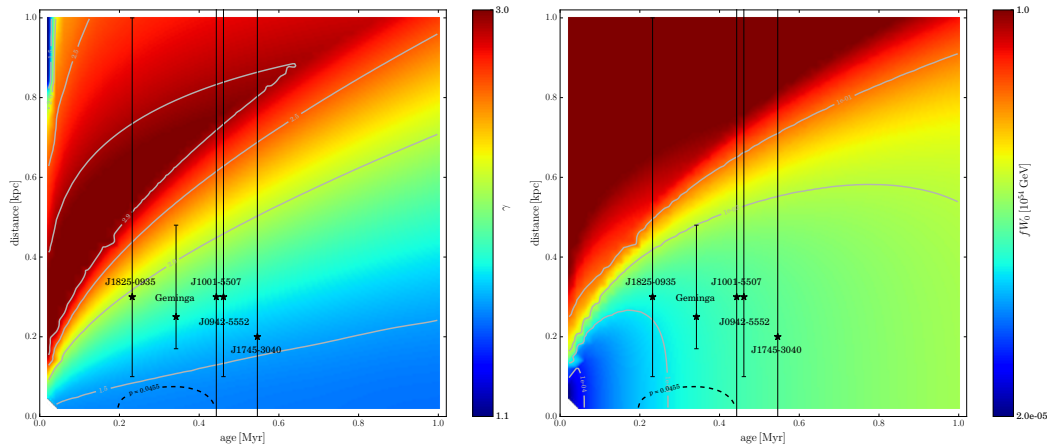


Figure 4.21: Same as figure 4.18 but with ten years of measurements of the positron fraction by AMS-02.

4.3.2.4 Conclusion

We have shown that the rise of the positron fraction can be alternatively explained by an additional contribution from a single pulsar. Indeed, five pulsars from the ATNF catalog have been identified to satisfy the experimental measurements within their distance uncertainties. For all the selected pulsars we obtain an excellent fit result even though the adjustment of the last few high energy data points is unsatisfactory. However, this can be improved by decreasing the pulsar distance within its uncertainty. AMS-02 is expected to take data for more than ten years reducing considerably its statistical uncertainties especially for the highest energies. If the trend of the positron fraction remains the same, our analysis shows that ten years of data could completely exclude the single pulsar hypothesis. Naturally, assuming a pulsar origin for the positron fraction rise leads to a cumulative contribution from all detected and yet undiscovered pulsars. Nevertheless, demonstrating that the positron fraction can be explained by a unique pulsar contribution provides us with a valid alternative to the DM explanation of this anomaly. As a matter of fact, if the single pulsar hypothesis is viable, the entirety of detected pulsars is hence capable of reproducing the experimental data. However, since the normalization of the pulsar source term and the annihilation cross-section of dark matter are treated as free parameters, both pulsars and dark matter could contribute to the positron anomaly.

Based on energetic arguments, the recent study of [Hooper 2017] shows that the gamma emission from the two pulsars Geminga and B0656+14 (measured by HAWC and Milagro experiments) is consistent with a production of leptons that could dominate in the positron fraction excess. Ultimately, anisotropies of the positron flux could disentangle between DM and the pulsar hypothesis. FERMI-LAT is currently

the most competitive experiment for measuring the lepton anisotropy. In the recent paper [Manconi 2017], it was shown that the first limits imposed by FERMI-LAT do not strongly constrain the models explaining the positron enhancement from single SNR, neither from single pulsar. However, some time later, the last release from the FERMI-LAT collaboration uses the 8 years of data available, and put more stringent constraints on positrons anisotropy [Abdollahi 2017], excluding some scenarios.

4.4 Refined constraints on dark matter using the antiproton flux

This section is mostly based on [Giesen 2015]. This study was made public right after the AMS-02 Collaboration presented its preliminary measurements of the \bar{p}/p ratio [AMS]. By reprocessing this analysis with the antiproton flux from the last AMS-02 release [Aguilar 2016a], it can be shown that the conclusions presented hereafter hold

As mentioned in section 4.2.2, the antiproton (\bar{p}) component in cosmic rays is recognized as an important messenger for energetic phenomena of astrophysical, cosmological and particle physics nature. Until now, the so-called *secondary* antiprotons (originating from collisions of CR primaries with the interstellar material) have been shown to account for the bulk of the measured flux [Donato 2009], thus allowing to derive constraints on the DM parameter space and to compute expected sensitivities, respectively based on updated PAMELA data [Adriani 2010] and projected AMS-02 data (see e.g. [Cirelli 2013, Boudaud 2015b, Evoli 2012, Bélanger 2012, Fornengo 2014b, Cirelli 2014, Bringmann 2014, Hooper 2015]). The AMS-02 Collaboration has presented its preliminary measurements of the \bar{p}/p ratio [AMS], with an improved statistical precision and energy range extending to 450 GeV. It is therefore crucial and timely to re-examine the situation and update existing results. In addition, AMS-02 has published the measurement of the proton (p) spectrum [Aguilar 2015b] and presented the measurement of the helium (α) one [AMS], in qualitative agreement with the previous determinations by PAMELA [Adriani 2013], but now with unprecedented precision and detail. This is important for our purposes since the p and α spectra are crucial input ingredients in the computation of the secondary antiproton flux, which is the minimal astrophysical antiproton background for indirect DM searches, as we will remind later. Hence, with the release of these exquisitely precise datasets, AMS-02 provides a coherent, high-statistics—albeit preliminary—picture in the hadronic component of CR's too, allowing for a scrutiny of possible exotic contributions.

However, the reach of any search for exotic physics is limited by the astrophysical uncertainties affecting the production and the propagation processes of cosmic antiprotons in the Galaxy and in the solar system. Indeed, while the basic processes involved in the production and propagation of CR antiprotons are rather well understood, the detailed parameters entering in such processes are far from being well

determined. The \bar{p} production, propagation and Solar modulation uncertainties can have a large impact on both the astrophysical and (in particular) the DM signal. Some sensible ranges for these parameters can and must be determined by studying ordinary CR fluxes like the ratio of Boron to Carbon (B/C ratio), which surely have a non-exotic origin. Indeed, in this way the traditional MIN-MED-MAX schemes [Donato 2004] are determined, and plausible ranges for the force field parameter of solar modulation (the so-called Fisk potential) are identified. However, these ranges are based on *past* CR data and are *not* necessarily guaranteed to work in describing the *current* status. We anticipate that this is what we will find in some cases discussed below. For instance, a string of recent papers, based on synchrotron radio emission [Fornengo 2014a, Orlando 2013, Bringmann 2012, Di Bernardo 2013] but also on positrons [Di Mauro 2014a, Lavalle 2014] and somewhat also on gamma rays [Ackermann 2012b], finds that the thin halo predicted by MIN is seriously disfavored. More generally, looking for DM on top of inadequate schemes can lead to non-robust or even wrong conclusions. Hence, one of the most crucial issues in the field is to update the uncertainty ranges of ordinary astrophysics in view of the more recent and precise experimental results, in order to build the DM search on a more solid basis. This will be possible after a careful analysis of accurate secondary over primary data like the B/C ratio, freshly published by AMS-02 and provided that theoretical uncertainties will be under better control [Genolini 2015]. For the time being, the search for DM signatures has to be pursued with the utmost care.

Within this broad context, the purpose of this study is twofold: 1) based on *existing* propagation models, derive the state-of-the-art astrophysical antiproton background, carefully appraising the related uncertainties; 2) on the basis of such background and fully taking into account such uncertainties, assess what can be said on the room left for a DM signal, and what can not.

This study is organized as follows. In section 4.4.1, we remind how the computation of the astrophysical antiproton background proceeds, we detail its uncertainties and we compare the result with the measured \bar{p}/p . In section 4.4.2 we introduce the DM contribution to \bar{p}/p and we derive constraints on the DM annihilation cross-section or decay rate, for several annihilation/decay channels and under different DM and astrophysical configurations. Finally in section 4.4.3, we conclude with a few final comments.

4.4.1 Re-evaluation of the astrophysical antiproton background

The secondary astrophysical antiproton background ⁸ is produced in collisions of the CR high energy protons and helium nuclei on the interstellar medium, mainly constituted of hydrogen and helium, the contributions of heavier nuclei in both projectiles and targets being a few percent correction. The locally measured flux is

⁸In some models one can also have a *primary* astrophysical source of background antiprotons, i.e. a significant antiproton population participating to the acceleration process, see e.g. [Blasi 2009] or [Cholis 2017] for an up to date version.

the result of the diffuse production in the Galactic environment and the subsequent propagation of the antiprotons to the location of the Earth. Hence, the main ingredients of the computation for the ‘(secondary) astrophysical \bar{p} source term’ are: i) the injection p and α primary fluxes from Galactic sources, ii) the collision cross-sections, iii) the propagation details. While we refer to [Boudaud 2015b, Bringmann 2007] and reference therein for a detailed discussion of all the aspects of the computation, here we just highlight the points of novelty.

For the p and α spectra needed in i), as mentioned above we use the data that have just been released by AMS-02 [Aguilar 2015b],[AMS]. The spectra are measured up to a rigidity of 1.8 and 3 TV for p and α nuclei, respectively, and, as already reported by the PAMELA Collaboration [Adriani 2011], they cannot be described by a single power law: a hardening at energies higher than ~ 300 GV is observed for both. At the practical level, we perform our own fits of the AMS-02 data points. The value of the Fisk potential which gives the best χ^2 for our fits is $\phi_F = 0.62$ GV, the upper bound of the interval set in [Aguilar 2015b]. The values of the best-fit parameters are reported in appendix. The uncertainties on the slope of the p and α spectra at high energies, $\Delta\gamma_{p,\alpha}$, induce an uncertainty band on the predicted astrophysical \bar{p}/p ratio. In figure 4.22, top left panel⁹, we show the result of our computation of the ratio with such uncertainty band. For the distribution of the sources of primary CR p and α , which can be determined from pulsar and supernova remnant surveys, we use the parameterization of [Yusifov 2004], slightly modified as in [Bernard 2012].

For the production processes we need the cross-sections $\sigma_{pH \rightarrow \bar{p}X}$, $\sigma_{pHe \rightarrow \bar{p}X}$, $\sigma_{\alpha H \rightarrow \bar{p}X}$, $\sigma_{\alpha He \rightarrow \bar{p}X}$, where the first index refers to the impinging primary CR while the second one to the target interstellar material. For σ_{pH} we use the new parameterization recently proposed by [di Mauro 2014b], instead of the traditional fitting relations given in [Tan 1982, Tan 1983a]. For the cross-sections of the other reactions we use the prescription of [Bringmann 2007], to which we refer the interested reader. We just remind that for the cross-section values that we adopt the pH reaction dominates, providing 60% to 65% of the total \bar{p} flux depending on the energy, while pHe and αH reactions yield 32 to 37%, and the reaction αHe contributes less than 3%. Another element which has only recently been appreciated is related to the contribution of antineutron production: on the basis of isospin symmetry, one would consider the production cross-section for antineutrons (e.g. $\sigma_{pH \rightarrow \bar{n}X}$ and the others) as equal to those for antiprotons; the antineutrons then rapidly decay and provide an exact factor of 2 in the \bar{p} flux. However, as pointed out in [di Mauro 2014b, Kappl 2014] and as already implemented in [Boudaud 2015b], it may be that this naïve scaling does not apply and that the antineutron cross-section is larger by up to 50% with respect to the \bar{p} one. Assessing uncertainties for reactions

⁹Each of the panels of the figure has to assume a choice for the uncertainties presented in the other panels. E.g. the first panel assumes definite values for the collision cross-sections, a model for \bar{p} propagation and a value for the Fisk potential. They are always chosen to be the central values, e.g. MED, the fiducial cross-section and 0.62 GV for this example.

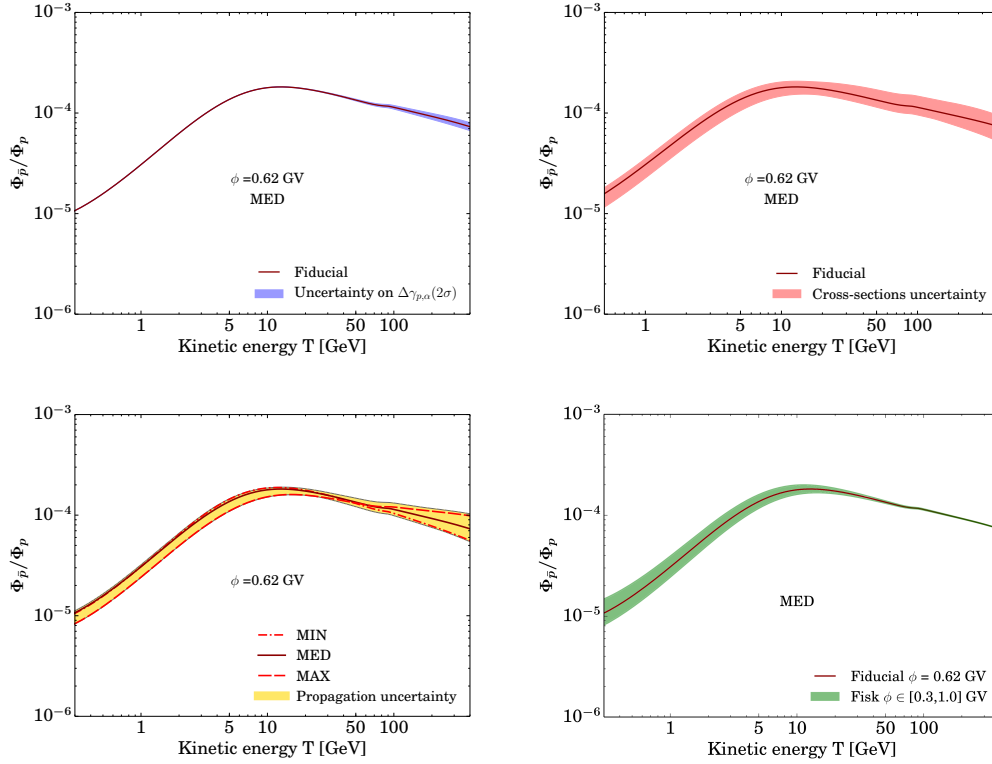


Figure 4.22: *Illustration of the individual partial uncertainties for secondary antiprotons.* The colored bands represent the uncertainties on the input p and α fluxes (upper left panel), \bar{p} production cross-sections in the interstellar medium (upper right panel), Galactic propagation (lower left panel) and Solar modulation (lower right panel).

involving He is even more challenging, since *no data are present*, and predictions are based on semi-empirical nuclear models calibrated on data involving either protons or heavier nuclei (see [Duperray 2003]). For sure, uncertainties involving these reactions are at least as large in percentage as the one of the $p\text{H}$ reaction, an assumption we will do in the following. More conservative assumptions would only make the error larger, and strengthen our main conclusion on the level of agreement of the data with a purely secondary antiproton flux. All these cumulated effects contribute to an uncertainty band for the astrophysical \bar{p}/p ratio which is represented in figure 8 of [di Mauro 2014b] and which we will adopt: it varies from about 20% to at most 50% (at large energies and in the most conservative conditions). In figure 4.22, top right panel, we show our prediction for the \bar{p}/p ratio with this uncertainty envelope.

Once produced, antiprotons have to propagate in the local Galactic environment before they are collected at Earth. We deal with this process in the usual way, by solving semi-analytically the full transport equation for a charged species in a 2D cylindrical ‘thick halo’ model of the Galaxy. We do not reproduce the full

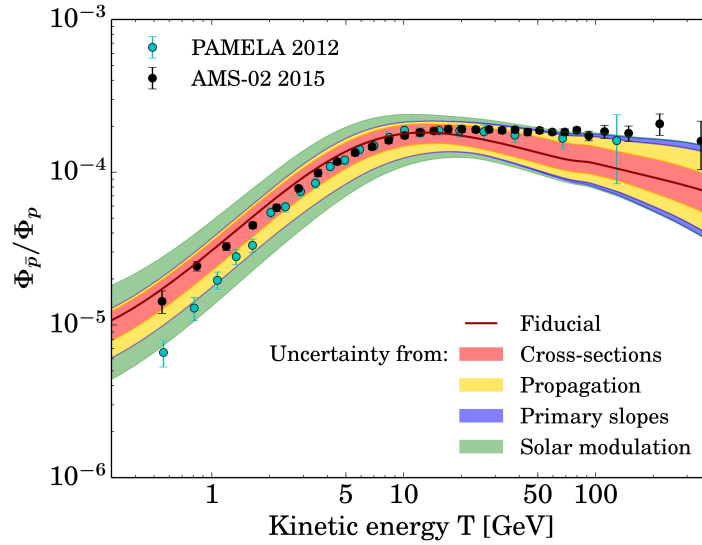


Figure 4.23: The combined total uncertainty on the predicted secondary \bar{p}/p ratio, superimposed to the older PAMELA data [Adriani 2013] and the new AMS-02 data. The curve labelled ‘fiducial’ assumes the reference values for the different contributions to the uncertainties: best fit proton and helium fluxes, central values for the cross-sections, MED propagation and central value for the Fisk potential. We stress however that the whole uncertainty band can be spanned within the errors.

treatment here (we refer again to [Boudaud 2015b] for a self-contained description and to [Mannheim 1994, Strong 1998, Bergström 1999, Donato 2001, Donato 2004, Bringmann 2007] for all the relevant details) but point out that we do include all the relevant processes. In particular, we take into account \bar{p} annihilation, energy losses, ‘tertiary production’, and diffusive reacceleration. Besides these effects, the propagation parameters governing diffusion and convection are as usual codified in the MIN, MED and MAX sets [Donato 2004], which are by definition those that minimize or maximize a hypothetical *primary*, DM \bar{p} flux at Earth. Note that these have not (yet) been revised on the light of recent secondary data like the preliminary B/C ratio of AMS-02, as discussed in the introduction, so the viability of these predictions for the \bar{p}/p ratio (which extends for instance to higher energies) is not trivially expected to hold. In figure 4.22, lower left panel, we show the impact of the propagation uncertainty. The curves which are labelled MIN, MED and MAX represent the modification which occurs by choosing these standard sets. The shaded yellow area envelops the results obtained by sampling more widely the propagation parameter space that has been shown in [Donato 2001] to be compatible with the B/C ratio and finding the values that minimize and maximize the *secondary*, rather than primary, \bar{p}/p flux. Notice that the shaded yellow area does not coincide with the MIN-MED-MAX envelope (see in particular between 50 and 100 GeV): this is

not surprising, as it just reflects the fact that the choices of the parameters which minimize and maximize the \bar{p}/p secondaries are slightly different from those of the primaries. However, the discrepancy is not very large. We also notice for completeness that an additional source of uncertainty affects the energy loss processes. Among these, the most relevant ones are the energy distribution in the outcome of inelastic but non-annihilating interactions or elastic scatterings to the extent they *do not fully* peak in the forward direction, as commonly assumed [Donato 2001]. Although no detailed assessment of these uncertainties exists in the literature, they should affect only the sub-GeV energy range, where however experimental errors are significantly larger, and which lies outside the main domain of interest of this article.

Finally, \bar{p} 's have to penetrate into the heliosphere, where they are subject to the phenomenon of Solar modulation (abbreviated with ‘SMod’ when needed in the following figures). We describe this process in the usual force field approximation [Gleeson 1968], parameterized by the Fisk potential ϕ_F , expressed in GV. As already mentioned in the introduction, the value taken by ϕ_F is uncertain, as it depends on several complex parameters of the Solar activity and therefore ultimately on the epoch of observation. In order to be conservative, we let ϕ_F vary in a wide interval roughly centered around the value of the fixed Fisk potential for protons ϕ_F^p (analogously to what done in [Cirelli 2014], approach ‘B’). Namely, $\phi_F = [0.3, 1.0]$ GV $\simeq \phi_F^p \pm 50\% \phi_F^p$. In figure 4.22, bottom right panel, we show the computation of the ratio with the uncertainties related to the values of the Fisk potential in the considered interval. Notice finally that the force field approximation, even if ‘improved’ by our allowing for different Fisk potentials for protons and antiprotons, remains indeed an “effective” description of a complicated phenomenon. Possible departures from it could introduce further uncertainties on the predicted \bar{p}/p , which we are not including. However it has been shown in the past [Fornengo 2014b] that the approximation grasps quite well the main features of the process, so that we are confident that our procedure is conservative enough.

Figure 4.23 constitutes our summary and best determination of the astrophysical \bar{p}/p ratio and its combined uncertainties, compared to the new (preliminary) AMS-02 data. The crucial observation is that the astrophysical flux, with its cumulated uncertainties, can reasonably well explain the new datapoints. Thus, our first—and arguably most important—conclusion is that, contrarily to the leptonic case, *there is no clear antiproton excess that can be identified in the first place, and thus, at this stage, no real need for primary sources*. This also means that, at least qualitatively, one expects a limited room left for exotic components, such as DM. Indeed in the following section we will proceed to compute the constraints on it.

However, before we can do so, we have to identify specific sets of astrophysical parameters to describe the background, as discussed in the introduction. We fix in turn MIN, MED and MAX and we vary the Solar modulation potential in the given interval. We model the uncertainties of the production cross-sections term by

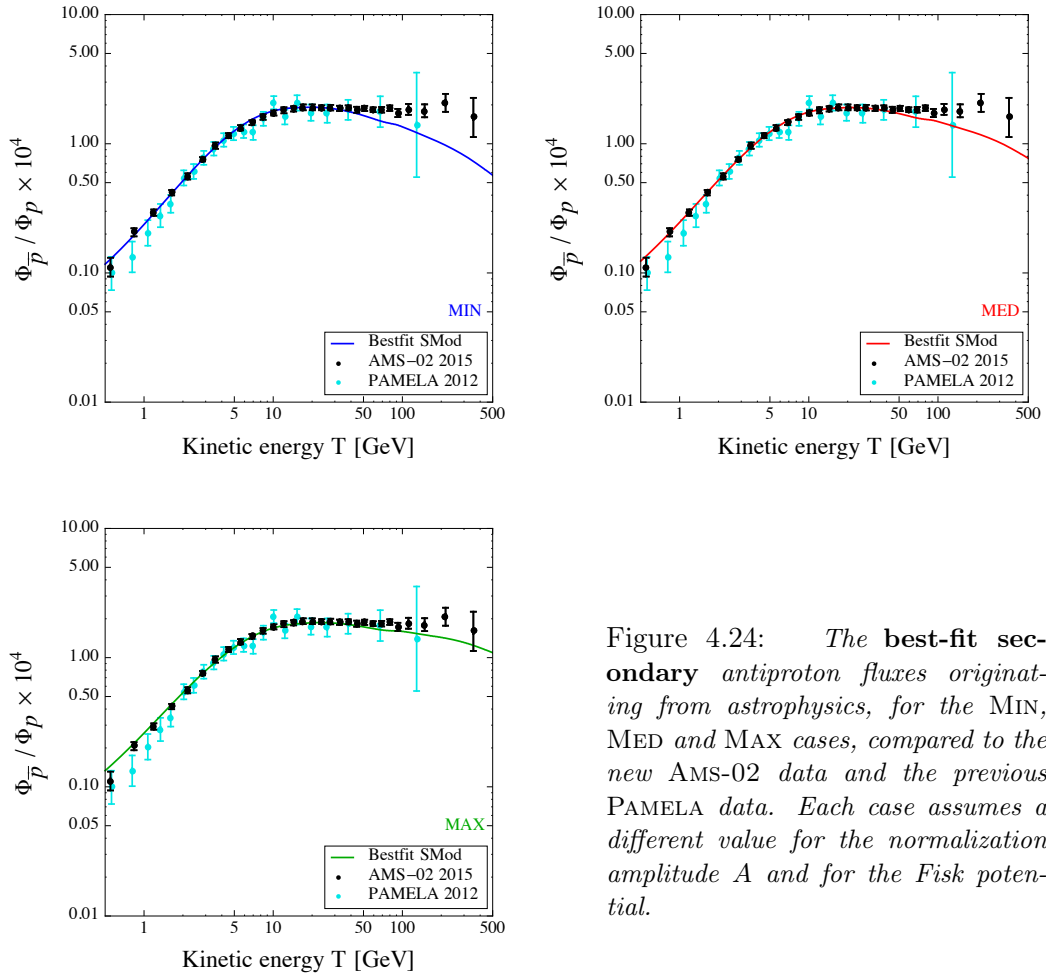


Figure 4.24: *The best-fit secondary antiproton fluxes originating from astrophysics, for the MIN, MED and MAX cases, compared to the new AMS-02 data and the previous PAMELA data. Each case assumes a different value for the normalization amplitude A and for the Fisk potential.*

allowing a renormalization of the background with an energy dependence and an amplitude A as dictated by the analysis presented above (namely, an uncertainty modulated as the pink band of figure 4.22). With this strategy, we look for the best fitting values of the amplitude A and of the potential ϕ_F and we trace the corresponding \bar{p}/p spectra. In concrete terms, for each propagation model, we minimize the chi-square $\chi_0^2(A, \phi_F)$ with respect to the AMS-02 data and hence determine the best fit amplitude A_0 and Fisk potential ϕ_F^0 . We show in figure 4.24 the different cases.

Even within the limitations of the data like those we are dealing with (namely their preliminary nature, their errors only partially accounted for and the partial collection time with respect to the full lifetime of the experiment), we can see that the MIN propagation scheme predicts an astrophysical background that can *not* reproduce the new \bar{p}/p data points above 30 GeV. The MED scheme provides a barely decent fit (still good up to ~ 30 GeV but rapidly degrading after) while choosing MAX the data can be well explained across the whole range of energies.

We have explicitly computed the corresponding χ^2 to support the above statements, with the MIN, MED, MAX cases yielding 106, 58 and 41, respectively (for 28 degrees of freedom). Given the preliminary nature of the data, of course they have only an indicative significance. This is our second conclusion: *the preliminary \bar{p}/p AMS-02 data seem to prefer a model, such as MAX, characterized by a relatively mild energy dependence of the diffusion coefficient at high energies.* Although it is too early to draw strong conclusions, this is an interesting observation and it goes in the same direction as the preference displayed by the preliminary B/C AMS-02 data [Genolini 2015]¹⁰.

It would of course be tempting to interpret the room left in the MIN and MED cases at large energies as an exotic contribution from DM. However we insist that this would be a wrong deduction in two respects: as long as a model within the uncertainties can fit the data, failure of other models just means a better selection of the background rather than evidence for an extra component; in any case, a new assessment of the viable propagation parameter space would be needed before any conclusion is drawn.

4.4.2 Updated constraints on Dark Matter

Primary antiprotons could originate from DM annihilations, or decays, in each point of the Galactic halo. They then propagate to the Earth subject to the same mechanisms discussed in the previous section, which are in particular described by the canonical sets of parameters MIN-MED-MAX. Concretely, we obtain the \bar{p} fluxes at Earth (post-propagation) from the numerical products provided in [Cirelli 2011], version 4. Notice that these include the subtle effects of energy losses, tertiaries and diffusive reacceleration which, as discussed at length in [Boudaud 2015b], are important to reach a detailed prediction.

We consider four primary annihilation (or decay) channels: $DM DM \rightarrow b\bar{b}, W^+W^-, \mu^+\mu^-$ and $\gamma\gamma$. These, for all practical purposes, cover very well the range of possible spectra. Indeed, annihilation (or decay) into $t\bar{t}$ or hh (with h the Higgs boson) would give spectra practically indistinguishable from those from $DM DM \rightarrow b\bar{b}$, and ZZ from those of W^+W^- . The $\mu^+\mu^-$ channel represents leptonic channels, in which a small yield of antiprotons is obtained thanks to electroweak corrections (namely, the radiation from the final state leptons of a weak boson which decays hadronically). Similarly, the $\gamma\gamma$ channel produces some subdominant \bar{p} flux via electromagnetic corrections¹¹.

We also consider two representative DM Galactic profiles: Einasto and Burkert, with the precise functional forms and definitions of the parameters as in [Cirelli 2011]. The former possesses a peaked distribution toward the Galactic cen-

¹⁰It is also backed by the results recently reported in [Evoli 2015]—appeared after the first version of this study in pre-print form—based on fits to PAMELA B/C, p and He data.

¹¹For simplicity, we consider only the production of \bar{p} from the final state. In principle, in this channel, additional hadronic production is possible from the states mediating the process of DM annihilation into photons.

ter and hence typically results in a more abundant yield of antiprotons with respect to the latter, which features a core in the inner few kpc.

We remind that, in section 4.4.1, we have obtained the re-evaluated astrophysical background fluxes and their uncertainties. In particular, we have computed the fluxes for the MIN, MED and MAX cases, displayed in figure 4.24. Armed with those and with the fluxes from DM as just presented, we can now compute the constraints in the usual planes ‘mass m_{DM} vs. thermally averaged annihilation cross-section $\langle\sigma v\rangle$ ’ or ‘mass m_{DM} vs. decay rate Γ ’. We refer to [Boudaud 2015b] for a detailed discussion of the practical procedure, of which we just repeat here the main lines. Having fixed a propagation model, for a given DM mass m_{DM} and annihilation cross-section $\langle\sigma v\rangle$ (or decay rate Γ) we add the DM signal to the secondary background. The total flux is then

$$\Phi_{\text{tot}}(m_{\text{DM}}, \langle\sigma v\rangle, A, \phi_F) = \Phi_{\text{bkg}}(A, \phi_F) + \Phi_{\text{DM}}(m_{\text{DM}}, \langle\sigma v\rangle, \phi_F) \quad (4.54)$$

and we again find the best fit amplitude and Fisk potential. Finally, we solve the following equation in $\langle\sigma v\rangle$

$$\chi_{\text{DM}}^2(m_{\text{DM}}, \langle\sigma v\rangle, A, \phi_F) - \chi_0^2 = 4, \quad (4.55)$$

(where χ_0 is the minimum chi-squared of the background-only case as computed in the previous section) in order to obtain the exclusion contour. We reproduce this for each mass point.

On the basis of the discussion in the previous section, it makes sense to derive constraints only within the propagation schemes that provide a decent explanation of the background. MAX is the favored scheme. MED provides overall a worse but still reasonable fit to the data, so that we will employ it. In addition, (see figure 4.24, middle panel) at small energies ($T \lesssim 30$ GeV) its fit is good, thus meaningful constraints on relatively light DM ($m_{\text{DM}} \lesssim 300$ GeV) can be derived. We discard instead the MIN case.

The results that we obtain with this strategy are presented in figure 4.25 for the DM annihilation case and in figure 4.26 for the DM decay case. In the left panels we fix a benchmark DM profile (Einasto) and the MED propagation model, and show the constraints for the different particle physics channels introduced above. We see for example that the thermal annihilation cross-section $\langle\sigma v\rangle = 3 \cdot 10^{-26}$ cm³/s is now touched by the exclusion line for $m_{\text{DM}} \sim 150$ GeV for the $\bar{b}b$ channel. In the right panels we explore the impact of changing the propagation parameters or the DM distribution. As already highlighted several times in the literature, the effect is sizable and can reach a factor of up to an order of magnitude. For instance, the previously quoted limit for the mass of a thermal relic can vary between 90 and 250 GeV for the range of models explored here. Of course, as MAX maximizes by definition the DM \bar{p} yield, its constraints are much stronger than those of the MED case. Turning the argument around, if the preference for MAX-like propagation schemes hinted at by preliminary AMS-02 data is confirmed, AMS-02 itself has the unprecedented possibility to exclude $m_{\text{DM}} \lesssim 250$ GeV for thermal annihilation cross-section in the $\bar{b}b$ channel.

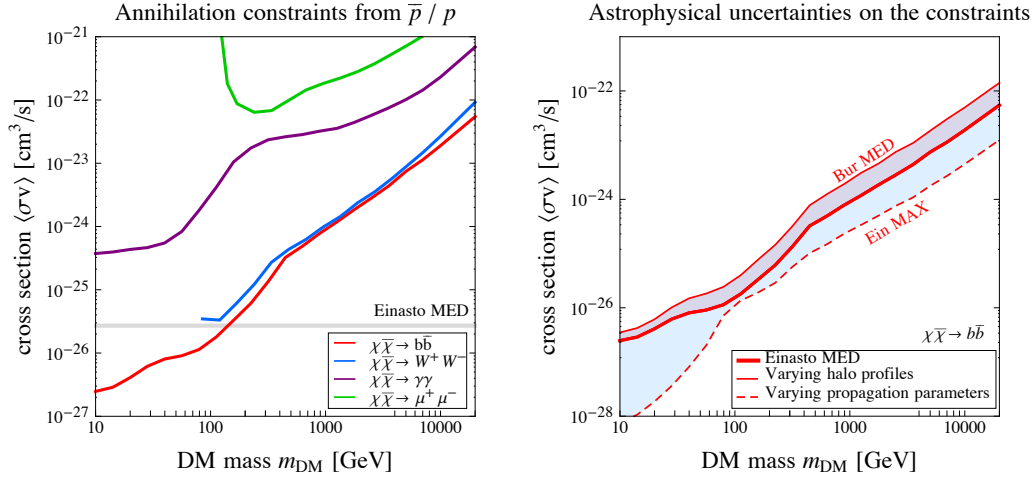


Figure 4.25: **Annihilating DM: current constraints.** Left Panel: *current constraints from the antiproton to proton ratio measurements by AMS-02, for different annihilation channels. The areas above the curves are excluded.* Right Panel: *illustration of the impact of DM-related astrophysical uncertainties: the constraint for the $b\bar{b}$ channel spans the shaded band when varying the propagation parameters (dashed lines) or the halo profiles (solid lines). Notice that in the MIN case the analysis is not sensible, hence not shown here (see text for details).*

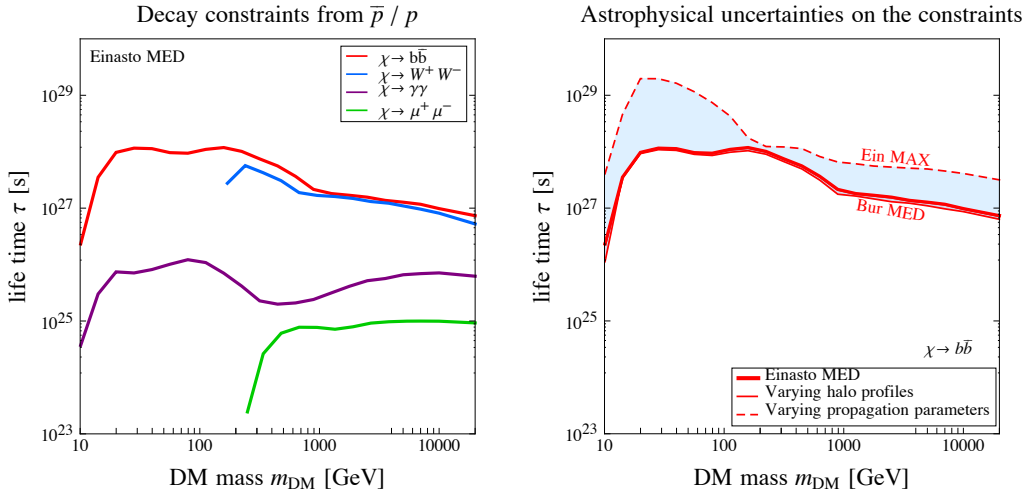


Figure 4.26: **Decaying DM: current constraints.** Left Panel: *current constraints from the antiproton to proton ratio measurements by AMS-02, for different decay channels. The areas below the curves are excluded.* Right Panel: *illustration of the impact of DM-related astrophysical uncertainties: the constraint for the $b\bar{b}$ channel spans the shaded band when varying the propagation parameters (dashed lines) or the halo profiles (solid lines). Notice that in the MIN case the analysis is not sensible, hence not shown here (see text for details).*

4.4.3 Final remarks

In the light of the new p flux published by AMS-02 and the preliminary AMS-02 results presented on the α flux as well as the \bar{p}/p ratio, and using the new results of the \bar{p} production cross-sections, we have re-evaluated the secondary astrophysical predictions for the \bar{p}/p ratio. We have accounted for the different sources of uncertainties: namely on the injection fluxes, on the production cross-sections, on the propagation process and those connected to Solar modulation. Our first and main result is that *there is no unambiguous antiproton excess that can be identified in the first place, and thus, at this stage, no real need for primary sources of antiprotons*. Within errors, secondary astrophysical production alone can account for the data. This conclusion is highly non-trivial, since we relied on updates of *existing* propagation schemes, which were not necessarily expected to work in the high precision and extended energy regime made accessible by AMS-02. Adopting a more conservative treatment of the uncertainties of antiproton production cross-sections involving He as either target or projectile nuclei would clearly reinforce this conclusion.

Next, we enter in the merit of which propagation schemes do account for the data, taking into account the other uncertainties. We find that the data seem to prefer a model, such as MAX, characterized by a relatively mild energy dependence of the diffusion coefficient at high energies. If confirmed, this would go in the same direction as other indications already obtained in different channels, as discussed above.

Finally, an important application concerns updated constraints on DM: within the framework of the propagation schemes that it is sensible to use, we derive bounds that are more stringent by about one order of magnitude with respect to the previous ones [Cirelli 2013, Boudaud 2015b] (based on PAMELA data).

Of course, this analysis is very preliminary and there is still room for improvements. First and foremost, by using the last release of the \bar{p}/p measurement [Aguilar 2016a] with systematic and statistical errors fully accounted for. Yet, this preliminary analysis allows to show that antiprotons confirm themselves as a very powerful probe for CR physics and for DM in particular. Actually, considering the puzzling excesses (with respect to the originally predicted astrophysical background) of undetermined origin in the electron and positron fluxes, considering the complicated background of most gamma-ray searches and considering the challenges of neutrino detection, \bar{p} 's might arguably still be the most promising avenue in DM indirect searches, since improving the knowledge of the background is relatively easier than for other channels and so perhaps seeing the emergence of a clear signal is possible. In this respect, the AMS-02 experiment can play a crucial role. So far it has essentially confirmed the results of previous experiments (most notably PAMELA), but it has done so with an impressively improved accuracy: the qualitative picture in DM indirect searches has been left largely unchanged by it, but AMS-02 has allowed improved pinning down of the parameters and tightening of the constraints.

Notice that the recent studies [Cuoco 2016] and [Cui 2016] based on the last release of the \bar{p} flux [Aguilar 2016a] and the numerical predictions from the Galprop code, claim an excess of antiprotons which would stem from annihilation of DM particles with a mass of 20 to 80 GeV. Quite curiously, these analyses provide a DM mass explaining also the galactic center excess [Calore 2015]. In this context, it is urgent to address the limitations stressed by our analysis:

- first, the main current limitations in the field of charged CRs, namely the determination of the propagation parameters. In this respect, analyzing the newly published B/C ratio, but also the upcoming accurate light nuclei measurements from AMS-02 will provide the community with a very powerful leverage for any search of exotics in CR's.
- secondly, the uncertainties in the production cross-section of antiprotons stress the need for new analyses and measurements. Recently, [Winkler 2017] has reassessed the production cross-section of antiprotons in proton-proton collisions, using the most recent collider data. Violation of Feynmann scaling, enhancement of strange hyperon production, and evolution with the energy of the isospin factor have been taken into account. Interestingly, this study also provides a correlation matrix to deal with the cross-section uncertainties. On the other hand, the work of [Donato 2017] provides suggestions for the region of the parameter space to probe in order to improve the precision on secondary antiproton predictions in the energy range covered by CR experiments.

These ongoing improvements will, at some point, make possible to assess whether or not excesses are present in antiproton data, for instance if the current small deficit increases in significance (although identifying their origin will remain very challenging [Pettorino 2014]). As noticed in the introduction, one should keep in mind that expected astrophysical mechanisms could provide viable explanations for such an excess, e.g. the production of secondary antiprotons at sources, studied by [Blasi 2009], and recently updated in [Cholis 2017].

Bibliography

- [Abbott 2016] B. P. Abbott, R. Abbott, T. D. Abbott, M. R. Abernathy, F. Acernese, K. Ackley, C. Adams, T. Adams, P. Addesso, R. X. Adhikari and et al. *Observation of Gravitational Waves from a Binary Black Hole Merger*. Physical Review Letters, vol. 116, no. 6, page 061102, February 2016. (Not cited.)
- [Abdollahi 2017] S. Abdollahi et al. *Search for Cosmic-Ray Electron and Positron Anisotropies with Seven Years of Fermi Large Area Telescope Data*. Phys. Rev. Lett., vol. 118, no. 9, page 091103, 2017. (Not cited.)
- [Accardo 2014] L. Accardo, M. Aguilar, D. Aisa, A. Alvino, G. Ambrosi, K. Andeen, L. Arruda, N. Attig, P. Azzarello, A. Bachlechner and et al. *High Statistics Measurement of the Positron Fraction in Primary Cosmic Rays of 0.5-500 GeV with the Alpha Magnetic Spectrometer on the International Space Station*. Physical Review Letters, vol. 113, no. 12, page 121101, September 2014. (Not cited.)
- [Ackermann 2012a] M. Ackermann, M. Ajello, A. Albert, L. Baldini, J. Ballet, G. Barbiellini, D. Bastieri, K. Bechtol, R. Bellazzini, E. D. Bloom, E. Bonamente, A. W. Borgland, T. J. Brandt, J. Bregeon, M. Brigida, P. Bruel, R. Buehler, S. Buson, G. A. Caliandro, R. A. Cameron, P. A. Caraveo, C. Cecchi, E. Charles, A. Chekhtman, J. Chiang, S. Ciprini, R. Claus, J. Cohen-Tanugi, J. Conrad, A. Cuoco, S. Cutini, F. D'Ammando, F. de Palma, C. D. Dermer, S. W. Digel, E. do Couto e Silva, P. S. Drell, A. Drlica-Wagner, R. Dubois, C. Favuzzi, S. J. Fegan, E. C. Ferrara, P. Fortin, Y. Fukazawa, P. Fusco, F. Gargano, D. Gasparri, S. Germani, N. Giglietto, M. Giroletti, T. Glanzman, G. Godfrey, G. A. Gomez-Vargas, T. Grégoire, I. A. Grenier, J. E. Grove, S. Guiriec, M. Gustafsson, D. Hadasch, M. Hayashida, K. Hayashi, X. Hou, R. E. Hughes, G. Jóhannesson, A. S. Johnson, T. Kamae, J. Knödlseider, M. Kuss, J. Lande, L. Latronico, M. Lemoine-Goumard, T. Linden, A. M. Lionetto, M. Llana Garde, F. Longo, F. Loparco, M. N. Lovellette, P. Lubrano, M. N. Mazziotta, J. E. McEnery, W. Mitthumsiri, T. Mizuno, C. Monte, M. E. Monzani, A. Morselli, I. V. Moskalenko, S. Murgia, M. Naumann-Godo, J. P. Norris, E. Nuss, T. Ohsugi, A. Okumura, M. Orienti, E. Orlando, J. F. Ormes, D. Paneque, J. H. Panetta, D. Parent, V. Pavlidou, M. Pesce-Rollins, M. Pierbattista, F. Piron, G. Pivato, S. Rainò, R. Rando, A. Reimer, O. Reimer, M. Roth, C. Sbarra, J. Schmitt, C. Sgrò, J. Siegal-Gaskins, E. J. Siskind, G. Spandre, P. Spinelli, A. W. Strong, D. J. Suson, H. Takahashi, T. Tanaka, J. B. Thayer, L. Tibaldo, M. Tinivella, D. F. Torres, G. Tosti, E. Troja, T. L. Usher, J. Vandenbroucke, V. Vasileiou, G. Vianello, V. Vitale, A. P. Waite, B. L. Winer, K. S. Wood, M. Wood, Z. Yang, S. Zimmer and E. Komatsu. *Publisher's Note: Anisotropies in the diffuse gamma-ray*

- background measured by the Fermi LAT [Phys. Rev. D 85, 083007 (2012)].*
Phys. Rev. D, vol. 85, no. 10, page 109901, May 2012. (Not cited.)
- [Ackermann 2012b] M. Ackermann *et al.* *Fermi-LAT Observations of the Diffuse γ -Ray Emission: Implications for Cosmic Rays and the Interstellar Medium.*
Astrophysical Journal, vol. 750, page 3, May 2012. (Not cited.)
- [Adhikari 2017] R. Adhikari, M. Agostini, N. A. Ky, T. Araki, M. Archidiacono, M. Bahr, J. Baur, J. Behrens, F. Bezrukov, P. S. Bhupal Dev, D. Borah, A. Boyarsky, A. de Gouvea, C. A. d. S. Pires, H. J. de Vega, A. G. Dias, P. Di Bari, Z. Djurcic, K. Dolde, H. Dorrer, M. Durero, O. Dragoun, M. Drewes, G. Drexlin, C. E. Düllmann, K. Eberhardt, S. Eliseev, C. Enss, N. W. Evans, A. Faessler, P. Filianin, V. Fischer, A. Fleischmann, J. A. Formaggio, J. Franse, F. M. Fraenkle, C. S. Frenk, G. Fuller, L. Gastaldo, A. Garzilli, C. Giunti, F. Glück, M. C. Goodman, M. C. Gonzalez-Garcia, D. Gorbunov, J. Hamann, V. Hannen, S. Hannestad, S. H. Hansen, C. Hassel, J. Heck, F. Hofmann, T. Houdy, A. Huber, D. Iakubovskiy, A. Ianni, A. Ibarra, R. Jacobsson, T. Jeltema, J. Jochum, S. Kempf, T. Kieck, M. Korzeczek, V. Kornoukhov, T. Lachenmaier, M. Laine, P. Langacker, T. Lasserre, J. Lesgourgues, D. Lhuillier, Y. F. Li, W. Liao, A. W. Long, M. Maltoni, G. Mangano, N. E. Mavromatos, N. Menci, A. Merle, S. Mertens, A. Mirizzi, B. Monreal, A. Nozik, A. Neronov, V. Niro, Y. Novikov, L. Oberauer, E. Otten, N. Palanque-Delabrouille, M. Pallavicini, V. S. Pantuev, E. Papastergis, S. Parke, S. Pascoli, S. Pastor, A. Patwardhan, A. Pilaftsis, D. C. Radford, P. C.-O. Ranitzsch, O. Rest, D. J. Robinson, P. S. Rodrigues da Silva, O. Ruchayskiy, N. G. Sanchez, M. Sasaki, N. Saviano, A. Schneider, F. Schneider, T. Schwetz, S. Schönert, S. Scholl, F. Shankar, R. Shrock, N. Steinbrink, L. Strigari, F. Suekane, B. Suerfu, R. Takahashi, N. T. H. Van, I. Tkachev, M. Totzauer, Y. Tsai, C. G. Tully, K. Valerius, J. W. F. Valle, D. Venos, M. Viel, M. Vivier, M. Y. Wang, C. Weinheimer, K. Wendt, L. Winslow, J. Wolf, M. Wurm, Z. Xing, S. Zhou and K. Zuber. *A White Paper on keV sterile neutrino Dark Matter.* J. Cosmology Astropart. Phys., vol. 1, page 025, January 2017. (Not cited.)
- [Adriani 2009] O. Adriani, G. C. Barbarino, G. A. Bazilevskaya, R. Bellotti, M. Boezio, E. A. Bogomolov, L. Bonechi, M. Bongi, V. Bonvicini, S. Bottai, A. Bruno, F. Cafagna, D. Campana, P. Carlson, M. Casolino, G. Castellini, M. P. de Pascale, G. de Rosa, N. de Simone, V. di Felice, A. M. Galper, L. Grishantseva, P. Hofverberg, S. V. Koldashov, S. Y. Krutkov, A. N. Kvashnin, A. Leonov, V. Malvezzi, L. Marcelli, W. Menn, V. V. Mikhailov, E. Mocchicutti, S. Orsi, G. Osteria, P. Papini, M. Pearce, P. Picozza, M. Ricci, S. B. Ricciarini, M. Simon, R. Sparvoli, P. Spillantini, Y. I. Stozhkov, A. Vacchi, E. Vannuccini, G. Vasilyev, S. A. Voronov, Y. T. Yurkin, G. Zampa, N. Zampa and V. G. Zverev. *An anomalous positron abundance in cosmic*

rays with energies 1.5-100GeV. Nature, vol. 458, pages 607–609, April 2009. (Not cited.)

[Adriani 2010] O. Adriani, G. C. Barbarino, G. A. Bazilevskaya, R. Bellotti, M. Boezio, E. A. Bogomolov, L. Bonechi, M. Bongi, V. Bonvicini, S. Borisov, S. Bottai, A. Bruno, F. Cafagna, D. Campana, R. Carbone, P. Carlson, M. Casolino, G. Castellini, L. Consiglio, M. P. de Pascale, C. de Santis, N. de Simone, V. di Felice, A. M. Galper, W. Gillard, L. Grishantseva, P. Hofverberg, G. Jerse, A. V. Karelin, S. V. Koldashov, S. Y. Krutkov, A. N. Kvashnin, A. Leonov, V. Malvezzi, L. Marcelli, A. G. Mayorov, W. Menn, V. V. Mikhailov, E. Mocchiutti, A. Monaco, N. Mori, N. Nikonov, G. Osteria, P. Papini, M. Pearce, P. Picozza, C. Pizzolotto, M. Ricci, S. B. Ricciarini, L. Rossetto, M. Simon, R. Sparvoli, P. Spillantini, Y. I. Stozhkov, A. Vacchi, E. Vannuccini, G. Vasilyev, S. A. Voronov, J. Wu, Y. T. Yurkin, G. Zampa, N. Zampa, V. G. Zverev and PAMELA Collaboration. *PAMELA Results on the Cosmic-Ray Antiproton Flux from 60 MeV to 180 GeV in Kinetic Energy*. Physical Review Letters, vol. 105, no.12, page 121101, September 2010. (Not cited.)

[Adriani 2011] O. Adriani, G. C. Barbarino, G. A. Bazilevskaya, R. Bellotti, M. Boezio, E. A. Bogomolov, L. Bonechi, M. Bongi, V. Bonvicini, S. Borisov, S. Bottai, A. Bruno, F. Cafagna, D. Campana, R. Carbone, P. Carlson, M. Casolino, G. Castellini, L. Consiglio, M. P. De Pascale, C. De Santis, N. De Simone, V. Di Felice, A. M. Galper, W. Gillard, L. Grishantseva, G. Jerse, A. V. Karelin, S. V. Koldashov, S. Y. Krutkov, A. N. Kvashnin, A. Leonov, V. Malakhov, V. Malvezzi, L. Marcelli, A. G. Mayorov, W. Menn, V. V. Mikhailov, E. Mocchiutti, A. Monaco, N. Mori, N. Nikonov, G. Osteria, F. Palma, P. Papini, M. Pearce, P. Picozza, C. Pizzolotto, M. Ricci, S. B. Ricciarini, L. Rossetto, R. Sarkar, M. Simon, R. Sparvoli, P. Spillantini, Y. I. Stozhkov, A. Vacchi, E. Vannuccini, G. Vasilyev, S. A. Voronov, Y. T. Yurkin, J. Wu, G. Zampa, N. Zampa and V. G. Zverev. *PAMELA Measurements of Cosmic-Ray Proton and Helium Spectra*. Science, vol. 332, page 69, April 2011. (Not cited.)

[Adriani 2013] O. Adriani *et al.* *Measurement of the flux of primary cosmic ray antiprotons with energies of 60-MeV to 350-GeV in the PAMELA experiment*. JETP Lett., vol. 96, pages 621–627, 2013. [Pisma Zh. Eksp. Teor. Fiz.96,693(2012)]. (Not cited.)

[Aguilar 2013a] M. Aguilar, G. Alberti, B. Alpat, A. Alvino, G. Ambrosi, K. Andeen, H. Anderhub, L. Arruda, P. Azzarello, A. Bachlechner and et al. *First Result from the Alpha Magnetic Spectrometer on the International Space Station: Precision Measurement of the Positron Fraction in Primary Cosmic Rays of 0.5-350 GeV*. Physical Review Letters, vol. 110, no. 14, page 141102, April 2013. (Not cited.)

- [Aguilar 2013b] M. Aguilar *et al.* *First Result from the Alpha Magnetic Spectrometer on the International Space Station: Precision Measurement of the Positron Fraction in Primary Cosmic Rays of 0.5-350 GeV*. Phys.Rev.Lett., vol. 110, page 141102, 2013. (Not cited.)
- [Aguilar 2014] M. Aguilar, D. Aisa, A. Alvino, G. Ambrosi, K. Andeen, L. Arruda, N. Attig, P. Azzarello, A. Bachlechner, F. Barao and et al. *Electron and Positron Fluxes in Primary Cosmic Rays Measured with the Alpha Magnetic Spectrometer on the International Space Station*. Physical Review Letters, vol. 113, no. 12, page 121102, September 2014. (Not cited.)
- [Aguilar 2015a] M. Aguilar, D. Aisa, B. Alpat, A. Alvino, G. Ambrosi, K. Andeen, L. Arruda, N. Attig, P. Azzarello, A. Bachlechner and et al. *Precision Measurement of the Helium Flux in Primary Cosmic Rays of Rigidities 1.9 GV to 3 TV with the Alpha Magnetic Spectrometer on the International Space Station*. Physical Review Letters, vol. 115, no. 21, page 211101, November 2015. (Not cited.)
- [Aguilar 2015b] M. Aguilar, D. Aisa, B. Alpat, A. Alvino, G. Ambrosi, K. Andeen, L. Arruda, N. Attig, P. Azzarello, A. Bachlechner and et al. *Precision Measurement of the Proton Flux in Primary Cosmic Rays from Rigidity 1 GV to 1.8 TV with the Alpha Magnetic Spectrometer on the International Space Station*. Physical Review Letters, vol. 114, no. 17, page 171103, May 2015. (Not cited.)
- [Aguilar 2016a] M. Aguilar, L. Ali Cavazonza, B. Alpat, G. Ambrosi, L. Arruda, N. Attig, S. Aupetit, P. Azzarello, A. Bachlechner, F. Barao and et al. *Antiproton Flux, Antiproton-to-Proton Flux Ratio, and Properties of Elementary Particle Fluxes in Primary Cosmic Rays Measured with the Alpha Magnetic Spectrometer on the International Space Station*. Physical Review Letters, vol. 117, no. 9, page 091103, August 2016. (Not cited.)
- [Aguilar 2016b] M. Aguilar, L. Ali Cavazonza, G. Ambrosi, L. Arruda, N. Attig, S. Aupetit, P. Azzarello, A. Bachlechner, F. Barao, A. Barrau, L. Barrin, A. Bartoloni, L. Basara, S. Başğmez-du Pree, M. Battarbee, R. Battiston, U. Becker, M. Behlmann, B. Beischer, J. Berdugo, B. Bertucci, K. F. Bindel, V. Bindi, G. Boella, W. de Boer, K. Bollweg, V. Bonnivard, B. Borgia, M. J. Boschini, M. Bourquin, E. F. Bueno, J. Burger, F. Cadoux, X. D. Cai, M. Capell, S. Caroff, J. Casaus, G. Castellini, F. Cervelli, M. J. Chae, Y. H. Chang, A. I. Chen, G. M. Chen, H. S. Chen, L. Cheng, H. Y. Chou, E. Choumilov, V. Choutko, C. H. Chung, C. Clark, R. Clavero, G. Coignet, C. Consolandi, A. Contin, C. Corti, W. Creus, M. Crispoltoni, Z. Cui, Y. M. Dai, C. Delgado, S. Della Torre, O. Demakov, M. B. Demirköz, L. Derome, S. Di Falco, F. Dimiccoli, C. Díaz, P. von Doetinchem, F. Dong, F. Donnini, M. Duranti, D. D’Urso, A. Egorov, A. Eline, T. Eronen, J. Feng, E. Fiandrini, E. Finch, P. Fisher, V. Formato, Y. Galaktionov, G. Gallucci, B. García,

R. J. García-López, C. Gargiulo, H. Gast, I. Gebauer, M. Gervasi, A. Ghelfi, F. Giovacchini, P. Goglov, D. M. Gómez-Coral, J. Gong, C. Goy, V. Grabski, D. Grandi, M. Graziani, K. H. Guo, S. Haino, K. C. Han, Z. H. He, M. Heil, J. Hoffman, T. H. Hsieh, H. Huang, Z. C. Huang, C. Huh, M. Incagli, M. Ionica, W. Y. Jang, H. Jinchi, S. C. Kang, K. Kanishev, G. N. Kim, K. S. Kim, Th. Kirn, C. Konak, O. Kounina, A. Kounine, V. Koutsenko, M. S. Krafczyk, G. La Vacca, E. Laudi, G. Laurenti, I. Lazzizzera, A. Lebedev, H. T. Lee, S. C. Lee, C. Leluc, H. S. Li, J. Q. Li, J. Q. Li, Q. Li, T. X. Li, W. Li, Y. Li, Z. H. Li, Z. Y. Li, S. Lim, C. H. Lin, P. Lipari, T. Lippert, D. Liu, Hu Liu, V. D. Lordello, S. Q. Lu, Y. S. Lu, K. Luebelsmeyer, F. Luo, J. Z. Luo, S. S. Lv, F. Machate, R. Majka, C. Mañá, J. Marín, T. Martin, G. Martínez, N. Masi, D. Maurin, A. Menchaca-Rocha, Q. Meng, V. M. Mikuni, D. C. Mo, L. Morescalchi, P. Mott, T. Nelson, J. Q. Ni, N. Nikonov, F. Nozzoli, A. Oliva, M. Orcinha, F. Palmonari, C. Palomares, M. Panicia, M. Pauluzzi, S. Pensotti, R. Pereira, N. Picot-Clemente, F. Pilo, C. Pizzolotto, V. Plyaskin, M. Pohl, V. Poireau, A. Putze, L. Quadrani, X. M. Qi, X. Qin, Z. Y. Qu, T. Rähä, P. G. Rancoita, D. Rapin, J. S. Ricol, S. Rosier-Lees, A. Rozhkov, D. Rozza, R. Sagdeev, J. Sandweiss, P. Saouter, S. Schael, S. M. Schmidt, A. Schulz von Dratzig, G. Schwering, E. S. Seo, B. S. Shan, J. Y. Shi, T. Siedenburger, D. Son, J. W. Song, W. H. Sun, M. Tacconi, X. W. Tang, Z. C. Tang, L. Tao, D. Tescaro, Samuel C. C. Ting, S. M. Ting, N. Tomassetti, J. Torsti, C. Türkoğlu, T. Urban, V. Vagelli, E. Valente, C. Vannini, E. Valtonen, M. Vázquez Acosta, M. Vecchi, M. Velasco, J. P. Vialle, V. Vitale, S. Vitillo, L. Q. Wang, N. H. Wang, Q. L. Wang, X. Wang, X. Q. Wang, Z. X. Wang, C. C. Wei, Z. L. Weng, K. Whitman, J. Wienkenhöver, H. Wu, X. Wu, X. Xia, R. Q. Xiong, W. Xu, Q. Yan, J. Yang, M. Yang, Y. Yang, H. Yi, Y. J. Yu, Z. Q. Yu, S. Zeissler, C. Zhang, J. Zhang, J. H. Zhang, S. D. Zhang, S. W. Zhang, Z. Zhang, Z. M. Zheng, Z. Q. Zhu, H. L. Zhuang, V. Zhukov, A. Zichichi, N. Zimmermann and P. Zuccon. *Precision Measurement of the Boron to Carbon Flux Ratio in Cosmic Rays from 1.9 GV to 2.6 TV with the Alpha Magnetic Spectrometer on the International Space Station*. Phys. Rev. Lett., vol. 117, page 231102, Nov 2016. (Not cited.)

[Aguilar 2016c] M. Aguilar, L. Ali Cavazonza, G. Ambrosi, L. Arruda, N. Attig, S. Aupetit, P. Azzarello, A. Bachlechner, F. Barao, A. Barrau and et al. *Precision Measurement of the Boron to Carbon Flux Ratio in Cosmic Rays from 1.9 GV to 2.6 TV with the Alpha Magnetic Spectrometer on the International Space Station*. Physical Review Letters, vol. 117, no. 23, page 231102, December 2016. (Not cited.)

[Alcock 2000] C. Alcock, R. A. Allsman, D. R. Alves, T. S. Axelrod, A. C. Becker, D. P. Bennett, K. H. Cook, N. Dalal, A. J. Drake, K. C. Freeman, M. Geha, K. Griest, M. J. Lehner, S. L. Marshall, D. Minniti, C. A. Nelson, B. A. Peterson, P. Popowski, M. R. Pratt, P. J. Quinn, C. W. Stubbs, W. Suther-

- land, A. B. Tomaney, T. Vandehei and D. Welch. *The MACHO Project: Microlensing Results from 5.7 Years of Large Magellanic Cloud Observations*. ApJ, vol. 542, pages 281–307, October 2000. (Not cited.)
- [AMS] *AMS-02 Collaboration, Talks at the ‘AMS Days at CERN’, 15-17 april 2015*. (Not cited.)
- [Anderson 2012] L. Anderson, E. Aubourg, S. Bailey, D. Bizyaev, M. Blanton, A. S. Bolton, J. Brinkmann, J. R. Brownstein, A. Burden, A. J. Cuesta, L. A. N. da Costa, K. S. Dawson, R. de Putter, D. J. Eisenstein, J. E. Gunn, H. Guo, J.-C. Hamilton, P. Harding, S. Ho, K. Honscheid, E. Kazin, D. Kirkby, J.-P. Kneib, A. Labatie, C. Loomis, R. H. Lupton, E. Malanushenko, V. Malanushenko, R. Mandelbaum, M. Manera, C. Maraston, C. K. McBride, K. T. Mehta, O. Mena, F. Montesano, D. Muna, R. C. Nichol, S. E. Nuza, M. D. Olmstead, D. Oravetz, N. Padmanabhan, N. Palanque-Delabrouille, K. Pan, J. Parejko, I. Pâris, W. J. Percival, P. Petitjean, F. Prada, B. Reid, N. A. Roe, A. J. Ross, N. P. Ross, L. Samushia, A. G. Sánchez, D. J. Schlegel, D. P. Schneider, C. G. Scóccola, H.-J. Seo, E. S. Sheldon, A. Simmons, R. A. Skibba, M. A. Strauss, M. E. C. Swanson, D. Thomas, J. L. Tinker, R. Tojeiro, M. V. Magaña, L. Verde, C. Wagner, D. A. Wake, B. A. Weaver, D. H. Weinberg, M. White, X. Xu, C. Yèche, I. Zehavi and G.-B. Zhao. *The clustering of galaxies in the SDSS-III Baryon Oscillation Spectroscopic Survey: baryon acoustic oscillations in the Data Release 9 spectroscopic galaxy sample*. MNRAS, vol. 427, pages 3435–3467, December 2012. (Not cited.)
- [Appelquist 2001] T. Appelquist, H.-C. Cheng and B. A. Dobrescu. *Bounds on universal extra dimensions*. Phys. Rev. D, vol. 64, no. 3, page 035002, August 2001. (Not cited.)
- [Babcock 1939] H. W. Babcock. *The rotation of the Andromeda Nebula*. Lick Observatory Bulletin, vol. 19, pages 41–51, 1939. (Not cited.)
- [Badhwar 1977] G. D. Badhwar, R. L. Golden and S. A. Stephens. *Analytic representation of the proton-proton and proton-nucleus cross-sections and its application to the sea-level spectrum and charge ratio of muons*. Phys. Rev. D, vol. 15, pages 820–831, February 1977. (Not cited.)
- [Baltz 1999] E. A. Baltz and J. Edsjö. *Positron propagation and fluxes from neutralino annihilation in the halo*. Phys. Rev. D, vol. 59, no. 2, page 023511, January 1999. (Not cited.)
- [Barwick 1997] S. W. Barwick, J. J. Beatty, A. Bhattacharyya, C. R. Bower, C. J. Chaput, S. Coutu, G. A. de Nolfo, J. Knapp, D. M. Lowder, S. McKee, D. Mueller, J. A. Musser, S. L. Nutter, E. Schneider, S. P. Swordy, G. Tarle, A. D. Tomasch, E. Torbet and HEAT Collaboration. *Measurements of the Cosmic-Ray Positron Fraction from 1 to 50 GeV*. ApJ, vol. 482, pages L191–L194, June 1997. (Not cited.)

- [Beatty 2004] J. J. Beatty, A. Bhattacharyya, C. Bower, S. Coutu, M. A. Duvernois, S. McKee, S. A. Minnick, D. Müller, J. Musser, S. Nutter, A. W. Labrador, M. Schubnell, S. Swordy, G. Tarlé and A. Tomasch. *New Measurement of the Cosmic-Ray Positron Fraction from 5 to 15 GeV*. Physical Review Letters, vol. 93, no. 24, page 241102, December 2004. (Not cited.)
- [Bélanger 2011] G. Bélanger, F. Boudjema, P. Brun, A. Pukhov, S. Rosier-Lees, P. Salati and A. Semenov. *Indirect search for dark matter with microOMEGAs_2.4*. Computer Physics Communications, vol. 182, pages 842–856, March 2011. (Not cited.)
- [Bélanger 2012] G. Bélanger, C. Boehm, M. Cirelli, J. Da Silva and A. Pukhov. *PAMELA and FERMI limits on the neutralino-chargino mass degeneracy*. J. Cosmology Astropart. Phys., vol. 11, page 028, November 2012. (Not cited.)
- [Bélanger 2014] G. Bélanger, F. Boudjema, A. Pukhov and A. Semenov. *microOMEGAs_3: A program for calculating dark matter observables*. Computer Physics Communications, vol. 185, pages 960–985, March 2014. (Not cited.)
- [Bergström 1999] L. Bergström, J. Edsjö and P. Ullio. *Cosmic Antiprotons as a Probe for Supersymmetric Dark Matter?* ApJ, vol. 526, pages 215–235, November 1999. (Not cited.)
- [Bernard 2012] G. Bernard, T. Delahaye, P. Salati and R. Taillet. *Variance of the Galactic nuclei cosmic ray flux*. A&A, vol. 544, page A92, August 2012. (Not cited.)
- [Betoule 2014] M. Betoule, R. Kessler, J. Guy, J. Mosher, D. Hardin, R. Biswas, P. Astier, P. El-Hage, M. König, S. Kuhlmann, J. Marriner, R. Pain, N. Regnault, C. Balland, B. A. Bassett, P. J. Brown, H. Campbell, R. G. Carlberg, F. Cellier-Holzem, D. Cinabro, A. Conley, C. B. D’Andrea, D. L. DePoy, M. Doi, R. S. Ellis, S. Fabbro, A. V. Filippenko, R. J. Foley, J. A. Frieman, D. Fouchez, L. Galbany, A. Goobar, R. R. Gupta, G. J. Hill, R. Hlozek, C. J. Hogan, I. M. Hook, D. A. Howell, S. W. Jha, L. Le Guillou, G. Leloudas, C. Lidman, J. L. Marshall, A. Möller, A. M. Mourão, J. Neveu, R. Nichol, M. D. Olmstead, N. Palanque-Delabrouille, S. Perlmutter, J. L. Prieto, C. J. Pritchett, M. Richmond, A. G. Riess, V. Ruhlmann-Kleider, M. Sako, K. Schahmanche, D. P. Schneider, M. Smith, J. Sollerman, M. Sullivan, N. A. Walton and C. J. Wheeler. *Improved cosmological constraints from a joint analysis of the SDSS-II and SNLS supernova samples*. A&A, vol. 568, page A22, August 2014. (Not cited.)
- [Blasi 2009] P. Blasi and P. D. Serpico. *High-Energy Antiprotons from Old Supernova Remnants*. Physical Review Letters, vol. 103, no. 8, page 081103, August 2009. (Not cited.)

- [Bonnivard 2015] V. Bonnavard, C. Combet, D. Maurin and M. G. Walker. *Spherical Jeans analysis for dark matter indirect detection in dwarf spheroidal galaxies - impact of physical parameters and triaxiality*. MNRAS, vol. 446, pages 3002–3021, January 2015. (Not cited.)
- [Bonnivard 2016] V. Bonnavard, D. Maurin and M. G. Walker. *Contamination of stellar-kinematic samples and uncertainty about dark matter annihilation profiles in ultrafaint dwarf galaxies: the example of Segue I*. MNRAS, vol. 462, pages 223–234, October 2016. (Not cited.)
- [Bosma 1981] A. Bosma. *21-cm line studies of spiral galaxies. II. The distribution and kinematics of neutral hydrogen in spiral galaxies of various morphological types*. AJ, vol. 86, pages 1825–1846, December 1981. (Not cited.)
- [Boudaud 2015a] M. Boudaud, S. Aupetit, S. Caroff, A. Putze, G. Belanger, Y. Genolini, C. Goy, V. Poireau, V. Poulin, S. Rosier, P. Salati, L. Tao and M. Vecchi. *A new look at the cosmic ray positron fraction*. A&A, vol. 575, page A67, March 2015. (Not cited.)
- [Boudaud 2015b] M. Boudaud, M. Cirelli, G. Giesen and P. Salati. *A fussy re-visit of antiprotons as a tool for Dark Matter searches*. J. Cosmology Astropart. Phys., vol. 5, page 013, May 2015. (Not cited.)
- [Boudaud 2016] M. Boudaud, E. F. Bueno, S. Caroff, Y. Genolini, V. Poulin, V. Poireau, A. Putze, S. Rosier, P. Salati and M. Vecchi. *The pinching method for Galactic cosmic ray positrons: implications in the light of precision measurements*. ArXiv e-prints, December 2016. (Not cited.)
- [Bovy 2012] J. Bovy and S. Tremaine. *On the Local Dark Matter Density*. ApJ, vol. 756, page 89, September 2012. (Not cited.)
- [Boylan-Kolchin 2011] M. Boylan-Kolchin, J. S. Bullock and M. Kaplinghat. *Too big to fail? The puzzling darkness of massive Milky Way subhaloes*. MNRAS, vol. 415, pages L40–L44, July 2011. (Not cited.)
- [Briel 1992] U. G. Briel, J. P. Henry and H. Boehringer. *Observation of the Coma cluster of galaxies with ROSAT during the all-sky survey*. A&A, vol. 259, pages L31–L34, June 1992. (Not cited.)
- [Bringmann 2007] T. Bringmann and P. Salati. *Galactic antiproton spectrum at high energies: Background expectation versus exotic contributions*. Phys. Rev. D, vol. 75, no. 8, page 083006, April 2007. (Not cited.)
- [Bringmann 2012] T. Bringmann, F. Donato and R. A. Lineros. *Radio data and synchrotron emission in consistent cosmic ray models*. J. Cosmology Astropart. Phys., vol. 1, page 049, January 2012. (Not cited.)

- [Bringmann 2014] T. Bringmann, M. Vollmann and C. Weniger. *Updated cosmic-ray and radio constraints on light dark matter: Implications for the GeV gamma-ray excess at the Galactic Center*. Phys. Rev. D, vol. 90, no. 12, page 123001, December 2014. (Not cited.)
- [Bulbul 2014] E. Bulbul, M. Markevitch, A. Foster, R. K. Smith, M. Loewenstein and S. W. Randall. *Detection of an Unidentified Emission Line in the Stacked X-Ray Spectrum of Galaxy Clusters*. ApJ, vol. 789, page 13, July 2014. (Not cited.)
- [Burkert 1995] A. Burkert. *The Structure of Dark Matter Halos in Dwarf Galaxies*. ApJ, vol. 447, pages L25–L28, July 1995. (Not cited.)
- [Cacciapaglia 2010] G. Cacciapaglia, A. Deandrea and J. Llodra-Perez. *A dark matter candidate from Lorentz invariance in 6D*. Journal of High Energy Physics, vol. 3, page 83, March 2010. (Not cited.)
- [Calmet 2017] X. Calmet and I. Kuntz. *What is modified gravity and how to differentiate it from particle dark matter?* European Physical Journal C, vol. 77, page 132, February 2017. (Not cited.)
- [Calore 2015] F. Calore, I. Cholis, C. McCabe and C. Weniger. *A tale of tails: Dark matter interpretations of the Fermi GeV excess in light of background model systematics*. Phys. Rev. D, vol. 91, no. 6, page 063003, March 2015. (Not cited.)
- [Cheng 2002] H.-C. Cheng, J. L. Feng and K. T. Matchev. *Kaluza-Klein Dark Matter*. Physical Review Letters, vol. 89, no. 21, page 211301, October 2002. (Not cited.)
- [Cholis 2013] I. Cholis and D. Hooper. *Dark matter and pulsar origins of the rising cosmic ray positron fraction in light of new data from the AMS*. Phys. Rev. D, vol. 88, no. 2, page 023013, July 2013. (Not cited.)
- [Cholis 2017] I. Cholis, D. Hooper and T. Linden. *Evidence for the Stochastic Acceleration of Secondary Antiprotons by Supernova Remnants*. ArXiv e-prints, January 2017. (Not cited.)
- [Ciafaloni 2011] P. Ciafaloni, D. Comelli, A. Riotto, F. Sala, A. Strumia and A. Urbano. *Weak corrections are relevant for dark matter indirect detection*. J. Cosmology Astropart. Phys., vol. 3, page 019, March 2011. (Not cited.)
- [Cirelli 2011] M. Cirelli, G. Corcella, A. Hektor, G. Hütsi, M. Kadastik, P. Panci, M. Raidal, F. Sala and A. Strumia. *PPPC 4 DM ID: a poor particle physicist cookbook for dark matter indirect detection*. J. Cosmology Astropart. Phys., vol. 3, page 051, March 2011. (Not cited.)

- [Cirelli 2013] M. Cirelli and G. Giesen. *Antiprotons from Dark Matter: current constraints and future sensitivities*. J. Cosmology Astropart. Phys., vol. 4, page 15, April 2013. (Not cited.)
- [Cirelli 2014] M. Cirelli, D. Gaggero, G. Giesen, M. Taoso and A. Urbano. *Antiproton constraints on the GeV gamma-ray excess: a comprehensive analysis*. J. Cosmology Astropart. Phys., vol. 12, page 045, December 2014. (Not cited.)
- [Cirelli 2015] M. Cirelli. *Status of Indirect (and Direct) Dark Matter searches*. ArXiv e-prints, November 2015. (Not cited.)
- [Clowe 2006] D. Clowe, M. Bradač, A. H. Gonzalez, M. Markevitch, S. W. Randall, C. Jones and D. Zaritsky. *A Direct Empirical Proof of the Existence of Dark Matter*. ApJ, vol. 648, pages L109–L113, September 2006. (Not cited.)
- [Cui 2016] M.-Y. Cui, Q. Yuan, Y.-L. Sming Tsai and Y.-Z. Fan. *Possible dark matter annihilation signal in the AMS-02 antiproton data*. ArXiv e-prints, October 2016. (Not cited.)
- [Cuoco 2016] A. Cuoco, M. Krämer and M. Korsmeier. *Novel dark matter constraints from antiprotons in the light of AMS-02*. ArXiv e-prints, October 2016. (Not cited.)
- [Delahaye 2008] T. Delahaye, R. Lineros, F. Donato, N. Fornengo and P. Salati. *Positrons from dark matter annihilation in the galactic halo: Theoretical uncertainties*. Phys. Rev. D, vol. 77, no. 6, page 063527, March 2008. (Not cited.)
- [Delahaye 2009] T. Delahaye, R. Lineros, F. Donato, N. Fornengo, J. Lavalle, P. Salati and R. Taillet. *Galactic secondary positron flux at the Earth*. A&A, vol. 501, pages 821–833, July 2009. (Not cited.)
- [Delahaye 2010] T. Delahaye, J. Lavalle, R. Lineros, F. Donato and N. Fornengo. *Galactic electrons and positrons at the Earth: new estimate of the primary and secondary fluxes*. A&A, vol. 524, page A51, December 2010. (Not cited.)
- [Di Bernardo 2013] G. Di Bernardo, C. Evoli, D. Gaggero, D. Grasso and L. Maccone. *Cosmic ray electrons, positrons and the synchrotron emission of the Galaxy: consistent analysis and implications*. J. Cosmology Astropart. Phys., vol. 3, page 036, March 2013. (Not cited.)
- [Di Mauro 2014a] M. Di Mauro, F. Donato, N. Fornengo, R. Lineros and A. Vitino. *Interpretation of AMS-02 electrons and positrons data*. J. Cosmology Astropart. Phys., vol. 4, page 6, April 2014. (Not cited.)
- [di Mauro 2014b] M. di Mauro, F. Donato, A. Goudelis and P. D. Serpico. *New evaluation of the antiproton production cross section for cosmic ray studies*. Phys. Rev. D, vol. 90, no. 8, page 085017, October 2014. (Not cited.)

- [Di Mauro 2016] M. Di Mauro, F. Donato, N. Fornengo and A. Vittino. *Dark matter vs. astrophysics in the interpretation of AMS-02 electron and positron data*. J. Cosmology Astropart. Phys., vol. 5, page 031, May 2016. (Not cited.)
- [Dodelson 2011] S. Dodelson. *The Real Problem with MOND*. International Journal of Modern Physics D, vol. 20, pages 2749–2753, 2011. (Not cited.)
- [Donato 2001] F. Donato, D. Maurin, P. Salati, A. Barrau, G. Boudoul and R. Taillet. *Antiprotons from Spallations of Cosmic Rays on Interstellar Matter*. ApJ, vol. 563, pages 172–184, December 2001. (Not cited.)
- [Donato 2004] F. Donato, N. Fornengo, D. Maurin, P. Salati and R. Taillet. *Antiprotons in cosmic rays from neutralino annihilation*. Phys. Rev. D, vol. 69, no. 6, page 063501, March 2004. (Not cited.)
- [Donato 2009] F. Donato, D. Maurin, P. Brun, T. Delahaye and P. Salati. *Constraints on WIMP Dark Matter from the High Energy PAMELA $p\bar{p}/p$ Data*. Physical Review Letters, vol. 102, no. 7, page 071301, February 2009. (Not cited.)
- [Donato 2017] F. Donato, M. Korsmeier and M. Di Mauro. *Prescriptions on antiproton cross section data for precise theoretical antiproton flux predictions*. ArXiv e-prints, April 2017. (Not cited.)
- [Drewes 2013] M. Drewes. *The Phenomenology of Right Handed Neutrinos*. International Journal of Modern Physics E, vol. 22, pages 1330019–593, August 2013. (Not cited.)
- [Duperray 2003] R. P. Duperray, C.-Y. Huang, K. V. Protasov and M. Buénerd. *Parametrization of the antiproton inclusive production cross section on nuclei*. Phys. Rev. D, vol. 68, no. 9, page 094017, November 2003. (Not cited.)
- [DuVernois 2001] M. A. DuVernois, S. W. Barwick, J. J. Beatty, A. Bhattacharyya, C. R. Bower, C. J. Chaput, S. Coutu, G. A. de Nolfo, D. M. Lowder, S. McKee, D. Müller, J. A. Musser, S. L. Nutter, E. Schneider, S. P. Swordy, G. Tarlé, A. D. Tomasch and E. Torbet. *Cosmic-Ray Electrons and Positrons from 1 to 100 GeV: Measurements with HEAT and Their Interpretation*. ApJ, vol. 559, pages 296–303, September 2001. (Not cited.)
- [Einasto 1965] J. Einasto. *On the Construction of a Composite Model for the Galaxy and on the Determination of the System of Galactic Parameters*. Trudy Astrofizicheskogo Instituta Alma-Ata, vol. 5, pages 87–100, 1965. (Not cited.)
- [Esmaili 2014] A. Esmaili, S. K. Kang and P. Dario Serpico. *IceCube events and decaying dark matter: hints and constraints*. J. Cosmology Astropart. Phys., vol. 12, page 054, December 2014. (Not cited.)

- [Evoli 2012] C. Evoli, I. Cholis, D. Grasso, L. Maccione and P. Ullio. *Antiprotons from dark matter annihilation in the Galaxy: Astrophysical uncertainties*. Phys. Rev. D, vol. 85, no. 12, page 123511, June 2012. (Not cited.)
- [Evoli 2015] C. Evoli, D. Gaggero and D. Grasso. *Secondary antiprotons as a Galactic Dark Matter probe*. J. Cosmology Astropart. Phys., vol. 12, page 039, December 2015. (Not cited.)
- [Ewen 1951] H. I. Ewen and E. M. Purcell. *Observation of a Line in the Galactic Radio Spectrum: Radiation from Galactic Hydrogen at 1,420 Mc./sec.* Nature, vol. 168, page 356, September 1951. (Not cited.)
- [Ferrière 2001] K. M. Ferrière. *The interstellar environment of our galaxy*. Reviews of Modern Physics, vol. 73, pages 1031–1066, October 2001. (Not cited.)
- [Fisk 1971] L. A. Fisk. *Solar modulation of galactic cosmic rays, 2*. J. Geophys. Res., vol. 76, page 221, 1971. (Not cited.)
- [Fixsen 2009] D. J. Fixsen. *The Temperature of the Cosmic Microwave Background*. ApJ, vol. 707, pages 916–920, December 2009. (Not cited.)
- [Fornengo 2014a] N. Fornengo, R. A. Lineros, M. Regis and M. Taoso. *The isotropic radio background revisited*. J. Cosmology Astropart. Phys., vol. 4, page 008, April 2014. (Not cited.)
- [Fornengo 2014b] N. Fornengo, L. Maccione and A. Vittino. *Constraints on particle dark matter from cosmic-ray antiprotons*. J. Cosmology Astropart. Phys., vol. 4, page 003, April 2014. (Not cited.)
- [Gamow 1946] G. Gamow. *Expanding Universe and the Origin of Elements*. Physical Review, vol. 70, pages 572–573, October 1946. (Not cited.)
- [García-Bellido 2017] J. García-Bellido. *Massive Primordial Black Holes as Dark Matter and their detection with Gravitational Waves*. ArXiv e-prints, February 2017. (Not cited.)
- [Genolini 2015] Y. Genolini, A. Putze, P. Salati and P. D. Serpico. *Theoretical uncertainties in extracting cosmic-ray diffusion parameters: the boron-to-carbon ratio*. A&A, vol. 580, page A9, August 2015. (Not cited.)
- [Genolini 2016] Y. Genolini, P. Salati, P. Serpico and R. Taillet. *Stable laws and cosmic ray physics*. ArXiv e-prints, October 2016. (Not cited.)
- [Ghelfi 2016] A. Ghelfi, F. Barao, L. Derome and D. Maurin. *Non-parametric determination of H and He interstellar fluxes from cosmic-ray data*. A&A, vol. 591, page A94, June 2016. (Not cited.)

- [Giesen 2015] G. Giesen, M. Boudaud, Y. Génolini, V. Poulin, M. Cirelli, P. Salati and P. D. Serpico. *AMS-02 antiprotons, at last! Secondary astrophysical component and immediate implications for Dark Matter*. J. Cosmology Astropart. Phys., vol. 9, page 023, September 2015. (Not cited.)
- [Gleeson 1968] L. J. Gleeson and W. I. Axford. *Solar Modulation of Galactic Cosmic Rays*. ApJ, vol. 154, page 1011, December 1968. (Not cited.)
- [Goodenough 2009] L. Goodenough and D. Hooper. *Possible Evidence For Dark Matter Annihilation In The Inner Milky Way From The Fermi Gamma Ray Space Telescope*. ArXiv e-prints, October 2009. (Not cited.)
- [Hohl 1971] F. Hohl. *Numerical Experiments with a Disk of Stars*. ApJ, vol. 168, page 343, September 1971. (Not cited.)
- [Hooper 2009] D. Hooper, P. Blasi and P. Dario Serpico. *Pulsars as the sources of high energy cosmic ray positrons*. J. Cosmology Astropart. Phys., vol. 1, page 25, January 2009. (Not cited.)
- [Hooper 2015] D. Hooper, T. Linden and P. Mertsch. *What does the PAMELA antiproton spectrum tell us about dark matter?* J. Cosmology Astropart. Phys., vol. 3, page 021, March 2015. (Not cited.)
- [Hooper 2017] D. Hooper, I. Cholis, T. Linden and K. Fang. *HAWC Observations Strongly Favor Pulsar Interpretations of the Cosmic-Ray Positron Excess*. ArXiv e-prints, February 2017. (Not cited.)
- [Hubble 1936] E. P. Hubble. *Realm of the Nebulae*. 1936. (Not cited.)
- [Jansky 1933] K. G. Jansky. *Radio Waves from Outside the Solar System*. Nature, vol. 132, page 66, July 1933. (Not cited.)
- [Jeltema 2015] T. Jeltema and S. Profumo. *Discovery of a 3.5 keV line in the Galactic Centre and a critical look at the origin of the line across astronomical targets*. MNRAS, vol. 450, pages 2143–2152, June 2015. (Not cited.)
- [Jeltema 2016] T. Jeltema and S. Profumo. *Deep XMM observations of Draco rule out at the 99 per cent confidence level a dark matter decay origin for the 3.5 keV line*. MNRAS, vol. 458, pages 3592–3596, June 2016. (Not cited.)
- [Jungman 1996] G. Jungman, M. Kamionkowski and K. Griest. *Supersymmetric dark matter*. Phys. Rep., vol. 267, pages 195–373, March 1996. (Not cited.)
- [Kalberla 1999] P. M. W. Kalberla, Y. A. Shchekinov and R.-J. Dettmar. *H_{α} dark matter in the galactic halo from EGRET*. A&A, vol. 350, pages L9–L12, October 1999. (Not cited.)

- [Kamae 2006] T. Kamae, N. Karlsson, T. Mizuno, T. Abe and T. Koi. *Parameterization of γ , $e^{+/-}$, and Neutrino Spectra Produced by p - p Interaction in Astronomical Environments*. ApJ, vol. 647, pages 692–708, August 2006. (Not cited.)
- [Kappl 2014] R. Kappl and M. W. Winkler. *The cosmic ray antiproton background for AMS-02*. J. Cosmology Astropart. Phys., vol. 9, page 051, September 2014. (Not cited.)
- [Kappl 2015] R. Kappl, A. Reinert and M. W. Winkler. *AMS-02 antiprotons reloaded*. J. Cosmology Astropart. Phys., vol. 10, page 034, October 2015. (Not cited.)
- [Kapteyn 1922] J. C. Kapteyn. *No. 230. First attempt at a theory of the arrangement and motion of the sidereal system*. Contributions from the Mount Wilson Observatory / Carnegie Institution of Washington, vol. 230, pages 1–27, 1922. (Not cited.)
- [Klein 1926] O. Klein. *Quantentheorie und fünfdimensionale Relativitätstheorie*. Zeitschrift für Physik, vol. 37, pages 895–906, December 1926. (Not cited.)
- [Korsmeier 2016] M. Korsmeier and A. Cuoco. *Galactic cosmic-ray propagation in the light of AMS-02: I. Analysis of protons, helium, and antiprotons*. ArXiv e-prints, July 2016. (Not cited.)
- [Lavalle 2014] J. Lavalle, D. Maurin and A. Putze. *Direct constraints on diffusion models from cosmic-ray positron data: Excluding the minimal model for dark matter searches*. Phys. Rev. D, vol. 90, no. 8, page 081301, October 2014. (Not cited.)
- [Lewis 2003] A. D. Lewis, D. A. Buote and J. T. Stocke. *Chandra Observations of A2029: The Dark Matter Profile Down to below $0.01r_{\text{vir}}$ in an Unusually Relaxed Cluster*. ApJ, vol. 586, pages 135–142, March 2003. (Not cited.)
- [Lin 2015] S.-J. Lin, Q. Yuan and X.-J. Bi. *Quantitative study of the AMS-02 electron/positron spectra: Implications for pulsars and dark matter properties*. Phys. Rev. D, vol. 91, no. 6, page 063508, March 2015. (Not cited.)
- [Linden 2013] T. Linden and S. Profumo. *Probing the Pulsar Origin of the Anomalous Positron Fraction with AMS-02 and Atmospheric Cherenkov Telescopes*. ApJ, vol. 772, page 18, July 2013. (Not cited.)
- [Malyshev 2009] D. Malyshev, I. Cholis and J. Gelfand. *Pulsars versus dark matter interpretation of ATIC/PAMELA*. Phys. Rev. D, vol. 80, no. 6, page 063005, September 2009. (Not cited.)
- [Malyshev 2014] D. Malyshev, A. Neronov and D. Eckert. *Constraints on 3.55 keV line emission from stacked observations of dwarf spheroidal galaxies*. Phys. Rev. D, vol. 90, no. 10, page 103506, November 2014. (Not cited.)

- [Manconi 2017] S. Manconi, M. Di Mauro and F. Donato. *Dipole anisotropy in cosmic electrons and positrons: inspection on local sources*. J. Cosmology Astropart. Phys., vol. 1, page 006, January 2017. (Not cited.)
- [Mannheim 1994] K. Mannheim and R. Schlickeiser. *Interactions of cosmic ray nuclei*. A&A, vol. 286, pages 983–996, June 1994. (Not cited.)
- [Maurin 2001] D. Maurin, F. Donato, R. Taillet and P. Salati. *Cosmic Rays below $Z=30$ in a Diffusion Model: New Constraints on Propagation Parameters*. ApJ, vol. 555, pages 585–596, July 2001. (Not cited.)
- [Milgrom 2015] M. Milgrom. *MOND theory*. Canadian Journal of Physics, vol. 93, pages 107–118, February 2015. (Not cited.)
- [Moore 1999] B. Moore, S. Ghigna, F. Governato, G. Lake, T. Quinn, J. Stadel and P. Tozzi. *Dark Matter Substructure within Galactic Halos*. ApJ, vol. 524, pages L19–L22, October 1999. (Not cited.)
- [Moskalenko 1998] I. V. Moskalenko and A. W. Strong. *Production and Propagation of Cosmic-Ray Positrons and Electrons*. ApJ, vol. 493, pages 694–707, January 1998. (Not cited.)
- [Navarro 1996] J. F. Navarro, C. S. Frenk and S. D. M. White. *The Structure of Cold Dark Matter Halos*. ApJ, vol. 462, page 563, May 1996. (Not cited.)
- [Navarro 1997] J. F. Navarro, C. S. Frenk and S. D. M. White. *A Universal Density Profile from Hierarchical Clustering*. ApJ, vol. 490, pages 493–508, December 1997. (Not cited.)
- [Navarro 2010] J. F. Navarro, A. Ludlow, V. Springel, J. Wang, M. Vogelsberger, S. D. M. White, A. Jenkins, C. S. Frenk and A. Helmi. *The diversity and similarity of simulated cold dark matter haloes*. MNRAS, vol. 402, pages 21–34, February 2010. (Not cited.)
- [Norbury 2007] J. W. Norbury and L. W. Townsend. *Parameterized total cross sections for pion production in nuclear collisions*. Nuclear Instruments and Methods in Physics Research B, vol. 254, pages 187–192, January 2007. (Not cited.)
- [Oort 1932] J. H. Oort. *The force exerted by the stellar system in the direction perpendicular to the galactic plane and some related problems*. Bull. Astron. Inst. Netherlands, vol. 6, page 249, August 1932. (Not cited.)
- [Orlando 2013] E. Orlando and A. Strong. *Galactic synchrotron emission with cosmic ray propagation models*. MNRAS, vol. 436, pages 2127–2142, December 2013. (Not cited.)
- [Paczynski 1986] B. Paczynski. *Gravitational microlensing by the galactic halo*. ApJ, vol. 304, pages 1–5, May 1986. (Not cited.)

- [Peccei 1977] R. D. Peccei and H. R. Quinn. *CP conservation in the presence of pseudoparticles*. *Physical Review Letters*, vol. 38, pages 1440–1443, June 1977. (Not cited.)
- [Penzias 1965] A. A. Penzias and R. W. Wilson. *A Measurement of Excess Antenna Temperature at 4080 Mc/s*. *ApJ*, vol. 142, pages 419–421, July 1965. (Not cited.)
- [Pettorino 2014] V. Pettorino, G. Busoni, A. De Simone, E. Morgante, A. Riotto and W. Xue. *Can AMS-02 discriminate the origin of an anti-proton signal?* *J. Cosmology Astropart. Phys.*, vol. 10, page 078, October 2014. (Not cited.)
- [Planck Collaboration 2014] Planck Collaboration, P. A. R. Ade, N. Aghanim, C. Armitage-Caplan, M. Arnaud, M. Ashdown, F. Atrio-Barandela, J. Aumont, C. Baccigalupi, A. J. Banday and et al. *Planck 2013 results. XV. CMB power spectra and likelihood*. *A&A*, vol. 571, page A15, November 2014. (Not cited.)
- [Planck Collaboration 2016] Planck Collaboration, P. A. R. Ade, N. Aghanim, M. Arnaud, M. Ashdown, J. Aumont, C. Baccigalupi, A. J. Banday, R. B. Barreiro, J. G. Bartlett and et al. *Planck 2015 results. XIII. Cosmological parameters*. *A&A*, vol. 594, page A13, September 2016. (Not cited.)
- [Poincare 1906] H. Poincare. *The Milky Way and the Theory of Gases*. *Popular Astronomy*, vol. 14, pages 475–488, October 1906. (Not cited.)
- [Ptuskin 1997] V. S. Ptuskin, H. J. Voelk, V. N. Zirakashvili and D. Breitschwerdt. *Transport of relativistic nucleons in a galactic wind driven by cosmic rays*. *Astronomy and Astrophysics*, vol. 321, pages 434–443, May 1997. (Not cited.)
- [Putze 2010] A. Putze, L. Derome and D. Maurin. *A Markov Chain Monte Carlo technique to sample transport and source parameters of Galactic cosmic rays. II. Results for the diffusion model combining B/C and radioactive nuclei*. *A&A*, vol. 516, page A66, June 2010. (Not cited.)
- [Randall 2008] S. W. Randall, M. Markevitch, D. Clowe, A. H. Gonzalez and M. Bradač. *Constraints on the Self-Interaction Cross Section of Dark Matter from Numerical Simulations of the Merging Galaxy Cluster 1E 0657-56*. *ApJ*, vol. 679, pages 1173–1180, June 2008. (Not cited.)
- [Rees 1974] M. J. Rees and J. E. Gunn. *The origin of the magnetic field and relativistic particles in the Crab Nebula*. *MNRAS*, vol. 167, pages 1–12, April 1974. (Not cited.)
- [Rico 2015] J. Rico, M. Wood, A. Drlica-Wagner, J. Aleksić, for the MAGIC Collaboration and the Fermi-LAT Collaboration. *Limits to dark matter properties from a combined analysis of MAGIC and Fermi-LAT observations of dwarf satellite galaxies*. *ArXiv e-prints*, August 2015. (Not cited.)

- [Riemer-Sorensen 2009] S. Riemer-Sorensen and S. H. Hansen. *Decaying dark matter in Draco*. ArXiv e-prints, January 2009. (Not cited.)
- [RT] *Dossier matière noire Richard Taillet*. http://lapth.cnrs.fr/pg-nomin/taillet/dossier_matiere_noire/matiere_noire.php. Accessed: 2017-01-30. (Not cited.)
- [Rubin 1970] V. C. Rubin and W. K. Ford Jr. *Rotation of the Andromeda Nebula from a Spectroscopic Survey of Emission Regions*. ApJ, vol. 159, page 379, February 1970. (Not cited.)
- [Salati 1996] P. Salati, P. Chardonnet, X. Luo, J. Silk and R. Taillet. *The gas deficiency of the galactic halo*. A&A, vol. 313, pages 1–7, September 1996. (Not cited.)
- [Shapiro 1983] S. L. Shapiro and S. A. Teukolsky. *Black holes, white dwarfs, and neutron stars: The physics of compact objects*. 1983. (Not cited.)
- [Springel 2005] V. Springel, S. D. M. White, A. Jenkins, C. S. Frenk, N. Yoshida, L. Gao, J. Navarro, R. Thacker, D. Croton, J. Helly, J. A. Peacock, S. Cole, P. Thomas, H. Couchman, A. Evrard, J. Colberg and F. Pearce. *Simulations of the formation, evolution and clustering of galaxies and quasars*. Nature, vol. 435, pages 629–636, June 2005. (Not cited.)
- [Strong 1998] A. W. Strong and I. V. Moskalenko. *Propagation of Cosmic-Ray Nucleons in the Galaxy*. ApJ, vol. 509, pages 212–228, December 1998. (Not cited.)
- [Strong 2001] A. W. Strong and I. V. Moskalenko. *Models for galactic cosmic-ray propagation*. Advances in Space Research, vol. 27, pages 717–726, 2001. (Not cited.)
- [Tan 1982] L. C. Tan and L. K. Ng. *Parameterization of π^+ invariant cross section in p - p collisions using a new scaling variable*. Phys. Rev. D, vol. 26, pages 1179–1182, September 1982. (Not cited.)
- [Tan 1983a] L. C. Tan and L. K. Ng. *Calculation of the equilibrium antiproton spectrum*. Journal of Physics G Nuclear Physics, vol. 9, pages 227–242, February 1983. (Not cited.)
- [Tan 1983b] L. C. Tan and L. K. Ng. *Parametrisation of hadron inclusive cross sections in p - p collisions extended to very low energies*. Journal of Physics G Nuclear Physics, vol. 9, pages 1289–1308, October 1983. (Not cited.)
- [Taoso 2008] M. Taoso, G. Bertone and A. Masiero. *Dark matter candidates: a ten-point test*. J. Cosmology Astropart. Phys., vol. 3, page 022, March 2008. (Not cited.)

- [Tegmark 2006] M. Tegmark, D. J. Eisenstein, M. A. Strauss, D. H. Weinberg, M. R. Blanton, J. A. Frieman, M. Fukugita, J. E. Gunn, A. J. S. Hamilton, G. R. Knapp, R. C. Nichol, J. P. Ostriker, N. Padmanabhan, W. J. Percival, D. J. Schlegel, D. P. Schneider, R. Scoccimarro, U. Seljak, H.-J. Seo, M. Swanson, A. S. Szalay, M. S. Vogeley, J. Yoo, I. Zehavi, K. Abazajian, S. F. Anderson, J. Annis, N. A. Bahcall, B. Bassett, A. Berlind, J. Brinkmann, T. Budavari, F. Castander, A. Connolly, I. Csabai, M. Doi, D. P. Finkbeiner, B. Gillespie, K. Glazebrook, G. S. Hennessy, D. W. Hogg, Ž. Ivezić, B. Jain, D. Johnston, S. Kent, D. Q. Lamb, B. C. Lee, H. Lin, J. Loveday, R. H. Lupton, J. A. Munn, K. Pan, C. Park, J. Peoples, J. R. Pier, A. Pope, M. Richmond, C. Rockosi, R. Scranton, R. K. Sheth, A. Stebbins, C. Stoughton, I. Szapudi, D. L. Tucker, D. E. vanden Berk, B. Yanny and D. G. York. *Cosmological constraints from the SDSS luminous red galaxies*. Phys. Rev. D, vol. 74, no. 12, page 123507, December 2006. (Not cited.)
- [Tisserand 2007] P. Tisserand, L. Le Guillou, C. Afonso, J. N. Albert, J. Andersen, R. Ansari, É. Aubourg, P. Bareyre, J. P. Beaulieu, X. Charlot, C. Coutures, R. Ferlet, P. Fouqué, J. F. Glicenstein, B. Goldman, A. Gould, D. Graff, M. Gros, J. Haissinski, C. Hamadache, J. de Kat, T. Lasserre, É. Lesquoy, C. Loup, C. Magneville, J. B. Marquette, É. Maurice, A. Maury, A. Milsztajn, M. Moniez, N. Palanque-Delabrouille, O. Perdureau, Y. R. Rahal, J. Rich, M. Spiro, A. Vidal-Madjar, L. Vigroux, S. Zylberajch and EROS-2 Collaboration. *Limits on the Macho content of the Galactic Halo from the EROS-2 Survey of the Magellanic Clouds*. A&A, vol. 469, pages 387–404, July 2007. (Not cited.)
- [Tully 2014] R. B. Tully, H. Courtois, Y. Hoffman and D. Pomarède. *The Laniakea supercluster of galaxies*. Nature, vol. 513, pages 71–73, September 2014. (Not cited.)
- [Valentijn 1999] E. A. Valentijn and P. P. van der Werf. *First Extragalactic Direct Detection of Large-Scale Molecular Hydrogen in the Disk of NGC 891*. ApJ, vol. 522, pages L29–L33, September 1999. (Not cited.)
- [Van de Hulst 1957] HC Van de Hulst, E Raimond and H Van Woerden. *Rotation and density distribution of the Andromeda nebula derived from observations of the 21-cm line*. Bulletin of the Astronomical Institutes of the Netherlands, vol. 14, page 1, 1957. (Not cited.)
- [van den Bosch 2001] F. C. van den Bosch, A. Burkert and R. A. Swaters. *The angular momentum content of dwarf galaxies: new challenges for the theory of galaxy formation*. MNRAS, vol. 326, pages 1205–1215, September 2001. (Not cited.)
- [Volders 1959] L. M. J. S. Volders. *Neutral hydrogen in M 33 and M 101*. Bull. Astron. Inst. Netherlands, vol. 14, page 323, September 1959. (Not cited.)

- [Winkler 2017] M. W. Winkler. *Cosmic ray antiprotons at high energies*. *J. Cosmology Astropart. Phys.*, vol. 2, page 048, February 2017. (Not cited.)
- [YM] *Historical papers Yann Mambrin*. http://www.ymambrini.com/My_World/History.html. Accessed: 2017-01-30. (Not cited.)
- [Yoon 2011] Y. S. Yoon, H. S. Ahn, P. S. Allison, M. G. Bagliesi, J. J. Beatty, G. Bigongiari, P. J. Boyle, J. T. Childers, N. B. Conklin, S. Coutu, M. A. DuVernois, O. Ganel, J. H. Han, J. A. Jeon, K. C. Kim, M. H. Lee, L. Lutz, P. Maestro, A. Malinine, P. S. Marrocchesi, S. A. Minnick, S. I. Mognet, S. Nam, S. Nutter, I. H. Park, N. H. Park, E. S. Seo, R. Sina, S. Swordy, S. P. Wakely, J. Wu, J. Yang, R. Zei and S. Y. Zinn. *Cosmic-ray Proton and Helium Spectra from the First CREAM Flight*. *ApJ*, vol. 728, page 122, February 2011. (Not cited.)
- [Yüksel 2009] H. Yüksel, M. D. Kistler and T. Stanev. *TeV Gamma Rays from Geminga and the Origin of the GeV Positron Excess*. *Physical Review Letters*, vol. 103, no. 5, page 051101, July 2009. (Not cited.)
- [Yusifov 2004] I. Yusifov and I. Küçük. *Revisiting the radial distribution of pulsars in the Galaxy*. *A&A*, vol. 422, pages 545–553, August 2004. (Not cited.)
- [Zwicky 1933] F. Zwicky. *Die Rotverschiebung von extragalaktischen Nebeln*. *Helvetica Physica Acta*, vol. 6, pages 110–127, 1933. (Not cited.)

Conclusion and prospects

Recent CR experiments, such as AMS-02, have reached an unprecedented level of precision, unveiling fine-details of the energy spectra. They are challenging the current models of production and propagation of these particles, fostering theoretical refinements.

Reaching the percent precision level, we have seen that the new CR measurements are able to probe the discrete nature of the sources, so far modeled as a continuum in space and time. We have proposed a statistical theory in order to compute the probability of measuring the actual flux, with respect to the ensemble average. The latter uses the generalized version of the central limit theorem which encodes large deviations from unknown local sources. As long as astrophysical observations cannot provide us with a comprehensive and precise understanding of the local production of CR, such a *theoretical* uncertainty should be included in any phenomenological study. In particular, this could reconcile part of the growing disagreement between the commonly used *ensemble average* predictions and the current data, leading to low quality fits. In practice, this calls for a more subtle generalization that would allow to deal with correlations of flux predictions at different energies, in a theory which, by now, can only be applied at a single energy. Nevertheless, our first study has shown its usefulness by quantitatively gauging the prominence of local sources through examples extracted from literature. We recall that the explanation of the proton hardening above ~ 200 GV involving local sources yields a probability below the percent in any homogeneous propagation models and should be accompanied by large anisotropies, contrarily to observations. Finally, it might be worth entertaining the possibility to extend this framework to other CR observables, notably the anisotropy.

Now more than ever, the improved precision of nuclei fluxes, and notably the last publication by AMS-02 of the B/C ratio, call for new spallation cross-section measurements. The situation has languished for almost 30 years, despite the fact that during this period it has been repeatedly realized how dramatic the lack of measurements could be for future CR analyses. Well, those once “future” analysis are the ones of concern at present. Fortunately, the awareness to this problem is gaining momentum in the astroparticle community, now facing the embarrassing situation to analyze the percent accurate data from the *billion of dollars* AMS-02 experiment with $\sim 20\%$ theoretical uncertainties, despite the fact that technology

and facilities exist to reduce uncertainties by an order of magnitude via sensibly cheaper laboratory experiments. New window of opportunities from CERN experiments such as LHCb, Shine-NA61, will soon start to address some of these concerns. In that respect, we will soon complete a wish list for each nuclei. We emphasise that these measurements are the basic requirements to better constrain CR nuclei propagation scenarios. Indeed, we have shown in the third part of this thesis that sophisticated propagation models are of little use for species which carry averaged information at the Galactic scale. Furthermore, we believe that the degeneracy of the propagation parameters with a “secondary” injection at sources could probably be lifted by including several nuclei fluxes in the analysis.

Despite these limitations, it is worth mentioning some preliminary results: By relying on a peculiar cross-section dataset, some studies report discrepancies between the propagation scenarios of *light* and *heavy* species, pointing toward a non homogeneous diffusion at the Galaxy scale. This option could be interesting to test by using other observables such as leptons and gamma-rays. Moreover, as highlighted in the thesis, the same hardening which fails to be explained by local source effects, could be well interpreted as break of the diffusion coefficient hidden in the featureless B/C ratio. This will be the main topic of a forthcoming paper. More comprehensive analyses would be performed at a later time, following the publication of AMS-02 light nuclei spectra, and hopefully, radioactive nuclei. Here it is worthy to recall that comparing the results from different analyses is a delicate task, since one has to take care of the underlying propagation hypothesis used. Important differences are often related to the cleavage between semi-analytical and numerical approaches, for which a detailed comparison should be performed.

Dark matter indirect searches in CR antiparticles rely on a precise secondary background estimation, and is thus completely entangled with the above mentioned problems. In the case of antiprotons, the tempting possibility to explain any excess by DM annihilation should better wait a time when theoretical uncertainties will be under control. It is wiser to settle for deriving conservative constraints, or to cross-check claims of signals from other channels. For the case of positrons, however, the excitement for a DM explanation triggered by the huge discrepancy between the data and the background rapidly vanished, constrained by the halo emission in several wavelengths, and the numerous alternative provided by astrophysics. We have strengthened these conclusions thanks to the newly devised *pinching method*, through which we have shown that the mere shape of the positron flux excludes any general DM annihilation, whatever the propagation model chosen in a very conservative set. Instead, one or several local pulsars could easily power enough positrons to explain the observed enhancement of the flux.

Needless to say, the mystery of the nature of DM is still there, and indirect DM detection has not yet said its last word. It is encouraging that advances in the diagnostic power are expected both via improved sensitivity in existing channels (think of the forthcoming Cherenkov Telescope Array for high energy gamma rays) or the opening of new channels altogether, in particular the low-energy antideutons with

the GAPS (General Antiparticle Spectrometer) experiment. By then, we should make all we can to make sure that theoretical capabilities will be able to match the forthcoming, unprecedented quality data.

Solutions of the transport equation

A.1 Analytical solutions

A.1.1 Simplification and solution at high energies

Having a glance at the timescales presented in the figure 1.11, we see that above 10 GeV/nuc one can safely neglect all the energy losses, the reacceleration and the effect of the convective wind. Moreover we have seen that the commonly used extrapolations of the cross sections reach a plateau above few GeV, and thus can be considered as energy independent. Hence the propagation equation 1.123 becomes:

$$\frac{\partial \psi_\alpha}{\partial t} - \nabla_{\mathbf{x}} K \nabla_{\mathbf{x}} \psi_\alpha + \sigma_\alpha v_\alpha n \psi_\alpha + \frac{\psi_\alpha}{\tau_\alpha} = q_\alpha + \sum_{Z_\beta \geq Z_\alpha}^{Z_{max}} \sigma_{\beta \rightarrow \alpha} v_\beta n \psi_\beta + \frac{\psi_\alpha}{\tau_\beta}. \quad (\text{A.1})$$

Let us first consider the solution of this equation in the 1D model, where the matter of the galactic disk is pinched inside an infinitesimally thin disk of height $2h$. That way, the processes of interaction of CRs with matter are in the plan $z = 0$, and we rewrite $n(\mathbf{x}) \rightarrow 2h \delta(z) n^0$. Furthermore, the sources of CRs which should in principle be considered as discrete in space and time, are here approximated by a continuous jelly also concentrated inside the Galactic plane of this 1D model. One can argue that this approximation is well justified since the propagation timescale is much longer than the injection period of CRs by SNRs. This assumption (discussed in deeper details for the primary species next chapter), and the fact that the relaxation is much shorter than the Galaxy age, let us consider equation A.1 in the stationary regime, and we obtain:

$$-K \frac{\partial^2 \psi_\alpha}{\partial z^2} + 2h \delta(z) \sigma_\alpha v_\alpha n \psi_\alpha + \frac{\psi_\alpha}{\tau_\alpha} = 2h \delta(z) q_\alpha + 2h \delta(z) \sum_{Z_\beta \geq Z_\alpha}^{Z_{max}} \sigma_{\beta \rightarrow \alpha} v_\beta n \psi_\beta + \frac{\psi_\alpha}{\tau_\beta}, \quad (\text{A.2})$$

To simplify the demonstration of the solution, let us consider a stable species. Above the galactic plane, so for $z > 0$, the equation writes:

$$-K \frac{\partial^2 \psi_\alpha}{\partial z^2} = 0, \quad (\text{A.3})$$

whose solution is:

$$\psi_\alpha(z, E_{kn}) = \psi_\alpha^0 \left(\frac{L-z}{L} \right), \quad (\text{A.4})$$

when we assume that the density of CRs is null outside the magnetic halo of size L ($\psi_\alpha(z=L) = 0$) and we introduce $\psi_\alpha^0 = \psi_\alpha(z=0)$. Then integrating across the Galactic plane, and using the symmetry of the CRs density with respect to this plane ($\psi_\alpha(z) = \psi_\alpha(-z)$), we obtain that

$$\frac{2K}{L} \psi_\alpha^0 + 2h \sigma_\alpha v_\alpha n \psi_\alpha^0 = 2h q_\alpha^0 + 2h \sum_{Z_\beta \geq Z_\alpha}^{Z_{max}} \sigma_{\beta \rightarrow \alpha} v_\beta n \psi_\beta^0. \quad (\text{A.5})$$

Using the fact that $v_\alpha(E_{kn}) = v_\beta(E_{kn})$ which readily obtain:

$$\psi_\alpha^0(E_{kn}) = \frac{\frac{q_\alpha^0}{v n} + \sum_{Z_\beta \geq Z_\alpha}^{Z_{max}} \sigma_{\beta \rightarrow \alpha} \psi_\beta^0}{\sigma_{diff} + \sigma_\alpha}, \quad (\text{A.6})$$

by introducing $\sigma_{diff} = K/(h L n v)$ a quantity homogeneous to a cross section, useful to gauge the relative impact of spallation and propagation. By Using the times scales defined in section 1.4, we can also rewrite this equation:

$$\psi_\alpha^0(E_{kn}) = \tau_{leak}^\alpha \left(q_\alpha^0 + \sum_{Z_\beta \geq Z_\alpha}^{Z_{max}} \psi_\beta^0 / \tau_{frag}^{\beta \rightarrow \alpha} \right). \quad (\text{A.7})$$

We deduce that the flux of a species α depends on the flux of all the heavier species β fragmenting into α . Once the flux of the heaviest species is known, we clearly see the triangular that equation A.6 leads to an analytical triangular system which can be simply solved. More advanced solutions are obtained in the cases of radioactive species and summarized in appendix A.1.2.

A more realistic geometry for the Galaxy and its magnetic halo is to consider a 2D cylindrical box of height L and radius R_{gal} . This change enables us to take into account the radial boundary which impact significantly the flux measured at Earth for large halos sizes. Furthermore this geometry may be used to include more realistic distribution of sources with a cylindrical symmetry. The calculation relies on the projection of the quantities on the basis of the zero order Bessel functions (J_0). These functions are used to force the radial boundary condition $\psi_\alpha(E_{kn}, r = R_{gal}, z)$ and enable a factorization of the radial dependence:

$$\psi_\alpha(E_{kn}, r, z) = \sum_i^\infty \psi_\alpha^i(E_{kn}, z) J_0(\xi_i \frac{r}{R_{gal}}), \quad (\text{A.8})$$

$$q_\alpha(E_{kn}, r, z) = \sum_i^\infty q_\alpha^i(E_{kn}, z) J_0(\xi_i \frac{r}{R_{gal}}), \quad (\text{A.9})$$

The ξ_i are the zeros of the J_0 function. The source term is calculated using the orthogonalization relation,

$$\int_{-1}^1 u J_0(\xi_i u) J_0(\xi_j u) du = \frac{\delta_{ij}}{2} J_1^2(\xi_i), \quad (\text{A.10})$$

to invert equation A.9, and we obtain:

$$q_\alpha^i(z, E) = \frac{2}{R_{gal}^2} \frac{1}{J_1^2(\xi_i)} \int_0^{R_{gal}} r J_0\left(\xi_i \frac{r}{R_{gal}}\right) q_\alpha(r, z, E) dr. \quad (\text{A.11})$$

A table summarizing the solutions for the 2D model is presented in appendix A.1.2. In the high energy approximation, the solutions remains analytical when including the galactic wind current but neglecting the adiabatic losses effects. The solutions of this precise case are also included in the table A.2. The simplified 1D solutions can be recovered from the 2D model in the limiting case where R_{gal} is taken to be infinite. In the same vein, taking the solutions in presence of the convective current with an infinitely small value of V_c let us recover the 1D solutions without wind.

A.1.2 Table of the high energy solutions for the 1D geometry

In the following tables we recall the solutions of the high energy approximation in different geometries. In theses solutions we have introduced the surface density of the Galaxy μ , and an effective mass for the interstellar hydrogen, including the helium abundance. The production and destruction cross sections are defined consistently.

Geometry	1D	2D Cylindrical (homogenous distribution of radius R)
Flux of a nucleus α	$\psi_\alpha^0(E_k)$	$\psi_\alpha^0(E_k, R_\odot) = \sum_i^N J_0(\xi_i \frac{R_\odot}{R_{gal}}) \psi_\alpha^{0,i}(E_k)$
Flux of stable nuclei : Stable $_\beta \rightarrow$ Stable $_\alpha$	$Q_\alpha + \frac{\sum_{Z_\beta \geq Z_\alpha}^{Z_{max}} \sigma_{\beta \rightarrow \alpha} \psi_\beta^0}{\sigma^{diff} + \sigma_\alpha}$	$\psi_\alpha^{0,i}(E_k) = \frac{Q_\alpha^i + \sum_{Z_\beta \geq Z_\alpha}^{Z_{max}} \sigma_{\beta \rightarrow \alpha} \psi_\beta^{0,i}}{\sigma^{diff,i} + \sigma_\alpha}$
Flux of radioactive nuclei : Stable $_\beta \rightarrow$ Instable $_\alpha$	$Q_\alpha + \frac{\sum_{Z_\beta \geq Z_\alpha}^{Z_{max}} \sigma_{\beta \rightarrow \alpha} \psi_\beta^0}{\sigma_\alpha^{diff-rad} + \sigma_\alpha}$	$\psi_\alpha^{0,i}(E_k) = \frac{Q_\alpha^i + \sum_{Z_\beta \geq Z_\alpha}^{Z_{max}} \sigma_{\beta \rightarrow \alpha} \psi_\beta^{0,i}}{\sigma_\alpha^{diff-rad,i} + \sigma_\alpha}$
Flux of nuclei products of radioactive nuclei : Instable $_{\beta_p} \rightarrow$ Stable $_\alpha$	$Q_\alpha + \frac{\sum_{Z_\beta \geq Z_\alpha}^{Z_{max}} \sigma_{\beta \rightarrow \alpha} \psi_\beta^0 + \sigma_{\beta_p}^{prod} \psi_{\beta_p}^0}{\sigma^{diff} + \sigma_\alpha}$	$\psi_\alpha^{0,i}(E_k) = \frac{Q_\alpha^i + \sum_{Z_\beta \geq Z_\alpha}^{Z_{max}} \sigma_{\beta \rightarrow \alpha} \psi_\beta^{0,i} + \sigma_{\beta_p}^{prod,i} \psi_{\beta_p}^0}{\sigma^{diff,i} + \sigma_\alpha}$
Diffusion term	$\sigma^{diff} = \frac{2Km_H}{v\mu L}$ and $\sigma_\alpha^{diff-rad} = \sigma^{diff} \frac{L}{\lambda_\alpha} \coth(\frac{L}{\lambda_\alpha})$ with $\lambda_\alpha = \sqrt{K\tau_\alpha}$	$\sigma^{diff,i} = \sigma^{diff} S_i \coth S_i$ $\sigma_\alpha^{diff-rad,i} = \sigma^{diff} S_i^\alpha \coth S_i^\alpha$ With $S_i = \xi_i \frac{L}{R_{gal}}$ and $S_i^\alpha = L \sqrt{\frac{\xi_i^2}{R_{gal}^2} + \frac{1}{\lambda_\alpha^2}}$
Source term	$Q_\alpha = \frac{q_\alpha}{4\pi n_{ISM}} = f_\alpha A_{isotopes} \alpha \left(\frac{R}{R_0 = 1GV}\right)^{-\alpha}$ With $[q_\alpha] = \#part.cm^{-3}.s^{-1}.(GeV/nuc)^{-1}$ $\sigma_{\beta_p}^{prod} = \sigma_{\beta_p}^{diff-rad} - \sigma^{diff}$ $= \sigma^{diff} \left[\frac{L}{\lambda_{\beta_p}} \coth\left(\frac{L}{\lambda_{\beta_p}}\right) - 1 \right]$	$Q_\alpha^i = \frac{q_\alpha q_i}{4\pi n_{ISM}} = f_\alpha A_{isotopes} \alpha q_i \left(\frac{R}{R_0 = 1GV}\right)^{-\alpha}$ $q_i = \frac{2}{J_1^2(\xi_i) \xi_i} \int_0^{\xi_i} X J_0(X) dX$ and $\sigma_{\beta_p}^{prod,i} = \sigma_{\beta_p}^{diff-rad,i} - \sigma^{diff,i}$ $= \sigma^{diff} (S_i^\alpha \coth S_i^\alpha - S_i \coth S_i)$

Table A.1: Summary of the high energy solutions of the propagation equation in the 1D and the 2D model

Geometry	1D with vertical convective wind V_c
Flux of a nucleus α	$\psi_\alpha^0(E_k)$
Flux of stable nuclei : Stable $_\beta \rightarrow$ Stable $_\alpha$	$\psi_\alpha^0(E_k) = \frac{Q_\alpha + \sum_{Z_\beta \geq Z_\alpha}^{Z_{max}} \sigma_{\beta \rightarrow \alpha} \psi_\beta^0}{\sigma_{diff,w}^{diff} + \sigma_\alpha}$
Flux of radioactive nuclei : Stable $_\beta \rightarrow$ Instable $_\alpha$	$\psi_\alpha^0(E_k) = \frac{Q_\alpha + \sum_{Z_\beta \geq Z_\alpha}^{Z_{max}} \sigma_{\beta \rightarrow \alpha} \psi_\beta^0}{\sigma_\alpha^{diff-rad,w} + \sigma_\alpha}$
Flux of nuclei products of radioactive nuclei : Instable $_{\beta_p} \rightarrow$ Stable $_\alpha$	$\psi_\alpha^0(E_k) = \frac{Q_\alpha + \sum_{Z_\beta \geq Z_\alpha}^{Z_{max}} \sigma_{\beta \rightarrow \alpha} \psi_\beta^0 + \sigma_{\beta_p}^{prod} \psi_{\beta_p}^0}{\sigma_{diff,w}^{diff} + \sigma_\alpha}$
Diffusion term	$\sigma_{diff,w}^{diff} = \sigma^{diff} \frac{\eta}{1 - \exp(-\eta)} \text{ and } \eta = \frac{V_c L}{K} = \frac{\tau_{conv}}{\tau_{diff}}$ $\sigma_\alpha^{diff-rad,w} = \sigma^{diff} \left(\frac{\eta}{2} + \frac{L}{\lambda_\alpha^w} \coth\left(\frac{L}{\lambda_\alpha^w}\right) \right)$ $\text{with } \lambda_\alpha^w = \left(\left(\frac{\eta}{2L}\right)^2 + \left(\frac{1}{\lambda_\alpha}\right)^2 \right)^{-1/2}$
Source term	$Q_\alpha = \frac{q_\alpha}{4\pi n_{ISM}} = f_\alpha A_{isotopes} \alpha \left(\frac{R}{R_0 = 1GV} \right)^{-\alpha}$ <p>With $[q_\alpha] = \# \text{part.cm}^{-3} \cdot \text{s}^{-1} \cdot (\text{GeV/nuc})^{-1}$</p> $\sigma_{\beta_p}^{prod,w} = \sigma_{\beta_p}^{diff-rad,w} - \sigma_{diff,w}^{diff}$ $= \sigma^{diff} \left[\frac{L}{\lambda_{\beta_p}^w} \coth\left(\frac{L}{\lambda_{\beta_p}^w}\right) - \frac{\eta}{2} \coth\left(\frac{\eta}{2}\right) \right]$

Table A.2: Summary of the high energy solutions of the propagation equation in the 1D model including convective current.

A.2 Semi-numerical solutions

A.2.1 Numerical method and convergence

In general we want to take into account all the low energy processes of the propagation, and so to solve equation 1.123. We directly deal with the 2D geometry, and for clarity we take the example of a stable nuclei for which the only relevant processes inside the magnetic halo are diffusion and convection. By projecting the quantities on the orthogonal basis of the zero Bessel functions (as in A.8) gives above the galactic disk:

$$\partial_z (V_C \psi_\alpha^i) - K \partial_z^2 \psi_\alpha^i + K \left\{ \frac{\xi_i^2}{R^2} \right\} \psi_\alpha^i = 0 .$$

Using the radial and vertical boundary conditions, we end up with the solution:

$$\psi_\alpha^i(z, E) = \psi_\alpha^i(0, E) \exp \left\{ \frac{V_C z}{2K} \right\} \mathcal{F}_i(z) , \quad (\text{A.12})$$

where,

$$\mathcal{F}_i(z) = \sinh \left\{ \frac{S_i}{2} (L - z) \right\} / \sinh \left\{ \frac{S_i}{2} L \right\} . \quad (\text{A.13})$$

and,

$$S_i^2 = \left(\frac{V_C}{K} \right)^2 + \left(\frac{2\xi_i}{R} \right)^2 .$$

As for the high energy solution we integrate the equation across the galactic disk, and we obtain the master equation:

$$\left\{ 2h\Gamma_\alpha + V_C + K S_i \coth \left(\frac{S_i L}{2} \right) \right\} \psi_\alpha^{i,0} + 2h \partial_E \{ b_{\text{tot}}(E) \psi_\alpha^{i,0} - K_{EE}(E) \partial_E \psi_\alpha^{i,0} \} = 2h Q_\alpha^i , \quad (\text{A.14})$$

where we have introduced the source term,

$$Q_\alpha^i = q_\alpha^i + \sum_{\substack{Z_{\max} \\ Z_\beta \geq Z_\alpha}} \Gamma_{\beta \rightarrow \alpha} \psi_\beta^{i,0} , \quad (\text{A.15})$$

and the destruction and production rate,

$$\Gamma_\alpha = \sigma_\alpha v_\alpha n \quad \text{and} \quad \Gamma_{\beta \rightarrow \alpha} = \sigma_{\beta \rightarrow \alpha} v_\beta n . \quad (\text{A.16})$$

Concerning unstable species, their master equation can be cast in a similar form than A.14, although the factors are different. The solutions are summarized in [Maurin 2001].

In any case the propagation equation can be cast into the following form:

$$u + \alpha(x) \frac{d}{dx} \left[\beta(x) u - \gamma(x) \frac{du}{dx} \right] = u^0 , \quad (\text{A.17})$$

Solving this system requires to fix boundary conditions. Physically at high energy the solution of the equation should correspond to the pure diffusive case where one can neglect safely the energy losses and the reacceleration. This suggest the following boundary condition:

$$u = u^0 \quad \rightarrow \quad \begin{cases} a_K = 0 \\ b_K = 1 \end{cases} \quad (\text{A.27})$$

The low energy condition, formerly used in the USINE code, assumes that $\frac{\partial^2 u}{\partial x^2} \Big|_{x_0} = 0$. This empirical prescription suggests that the spectrum is linear around x_0 using a log scale in energy. This can be motivated by looking at the data available for such low energies. Such a condition leads to the following first coefficients in the matrix:

$$\frac{\partial^2 u}{\partial x^2} \Big|_{x_0} = 0 \quad \rightarrow \quad \begin{cases} b_0 = 1 - \frac{\alpha_0}{\Delta x} \left(\beta_0 - \frac{\gamma_{\frac{1}{2}} - \gamma_{-\frac{1}{2}}}{\Delta x} \right) \\ c_0 = \frac{\alpha_0}{\Delta x} \left(\beta_1 - \frac{\gamma_{\frac{1}{2}} - \gamma_{-\frac{1}{2}}}{\Delta x} \right) \end{cases} \quad (\text{A.28})$$

Using the prescription of [LeVeque 1998] for a second order accurate method:

$$\frac{\partial^2 u}{\partial x^2} \Big|_{x_0} = \frac{\frac{u_1 - u_0}{\Delta x} - \frac{u_0 - u_{-1}}{\Delta x}}{\Delta x} = 0 \quad \rightarrow \quad u_{-1} = 2u_0 - u_1 \quad (\text{A.29})$$

We obtain the following condition:

$$\frac{\partial^2 u}{\partial x^2} \Big|_{x_0} = 0 \quad \rightarrow \quad \begin{cases} b_0 = 1 + \frac{\alpha_0}{\Delta x} \left(-\beta_{-1} + \frac{\gamma_{\frac{1}{2}} - \gamma_{-\frac{1}{2}}}{\Delta x} \right) \\ c_0 = \frac{\alpha_0}{\Delta x} \left(\frac{\beta_1 + \beta_{-1}}{2} - \frac{\gamma_{\frac{1}{2}} - \gamma_{-\frac{1}{2}}}{\Delta x} \right) \end{cases} \quad (\text{A.30})$$

At the upper bound for the energy the condition would read:

$$\frac{\partial^2 u}{\partial x^2} \Big|_{x_K} = 0 \quad \rightarrow \quad \begin{cases} b_K = 1 + \frac{\alpha_K}{\Delta x} \left(\beta_{K+1} - \frac{\gamma_{K+\frac{1}{2}} - \gamma_{K-\frac{1}{2}}}{\Delta x} \right) \\ a_K = \frac{\alpha_K}{\Delta x} \left(-\frac{\beta_{K+1} + \beta_{K-1}}{2} + \frac{\gamma_{\frac{1}{2}} - \gamma_{-\frac{1}{2}}}{\Delta x} \right) \end{cases} \quad (\text{A.31})$$

At the low energy boundary one can also assume the energy current to be 0, $J = 0$, which means that no energy flows in and out of the system. Physically this means that at the minimal energy the outward current from energy losses balances exactly

the inward reacceleration current. This condition thus depends on the coefficients α , β and γ of the equation, and from Eq. A.17 one can infer that for very small values of γ this will create a strong gradient of u to maintain $J = 0$. This condition writes:

$$J_{-\frac{1}{2}} = 0 \quad \rightarrow \quad \begin{cases} b_0 = 1 + \frac{\alpha_0}{\Delta x} \left(\frac{\beta_0}{2} + \frac{\gamma_{\frac{1}{2}}}{\Delta x} \right) \\ c_0 = \frac{\alpha_0}{\Delta x} \left(\frac{\beta_1}{2} - \frac{\gamma_{\frac{1}{2}}}{\Delta x} \right) \end{cases} \quad (\text{A.32})$$

At the upper bound for the energy the condition would read:

$$J_{K+\frac{1}{2}} = 0 \quad \rightarrow \quad \begin{cases} b_K = 1 + \frac{\alpha_K}{\Delta x} \left(-\frac{\beta_K}{2} + \frac{\gamma_{K-\frac{1}{2}}}{\Delta x} \right) \\ a_K = -\frac{\alpha_K}{\Delta x} \left(\frac{\beta_{K-1}}{2} + \frac{\gamma_{K-\frac{1}{2}}}{\Delta x} \right) \end{cases} \quad (\text{A.33})$$

Finally may be a even more physical condition, also used in [Evoli 2016](#) (p10), is to impose $\partial f / \partial p|_{p_0} = 0$. With our variables this condition translate to:

$$\left. \frac{\partial f}{\partial p} \right|_{p_0} = \left. \frac{\partial}{\partial p} \left(\frac{\phi}{p^2} \right) \right|_{p_0} = \left. \frac{\partial}{\partial p} \left(\frac{u}{pE} \right) \right|_{E_0} = 0. \quad (\text{A.34})$$

In terms of $x = \ln E_k$, one ends up with the following condition:

$$\left. \frac{\partial u}{\partial x} \right|_{x_0} = \frac{E_{k,0}}{E_0} \left(1 + \frac{E_0^2}{p_0^2} \right) u(x_0) = \delta_0 u(x_0). \quad (\text{A.35})$$

If we discretise this condition we get:

$$\left. \frac{\partial u}{\partial x} \right|_{x_0} = \frac{u_1 - u_{-1}}{2\Delta x} = \delta_0 u_0. \quad (\text{A.36})$$

Injecting this condition into the differentiation scheme, its leads to the following first coefficients in the matrice M:

$$\left. \frac{\partial f}{\partial p} \right|_{p_0} = 0 \quad \rightarrow \quad \begin{cases} b_0 = 1 + \frac{\alpha_0}{\Delta x} \left(\beta_{-1} \Delta x \delta_0 + \frac{\gamma_{\frac{1}{2}} + \gamma_{-\frac{1}{2}} + \gamma_{-\frac{1}{2}} 2\Delta x \delta_0}{\Delta x} \right) \\ c_0 = \frac{\alpha_0}{\Delta x} \left(\frac{\beta_1 - \beta_{-1}}{2} - \frac{\gamma_{\frac{1}{2}} + \gamma_{-\frac{1}{2}}}{\Delta x} \right) \end{cases} \quad (\text{A.37})$$

Model	δ	$K_0[\text{kpc}^2/\text{Myr}]$	$L[\text{kpc}]$	$V_c[\text{km/s}]$	$V_a[\text{km/s}]$
MIN	0.85	0.0016	1	13.5	22.4
MED	0.70	0.0112	4	12	52.9
MAX	0.46	0.0765	15	5	117.6

Table A.3: Propagation parameters from the MIN, MED, and MAX models as chosen in Donato 2004

At the upper bound for the energy the condition would read:

$$\left. \frac{\partial f}{\partial p} \right|_{p_K} = 0 \quad \rightarrow \quad \begin{cases} b_K = 1 + \frac{\alpha_K}{\Delta x} \left(\beta_{K+1} \Delta x \delta_K + \frac{\gamma_{K+\frac{1}{2}} + \gamma_{K-\frac{1}{2}} - \gamma_{K+\frac{1}{2}} 2\Delta x \delta_K}{\Delta x} \right) \\ a_K = \frac{\alpha_K}{\Delta x} \left(\frac{\beta_{K+1} - \beta_{K-1}}{2} - \frac{\gamma_{K+\frac{1}{2}} + \gamma_{K-\frac{1}{2}}}{\Delta x} \right) \end{cases} \quad (\text{A.38})$$

This gives according to [LeVeque 1998] a second order accurate method.

The choice of the conditions (A.32, A.30 or A.37) for the lowest energy of the resolution can be view as a systematic in the prediction of a cosmic ray flux. However, we showed that beginning the numerical resolution at a sufficiently low energy –chosen to be 1 MeV– yields comparable fluxes at 100 MeV at a level of 0.1%-1% for all of these conditions. The calculation of the carbon flux for each of these three conditions is displayed Fig. A.1 using a starting energy of 1 MeV and 100 MeV. Notice that in some other numerical codes like GALPROP and PICARD they surprisingly do not seem to need any boundary condition ([Man](bottom p35) and [Kissmann 2014] (p5), respectively).

A.2.2 The example of the MIN, MED, and MAX models

In Table A.3 we recall the values of benchmark propagation models used in Donato 2004. Note that for our concerns in chapter. 2, only K_0 , δ and L are relevant, since by virtue of the generalised central limit theorem, convection and reacceleration do not affect the shape of the distribution but only its mean.

Important remark: Note that these parameters were obtained with a reacceleration coefficient K_{EE} written as:

$$K_{EE} = 2 \times \beta^2 K_{pp} = 2 \times \beta^2 \times \frac{1}{9} \frac{p^2 V_a^2}{K}. \quad (\text{A.39})$$

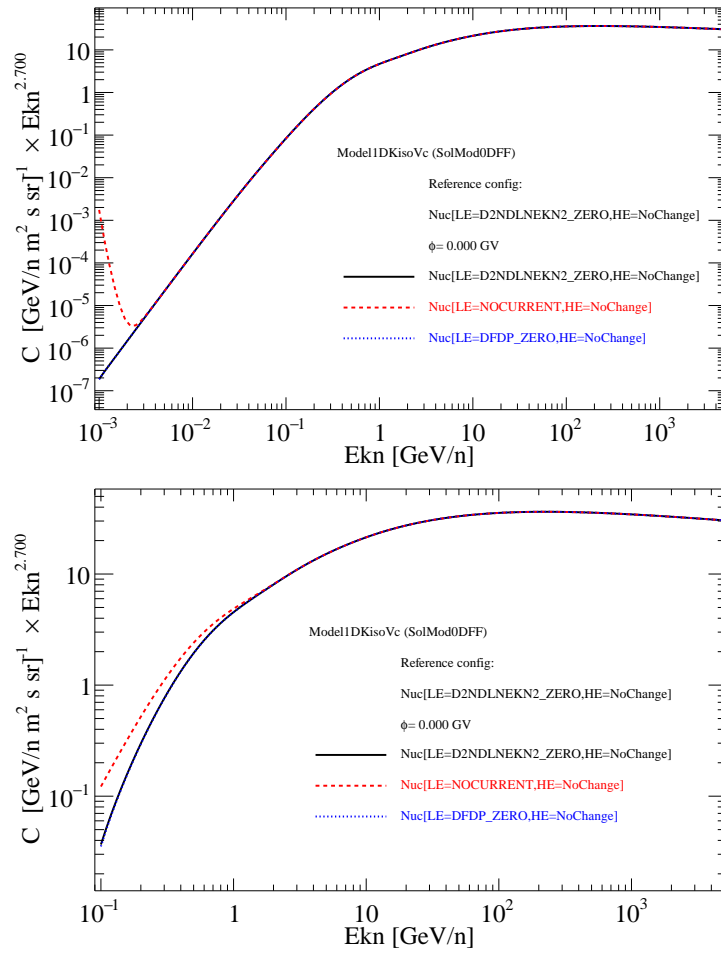


Figure A.1: Calculation of the carbon flux for each of these three conditions using a starting energy of 1 MeV (*left*) and 100 MeV (*right*). Figures obtained with USINE.

Bibliography

- [Donato 2004] F. Donato, N. Fornengo, D. Maurin, P. Salati and R. Taillet. *Antiprotons in cosmic rays from neutralino annihilation*. Phys. Rev. D, vol. 69, no. 6, page 063501, March 2004. (Not cited.)
- [Evoli 2016] C. Evoli, D. Gaggero, A. Vittino, G. Di Bernardo, M. Di Mauro, A. Ligorini, P. Ullio and D. Grasso. *Cosmic-ray propagation with DRAGON2: I. numerical solver and astrophysical ingredients*. ArXiv e-prints, July 2016. (Not cited.)
- [Kissmann 2014] R. Kissmann. *PICARD: A novel code for the Galactic Cosmic Ray propagation problem*. Astroparticle Physics, vol. 55, pages 37–50, March 2014. (Not cited.)
- [LeVeque 1998] Randall J LeVeque. *Finite difference methods for differential equations*. Draft version for use in AMath, vol. 585, no. 6, 1998. (Not cited.)
- [Man] *GALPROP Version 54: Explanatory Supplement*. http://galprop.stanford.edu/download/manuals/galprop_explanatory_supplement.pdf. Accessed: 2017-01-30. (Not cited.)
- [Maurin 2001] David Maurin. *Propagation des rayons cosmiques dans un modele de diffusion: une nouvelle estimation des parametres de diffusion et du flux d'antiprotons secondaires*. PhD thesis, Université de Savoie, 2001. (Not cited.)

On the mean galactic flux

The mean flux of cosmic rays is a very useful observable whose theoretical derivation is relatively simple in the high-energy limit where diffusion is the dominant propagation mechanism. Two simplifications are commonly used in the literature and lead to very good approximations compared to more sophisticated models.

To commence, sources are assumed to lie within an infinite plane with half-thickness h sandwiched by two larger diffusion volumes with height L . Inside this magnetic halo, propagation is characterized by the diffusion coefficient K . The so-called *infinite slab* model requires in addition to consider the disk as infinitesimally thick. In the steady state regime, the total mean flux satisfies the equation

$$-K \nabla^2 \langle \Psi \rangle_{slab} = 2 h \delta(z) Q . \quad (\text{B.1})$$

Assuming that the CR density vanishes at the vertical boundaries $z = \pm L$, one readily gets

$$\langle \Psi \rangle_{slab} = Q \frac{h L}{K} \equiv Q \tau_D \quad \text{with} \quad [Q] = [\text{time}]^{-1} [\Psi] . \quad (\text{B.2})$$

In this equation, Ψ is homogeneous to the density of cosmic rays expressed in particles per unit of energy and of volume or, equivalently for the discussion, to the flux expressed in particles per unit of energy, time, surface, and solid angle. A simple rescaling by the factor $v_{CR}/4\pi$, where v_{CR} is the cosmic ray velocity, can be applied to switch from one quantity to the other. Choosing the former, the injection rate Q is interpreted as the number of particles injected per unit of energy, time and volume in the Galaxy. It may be useful to factorize $Q = q \nu / V_{MW}$. Here, the spectrum q of the particles injected by a single source is expressed in particles per unit of energy. Sources appear with a rate ν . Assuming these are supernova remnants implies a value of three SN explosions per century. Finally, the Galactic disk with half-thickness h and radius R encompasses a volume $V_{MW} = 2 \pi h R^2$.

To go a step forward, we may now assume that the sources are no longer pinched inside an infinitesimally thick Galactic disk, but are spread over a vertical distance of $2h$. As long as steady state holds, the total mean flux now satisfies the equation

$$-K \nabla^2 \langle \Psi \rangle_{vol} = \Theta(h - |z|) Q , \quad (\text{B.3})$$

whose solution, derived with the same vertical boundary conditions as previously, may be expressed as

$$\langle \Psi \rangle_{vol} = \langle \Psi \rangle_{slab} \left(1 - \frac{h}{2L} \right) . \quad (\text{B.4})$$

Sources extend now along the vertical direction and are no longer packed at $z = 0$. They yield a flux $\langle \Psi \rangle_{vol}$ slightly smaller than $\langle \Psi \rangle_{slab}$.

The theoretical expression of the probability $P(\Psi)$ is provided by the stable law of Eq. (2.26). Its argument depends on the average value $\langle \Psi \rangle_{th}$ which should be consistently derived within the Milky Way model to which the pdf $P(\Psi)$ is associated. Although expressions (B.2) and (B.4) are excellent approximations to the theoretical mean $\langle \Psi \rangle_{th}$, they should not be used. In particular, the solid green (2D) and dashed red (3D) curves of Fig. 2.8 and 2.10 are based on the assumption that the Galactic disk has radius R and that sources cannot be older than $T = 3\tau_0$. Furthermore, all sources contribute to the theoretical average $\langle \Psi \rangle_{th}$, including those lying outside the light cone of the observer. Causality is not implemented and the heavy tail behavior, which the theoretical pdf $p(\psi)$ should exhibit, is not suppressed.

In order to compare the theoretical pdf $P(\Psi)$ with the simulations, $\langle \Psi \rangle_{th}$ needs to be calculated from the convolution of the source term $\mathcal{Q}(\mathbf{x}_S, t_S)$ with the diffusive propagator \mathcal{G}_B over the volume of space-time \mathcal{V} covered by the simulation

$$\mathcal{V} = V_{MW} \times 3\tau_0 \quad \text{where} \quad \tau_0 \equiv \frac{\pi}{4} \frac{L^2}{K}. \quad (\text{B.5})$$

This typical time τ_0 corresponds to the integration time needed to recover the $\langle \Psi \rangle_{slab}$ under the simplified assumption that no leakage happens at the ridges of the Galaxy. More explicitly, under this assumption, the contribution of one source $\langle \psi \rangle_T$ averaged over a time T writes:

$$\begin{aligned} \langle \psi \rangle_T &= q \int^T d\tau_S \int_{V_{MW}} d\mathbf{r}_S 2h\delta(z - z_s)\mu \mathcal{G}_{NB}(\mathbf{r}_S, \mathbf{r}, \tau_S \rightarrow 0) \\ &= \frac{q}{\pi R^2 T} \int^T d\tau_S \underbrace{\int_0^R 2\pi r_S dr_S \left\{ \frac{\exp(-r_S^2/4K\tau_S)}{4\pi K\tau_S} \right\}}_{=1 \text{ when } R \rightarrow \infty} \underbrace{\int_{-L}^L dz_s \delta(z - z_s) \mathcal{G}_{1D}(\tau_S, z, z_s)}_{\text{for } z=0} \\ &= \frac{q}{\pi R^2 T} \int_0^T d\tau_S \frac{1}{\sqrt{4\pi K\tau_S}} \\ &= \frac{2q}{\pi R^2} \frac{1}{\sqrt{4\pi KT}} \end{aligned}$$

Then, as $N = \nu T$, one recover the total flux $\langle \Psi \rangle_{slab}$ for $T \equiv \tau_0$ so that:

$$\langle \Psi \rangle_{slab} = N \langle \psi \rangle_{\tau_0} = \frac{\nu q}{\pi R^2} \sqrt{\frac{\tau_0}{\pi K}} \Rightarrow \tau_0 = \frac{\pi}{4} \frac{L^2}{K} \quad (\text{B.6})$$

This let define a finite typical time overwhich the simulations should be run. We actually choose $3\tau_0$ for which $\langle \psi \rangle_{3\tau_0}$ is quite close to $\langle \psi \rangle_{T \rightarrow \infty}$ as shown in Fig. B.1 or Table B.1.

The theoretical average corresponding to the 2D case, where the sources are pinched inside an infinitesimally thick disk, is denoted by $\langle \Psi \rangle_{2D, R, T=3\tau_0}$ whereas

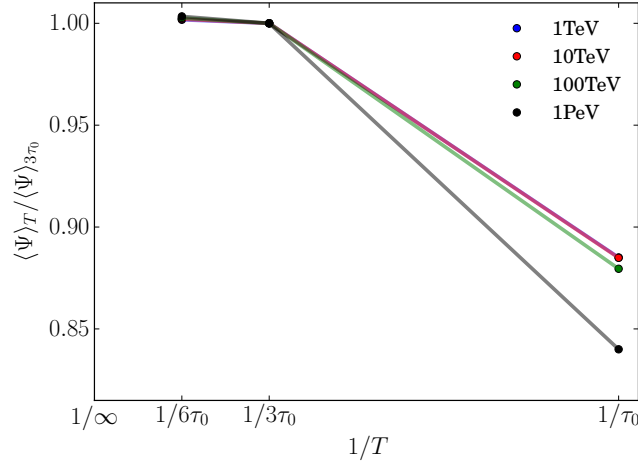


Figure B.1: Convergence of the mean flux in the simulation with respect to the inverse of the integration times τ_0 , $3\tau_0$ and $6\tau_0$. The ratio $\langle \Psi \rangle_T / \langle \Psi \rangle_{3\tau_0}$ is displayed for different energies. The points at 1TeV and 10TeV overlap.

the result corresponding to the 3D case, for which the sources are vertically spread over a distance $2h$, is denoted $\langle \Psi \rangle_{3D, R, T=3\tau_0}$. These quantities are calculated as follows

$$\left. \begin{aligned} \langle \Psi \rangle_{3D, R, T=3\tau_0} \\ \langle \Psi \rangle_{2D, R, T=3\tau_0} \end{aligned} \right\} = \frac{q\nu}{V_{\text{MW}}} \times \int_0^{3\tau_0} d\tau_S \int_0^R 2\pi r_S dr_S \left\{ \frac{\exp(-r_S^2/4K\tau_S)}{4\pi K\tau_S} \right\} \\ \times \int_{-h}^h dz_S \mathcal{V}_B(z_S, \tau_S) \times \begin{cases} 1 & \text{in 3D, or} \\ 2h\delta(z_S) & \text{in 2D.} \end{cases} \quad (\text{B.7})$$

The function $\mathcal{V}_B(z_S, \tau_S)$ describes the CR vertical propagation and takes into account the boundary conditions at $z = \pm L$. It gauges the contribution at the observer located at $z = 0$ from a source that exploded a time τ_S ago at $z = z_S$. It can be expressed as the series

$$\mathcal{V}_B(z_S, \tau_S) = \sum_{n=-\infty}^{+\infty} (-1)^n \frac{\exp(-z_n^2/4K\tau_S)}{\sqrt{4\pi K\tau_S}} \quad (\text{B.8})$$

where the n th image is located at $z_n = 2Ln + (-1)^n z_S$.

Hereafter, we show that to recover the average of the slab model, the integral for

the 2D case needs to be extended to an infinite age T and Galactic radius R .

$$\begin{aligned}
\langle \Psi \rangle_{2D} &= q \int_0^\infty d\tau_S \int_{V_{MW}} d\mathbf{r}_s 2h\delta(z - z_s)\mu_s \mathcal{G}_B(\mathbf{r}_s, \mathbf{r}, \tau_S \rightarrow 0) \\
&= \frac{q \nu}{\pi R^2} \int_0^\infty d\tau_S \int_0^R 2\pi r_S dr_S \left\{ \frac{\exp(-r_S^2/4K\tau_S)}{4\pi K\tau_S} \right\} \underbrace{\int_{-L}^L dz_s \delta(z - z_s) \mathcal{V}_B(\tau_S, z, z_s)}_{\text{for } z=0} \\
&= \frac{q \nu}{\pi R^2} \int_0^\infty d\tau_S \int_0^R 2\pi r_S dr_S \left\{ \frac{\exp(-r_S^2/4K\tau_S)}{4\pi K\tau_S} \right\} \mathcal{V}_B(\tau_S, 0, 0) \\
&= \frac{2q\nu}{\pi R^2 L^3} \int_0^\infty d\tau_S \int_0^R r_S dr_S \eta \exp\left(-\frac{r_S^2}{L^2}\eta\right) \sum_{n=1}^\infty \exp\left(-\frac{1}{4\eta}\pi^2\left(n - \frac{1}{2}\right)^2\right) \text{ with } \eta = \frac{L^2}{4K\tau_S}, \\
&= \frac{q\nu}{\pi R^2 L} \int_0^\infty d\tau_S \sum_{n=1}^\infty \exp\left(-\frac{1}{4\eta}\pi^2\left(n - \frac{1}{2}\right)^2\right) \text{ by taking } R \rightarrow \infty, \\
&= \frac{q\nu L}{4\pi R^2 K} \sum_{n=1}^\infty \int_0^\infty d\eta \frac{1}{\eta^2} \exp\left(-\frac{1}{4\eta}\pi^2\left(n - \frac{1}{2}\right)^2\right) \\
&= \frac{q\nu L}{\pi^3 R^2 K} \sum_{n=1}^\infty \underbrace{\frac{1}{\left(n - \frac{1}{2}\right)^2}}_{\pi^2/2} \\
&= \frac{q\nu L}{2\pi R^2 K}
\end{aligned}$$

Hence, we may write $\langle \Psi \rangle_{slab} \equiv \langle \Psi \rangle_{2D, R=\infty, T=\infty}$. When the same integration limits are taken for the 3D case, we recover the expression of $\langle \Psi \rangle_{vol}$, which may also be defined as $\langle \Psi \rangle_{3D, R=\infty, T=\infty}$.

In Table B.1, we report the average fluxes calculated with the approaches discussed above, and compare them with the simulations. Below 10 TeV, all the values are very close to each other within $\mathcal{O}(1\%)$. Above that energy, the mean from the simulations $\langle \Psi \rangle_{sim}$ becomes significantly lower than the theoretical one when the light cone cut-off is imposed on simulations. This effect can be checked by calculating the average flux $\langle \Psi \rangle_{sim}^{NC}$ yielded by numerical simulations for which no causality constraint has been imposed. We get results that are always within the one sigma Poissonian error of theoretical one $\langle \Psi \rangle_{3D, R, T=3\tau_0}$.

Ek (GeV)	$\langle\Psi\rangle_{slab} \equiv \langle\Psi\rangle_{2D, R=\infty, T=\infty}$	$\langle\Psi\rangle_{2D, R, T=3\tau_0}$	$\langle\Psi\rangle_{vol} \equiv \langle\Psi\rangle_{3D, R=\infty, T=\infty}$
10^2	1.605e-01	1.599e-01	1.585e-01
10^3	2.070e-04	2.062e-04	2.044e-04
10^4	2.612e-07	2.601e-07	2.579e-07
10^5	3.289e-10	3.270e-10	3.248e-10
10^6	4.141e-13	4.105e-13	4.089e-13
Ek (GeV)	$\langle\Psi\rangle_{3D, R, T=3\tau_0}$	$\langle\Psi\rangle_{sim}$	$\langle\Psi\rangle_{sim}^{NC}$
10^2	1.579e-01	1.580e-01	1.579e-01
10^3	2.037e-04	2.036e-04	2.037e-04
10^4	2.571e-07	2.554e-07	2.577e-07
10^5	3.236e-10	3.075e-10	3.241e-10
10^6	4.072e-13	2.923e-13	4.071e-13

Table B.1: In this table we report the theoretical average of the flux calculated within the slab model $\langle\Psi\rangle_{slab}$, the slab model taking into account the thickness of the source disk $\langle\Psi\rangle_{vol}$, the 2D model in the conditions of the simulations $\langle\Psi\rangle_{2D, R, T=3\tau_0}$, and the 3D model in the conditions of the simulations $\langle\Psi\rangle_{3D, R, T=3\tau_0}$. We also show the average of the flux obtained from the simulations without the contribution of non-causal sources $\langle\Psi\rangle_{sim}$, and with their contributions $\langle\Psi\rangle_{sim}^{NC}$. The values are given in units of $[q_0.kpc^{-2}.str^{-1}]$ for the kinetic energies probed by the simulations.

Primary fits for antiproton computation

To fit the AMS-02 p and α fluxes we used the following rigidity dependent function (in particles $\text{m}^{-2} \text{s}^{-1} \text{sr}^{-1} \text{GV}^{-1}$):

$$\Phi = C \cdot (1 - \beta e^{\lambda R}) \cdot \left(\frac{R}{R + \phi_F} \right)^2 \cdot (R + \phi_F)^\gamma \cdot \left[1 + \left(\frac{R + \phi_F}{R_B} \right)^{\frac{\Delta\gamma}{s}} \right]^s. \quad (\text{C.1})$$

We proceed in two steps. First γ , $\Delta\gamma$, R_B , s are fixed using the high energy part ($R > 45$ GV) of the spectrum. Then C , α and β are determined over the all energy range. The value of the Fisk potential which gives the best χ^2 for our fits is $\phi_F = 0.62$ GV, the upper bound of the interval set in [Aguilar 2015]. The values of the best-fit parameters are reported in table C.1.

	p	α
C	23566 ± 30	4075 ± 2
λ	-0.519 ± 0.007	-0.163 ± 0.004
β	1.21 ± 0.02	0.41 ± 0.02
γ	-2.849 ± 0.002	-2.795 ± 0.009
R_B	355 ± 33	284 ± 38
$\Delta\gamma$	0.146 ± 0.02	0.162 ± 0.009
s	0.0325 ± 0.0131	0.078 ± 0.035
χ_{ndof}^2	$29.02/(73-7)$	$2.62/(54-7)$

Table C.1: **Best-fit values for p and α fluxes.**

Bibliography

- [Aguilar 2015] M. Aguilar, D. Aisa, B. Alpat, A. Alvino, G. Ambrosi, K. Andeen, L. Arruda, N. Attig, P. Azzarello, A. Bachlechner and et al. *Precision Measurement of the Proton Flux in Primary Cosmic Rays from Rigidity 1 GV to 1.8 TV with the Alpha Magnetic Spectrometer on the International Space Station*. Physical Review Letters, vol. 114, no. 17, page 171103, May 2015. (Not cited.)

Abstract: One hundred years ago, pioneering observations of air ionization revealed that the Earth is showered with particles coming from the Galaxy and beyond. Because of their high energies, these particles, or cosmic rays, are still a crucial tool in the field of particle physics, complementary to man-made accelerators. From an astrophysical point of view, the origin of cosmic rays and the mechanisms which accelerate them remain poorly understood. The current paradigm involves the sporadic production of the particles, associated with expanding shock waves from dying stars, or supernova remnants (SNRs).

Recent experiments (notably PAMELA and, more recently, AMS-02) are ushering us into a new era of measurements of cosmic ray fluxes with greatly reduced statistical uncertainties. In this dissertation, we propose and investigate new theoretical refinements of our predictions to fully benefit from these advances.

After a general introduction on cosmic ray physics, we first focus on the so-called primary species, which are directly produced by SNRs. In the context of precision measurements, the discrete nature of the SNRs in space and time, together with our substantial ignorance of their precise age and location (with the possible exception of the nearest and most recent) results in significant uncertainties in the predictions of fluxes on Earth. Until now, the conventional approach has relied on average trends. Here, we elaborate a statistical theory in order to compute the probability of measuring the actual flux, with respect to the ensemble average. Using the generalized version of the central limit theorem, we demonstrate that the probability distribution function of the flux is intimately related to the source distribution and follows a stable law with a heavier tail than the Gaussian distribution. Not only can our theoretical framework be extended to other cosmic ray observables, such as the lepton flux, it also can be enhanced to include a more comprehensive description of the correlations between the sources. Moreover, the method which we have developed may be applied to a variety of problems in physics/astrophysics involving heavy tail distributions.

Secondly, we concentrate on secondary CRs, for example the boron nuclei, which are thought to be produced only by the collisions of cosmic rays on the interstellar medium. More precisely, the boron to carbon flux ratio is a traditional tool used to understand and gauge the propagation of cosmic rays in the Galaxy. Hence a precise measurement of this ratio leads to stringent constraints on the propagation scenario. However we show that this theoretical calculation strongly depends on where these secondary species are produced, as well as on the chosen set of nuclear cross-sections. Hence, we have shown that there is at least 20% uncertainty amongst these propagation parameters. Following novel data from AMS-02 that has just been published, we present the starting points of a comprehensive analysis for which we use the semi-analytical code USINE.

Finally, these high precision measurements offer new opportunities for a number

of astroparticle problems. The third and final part of the thesis targets one such problem, indirect dark matter searches. Antimatter cosmic rays are thought to be secondary species and their relatively low flux make them the perfect target to look for rare processes, such as dark matter annihilation. Nonetheless, predictions of the expected background rely on the precise modelling of cosmic ray propagation and interactions in the Galaxy. We assess them under simplified assumptions and discuss two studies where we re-evaluate the antiproton and the positron fluxes in light of the new AMS-02 data. Finally, we discuss the implications of our results on dark matter and astrophysics.

Keywords: Cosmic rays phenomenology, local sources, stable laws, boron over carbon ratio, indirect dark matter searches.//

French summary

Il y a tout juste cent ans que les premières mesures du taux d'ionisation de l'air dévoilaient que la terre est sans cesse bombardée par une pluie de particules énergétiques provenant de la Galaxie comme des confins de l'Univers. Ces particules relativistes que l'on appelle rayons cosmiques (CRs) furent un des premiers outils de la découverte de nouvelles particules et leurs interactions. Elles restent cependant d'une importance fondamentale en physique des particules, où les énergies atteintes par les collisionneurs restent bien inférieures au maximum observé dans les CRs. D'un point de vue astrophysique, l'origine des CRs et leur mécanismes d'accélération restent très peu connus.

Le paradigme actuel suppose une injection sporadique des CRs accélérés par la propagation d'ondes de choc déclenchées par la mort de certaines étoiles. On retrouve ces conditions notamment dans les rémanents de supernovae (SNRs). Les CRs sont des particules chargées, ils subissent donc les effets du champ magnétique galactique. Les moins énergétiques restent confinés au sein de la Galaxie pendant plusieurs millions d'années. Ils suivent une trajectoire de type "marche aléatoire", pilotée par la turbulence électromagnétique. Phénoménologiquement leur mouvement s'apparente à celui de particules diffusant dans un fluide sous l'action du mouvement brownien. Les particules les plus énergétiques, dont le rayon de Larmor est de l'ordre de grandeur, ou supérieur à celui de la Galaxie, s'échappent rapidement de son influence magnétique. La vitesse de diffusion est donc le coefficient de diffusion K dépendent donc de l'énergie des particules. Dans la gamme d'énergie qui nous intéresse dans cette thèse, du GeV au TeV, il est possible de montrer qu'il prend la forme suivante :

$$D = D_0 \beta^\eta \left(\frac{\mathcal{R}}{1\text{GV}} \right)^\delta, \quad (\text{D.1})$$

où $R = p/Z$ est la rigidité de la particule, K_0, η et δ des paramètres dont les valeurs typiques sont ($10^{-2} \text{kpc}^2 \cdot \text{Myr}^{-1}$, 1, 0.5). De la même manière que la diffusion, d'autres processus physiques tels que la fragmentation des CRs sur le milieu interstellaire ou la convection, modifient la concentration des CRs dans la Galaxie. Il convient de déterminer précisément les paramètres qui les contrôlent dès que l'on souhaite faire une prédiction du flux de rayon cosmique.

Et pour cause, les mesures récentes des flux de CRs (par les expériences PAMELA et AMS-02, par exemple) inaugurent une nouvelle ère de précision, dans la mesure où les incertitudes statistiques sont considérablement réduites. Dans ce mémoire de thèse, nous proposons et approfondissons de nouvelles pistes théoriques de manière à maximiser l'information extraite de ces nouvelles données.

Raffinement des prédictions pour les espèces primaires

Après une introduction générale sur la physique des CRs, on se concentre sur les espèces dites primaires, qui sont produites directement par les SNRs. Comparée aux échelles spatio-temporelles du processus de diffusion, la production de CRs par un SNR doit être vue comme une injection ponctuelle de particules dans l'espace et dans le temps. De ces objets, nous n'avons qu'une connaissance parcelaire des plus proches et des plus jeunes d'entre eux. Le flux de CRs sur Terre provient en fait d'une myriade de SNRs dont pour la plupart, nous ne connaissons ni l'âge, ni la distance. Sa prédiction est donc affectée par une incertitude théorique qui nécessite d'être estimée.

Jusqu'alors ces prédictions se contentent d'établir la moyenne d'ensemble de ce flux, c'est à dire la valeur du flux moyennée sur plusieurs réalisations de la Galaxie, chacune avec sa propre disposition de sources dans l'espace et dans le temps. Dans le monde des possibles, la configuration dans laquelle nous vivons nous donne le flux que nous mesurons actuellement. Dans cette thèse nous développons la théorie statistique qui permet de calculer la probabilité de mesurer un tel flux, en supposant un flux moyen. Nous sommes amenés à utiliser une version généralisée du théorème de la limite centrale, et nous montrons que la loi de probabilité est intimement reliée à la distribution des sources et converge vers une loi stable. Cette dernière diffère de la gaussienne par sa queue lourde en loi de puissance. Suivant le choix de la distribution des sources, 2D (sources éparpillées dans un disque galactique) ou 3D (dans un cylindre), nous notons deux comportements extrêmes différents pour la queue de la loi de probabilité qui converge respectivement vers une loi stable d'indice $4/3$ et une autre d'indice $5/3$. Bien que certaines hypothèses du théorème centrale limite généralisé ne sont pas satisfaites, par des simulations numériques, nous avons vérifié que la loi de probabilité converge bien vers la loi 2D puis vers la loi 3D établies théoriquement. Ceci est illustré sur la figure D.1 pour une énergie de 1TeV. Il est possible de montrer que l'étalement de la loi de probabilité augmente avec l'énergie, où l'effet de l'environnement local est important.

La loi stable peut donc être utilisée pour quantifier la probabilité de mesurer un certain flux étant donné un flux moyen. Sur la figure D.2 est présenté l'exemple du flux de protons, dont la mesure à haute énergie dévie de l'extrapolation en loi de puissance à basse énergie. En utilisant les modèles de propagation classiques et la loi stable, on peut montrer que moins de 1% des configurations reproduisent une telle fluctuation.

Le cadre théorique développé ici peut non seulement être étendu à d'autres observables du rayonnement cosmique, mais aussi enrichi en incluant une description plus complète des corrélations entre les sources. De plus la méthode que nous avons développée peut être appliquée à d'autres problèmes de physique/astrophysique impliquant des distributions à queue lourde.

Raffinement des prédictions pour les espèces secondaires

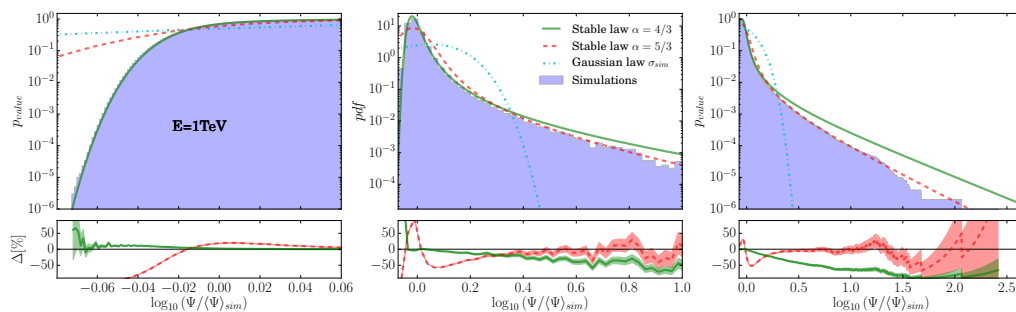


Figure D.1: Histogrammes des cumulantes droite et gauche de la loi de probabilité (au centre) correspondant à 10^6 réalisations Monte Carlo de population galactiques. Le modèle de propagation MED est utilisé. La courbe continue verte représente la prédiction théorique pour une distribution 2D des sources et la rouge pour une distribution 3D. Les résidus sont aussi affichés ainsi que l'incertitude poissonnienne à $1-\sigma$.

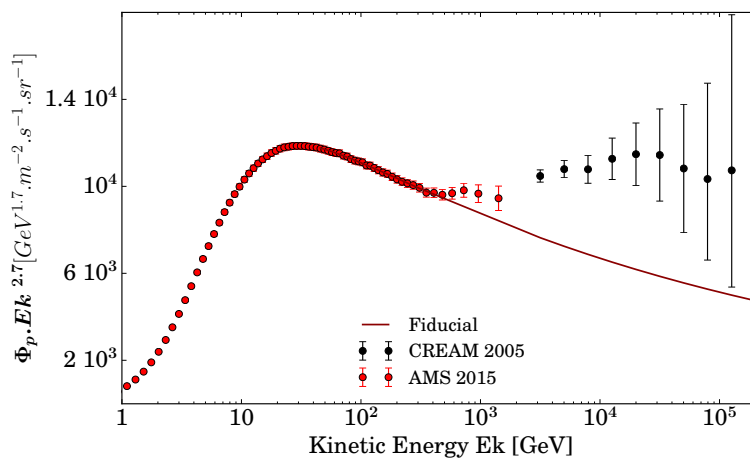


Figure D.2: Flux de protons mesuré par AMS-02 et CREAM, ainsi qu'un ajustement du spectre en loi de puissance entre 45 GeV et 200 GeV.

Deuxièmement, nous nous penchons sur les CRs dits secondaires (comme le bore), dont on pense qu'ils sont produits par les collisions des espèces primaires sur le milieu interstellaire. Plus précisément nous nous concentrons sur le rapport du flux du bore sur celui du carbone qui est traditionnellement utilisé pour comprendre la propagation des CRs. Dans le cas des hautes énergies (au dessus de 10GeV) où le processus de diffusion domine, on peut montrer qu'il est directement proportionnel

à l'inverse du coefficient de diffusion :

$$\frac{\mathcal{J}_B}{\mathcal{J}_C} \propto \frac{1}{D(R)}. \quad (\text{D.2})$$

Ainsi on s'attendrait à ce que des mesures extrêmement précises de ce rapport résultent de fortes contraintes sur les scénarios de propagation. Malheureusement il n'en est rien, et nous montrons que le calcul théorique dépend fortement d'hypothèses telles que le lieu de production des secondaires et du choix des sections efficaces d'interaction. Sur la figure D.3 est illustrée la variation relative de δ et D_0 , à gauche : lorsqu'une petite fraction de bore primaire est ajoutée, normalisée par rapport au carbone ; à droite : lorsque les sections efficaces de production $\sigma_{a \rightarrow b}$ et de destruction σ_a sont modifiées de manière anti-corrélées. Nous estimons à au moins 20 % les incertitudes sur les paramètres de propagation dérivés jusqu'à maintenant.

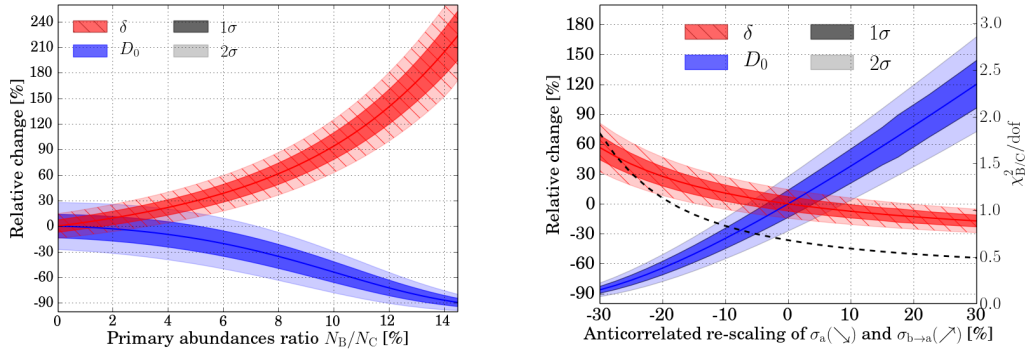


Figure D.3: Effet relatif sur les paramètres de propagation de l'ajout d'une composante primaire de bore ou d'une renormalisation des sections efficaces.

En décembre dernier l'expérience AMS-02 a réactualisé la mesure du B/C avec une précision inégalée. Dans cette thèse nous présentons les points de départ de notre nouvelle analyse pour laquelle nous utilisons le code semi-analytique USINE. Nous mettons en évidence une probable brisure du coefficient de diffusion au delà d'une rigidité caractéristique R_c . Celui-ci est alors paramétré de la manière suivante :

$$D(R) = D_0 \frac{R^\delta}{\left(1 + \left(\frac{R}{R_c}\right)^{-\Delta\gamma/s}\right)^s}. \quad (\text{D.3})$$

Ce changement de pente permet d'expliquer celui observé dans le flux de protons et celui d'hélium autour de 300GV. Plusieurs développements théoriques prédisent une telle brisure. Certains évoquent une transition du régime de turbulence dominé à basse énergie par les ondes d'alfvén générées par les rayons cosmiques eux même, et à haute énergie par la turbulence de l'injection des ondes de SNRs.

Recherche de matière noire à l'aide des rayons cosmiques d'anti-matière

Enfin, dans une troisième partie, nous utilisons ces données de précision pour réactualiser les analyses portant sur la recherche indirecte de matière noire. En effet, on pense que les CRs d'antimatière sont au même titre que le bore, des particules secondaires. La prédiction de leur fond astrophysique repose sur une connaissance précise de la propagation des CRs et de leurs interactions dans la Galaxie. Nous les traitons ici sous les hypothèses habituelles et réévaluons les flux de positrons et d'antiprotons à la lumière des nouvelles données d'AMS-02.

Dans le cas des positrons, le flux mesuré est largement au dessus de toutes les prévisions théoriques standards et nécessite d'invoquer de nouveaux mécanismes de production. L'hypothèse actuelle la plus probable invoque des sources astrophysiques, les pulsars, dont les plus proches et les plus jeunes contribueraient de manière significative au flux de positrons à haute énergie. Une autre explication pourrait être fournie par la matière noire astrophysique dont une fraction s'annihilerait en particules du modèle standard, notamment en positrons. Ces deux explications ont tout d'abord été mises à l'épreuve sur la fraction positronique à haute énergie ($>10\text{GeV}$), et ce sont révélées être viables bien que fortement contraintes. Pour l'hypothèse des pulsars, nous avons identifié cinq pulsars référencés, suffisamment proche dans l'espace et dans le temps, pour que chacun puisse expliquer à lui seul l'excès de positrons observé. Dans le cas de la matière noire, seule une annihilation en quatre leptons (taus et électrons) pour une masse entre 500GeV et 1TeV résiste alors aux limites contraignantes données par les rayons gamma. Cette conclusion valable pour le modèle MED reste cependant très dépendante du modèle de propagation choisi. La figure D.4 illustre le type d'ajustement réalisé pour le cas des pulsars à gauche et de la matière noire à droite.

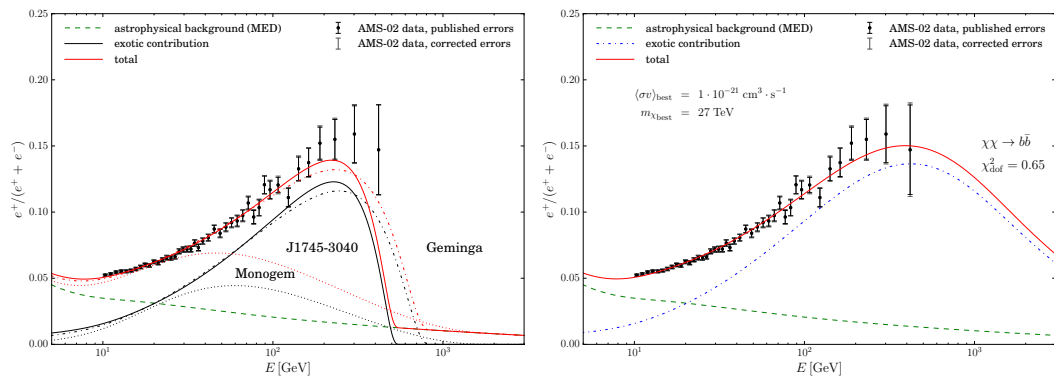


Figure D.4: Ajustement de la fraction positronique au dessus de l'énergie de 10GeV dans l'hypothèse pulsar (à gauche) ou matière noire (à droite). La prédiction de secondaires est en verte, celle des primaires en noir et le flux total en rouge. Pour le cas des pulsars la contribution de trois pulsars différents est représentée. Pour la matière noire ils s'agit du canal d'annihilation en $b\bar{b}$. Le modèle MED est le modèle de propagation utilisé.

Dans cette dernière analyse, on se focalisait sur la fraction positronique à haute énergie ($>10\text{GeV}$). Cette limitation à haute énergie nous était imposée par notre méthode de résolution semi-analytique. Le développement d'une nouvelle méthode, dites "pinching method" nous a permis de tenir compte des données de basses énergies du flux de positrons et de tester leur adéquation avec l'hypothèse matière noire. Nous avons alors montré que l'annihilation de la matière noire en une combinaison de particules du modèle standard, ne peut expliquer le flux de positrons observé, et ce quelque soit le modèle de propagation choisi. Sur la figure D.5 est représenté le meilleur ajustement obtenu, celui-ci ne permet pas de reproduire les hautes et les basses énergies simultanément. Ce résultat important nous permet donc de rejeter indépendamment l'explication invoquant la matière noire pour ces canaux d'annihilation.

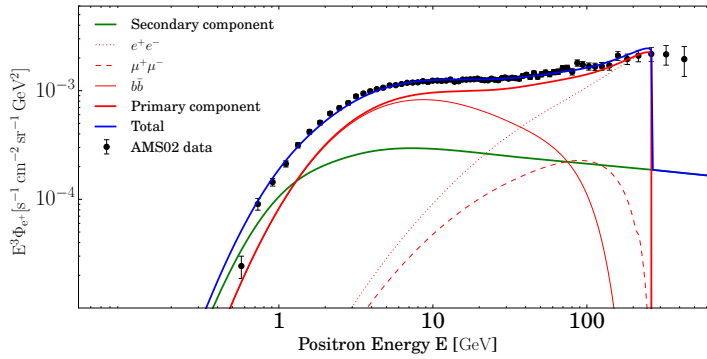


Figure D.5: Meilleur ajustement du flux de positrons avec une composante secondaire (vert) et une composante primaire (rouge) issue de l'annihilation de particules de matière noire en particules du modèle standard. Les rapports d'embranchement des différents canaux ainsi que la section efficace d'annihilation sont des paramètres libres.

Concernant les antiprotons, aucun véritable excès des données, par rapport à la prédiction des secondaires, n'a jusqu'alors été reporté. Avec la parution des nouvelles données d'AMS-02 nous avons réactualisé les incertitudes qui affectent le calcul des antiprotons secondaires, et montré (figure D.6) que les sections efficaces de production ainsi que les incertitudes sur le modèle de propagation sont les deux principaux facteurs limitant la recherche d'un signal d'annihilation de matière noire à haute énergie.

À l'heure actuelle le mystère de la matière noire reste entier. Cependant le secteur de la recherche indirecte n'a pas donné son dernier mot. Le raffinement de certaines mesures (comme celle des rayons gamma grâce à l'expérience CTA) ainsi que l'ouverture de nouveaux canaux d'observation (comme les antideutons avec l'expérience GAPS) sont ces titres très prometteurs.

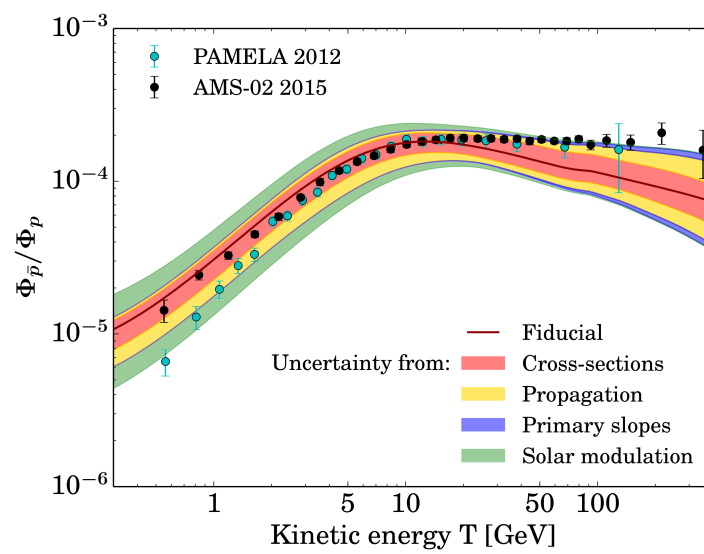


Figure D.6: Mesure de la fraction d'antiprotons sur protons de PAMELA et de AMS-02 ainsi que la prédiction secondaire où les incertitudes sont représentées par différentes bandes colorées.

